Dissertation
submitted to the
Combined Faculties of the Natural Sciences and Mathematics
of the Ruperto-Carola-University of Heidelberg, Germany
for the degree of
Doctor of Natural Sciences

Put forward by
Frederik Schönebeck
born in: Bobingen
Oral examination: 23.07.2015

VELOCITY DISPERSION MEASUREMENTS OF MILKY WAY GLOBULAR CLUSTERS WITH VLT/X-SHOOTER SPECTROSCOPY

Referees:

Prof. Dr. Eva K. Grebel

PD Dr. Sabine Reffert

ZUSAMMENFASSUNG

Wir haben 29 Kugelsternhaufen in den Magellanschen Wolken und der Milchstraße mit VLT/X-SHOOTER beobachtet, einem Spektrograph mit einer relativ hohen Auflösung und einem außergewöhnlich großem spektralen Bereich vom Ultravioletten bis hin zum nahen Infraroten. Die Beobachtungen wurden im Driftmodus durchgeführt, in dem das Teleskop während der Integration über den Haufen bewegt wird. Unsere umfangreiche Datenreduktion ermöglicht eine Ungenauigkeit $\lesssim 10\%$ in der absoluten Flusskalibration und $\lesssim 0.02$ Å in der Wellenlängenkalibration der reduzierten Spektren. Für elf Haufen ist präzise Photometrie des Hubble Weltraumteleskops verfügbar, welche benutzt wird um detaillierte synthetische zusammengesetzte Spektren zu konstruieren, die die zugrunde liegenden stellaren Populationen widerspiegeln. Diese Spektren werden als Vorlage benutzt um für jeden Haufen das Geschwindigkeitsdispersionsprofil und das Radialgeschwindigkeitsprofil zu messen. Die Radialgeschwindigkeitsmesswerte weisen auf eine geordnete Rotation von einigen Sternhaufen hin. Wir benutzen die zentralen Geschwindigkeitsdispersionen um die dynamischen Massen und Masse-zu-Leuchtkraft Verhältnisse für unsere Stichprobe zu berechnen. Der Median der Masse-zu-Leuchtkraft Verhältnisse unserer Stichprobe ist $1.7\,M_\odot\,L_\odot^{-1}$ und damit konsistent mit einer Sternhaufenmasse die sich ausschließlich aus Sternen und ihren Überresten zusammensetzt. In Verbindung mit unseren Ergebnissen sollte es zukünftigen numerischen Simulationen möglich sein Aussagen über die Massenprofile der Sternhaufen zu treffen.

ABSTRACT

We have observed 29 globular clusters in the Magellanic Clouds and the Milky Way with VLT/X-SHOOTER, a spectrograph with an exceptionally large spectral range from the ultraviolet to the near-infrared at moderately high resolution. The observations have been performed in drift-scan mode, where the telescope is slewed across the cluster during integration. Our comprehensive cascade of reduction steps allows for an uncertainty $\lesssim 10\%$ in the absolute flux calibration and $\lesssim 0.02$ Å in the wavelength calibration of the reduced spectra. For a subset of eleven clusters, for which accurate Hubble Space Telescope photometry is available, we construct detailed synthetic composite spectra based on their stellar populations, and subsequently use them as spectral templates to measure the velocity dispersion profile and radial velocity profile for each cluster. The obtained radial velocities indicate ordered rotation of some clusters. We use the central velocity dispersions to compute the dynamical masses and mass-to-light ratios for our sample. The sample median mass-to-light ratio is $1.7\,M_\odot\,L_\odot^{-1}$ and fully consistent with a cluster mass that is entirely made up of stars and their remnants. In conjunction with our kinematic results follow-up numerical simulations will help to constrain the cluster mass profiles.

To Yvonne

PUBLICATIONS

The data reduction procedures explained in Chapter 3 have been previously published in Schönebeck et al., **"The Panchromatic High-Resolution Spectroscopic Survey of Local Group Star Clusters. I. General data reduction procedures for the VLT/X-shooter UVB and VIS arm"**, 2014, A&A, 572, A13 (22 pages).

CONTENTS

Part I

INTRODUCTION

1 GLOBULAR CLUSTERS

Globular clusters (GCs) are gravitationally bound stellar systems with $10^4 - 10^7$ stars and it can be safely stated that they are among the most versatile of all astronomical composite objects. While being fascinating objects each on their own, galaxies typically contain entire GC systems with hundreds or even thousands of GCs that surround and penetrate various parts of their host galaxy. The current number estimate for the Milky Way is 157 as of 2010 (Harris 1996, 2010 edition), but there may be more hidden behind the Galactic disc and bulge. The largest number of GCs in any one galaxy in the local Universe is contained in M87, the cD giant elliptical in the Virgo cluster, and it comprises $\sim 14,000$ GCs (McLaughlin et al. 1994; Tamura et al. 2006; Harris 2009). The number of GCs per unit luminosity of the host galaxy can be parametrized as

$$S_N = N_{GC} \cdot 10^{0.4(M_V+15)}, \tag{1}$$

where M_V is the absolute V-band magnitude of the galaxy, N_{GC} is the number of GCs, and S_N is the *specific frequency* (Harris & van den Bergh 1981). S_N varies significantly between different galaxy types and typically is $\lesssim 1$ for spiral galaxies, while S0 galaxies, dwarf ellipticals and ellipticals have $2 \lesssim S_N \lesssim 6$ (lower values in isolated regions). Giant cD galxies have the highest number with $S_N \approx 10 - 20$ (Elmegreen 1999, and references therein). Several explanations have been put forward to explain this spread, including tidal stripping and interaction / starburst scenarios, but so far no conclusive answer could be given.

In this introduction we will summarize some of the main characteristics of globular clusters, with a focus on the Milky Way GC system. As this work is concerned with the measurement of GC velocity dispersions, we will concentrate on the dynamical properties of GCs, however more from a qualitative rather than a quantitative point-of-view. In Section 1.1 we will briefly discuss the possible origins of the Galactic GC system. Some of the main characteristics of the stellar populations in GCs are introduced in Section 1.2. In Section 1.3 we present a short overview of typical structural and dynamical parameters. GC formation will be briefly addressed in Section 1.4, and Section 1.5 covers several aspects on the mass-to-light ratios of GCs. Finally, Section 1.6 gives a short overview of ongoing searches for intermediate-mass black holes in GCs.

Objects as rich and comprehensive as globular clusters cannot be addressed in detail in this introduction, and thus the presented information should be merely considered a motivation to delve deeper into this fascinating topic. A nice summary that covers observational aspects of the GCs in the Local Group is presented in the article of Grebel (2000). A more theoretical view with an emphasis on stellar interactions is offered by Benacquista & Downing (2013), and the book by Spitzer (1987) can be recommended as a comprehen-

sive reference for the dynamical evolution of GCs. Readers interested in further studies of IMBHs are referred to the review by van der Marel (2004). One of the most complete sources for the topic of Galactic and extragalactic GCs, however, are the lecture notes of Carney (2001) and Harris (2001). All of these ressources have found their way into the work presented here.

1.1 GALACTIC GLOBULAR CLUSTERS

Milky Way GCs have typical ages $\gtrsim 10$ Gyr (e.g., Carretta et al. 2000; Dotter et al. 2010), implying that many of them may have witnessed the birth of the Galaxy itself. Although their lifetimes may be comparable to a Hubble time for many of them, there are yet various destruction mechanisms that can operate on significantly shorter timescales, and thus the currently observed numbers are probably only a lower limit on their initial abundance. In Figure 1 we present the distribution of all currently known Galactic GCs in the halo of the Milky Way, with a focus to the innermost ± 15 kpc. The positions are taken from the catalogue of Galactic GCs by Harris (2010) and reflect a coordinate system, in which X points toward the Galactic center (the Sun is located at X$= -8$ kpc), Y in direction of Galactic rotation, and Z toward the North Galactic pole (the Galactic center is located at $\sim 0, 0, 0$). The disk and bulge of the Milky Way are indicated with their approximate sizes (Sparke & Gallagher 2007). The GCs contained in our observational sample are highlighted in blue.

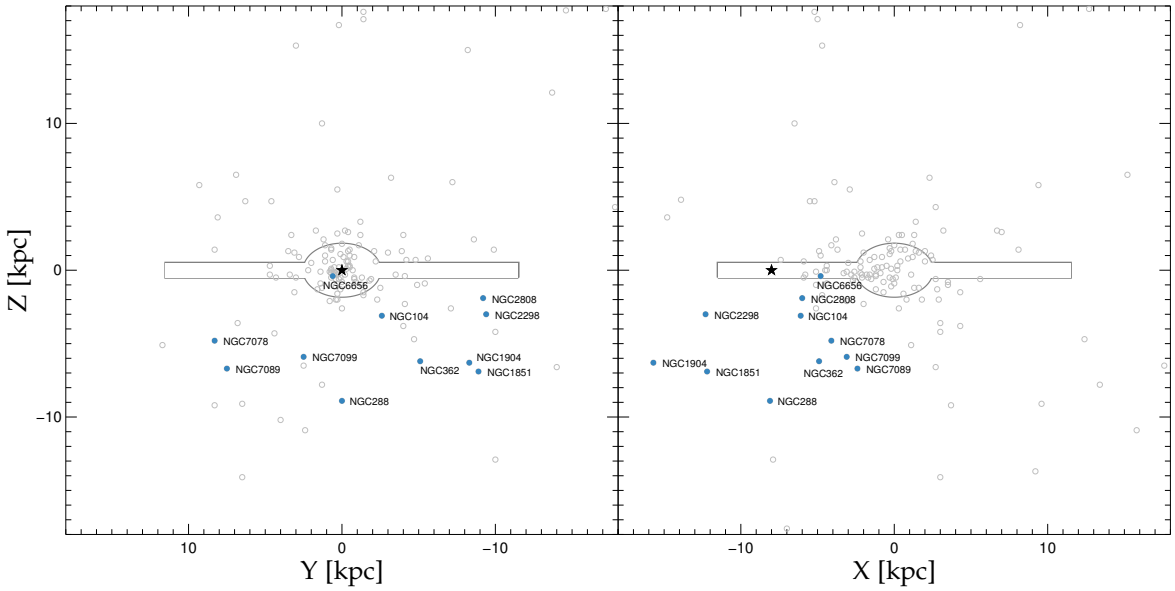

Figure 1: Space distribution of Galactic GCs (open circles; positions taken from Harris 2010). X points toward the Galactic center, Y in direction of Galactic rotation, and Z toward the North Galactic pole. The GCs contained in our sample are highlighted in blue. The disk and bulge of the Milky Way are indicated with their approximate sizes. The Sun is located at $\sim(-8, 0, 0)$ kpc and denoted by a star symbol.

The question of where and when the population of Galactic GCs was formed has been a long-standing puzzle. In a Λ cold dark matter Universe, Milky-Way-like galaxy haloes are assembled by the continous *accretion* of smaller sub-haloes (e.g., Bullock & Johnston 2005; Abadi et al. 2006), which themselves contain stars, gas, dark matter, and in some case already existing GCs. Due to the high densities in the central regions of GCs, simulations suggest that some GCs might survive the tidal forces in the accretion process (Peñarrubia et al. 2009), and become a member of the GC population of the merger system, whereas chances of survival for the accompanying dwarf galaxies are generally low (Searle & Zinn 1978; White & Rees 1978; Abadi et al. 2006). As a consequence, the resulting composite population in the merged system will contain accreted components as well as stars and clusters that formed *in situ* in the host galaxy (the largest galaxy in the considered halo). The results of Zolotov et al. (2009) indicate that at a distance $r \approx 20$ kpc from the Galactic center a transition between the relative contributions can be seen. While the outer regions are exclusively populated through accreted and disrupted satellites, the inner region contains contributions of both in-situ-formed and accreted stars.

From an observational point-of-view, the great abundance of stellar streams in the Galactic halo is widely interpreted as a clear sign for the accretion and subsequent disruption of dwarf galaxies (e.g., Ibata et al. 1994; Helmi et al. 1999; Newberg et al. 2002; Duffau et al. 2006; Belokurov et al. 2006; Grillmair 2009, 2014). Even more striking, however, are the findings of Carollo et al. (2007), who analyzed Sloan Digitial Sky Survey (SDSS) data and found evidence for a net prograde rotation of the stars in the inner halo and a net-retrograde rotation (accompanied by a significantly depleted metallicity) in the outer halo. This hints at an entirely different dynamical history of the two components, but it should be noted that a recent follow-up analysis by Schönrich et al. (2014) could not confirm these results and traced them back to improper error treatment and neglect of selection effects. They concluded that the results do not favor a dual-component Galactic halo over a single halo with substructure.

A different way to search for accretion features in the Galactic GC population is the analysis of their locii in the {age,metallicity}-plane. Recent results of Forbes & Bridges (2010) show two distinct age-metallicity relations: one sequence has a nearly constant age of $\sim$ 12.8 Gyr and spans the full metallicity range $\sim -2.5 \lesssim$ [Fe/H][1] $\lesssim -0.5$, while the other track hosts GCs with significantly younger ages (at a given metallicity) and distinctly emerges from the first sequence at intermediate metallicities [Fe/H] ≈ -1.5. The young track is dominated by GCs that are associated with the Sagittarius and Canis Major dwarf galaxies, but even after their removal several GCs remain on that sequence. More interstingly, some of these remaining GCs show retrograde orbits (a key feature of accretion) and others lie close to the Fornax-Leo-Sculptor stream (Lynden-Bell 1982). Taken together, the authors conclude that about one fourth of the Milky Way's entire GC system might have been accreted from a total of six to eight dwarf galaxies.

1 We adopt the usual spectroscopic notation, i.e., $[X] = \log[X]_{star} - \log[X]_{\odot}$ for any elemental abundance X.

1.2 STELLAR POPULATIONS

For a long time GCs have been considered to be almost ideal *Simple Stellar Populations* (SSPs), i.e., systems of coeval stars that all have the same chemical composition. In such a system the stars only differ by their masses, as determined by the initial stellar mass function (IMF). This function describes the number of stars N in a given mass bin around mass M and is usually parametrized with a broken power law of the form

$$\frac{dN}{dM} \propto M^{-\alpha_j} \Delta M, \tag{2}$$

where α_j depends on the mass range considered. It is still a matter of debate whether this IMF is universal, i.e., does not depend on environmental conditions, however there are indications that at least the number distribution of stars with $M \gtrsim 0.08\,M_\odot$ (thus excluding substellar objects like brown dwarfs) can be consistently described (Bastian et al. 2010, and references therein). One possible form is proposed by Kroupa (2001, 2002) and reads

$$\begin{aligned} \alpha_1 &= 1.3 \pm 0.5 & 0.08 \leqslant M/M_\odot < 0.5, \\ \alpha_2 &= 2.3 \pm 0.3 & 0.5 \leqslant M/M_\odot < 1, \\ \alpha_3 &= 2.3 \pm 0.7 & 1 \leqslant M/M_\odot < 1, \end{aligned} \tag{3}$$

but it is evident that the uncertainties are significant. In this context it should be noted that the present day mass function (PDMF) shows substantial differences between individual GCs, which is a clear signature of the dynamical evolution of these stellar systems (e.g., Bonatto & Bica 2012). The SSP picture has been challenged in recent years, as observations revealed significant star-to-star elemental abundance variations within individual GCs. While spectroscopic studies demonstrated that most clusters have only insignificant spread in their iron content and s-process (slow-neutron-capture-process; assumed to be a dominant effect in asymptotic giant branch (AGB) stars; see e.g., Herwig 2005; Renzini 2008 for more information on this process) elements (e.g., Carretta et al. 2009a, although it should be noted that there is evidence that some cluster do show variations in these elements, see Marino et al. 2011), signifcant variations in C, N, O, Na, and Al have been detected in all clusters studied so far (e.g., Carretta et al. 2009b; Pancino et al. 2010; Milone et al. 2012). In particular the often-observed [Na/O]-anticorrelation is thought to originate from special proton-capture chains in high-temperature H-burning in now extinct massive stars that belonged to an earlier stellar generation (Carretta et al. 2009b).

Some of these variations have been known for many decades, but recent systematic spectroscopic surveys were triggered by photometric observations in the last ~ 15 years (mainly by the Hubble Space Telescope, HST), which spectacularly revealed the presence of multiple sequences in the color-magnitude diagrams (CMDs) of several GCs. Today, light element abundance variations in GCs are widely intepreted as support for the presence of multiple stellar populations. In such a scenario, the second generation is believed to have formed from the processed / enriched material of the first generation of stars

(e.g., Conroy & Spergel 2011), although the exact nature of these enrichment processes is still a matter of debate (see Gratton et al. 2012, for a comprehensive review of multiple populations in GCs).

Evidently, this change of paradigm opens up a number of interesting questions concerning the dynamical evolution of GCs, in particular about the kinematical and spatial mixing of the various populations. Recent theoretical investigations suggest that a radial gradient in the number ratio of first and second generation stars is to be expected (Vesperini et al. 2013) and that any initial differences in the velocity dispersion and velocity anisotropy between first and second generation can survive for a Hubble time (Hénault-Brunet et al. 2015). Interestingly, Richer et al. (2013) indeed find clear kinematical differences between member stars of the different populations in NGC104, such that the bluest main-sequence (MS) population exhibits the largest proper motion anisotropy and the highest central concenration. If these results are confirmed for other clusters that are assumed to host multiple stellar populations, they will certainly help to constrain the birth history of the GCs. In this context it should be noted that in the work presented here we still consider GCs to be classical SSPs and argue that the presence of multiple stellar populations affects our velocity dispersion measurements only insignificantly (the detailed procedure is described in Chapter 4).

1.3 STRUCTURAL PARAMETERS

Globular clusters can be considered the ideal astrophysical system to study stellar dynamics. They are classically modelled as a spherical N-body system, in which the particles interact under their mutual gravitational attraction. Sphericity is generally a valid approximation, given the observed, relatively low excentricities (the mean ellipticity is 0.08; see the catalogue of Harris 2010).

GCs show a core-halo structure. The core is typically highly concentrated and strongly self-gravitating, while the surrounding halo can be very diffuse and only weakly self-gravitating. The spatial structure is typically described with three basic radii: the core radius r_c, the half-mass (half-light) radius r_h, and the tidal radius r_t. Observationally speaking, the core radius defines the location where the surface brightness drops to half its central value, the half-light radius defines the area within which half of the cluster's total luminosity is emitted, and the truncation radius defines the distance from the center, at which the cluster's stellar density is indistinguishable from the Galactic background. Typical values are of the order of some parsecs (or some tens of parsecs for r_t), with $r_c < r_h < r_t$.

There are two fundamental timescales involved in the characterization of the dynamical evolution of a GC. The *crossing time* t_{cross} denotes the time that it takes a star travelling with a typical velocity to cross a characteristic scale in the GC. Natural choices are r_c or r_h for the distance, and the velocity dispersion σ (typically taken to be the root-mean-square

deviation) for the velocity. With $r_c \approx 1\text{pc}$ and $\sigma \approx 10\,\text{km}\,\text{s}^{-1}$ (typical values from the catalogue of Harris 2010), a characteristic crossing time is

$$t_{\text{cross}} \approx 2\,\frac{r_c}{\sigma} \approx 0.1\,\text{Myr}, \tag{4}$$

but evidently it will be much shorter in the innermost core regions and significantly longer at outer radii.

The *relaxation time* t_{relax} describes the time that it takes the velocity of a star to be altered by an amount that is comparable to its original motion $|\delta v| \approx |v|$, or more specifically, the time after which the original moving direction has been deflected by 90° (Spitzer 1987; Sparke & Gallagher 2007). This timescale thus predicts when a GC is expected to lose the memory of its initial conditions and it can be shown that the mean relaxation time is (Spitzer 1987; Binney & Tremaine 1987)

$$t_{\text{relax}} \propto \frac{N}{\ln N} \cdot t_{\text{cross}}. \tag{5}$$

With typical values $N \approx 10^5$ stars and the crossing time from Equation 4, the relaxation time is on the order of $0.1 - 1\,\text{Gyr}$, and thus $t_{\text{cross}}/t_{\text{relax}} \approx 10^{-3..-4}$ for GCs. It should be emphasized that the deflection of a star is not caused by a single (or a few) strong and close encounter, but by many weak and distant interactions between pairs of stars (hence "two-body" relaxation). In general, the relaxation time depends on the stellar density (there are various definitions with slightly different numbers; compare e.g. Spitzer 1987), and is therefore a strong function of the radial distance from the cluster center. It can vary by several orders of magnitudes for different regions in a GC. Cores are typically well relaxed, but the relaxation time in the halo may be longer than the age of the Universe. From a modelling point-of-view, on timescales much shorter than t_{relax} interactions between individual stars have no major influence on the orbit of a star. Thus, its trajectory can be modelled with a smooth gravitational force and the "granularity" of the gravitational potential can be ignored. This assumption is typically valid for many orbits of a star in a GC because $t_{\text{cross}} \ll t_{\text{relax}}$. Nevertheless, given the old ages of GCs in the Galaxy with $t_{\text{age}} \approx 10\,t_{\text{relax}}$ in many cases, the two-body relaxation eventually leads to a significant redistribution of the stellar kinetic energies, which ultimately approach a Maxwellian energy distribution (Binney & Tremaine 1987), where the velocity dispersion σ is related to the "kinetic temperature" T via

$$\frac{1}{2} m \sigma = \frac{3}{2} k_B T. \tag{6}$$

Here, k_B is Boltzmann's constant and m is the mass of a star. This is the concept of *energy equipartition* and Equation 6 indicates that less massive stars will on average have higher velocities, which ultimately leads to a preferred *evaporation* of low-mass stars from the cluster if their velocities become higher than the escape velocity of the cluster. A Maxwellian energy distribution always has a non-zero fraction of stars with sufficiently

high velocities and so it is the fate of all star clusters to eventually evaporate. A good estimate for the evaporation t_{evap} is

$$t_{evap} \approx 136\, t_{relax}, \tag{7}$$

and thus much longer than a Hubble time for most clusters (Sparke & Gallagher 2007). It can, however, be accelerated significantly by tidal interaction with the potential of the host galaxy (e.g., Gieles & Baumgardt 2008; Ernst et al. 2009), and it therefore seems likely that these additional interactions represent the most probable destruction method for the majority of GCs (Gnedin & Ostriker 1997).

The ultimate fate of a GC in the Galaxy mostly depends on its position. According to Harris (2001) the following rather general statements can be made: at short distances from the Galactic center, i.e $R_{GC} \lesssim 1-2\,kpc$, dynamical friction (Chandrasekhar 1943a,b, an effect in which a gravitational pull is exerted onto a massive object (GC) passing through a collection of many smaller objects (stars, e.g., in the bulge), thereby slowing it down) is the dominant destruction method and removes the most massive clusters. This effect becomes neglible for larger distances. At distances $R_{GC} \lesssim 6\,kpc$, bulge shocking and disc shocking are the dominant modes of destruction. They particularly affect lower-mass clusters ($M \lesssim 10^5\,M_\odot$) and partially erode the more massive ones. At even larger distances out in the halo, external interactions take place only on timescales larger than a Hubble time and above mentioned effect of evaporation leads to a slow dissolution of the cluster.

1.4 FORMATION AND DYNAMICAL PROPERTIES

Though only weakly contrained observationally, it is generally assumed that all stars in a GC formed by the collapse and subsequent fragmentation of a single giant molecular cloud (Brodie & Strader 2006). The exact details of the collapse are still under investigation, but the classical picture suggests that the GC forms in a single collapse event. As a consequence, all stars are assumed to have the same age and chemical composition with only neglible spread in these quantities. Nonetheless, depending on the star formation efficiency (SFE) not all primoridal gas is converted to stars, and thus left-overs of the gas cloud are expected after the star formation is terminated. This residual gas is assumed to be expelled by a combination of highly energetic supernovae type II (SNII), occurring when the nuclear reactions in the most massive stars are exhausted, and by the ionizing radiation from young and luminous stars (e.g., Goodwin 1997). For low SFE values, where the gravitational potential of the resulting GC is still dominated by the residual gas of the giant molecular cloud, subsequent gas expulsion can leave the cluster out of virial equilibrium and may lead to its immediate dissolution (Goodwin & Bastian 2006). This rapid change in potential is called violent relaxation (Lynden-Bell 1967) and it implies that the masses, positions, and velocities of the stars will be initially uncorrelated.

As mentioned in Section 1.2, this simple picture of a single collapse with a single star formation episode has been recently challenged by observations. The observed abundance variations and the multiple sequences in the GC CMDs suggest multiple epochs of star

formation, where a first generation of stars forms, evolves, and enriches the surrounding gas by various mechanisms. Subsequently formed generation of stars carry the chemical imprints of this enrichment and mix with the stars of the first generation. The exact details of this process are still poorly understood, but is conceivable that the initial cloud undergoes a global collapse, then experiences a first episode of star formation which is temporarily stopped by the onset of stellar feedback, and re-collapses to form the second generation (or even greater numbers). In an alternative theory, different parts of the giant molecular cloud could undergo separate, decoupled collapses at different times, and pollute adjacent regions with their ejecta. Stars from these collapsed sub-clumps would then merge to form the composite stellar populations that make up todays GCs. For more details we refer the reader to the review of Gratton et al. (2012) and the references therein.

Independent of the exact nature of the cluster formation process, violent relaxation implies that the stellar velocities, positions, and masses are uncorrelated once all gas is expelled, and thus more massive stars will on average have higher kinetic energies. The starting two-body relaxation leads to a redistribution of energies, in which kinetic energy of high-mass stars is transferred to low-mass stars through stellar encounters (see Section 1.3). As a consequence, the more massive stars will sink to the center due to the loss of kinetic energy, whereas the low-mass stars with their enhanced velocities move to the outer halo. This *mass segregation* has been observed in a number of clusters (e.g., Meylan 2000; Frank et al. 2013) and is a runaway process: the more massive stars form a core with an ever-increasing density, while the halo of low-mass stars is expanding further and further. Consequently, the mass function becomes shallower not only in the cluster center, but also globally due to evaporation of low-mass stars at large radii (Vesperini & Heggie 1997; Baumgardt & Makino 2003). Interestingly, by comparing numerical simulations and observationally derived mass function slopes of Galactic GCs, Baumgardt et al. (2008) find a number of clusters that show a significantly higher depletion in low-mass stars than expected from dynamical evolution models with a Kroupa (2002) IMF (see Equation 3), and they argue that this can be interpreted as a sign for primordial mass segregation.

In this context it should be emphasized that two-body relaxation shapes the dynamical evolution of a star cluster even if all stars have similar masses: Stars close to the center have on average higher orbital speeds and via two-body interaction some fraction of this energy is always transferred to stars at outer radii. This effect ultimately results in the so-called *gravothermal catastrophe*, which is a mere outcome of the principles of thermodynamics. If the cluster is in thermodynamical equilibirum, which holds for most clusters because they are all well relaxed (see Section 1.3), the Virial Theorem

$$2T = -U \tag{8}$$

relates the kinetic energy T to the potential energy U in a well-defined manner. The total energy E is thus given by

$$E = T + U = -T = -\frac{3}{2} N k_B T, \tag{9}$$

where N is the total number of stars, and Equation 6 was used in the last step. Interestingly, the heat capacity $c \equiv dE/dT$ turns out to be negative in self-gravitating systems, since

$$c = \frac{dE}{dT} = -\frac{3}{2} N k_B. \tag{10}$$

The implications are counter-intuitive at first glance: heating a self-gravitating systems causes it to lose energy and to contract further. In a core-halo cluster the core is much more strongly self-gravitating than the halo, and so the latter can be considered a heat sink for the first. Any instability by which the core becomes dynamically hotter results in energy flowing into the halo (by means of ejected stars), which, according to Equation 10, surprisingly further increases the temperature of the core (since $dT \propto -dE$). As a consequence, the energy flow into the halo becomes even stronger, leading to an ever-increasing temperature and subsequent contraction of the core, which might ultimately result in a *core collapse*. This runaway process affects all self-gravitating systems and was first noted by Antonov (1962) in the context of star clusters (in multi-mass systems this effect may even be accelerated due to mass segregation; see Spitzer 1969). In the sample of GCs presented in this work, NGC362, NGC1904, NGC7078, and NGC7099 are thought to have undergone core collapse (derived mostly from an analysis of their surface brightness profiles; see Harris 2010). Core collapse can eventually be halted by supplying additional energy to the core. Numerical simulations suggest that tightly bound binaries might serve this role, by super-elastically scattering infalling stars at the expense of their own orbital energy. In analogy to stars (also self-gravitating systems), where the collapse is counter-balanced by nuclear burning, this effect is called "binary burning". The required binaries may either be formed in the numerous dynamical interactions at these high stellar densities, or may have been formed primordially (Fregeau et al. 2009). For some clusters theoretical investigations indicate that the resulting core expansion could alternate with subsequent additional collapses, leading to so-called gravothermal oscillations (Bettwieser & Sugimoto 1984; Makino et al. 1986; Heggie & Ramamani 1989).

1.5 MASS-TO-LIGHT RATIOS

GCs were among the first stellar systems on sub-galactic scales, and thus can be considered as one of the "building blocks" of galaxies. With masses of $\sim 10^4 - 10^6\,M_\odot$ they are distinct from their less massive cousins, open clusters, however the traditional boundary to the more massive dwarf galaxies has recently become blurred with the discovery of an ever–increasing number of very low-mass dwarf galaxies (e.g., Willman 1; Martin et al. 2007). Since then, several classification criteria have been put forward in an attempt to conclusively answer the question "What is a galaxy?" (e.g., Kroupa 2008; van den Bergh 2008a,b; Forbes & Kroupa 2011; Willman & Strader 2012), comprising parameters like size, relaxation time, presence of complex stellar populations, presence of a satellite system, and the presence of non-baryonic matter. Especially the last argument is traditionally used to distinguish between star clusters (without dark matter) and galaxies (most being even dominated by dark matter). Stellar population synthesis models that do not incorporate

any form of non-baryonic matter predict typical GC mass-to-light ratios[2] $\Upsilon \approx 2\,M_\odot/L_\odot$, which is in indeed in good agreement with observationally inferred dynamical mass measurements (e.g. Illingworth 1976; Mandushev et al. 1991; McLaughlin & van der Marel 2005; McLaughlin & Fall 2008), and thus the necessity for dark matter in GCs is generally denied. Interestingly, the recently discovered class of ultra compact dwarf *galaxies* (UCDs), which overlap at least partly in size and luminosity with the high-luminosity tail of the Galactic GC population, shows mass-to-light ratios very similar to GCs, with typical values $\Upsilon = 2-5$ (e.g. Hilker et al. 1999; Drinkwater et al. 2003; Haşegan et al. 2005; Mieske et al. 2008; Dabringhausen et al. 2008; Taylor et al. 2010; Frank et al. 2011). These values are in principle still consistent with an exclusively stellar nature of their mass-to-light ratios, however Willman & Strader (2012) hypothesize that this effect originates from the fact that the stars of UCDs only populate the innermost regions of their halo, and thus information based on their light samples only a small part of the surrounding dark matter halo and naturally leads to a depleted Υ in dynamical measurements. In this context it is interesting to note that Taylor et al. (2015) systematically analyzed the star cluster system of the giant elliptical galaxy NGC5128 (Centaurus A) and find $\Upsilon \approx 30$ for objects, which, based on their luminosities ($M_V \approx -8$) and sizes ($r_h \approx 4\,pc$) alone, occupy traditional GC parameter spaces.

Apparently, any classification based solely on the mass-to-light ratio of the system seems to yield ambiguous results in this mass range and an approach based on a number of different parameters should be used instead. A possible distinction could be based on the two-body relaxation time, with all known GCs (excluding the Taylor et al. 2015 sample, as it is not yet clear what class these objects belong to) having relaxation times shorter than a Hubble time, and all known dwarf galaxies exhibiting relaxation times that are clearly longer than the age of the Universe (Willman & Strader 2012).

Nonetheless, in this work we will revisit the mass-to-light ratios for a sample of eleven Milky Way GCs. The presented approach to measure the cluster masses does not require any explicit assumptions on the stellar content of the system, and thus should yield a good approximation to the true "dynamical mass" of a GC.

1.6 BLACK HOLES IN GLOBULAR CLUSTERS

Although theoretical considerations on black holes (BHs) date back to almost a century ago, when Schwarzschild (1916) calculated the gravitational potential of a point mass with the principles of general relativity, first observational evidence for a potential stellar BH was only found ~ 50 years later in the binary system Cygnus X-1 (e.g., Oda et al. 1971; Kristian et al. 1971; Braes & Miley 1971). The majority of all currently known candidate stellar BHs were identified by their strong and localized X-ray emission, resulting from the accretion of matter from a companion star onto the BH (e.g., Casares 2007). The mass range of these X-ray compact binary systems is $\sim 3-20\,M_\odot$ (excluding the mass of the companion star, which can be observed with optical telescopes) and agrees with predic-

2 Throughout this work mass-to-light ratios are given in units of solar masses divided by solar V-band luminosities.

tions of core-collapse supernovae models (Prestwich et al. 2007; Altamirano et al. 2011). Interestingly, Strader et al. (2012) found two stellar mass BHs in NGC6656 based on radio emission, which represents the first direct evidence for these objects in Milky Way GCs. This came as a suprise, since it was proposed that most of the formed stellar mass BHs in GCs would be dynamically ejected on a relatively short time scale, and thus the detection probability today should be relatively low (Kulkarni et al. 1993; Sigurdsson & Hernquist 1993; Portegies Zwart & McMillan 2000).

The other end of the known BH mass spectrum is occupied by super-massive black holes (SMBHs) with masses $\gtrsim 10^6\,M_\odot$. These are believed to reside in the centers of almost all massive galaxies (Antonucci 1993; Urry & Padovani 1995), including the Milky Way (Schödel et al. 2002). Their masses obey a very strict empirical scaling relation with the velocity dispersion of their host spheroid, with a scatter that is compatible entirely with measurement uncertainties(Ferrarese & Merritt 2000). The fact that they are observed already in high-redshift quasars implies that these objects formed at a very early stage of galaxy formation. Intermediate-mass black holes (IMBHs) with masses of $\sim 10^2 - 10^4\,M_\odot$ are proposed as possible seeds of these SMBHs, but so far no compelling evidence has been presented for the existence of these objects. Recently, Pasham et al. (2014) found a candidate IMBH with $\sim 500\,M_\odot$ in the nearby irregular galaxy M82, but their analysis relies on the extrapolation of known scaling relations of stellar-mass BHs and so the detection remains inconclusive.

From a theoretical point-of-view, dense star clusters with $N > 10^7$ Stars are suspected as a possible formation site for IMBHs (Lee 1987; Quinlan & Shapiro 1989). The afore mentioned gravothermal catastrophe might lead to densities that are high enough to trigger direct stellar collisions. These collisions might induce a runaway-merging of stars, which could ultimately trigger the formation of a supermassive star that collapses into a BH once its mass is sufficiently large (Lee 1993). While it was previously thought that star clusters with $\lesssim 10^6 - 10^7$ stars would not produce sufficiently dense regions due to binary burning, more recent results indicate that mass-segregation might boost the merging process and IMBHs could be formed if the core collapse proceeds faster than the MS lifetime of the massive stars (Portegies Zwart & McMillan 2002). Unfortunately, the exact physical conditions under which the Milky Way GCs formed are only poorly known and so it remains unclear whether they harbor IMBHs today.

Recent searches for IMBHs concentrate on central gradients in the velocity dispersion profiles in combination with shallow cusps in the surface brightness profiles (Lützgendorf et al. 2011, 2012b, 2013). However, care has to exercised with this approach, as the N-body simulations of Baumgardt et al. (2005) suggest that GCs harboring an IMBHs will show a rather constant dispersion profile and surface brightnesses only slightly rising toward the center, concluding that core-collapsed clusters (i.e., GCs with a distinct surface brightness cusp in the center) are unlikely candidates to host IMBHs. Indeed, theoretical considerations by Vesperini & Trenti (2010) revealed that surface brightness cusps are not an unequivocal signature of a central IMBH, and that mass segregation, core collapse, or the presence of binary stars in the center can generate similar cusps. In addition, it should be emphasized that not accounting for kinematical properties like velocity anisotropy and

/ or (differential) ordered rotation might likewise lead to a wrong interpretation of the velocity dispersion profile.

Although the work presented here does not focus on the search for IMBHs, we note that for some GCs our data reveal the above mentioned steep gradients in the velocity dispersion profiles at the cluster centers. We will not interpret this feature as an indication for the presence of an IMBH, yet we will compare our measured central velocity dispersions to the values that have been used in the literature to constrain the masses of the potential IMBHs.

Part II

OBSERVATIONS

We have observed 29 globular clusters in the Magellanic Clouds and the Milky Way with X-SHOOTER, a single target slit spectrograph mounted at the ESO Very Large Telescope. The observations have been performed in drift-scan mode, where the telescope is slewed across the cluster during integration. This technique allows us to collect in one scan the average spectrum of all GC stars located in a stripe defined by the GC half-light diameter and the slit length. In order to statistically sample the stellar content of each GC we have mapped the area within its half-light radius with repeated scans. Our X-SHOOTER spectra have a resolving power of $\lambda/\Delta\lambda \approx 10,000$ and cover the spectral range between 3,000 Å and 25,000 Å. The main motivation for our observational project are detailed chemical abundance measurements. The work presented here will focus on the secondary goal, the measurement of the dynamical masses of the clusters. In particular, we will derive the dynamical masses of a sub-sample of eleven GCs that have been extensively studied with the Hubble Space Telescope.

2

VLT/X-SHOOTER SPECTROSCOPIC OBSERVATIONS OF GALACTIC GLOBULAR CLUSTERS

2.1 MOTIVATION FOR THE DATA SET

High-resolution spectroscopy of GCs provides the possibility to address some of the most pressing questions in astrophysics, in particular, the star formation and chemical enrichment processes in the early phases of the Universe. Hosting populations of stars that typically have an age spread $\lesssim 100\,\mathrm{Myr}$ (and thus essentially negligible compared to their absolute ages of $\sim 10\,\mathrm{Gyr}$) on the one hand, and the ability to survive longer than a Hubble time on the other hand is a unique combination. As a consequence, their stellar populations preserve crucial information on the chemical evolution during major star formation episodes, and thus GCs can be considered the ideal tool to study the assembly and enrichment histories of their host galaxies. This idea, i.e, to reconstruct the chemical and dynamical evolution of massive galaxies based on tracer sub-populations (e.g., GCs) is referred to as "chemodynamical tagging" and has been a popular idea in the scientific community for many years (e.g., Freeman & Bland-Hawthorn 2002; West et al. 2004; Yoon et al. 2006).

With individual GCs probably being the closest approximation to SSPs that exist in the Universe, their integrated light can be robustly compared to population synthesis model predictions. An analysis of this kind will be much more reliable than investigations based directly on the integrated light of their host galaxies, since the latter is always a composite over several episodes of star formation with considerable spreads in age and element abundances. Moreover, although the integrated light of nearby galaxies in principle delivers enough flux for high-resolution spectroscopy at $R \equiv \lambda/\Delta\lambda \approx 20,000$ for current state-of-the-art telescopes, their internal velocity dispersions of $\sigma \geqslant 50\,\mathrm{km\,s^{-1}}$ render detailed investigations of individual spectral features almost useless. Conversely, $R \approx 10,000$ spectroscopy of their GC systems with typical GC velocity dispersions $\sigma \leqslant 30\,\mathrm{km\,s^{-1}}$ allows for a detailed access to the underlying chemical abundances out to distances of $\sim 4\,\mathrm{Mpc}$ (Taylor et al. 2015) with today's $8-10$m class telescopes. With the next generation of $30-40$m class telescopes (E-ELT, GMT, TMT), thousands of extragalactic GCs out to the distance of the Coma cluster at $D \approx 100\,\mathrm{Mpc}$ will become accessible in this way. With spectral diagnostics limited only by the internal velocity dispersion, the integrated light of GCs in distant galaxies is our only way to access the enrichment histories of these remote stellar systems in a detailed way. In this context it is interesting to note that even an adaptive-optics near-infrared imager on the E-ELT will be able to push resolved star studies only to Virgo distances at $D \approx 16\,\mathrm{Mpc}$ (Greggio et al. 2012), but the aforementioned integrated-light spectroscopic observations will reach ten times further.

Because of the washed-out features in the spectra of high-σ stellar systems, several index systems have been developed to derive ages and metallicities from integrated-light spectra of their unresolved stellar populations. The Lick system of absorption-line indices in the range $\sim 4,000$ Å $- 6,500$ Å at ~ 8 Å $- 10$ Å resolution (see e.g., Burstein et al. 1984) and the Ca II triplet around $\sim 8,600$ Å at 2 Å resolution (Cenarro et al. 2001a,b) are probably the best-studied and most popular index systems of this kind, and comparisons of line-index measurements with population synthesis models are widely used to derive ages, metallicities, and abundance ratios for large samples of galaxies (Trager et al. 2000b,a, 2008), spiral bulges (e.g., Thomas & Davies 2006), and Galactic and extragalactic GCs (Puzia et al. 2002, 2005a,b, 2006; Beasley et al. 2004, 2005; Schiavon et al. 2005, 2012; Puzia & Sharina 2008; Thomas et al. 2011). It should be pointed out, however, that these index systems have been developed especially for the purpose of studying high velocity dispersion systems at rather low resolution. This implies that an application to high-resolution data of low-dispersion objects is in principle feasible, but forfeits most of the available spectral information and thus is far from optimally suited. It is therefore important to develop tools and techniques that exploit the full spectral range and resolution in order to be ready when the next generation of telescopes see first light and thus the number of extragalactic GCs with available high-resolution integrated-light spectroscopy dramatically increases.

Galactic GCs are ideal test objects to develop theses techniques since most of them are very well-studied (e.g., Harris 2010) and have high-resolution spectroscopy of individual stars available (e.g., Pritzl et al. 2005). Furthermore, many Galactic GCs are covered by large-scale multi-band photometric surveys with the Hubble Space Telescope (HST), and thus detailed resolved color information of their stellar populations is available (Piotto et al. 2002; Sarajedini et al. 2007). On the other hand, X-SHOOTER with its unique combination of an exceptionally large spectral range (from the ultraviolet atmospheric cutoff at 3,000 Å to the thermal near-infrared at 25,000 Å), a moderately high resolving power $R = \lambda/\Delta\lambda \approx 10,000$, and a very high overall throughput, represents the instrument of choice to undertake such a systematic study. At a given total observing time, this list of features allows for an nearly maximal amount of information, while simultaneously safeguarding the consistency of the acquired data set because the entire spectrum is recorded in one observation. X-SHOOTER spectroscopic data of Galactic GCs should therefore be ideally suited to determine accurate chemical abundances over a large spectral range, and the comparison with existing data should facilitate a robust calibration of any newly developed abundance determination method.

While detailed investigations of the GC chemistries have been the main motivation for the acquisition of our spectroscopic data set, integrated-light spectra also allow for direct dynamical mass estimates of the GCs, provided that the instrumental resolution is sufficiently high to resolve the Doppler-broadening of the spectral features due to the random motions of the stars in the cluster potential. The measurement of the velocity dispersions of our sample of GCs constitutes the main part of the work presented here, but it should be noted that any further analyses of our data set with regard to abundance measurements will tremendously benefit from the techniques that we developed in the course of this work.

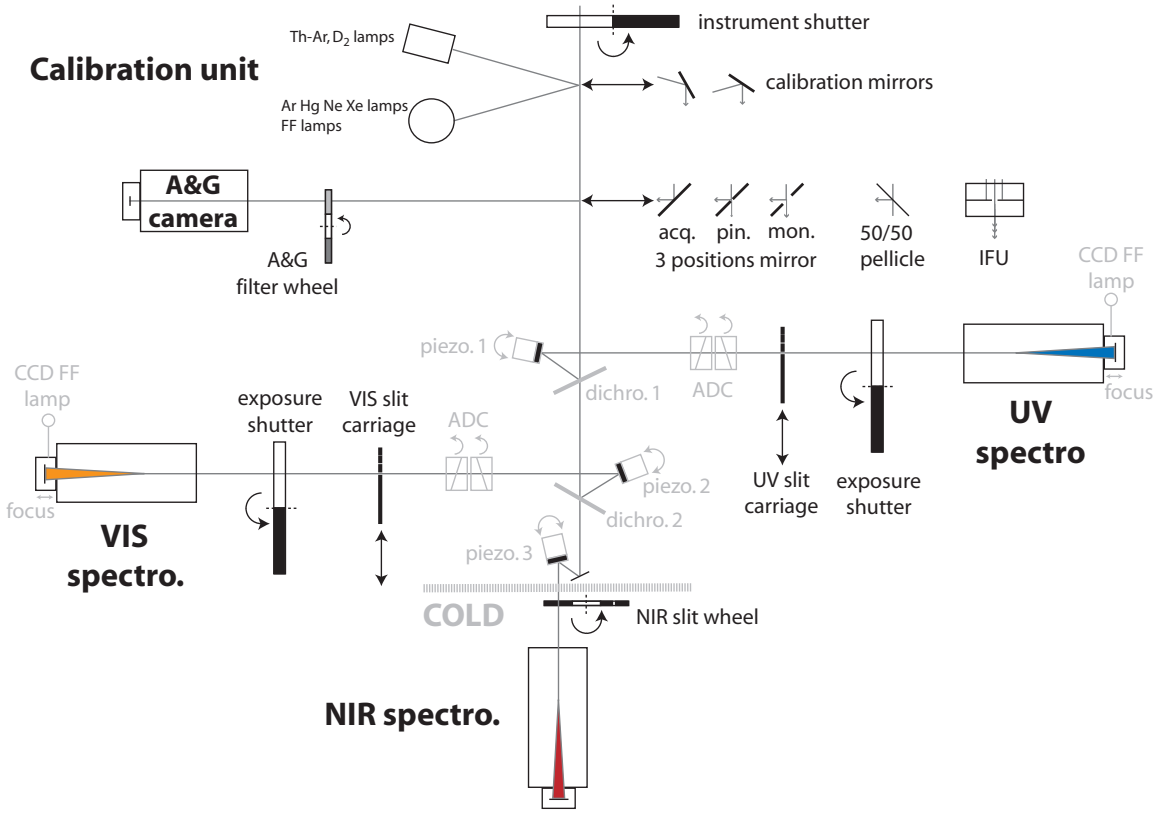

Figure 2: Layout of X-SHOOTER . The light enters the instrument from the top and is distributed into three separate arms (UVB, VIS, NIR). Figure taken from Vernet et al. (2011).

2.2 X-SHOOTER - AN INTRODUCTION TO THE INSTRUMENT

X-SHOOTER is a single target, slit échelle spectrograph that covers a very wide spectral range (3,000 Å – 25,000 Å) at moderate resolving power R ≈ 10,000 (Vernet et al. 2011). It is the first of the European Southern Observatory's (ESO) second-generation instruments installed at the Very Large Telescope (VLT) on Cerro Paranal in the Chilean Atacama Desert. By splitting the incoming beam into three independent arms (ultraviolet-blue, UVB: 3,000 Å – 5,900 Å; visible, VIS: 5,300 Å – 10,200 Å; near-infrared, NIR: 9,800 Å – 25,000 Å), each one equipped with optimized optics, coatings, dispersive elements, and detectors, the design allows for an extremely high sensitivity throughout the entire spectral range. The instrument layout is sketched in Figure 2 (taken from Vernet et al. 2011) and will be briefly explained here. We will follow the descriptions presented by Vernet et al. (2011), but it should be noted that we mainly concentrate on the UVB and VIS arms, since the work presented here does not deal with the NIR arm data.

The converging beam from the telescope passes the instrument shutter (top part of Figure 2) and arrives at the acquisition and guiding (A&G) slide. This structure allows for the insertion of various components into the beam, e.g., the integral field unit (IFU) or

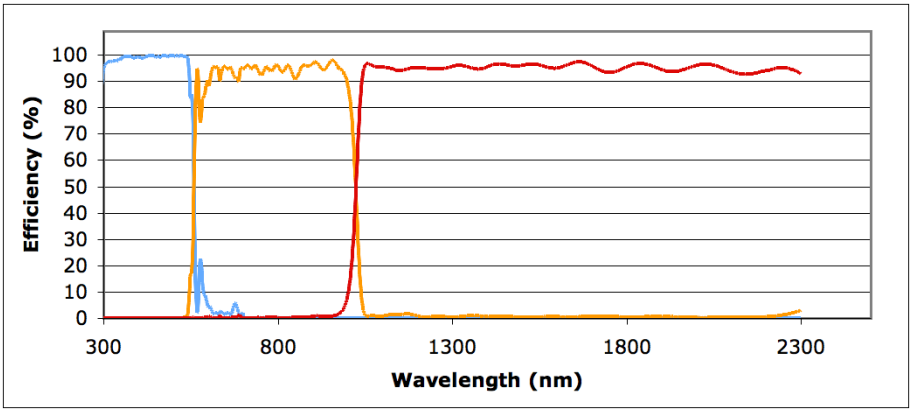

Figure 3: Combined efficiency of the two dichroic beamsplitters as a function of wavelength. The blue curve depicts reflection on the first dichroic (UVB), the orange curve indicates transmission through the first dichroic, but reflection on the second (VIS). The red curve is the combined transmission through both dichroics (NIR). Figure taken from Vernet et al. (2011).

beam splitters used for engineering purposes. In regular science mode a 45° mirror with a slot is installed that transmits the central $10'' \times 15''$ to the subsequent spectrographs and reflects the peripheral field onto the A&G camera[1]. The first optical elements encountered by the transmitted beam are the two dichroic beam splitters, which distribute the light to the three instrumental arms. The first dichroic decouples the blue part of the spectrum by reflecting more than 98% of the light in the range $3500\,\text{Å} - 5430\,\text{Å}$, and transmitting $\sim 95\%$ of the light between $6,000\,\text{Å}$ and $23,000\,\text{Å}$. The second dichroic separates the VIS arm from NIR arm with a reflectivity $\gtrsim 98\%$ in the range $5,350\,\text{Å} - 9,850\,\text{Å}$ and a transmissivity $\gtrsim 96\%$ between $10,450\,\text{Å}$ and $23,000\,\text{Å}$. The combined efficiency of both dichroics is plotted in Figure 3 (taken from Vernet et al. 2011) and is $\gtrsim 90\%$ over most of the spectral range. Each arm is equipped with a folding mirror mounted on a piezo tip-tilt mount, which allow for a correction of backbone flexure, and thus keep the relative alignments of the three spectrographs fixed for all telescope positions. The flexure arises from the instrument's weight of ~ 2.5 metric tons in combination with its mount at the Cassegrain focus. Both UVB and VIS arms contain an atmospheric dispersion correction (ADC) device, that compensates for differential atmospheric dispersion in order to minimize slit losses. The respective zero deviation wavelengths are 4050 Å and 6330 Å and dispersion induced shifts are measured and corrected with respect to these reference wavelengths (Note that the NIR arm does not contain an ADC). After the ADCs the beam approaches the slit carriages, which contain a number of different slits. Available slit widths range from a minimum of $0.4''$ (UVB: $0.5''$) to $5.0''$ and can be specified independently for each arm. The slit length, however, is fixed at $11''$. In addition, there are two pinhole masks available for calibration purposes. The UVB and VIS spectrographs share

1 For the sake of completeness it should be noted that prior to the A&G slide, light from calibration lamps (for flat fielding and wavelength calibration purposes) can be coupled into the optical path with special mirrors, allowing for calibrations, like flat fielding or the wavelength calibration, with a closed instrument shutter.

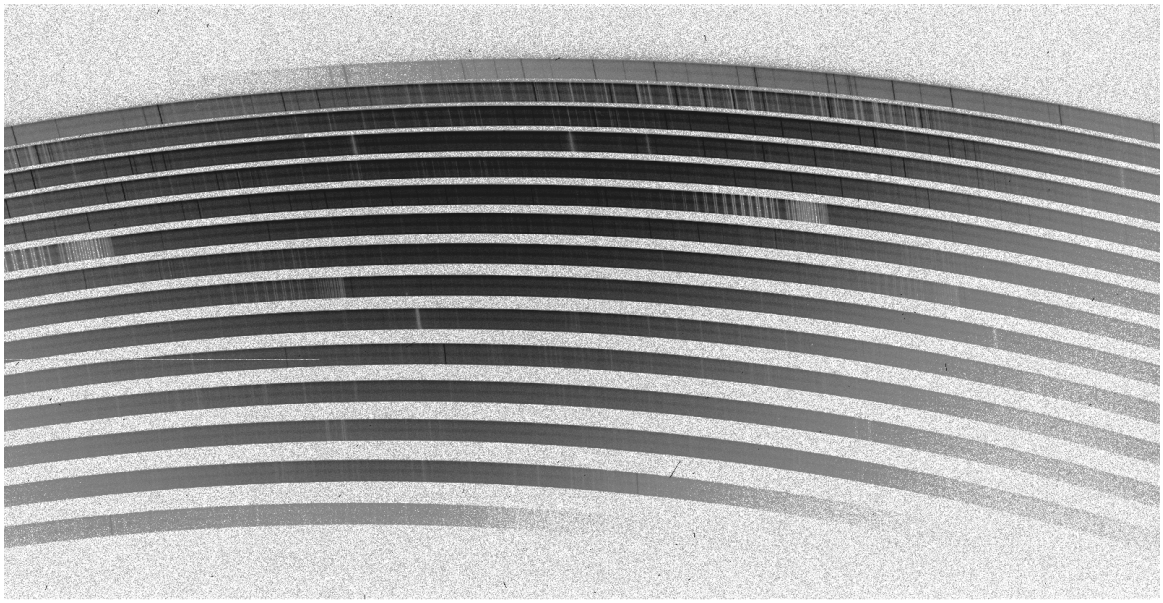

Figure 4: GC (NGC104) raw frame of X-SHOOTER's VIS arm, rotated by 90° and plotted in negative colors. A total of 15 spectral orders are visible, ranging from ~ 5,300 Å (order at the bottom) to ~ 10,000 Å (top). Within individual orders the wavelength increases from right to left. The spectral range of each order partly overlaps with those of the adjacent orders. This is particularly evident for the strong absorption bands in order ten (starting from the bottom), which is also imaged into the blue part of order nine.

a very similar layout: The collimated beam passes through a prism twice to gain enough cross-dispersion. An échelle grating with a blaze angle ~ 45° is responsible for the main dispersion. The dispersed light is imaged onto a 2k × 3k (VIS: 2k × 4k) detector at a plate scale of ~ 9″ mm^{-1}. Due to the échelle layout of the individual spectrographs, the target spectral energy distribution (SED) is split into 12–16 curved and highly distorted spectral orders per arm (see Figure 4 for a showcase VIS raw frame), requiring a sophisticated reduction process for the best possible results. With a typical resolving power $R \gtrsim 10,000$ and a total efficiency of ~ 30% (including telescope and detector) for most of the covered spectral range, X-SHOOTER is armed with state-of-the-art technology and can address a vast number of astrophysical applications. The broad spectral coverage and its mount on the 8.2-meter VLT turn X-SHOOTER into a powerful multi-purpose tool that offers the ability to constrain parameter spaces that otherwise would need to be studied with a number of different instruments.

2.3 OBSERVING STRATEGY

We have observed 29 GCs in the Milky Way and the Magellanic Clouds with VLT/X-SHOOTER, utilizing a slit width of 0.5″ for the UVB arm ($R \approx 9,100$) and 0.4″ for the VIS ($R \approx 17,400$) and NIR arms ($R \approx 11,300$), respectively. The observations were conducted in two distinct visitor-mode observing runs of four nights each, during October 22-25th

and November 7-9th, 2009 (ESO Program 084.D-1061). An additional service-mode run on February 9th, 2010 added one GC to the sample. The seeing conditions varied throughout the observations between 0.6″ and 2.5″ with a median of ~ 1.0″ at airmass values ranging from 1.0 to 2.6 with a median of ~ 1.5. The journal of observations is presented in Table 1. Cluster frames are denoted O (object), sky frames are denoted S. Since the work presented here focuses on a sub sample of eleven GCs for which detailed *HST/ACS* and *HST/WFPC2* photometric data are available (Piotto et al. 2002; Sarajedini et al. 2007), we excluded all other GCs from the journal. A graphical timeline of the observations is presented in Figure 5. Each frame (object and sky) is indicated by a green box, whose position along the time-axis denotes the time of observation. The exposure time corresponds to the width of a box. Flux standard stars are marked with solid blue lines and flexure compensation frames are indicated with dashed red lines. They were usually obtained once for each cluster at the start of the observing sequence. In this context it should be noted that during the first visitor-mode run no flux standard star observations were performed, which complicated the subsequent flux-calibration of the data. Further details will be given in Section 3.4.10.

GC	Observing date	Airmass	Exposure time	Obs. Sequence	δ R.A. [″/s]
			Visitor-mode run 1		
NGC104	Oct. 22nd, 2009	1.68 – 1.50	9 × 300 s = 0:45 h	S-OOO-S-OOO-S-OOO-S	0.69747
NGC2298	Oct. 22nd, 2009	1.24 – 1.04	5 × 1200 s = 1:40 h	S-OOOOO	0.04875
NGC7089	Oct. 23rd, 2009	1.10	4 × 300 s = 0:20 h	OO-S-OO-S	0.23253
NGC362	Oct. 23rd, 2009	1.60 – 1.53	5 × 300 s = 0:25 h	S-OOOOO-S	0.20253
NGC7099	Oct. 24th, 2009	1.00 – 1.07	5 × 600 s = 0:50 h	S-OOOOO-S	0.14373
NGC7078	Oct. 24th, 2009	1.50 – 1.82	5 × 300 s = 0:50 h	S-OOOOO-S	0.26500
			Visitor-mode run 2		
NGC288	Nov. 7th, 2009	1.10 – 1.03	3 × 1200 s = 1:00 h	OOO	0.16650
NGC6656	Nov. 8th, 2009	2.13 – 2.59	4 × 300 s = 0:20 h	OOOO	0.97800
NGC1851	Nov. 8th, 2009	1.11 – 1.15	3 × 300 s = 0:15 h	O-S-OO	0.13000
NGC6656	Nov. 9th, 2009	1.82 – 2.59	6 × 1800 s = 3:00 h	OO-S-OOOO	0.97800
NGC288	Nov. 10th, 2009	1.05 – 1.00	4 × 1200 s = 1:20 h	OOO-S-O	0.16650
NGC1904	Nov. 10th, 2009	1.00 – 1.04	3 × 600 s = 0:30 h	OOO-S	0.10000
			Service-mode run		
NGC2808	Feb. 10th, 2010	1.39 – 1.33	7 × 300 s = 0:35 h	OOOOO-S-OO	0.19000

Table 1: Journal of GC observations. Consecutive columns list the cluster number, the observing date, the respective airmass range, the total on-target exposure time, the sequence of observations (with S denoting sky frames and O denoting object frames), and the drift-speed of the telescope along the right ascension (R.A.) axis (in units of arcseconds per second).

On-target integration times are ~ 900 – 10,800 s and depend on the respective cluster size and brightness. The observing campaign was designed to yield a minimum signal-to-noise (S/N) of ~ 50 per resolution element at 5,000 Å if all frames of a GC are stacked. All frames have been executed as *drift scans*, i.e., the telescope was slewed across the

cluster during integration. This special observing setup is illustrated in Figure 6. Each cluster is represented by an image from the Digitized Sky Survey, over which we plot a green circle indicating the respective approximate half-light radius. Each rectangular orange box indicates the area covered by one drift scan. The initial pointing of each frame is marked by a red cross and corresponds to the position of the slit center at the start of the integration. The slit length was aligned with the declination (DEC) direction. Each scan was performed at fixed DEC and along the right ascension (R.A.) axis. The vertical extent (i.e., along DEC-direction) of one box corresponds to the slit length and is 11″. The horizontal extent of one box corresponds to the covered distance by the scan along the R.A.-dimension and is given by δR.A. $\cdot\, t_{exp}$, where t_{exp} is the exposure time of the scan, and δR.A. the drift-scan speed. Both values have been matched to achieve the desired S/N on the one hand, and a spatial sampling of approximately one half-light diameter about the cluster center, i.e., from R.A.$_0 + r_h$ to R.A.$_0 - r_h$ (R.A.$_0$ denotes the right ascension of the cluster center and is presented together with central declination DEC$_0$ in the top right corner of each panel in Figure 6), on the other hand. We list the adopted values in Table 1. The spatial sampling along the DEC-dimension is given by the slit length (fixed at 11″) and the number of executed scans. The drift-scan technique has been chosen to attenuate the influence of bright giant stars in the composite spectrum, and thus to sample sufficiently the constituent stellar populations of the GCs. For the sky frames the telescope has been typically offset by $\sim 1^\circ$ relative to the cluster center, and then slewed in the same way as for the object frames. Most clusters are covered with $1-2$ sky frames. NGC104 forms an exception because it is located close to the Small Magellanic Cloud (SMC) on the projected sky plane, and therefore substantial background contamination is expected. This issue was addressed by taking a total of four sky frames that homogenously sample the background north, south, east, and west of the cluster.

It should be noted that in particular for the clusters with $r_h \gtrsim 100''$ (NGC104, NGC288, NGC6656) the initial pointings for some scans have not been properly aligned with the half-light radius and show displacements of up to $\sim 30''$ relative to the desired position (see Figure 6). For NGC1851 R.A.$_0$ seems to be slightly shifted with respect to the distribution of stars from the *HST/ACS* survey (black dots in Figure 6). These deviations, however are expected to affect the spectral content only marginally (the true center of the cluster, which has the highest contribution to the integrated flux, is always contained in our scans), and thus will not be addressed further in the remainder of this work.

Figure 5: Timeline of the observations. Each night is represented by two panels. Each frame is indicated by a green box. The position of the box on the time-axis indicates when the frame was taken, the width of the box corresponds to the exposure time. Flux standard stars are indicated by blue lines and the flexure compensation frames are indicated by dashed red lines. For each frame the average FWHM seeing is indicated by a filled black circle.

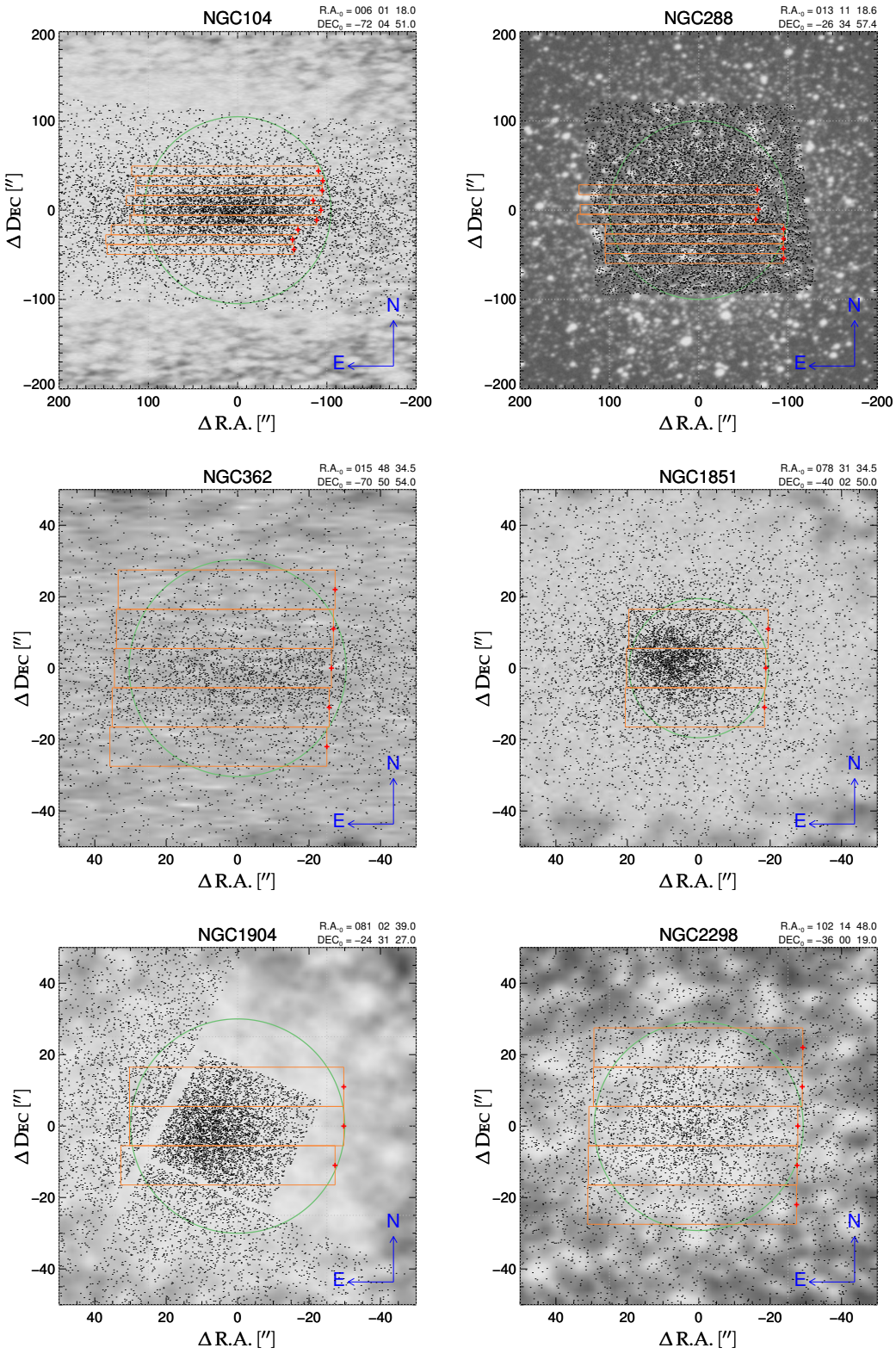

Figure 6: Scan overview for each GC in the target sample. The green circle indicates r_h. Each rectangular orange box corresponds to the area covered by one drift-scan. The red crosses indicate the initial pointings of the scans, and denote the central slit position at the start of the integration. The drift scans were performed at fixed DEC along the R.A.-axis. The covered distance corresponds approximately to one half-light diameter. The cluster center coordinates R.A.$_0$, DEC$_0$ are denoted in the top right corner of each panel. The black dots indicate the respective $\sim 10^4$ brightest stars from the *HST/ACS* survey (Sarajedini et al. 2007, for NGC1904 they are taken from the *HST/WFPC2* survey by Piotto et al. 2002). The background images are taken from the Digitized Sky Survey. The figure is continued on the next page.

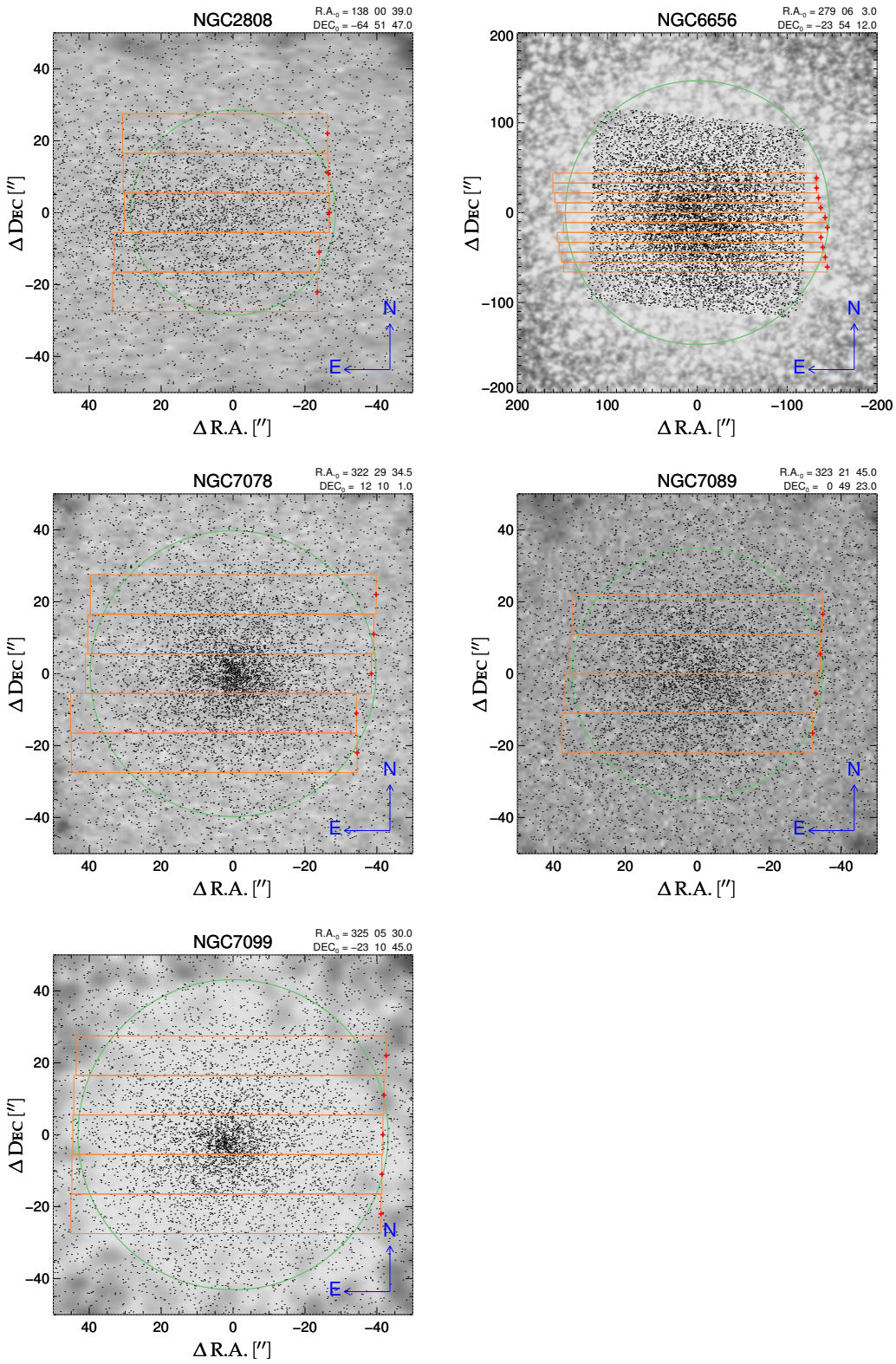

Figure 6 – Cont.: Scan overview for each GC in the target sample.

Part III

DATA REDUCTIONS

We aim for a reliable and consistent reduction of our spectroscopic observations. The available ESO X-SHOOTER pipeline (v1.5.0) produces accurate results for the wavelength calibration and the associated rectification of the spectra, but shows major shortcomings in other reduction steps. We account for these issues with the implementation of additional calibration steps, such as bad pixel interpolation, flat fielding, and slit illumination correction. For a point-like object the instrumental point spread function is analytically modeled and used to reconstruct flux losses at slit transit and to optimally extract the object from the two-dimensional spectrum. Instrumental throughput variability is detected by evaluating regular observations of spectrophotometric standard stars available in the X-SHOOTER archive. The sensitivity function is computed for each spectral order independently and the flux-calibrated orders are eventually merged into a final spectrum, ranging from $3,000\,\text{Å}$ to $10,000\,\text{Å}$. Our improved reduction cascade allows for an uncertainty $\lesssim 10\%$ in the absolute flux calibration, provided that the signal-to-noise is sufficiently high. The optimal extraction typically increases the signal-to-noise by a factor of 1.5. The wavelength calibration is found to be accurate within $\Delta\lambda \simeq 0.02\,\text{Å}$.

3

X-SHOOTER UVB AND VIS ARM DATA REDUCTION

Our data set contains over 400 raw frames and ~ 1500 calibration frames, and thus requires that great importance is attached to consistency and reproducibility of the applied reductions. Regrettably, at the time when we started with the data reduction the X-SHOOTER pipeline provided by ESO (v1.5.0, see Modigliani et al. 2010) showed severe shortcomings at various steps in the reduction cascade. We therefore started with a general assessment of the reduction quality based on regularly acquired standard star observations[1] (primarly of the white dwarf GD71), because they form an excellent tool to search for hidden systematic effects and to monitor the temporal stability of the instrument. We carefully analyzed the result of each pipeline step and – if necessary – adjusted the available parameters to optimize the output. In case of unsatisfactory results or lack of treatment of instrument systematics by the ESO pipeline, we implemented the necessary modifications to the standard calibration steps with additional custom code. We concentrated exclusively on the UVB and VIS arm reduction[2], and thus the remainder of this work will only deal with the wavelength range ~ 3,000 Å – 10,000 Å. Once satisfactory and reliable results could be obtained, we applied the final procedure consistently to all our GC observations. It should be emphasized, however, that the methods presented here are not limited to this particular data set. Converserly, they are ready to be applied to a wide variety of astronomical objects without major modifications. We have already successfully tested them for early-type galaxies and for Kuiper belt objects.

The data reduction is organized as follows. We start with an overview of the reduction cascade in Section 3.1. Calibration steps executed prior to invoking the ESO pipeline are explained in Section 3.2, whereas Section 3.3 briefly summarizes the steps executed inside the ESO pipeline. Most of our calibrations, however, are applied to the spectra after the pipeline rectification procedure, and are explained in Section 3.4.

The derivations presented in this chapter are largely based on work that has been previously published in Schönebeck et al., **"The Panchromatic High-Resolution Spectroscopic Survey of Local Group Star Clusters. I. General data reduction procedures for the VLT/X-shooter UVB and VIS arm"**, 2014, A&A, 572, A13 (22 pages)

3.1 OVERVIEW OF THE DATA REDUCTION CASCADE

The entire cascade of reduction steps is executed with a global script that first sorts all calibration frames for each observing night based on header information and subsequently runs the set of calibration recipes on the respective frames in a predefined sequence. The

1 Available in the ESO archive at http://archive.eso.org/eso/eso_archive_main.html

2 We have gained first experience with the NIR arm reduction and plan to complete our scripts in the near future.

script is designed to operate fully automatically except for the flux calibration part, where the sensitivity function computation can be performed in interactive mode. Our code can likewise handle extended objects and point sources and accepts all three observation (OB) modes offered by X-SHOOTER : *OFFSET* (object and background are imaged onto different frames), *NOD* (object is observed multiple times at different slit positions), and *STARE* (object and background are observed only once within the same frame). In this context we note again that the presented methods only cover the reduction of UVB and VIS.

Our calibration recipes are implemented in *IDL (Interactive Data Language)* and *PyRAF (IRAF[3] command language based on Python)* and, together with the ESO pipeline, are part of a *Python* script that runs each step in a predefined order. Generally, the data reduction sequence can be categorized in three steps: 1) calibrations performed on the raw frames (pre-processing), 2) steps executed within the code provided by ESO (pipeline), and 3) calibrations applied to the rectified spectra (post-processing). An overview of the calibration sequence is given in Table 2, where the presented order corresponds to the order of execution. We note that we do not include the telluric correction in this work, and therefore exclude the affected wavelength regions from all further analyses. There have been several groups working on telluric correcions for X-SHOOTER data, either with statistical methods (Chen et al. 2014) or with the radiative transfer code *Molecfit* (Smette et al. 2015; Kausch et al. 2015), and so we refer the interested reader to these publications.

Most of our additional calibrations were implemented after the rectification for reasons of technical simplicity and user friendliness. Nevertheless, we want to emphasize that for a fully consistent error propagation a rectification and resampling of the curved echelle orders should be avoided, as the accompanying kernel convolution interpolation does not preserve the fundamental noise characteristics of the data. Despite this, we decided to maintain the overall *modus operandi* predetermined by the ESO pipeline (i.e., extracting and rectifying the echelle orders) and provide reasonable error estimates for all additionally required steps. Depending on the data type (extended object or point source) and OB mode (*STARE, NOD, OFFSET*) only a subset of the presented recipes is executed. For most of the mentioned recipes, our code produces various control plots, with which the quality of the calibration performance can be evaluated and optimized, if required.

3.2 PRE-PROCESSING REDUCTIONS

Several calibrations have to be performed directly on the raw frames, as the underlying systematic effects are not limited to individual echelle orders, but affect the global count distribution of the entire CCD.

3 IRAF is distributed by the National Optical Astronomy Observatories, which are operated by the Association of Universities for Research in Astronomy, Inc., under cooperative agreement with the National Science Foundation.

Section	task description	data type	OB mode
	pre-processing reductions		
3.2.1	pick-up noise elimination in bias frames	all	all
3.2.2	inter-order background and pick-up noise modeling in science frames	all	all
	pipeline reductions		
3.3.1	bias subtraction	all	all
3.3.2	cosmic-ray hits removal	all	all
3.3.3	wavelength calibration and extraction (rectification)	all	all
	post-processing reductions (on rectified spectra)		
3.4.1	error map rescaling	all	all
3.4.2	illumination background and pick-up noise subtraction	all	all
3.4.3	bad pixel interpolation	all	all
3.4.4	flat fielding	all	all
3.4.5	illumination correction	all	all
3.4.6	nodding	point source	*NOD*
3.4.7	sky subtraction	point source	*STARE*
3.4.9	optimal extraction	point source	all
3.4.10	absolute flux calibration and order merging	all	all
3.4.11	fine-tuning of the wavelength calibration	all	all

Table 2: Calibration sequence for X-SHOOTER data. Column 1 shows the sections under which the various calibration steps (Col. 2) are described in this work. The data types (*point source*, *all*) for which the recipes are applicable are given in the Col. 3. Column 4 contains information about the OB modes (*STARE, NOD, OFFSET, all*) that can be handled by the recipes.

3.2.1 *Pick-up Noise Elimination in Bias Frames*

The UVB CCD of X-SHOOTER is susceptible to pick-up noise in calibration and science frames, which manifests itself as an additional periodic pattern that fluctuates around the bias level with an amplitude of up to ∼2 counts distributed over various frequencies, with a phase that changes from frame to frame. The extrema are orientated along the NAXIS1 axis and have a typical spacing of approximately 10 pixels. This alignment offers the possibility of removing the pick-up noise pattern by a one-dimensional Fourier filtering technique. For this, the raw bias frames are first checked for outliers (cosmic ray hits, bad pixels), which are then replaced by a locally estimated median. In order to appropriately check for outliers, we implemented a $\kappa - \sigma$ (throughout the course of this chapter σ denotes uncertainties)clipping and carefully adjusted the involved parameters. The box that is used to compute the local median and standard deviation is a vertical one-dimensional stripe of 51 pixels in length and the clipping threshold is chosen to be $8\,\sigma$. The chosen box size represents a compromise that reliably eliminates both extended cosmic ray hits (CRH) and CCD blemishes, and at the same time is sufficiently small in order not to wash out any global trends in the overall bias structure.

Each column treated in this way is then FOURIER-transformed separately and the absolute values of the FOURIER modes are computed. A κ-σ clipping process is applied to the power spectrum that flags any dominant frequencies that are $6\,\sigma$ outliers. Their real and imaginary parts are then replaced by the corresponding mean values of the adjacent modes, thereby preserving the amplitude and phase of the overall noise pattern. Back-transforming the clipped Fourier spectrum finally yields bias frames that are free of pick-up noise and thus can be used in subsequent processing steps. Pick-up noise has not been detected in the VIS data for any of our reduced frames. Therefore, this calibration step is only applied to the UVB data.

3.2.2 *Inter-Order Background and Pick-up Noise Modeling in Science Frames*

Regrettably, the algorithm presented in Section 3.2.1 does not work for inhomogeneously illuminated CCDs with pronounced discontinuities in the global light distribution. The cross-disperser of X-SHOOTER produces strongly curved echelle orders that have separations of $5-70$ pixels, depending on the spectral order number. The inter-order (i.e., between the individual echelle orders) background count level, caused by a combination of the stray light, light diffusion inside the prism, and the change in order spacing, is a highly non-linear pattern that follows the illumination intensity of the adjacent echelle orders, which themselves are functions of both the spectral energy distribution (SED) and the blaze function. The illumination background inside each order can only be reconstructed by propagating the illumination pattern between the orders with interpolation and/or fitting techniques. In the inter-order background subtraction implemented in the X-SHOOTER pipeline package (v1.5.0), the user has the possibility of fitting a global two-dimensional polynomial of low order to selected background regions. This yields a smooth surface that follows the overall shape of the background counts distribution. However, it fails to

reproduce small-scale effects like additional pick-up noise or enhanced stray light by line emission. Furthermore, the VIS arm throughput shows a rapid increase between order 12 and its maximum at order 14, as well as a steep drop-off for even longer wavelengths, which cannot be modeled satisfactorily by the pipeline owing to the comparatively large correlation length of the fitted surface. An example plot demonstrating this issue is presented in Figure 7, where we show a horizontal cut through a GD71 VIS raw frame in which the echelle orders have been masked out so that the underlying illumination surface can emerge. The best fit obtained with the pipeline is overplotted in dashed green, which does not reproduce the scattered light component close to the strongly illuminated orders 14+15. These shortcomings encouraged us to implement a subtraction technique that can reproduce both the global trend of the general background illumination as well as additional small-scale effects, such as pick-up noise and line emission. For this, we decided to model the background of each CCD row individually, thereby naturally including the horizontally aligned pick-up noise described in the previous section.

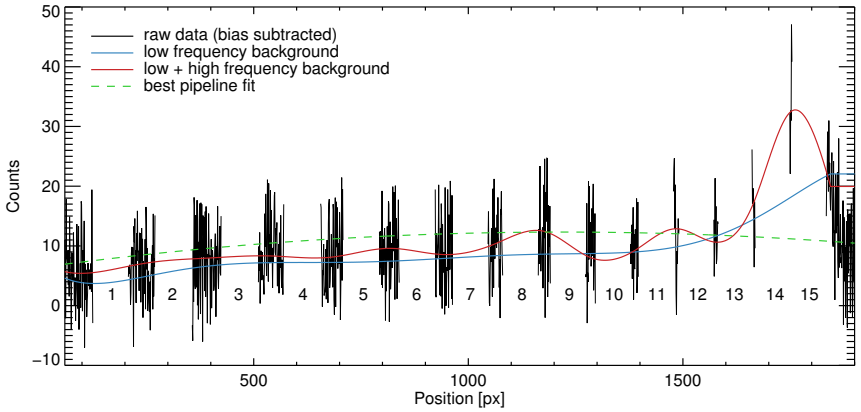

Figure 7: Horizontal cut through a bias subtracted VIS raw frame of GD71. The blue curve shows the low order CHEBYSHEV fit and the red curve the superposition of the CHEBYSHEV fit and an additional spline fit. The best background fit obtained with the ESO pipeline is overplotted as a dashed green line. The gaps in the data (black curve) indicate the positions of the echelle orders. The respective order numbers are specified.

First, the two-dimensional raw frame is bias subtracted with a master bias frame, which is a median stack of a time series of bias exposures corrected for pick-up noise and is calculated within the original pipeline (see Section 3.3.1). The echelle order positions are then read out from the corresponding table that is produced during the wavelength calibration (see Section 3.3.3). Since diffraction at the slit ends is considerable in case of bright and extended objects, e.g., sky lines, we add an additional safety margin of up to 6 pixels on either side of the echelle order because additional diffraction counts are not to be included in the inter-order background level, as they only occur outside but not inside the echelle order. The actual size of the margin depends on the amplitude of the blaze function and the associated level of diffraction at the particular pixel position of interest, i.e., wider margins for more strongly illuminated orders.

Next, the statistical outliers in the inter-order sections are removed in a similar way to that described in Section 3.2.1, with $\kappa = 4$ and a vertical box size of 151 pixels, allowing for a better treatment of the significant number of cosmic ray hits. We choose the vertical direction because the extent of the inter-order space decreases monotonically along the horizontal direction, approaching only a handful of pixels between the reddest orders in the VIS arm. Pixels masked by the echelle order apertures are excluded from the boxcar median estimate during the $\kappa - \sigma$ rejection, implying that the box size is reduced in the direct vicinity of the echelle orders if necessary.

In case of low S/N data, in which the object only produces a very weakly illuminated background level (on average < 2 counts per pixel), we found it sufficient to fit the inter-order sections of each row with a low-order polynomial. For this, the median of each inter-order section (per row) is computed, resulting in $n+1$ values for n echelle orders. Before the bluest order (1) and after the reddest order (UVB: 12, VIS: 15) we specify a rather narrow margin of 10 pixels for the median estimate, accounting for the fact that the information content on the illumination background decreases with increasing distance to the echelle orders. The section medians are subsequently fitted with a fifth-order Chebyshev polynomial and the row-by-row fits are stored into a two-dimensional frame. The low polynomial order is chosen to ensure that even low S/N data with average background count levels of less than one can be robustly fitted and pick-up noise can be reliably detected even in the absence of strong stray light and light-diffusion components.

In cases where the inter-order background signal is on average > 2 counts per pixel and follows the illumination distribution inside the orders, a two-step modeling approach is implemented. We first mask out inter-order sections that typically show an enhanced level of background illumination (i.e., VIS orders 13, 14, 15), and fit the remaining sections row by row with an eighth-order Chebyshev polynomial. The residuals between fit and data are checked for statistical outliers with a $2\,\sigma$-clipping and, if necessary, a second fitting iteration is performed without the sections not well modeled by the fit (e.g,. due to line emission). This yields a background model that is well adjusted to the smooth, low frequency component of the illumination surface. Subsequently, the section medians of the residuals between data and low-order background model are interpolated with a third order spline function that accounts for localized line emission and large gradients in the throughput function. This component (red minus blue fit in Figure 7) is then added to the low-order estimate and the row-by-row models computed this way are stored into a global background model. Examples for the obtained low (blue) and low + high (red) frequency background components are shown in Figure 7 and present a considerably better fit than the one obtained with the built-in pipeline recipe (dashed green). Similar to the treatment of the bias frames, the superposition is eventually Fourier transformed column by column. Any dominant modes are extracted and back-transformed into a separate frame, while the remaining spectrum (with the extracted modes replaced by the amplitudes of the adjacent channels; similar to Section 3.2.1) is back transformed separately, and subsequently smoothed with a 7×7 pixel boxcar median to suppress possible fitting artifacts (i.e., random line-to-line fluctuations).

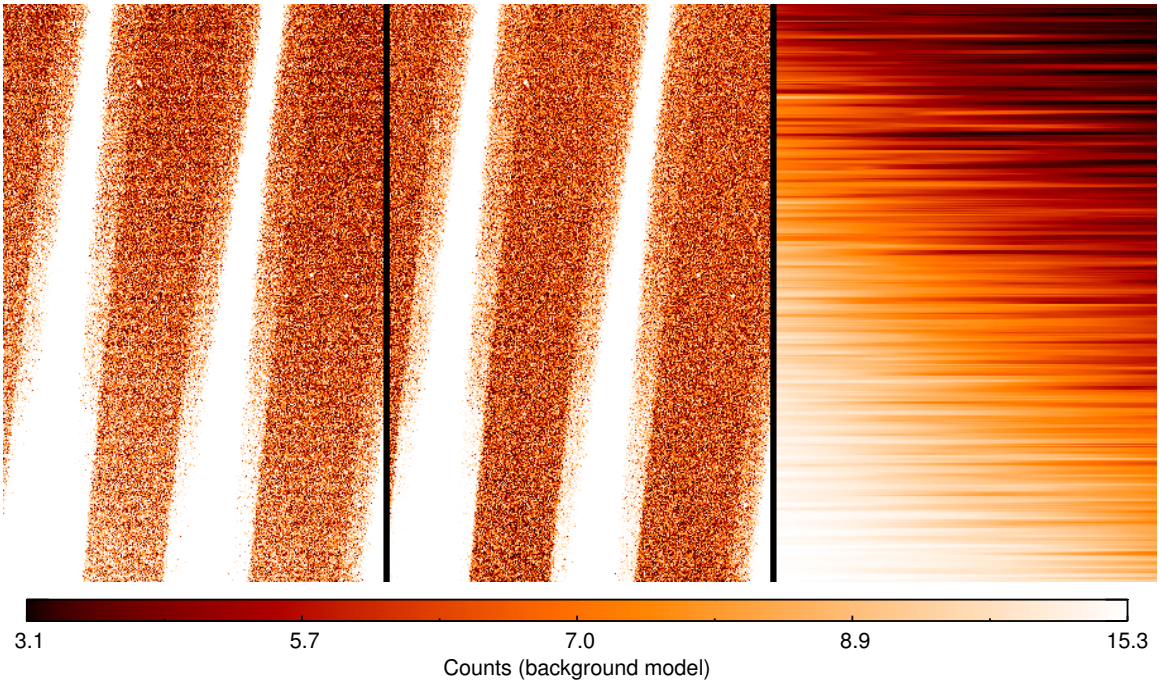

Figure 8: Inter-order background subtraction results for GD71. The left panel shows a section of a UVB raw frame (two illuminated echelle orders and the inter-order space between them), with illumination background (including pick-up noise). The central panel shows the same CCD section with applied inter-order background corrections. The corresponding illumination background model is presented in the right panel and its color scaling is illustrated in the bar at the bottom (bar valid only for right panel). The horizontally aligned pick-up noise shows up as a periodically alternating level of reduced and enhanced counts and is accurately fitted by the model. The color scales of all images have been histogram equalized.

To demonstrate the two-dimensional performance of our approach with an emphasis on the correction for pick-up noise, the left and central panels of Figure 8 show a before and after comparison of a GD71 UVB exposure using the inter-order background subtraction. The right panel contains the corresponding two-dimensional background model with the characteristic pick-up noise pattern, which is significantly reduced after subtraction (central panel).

The two-dimensional inter-order background model is stored in a FITS file and the subtraction is performed after rectification (see Section 3.4.2), in order to correctly propagate the flux uncertainties into the rectified frame. In this context it should be noted that the ESO pipeline computes Poisson flux errors from the raw frame.

3.3 PIPELINE DATA REDUCTION STEPS

Although the X-SHOOTER pipeline can in principle be used for the complete reduction work flow, we restrict the usage to the construction of the master bias frame and the extraction and rectification of the échelle orders. This includes the wavelength calibration and the removal of cosmic ray hits (CRHs). We will briefly summarize the involved steps below.

3.3.1 *Bias Subtraction*

Typically, five bias frames corrected for pick-up noise (see Section 3.2.1) are specified as input for *xsh_mbias*, which generates a master bias frame and the associated error map. The master frame is a median stack of all supplied frames and the error values are set to the readout noise level. The master bias frame serves as input for all subsequent pipeline recipes. A more detailed explanation is given by Modigliani et al. (2010) and the corresponding pipeline manual[4].

3.3.2 *Removal of Cosmic Ray Hits*

The cosmic ray hit rejection algorithm implemented in the X-SHOOTER pipeline (v.1.5.0) is based on edge detection by Laplacian convolution (van Dokkum 2001) and is performed on the raw frames. We obtained the best CRH rejection results with the following parameter settings: *–removecrhsingle-sigmalim=2.0* (Poisson fluctuation threshold, default=5.0) and *–removecrhsingle-flim=1.1* (minimum contrast between Laplacian image and fine structure image, default=2.0).

To check for possible side effects we carefully compared the results of our parameter choice to the ones obtained with the default values. In particular, we focused on targets with bright emission lines in narrow slit setups, for which we expect the risk of confusion between CRH and line spread function to be the highest. We could detect no significant flux changes by the CRH rejection algorithm except for one case in which the Hα transition

4 http://www.eso.org/sci/software/pipelines/

was saturated. In this case, the resulting discontinuities were flagged by the algorithm, and the associated count values slightly altered. Such a scenariom, however, can be considered unrealistic for our set of GC spectra.

By contrast, the direct vicinity of bad pixels in highly exposed parts of the CCD form the only scenario for which we could systematically detect undesired flux changes for our choice of parameters (apart from true CRHs), which typically result in count drops $\gtrsim 20\%$ per affected pixel. This effect is particularly pronounced for the two bad pixel columns intersecting echelle order 5 of the VIS arm. Apparently, the prior information on bad pixel positions is not used during the CRH flagging, as otherwise the detection algorithm should have been adjusted accordingly to the underlying bad pixel map to avoid the above mentioned side effect. Unfortunately, as of v1.5.0 of the ESO X-SHOOTER pipeline, the location of flagged CRH pixels is not directly propagated into the quality control maps. However, the CRH positions are stored in a separate *FITS* extension, which we cross correlate with our master bad pixel map (see Section 3.4.3 for a detailed description of its derivation and the subsequent use) to find any CRH-affected pixels in the direct vicinity of bad pixels. The threshold distance (with respect to the closest bad pixel) for a CRH position to be flagged as critical is set to 2 pixels, whereas the standard two-dimensional Euclidean norm is used to compute the necessary separations. Only these CRH positions are inherited by our master bad pixel map and are later corrected for possible flux changes. For all other locations we rely on the built-in CRH rejection routine to estimate and recover the original values.

3.3.3 *Wavelength Calibration and Order Extraction*

The wavelength calibration and order extraction processes of both the UVB and VIS arm are based on a series of ThAr lamp and flat field lamp frames (which are located inside the instrument; see Figure 2). A first spectral format estimate is generated with two-dimensional Gaussian fits to the spectral lines of a single-pinhole (0.5″ diameter) arc lamp exposure . Crossmatching the obtained line positions with a reference line catalogue yields an optimization of the instrument's physical model, which is based on a ray-tracing algorithm for different wavelengths and slit positions, and includes various ambient parameters (Bristow et al. 2010). Subsequently, the centers of the individual echelle orders are traced with a single-pinhole flat lamp exposure. In order to obtain a full, two-dimensional wavelength solution that maps the pixel coordinates of the raw frame (x, y) onto the physical grid of wavelength and slit position (λ, s), an additional nine pinhole ThAr frame is acquired. Applying the same fitting techniques as for the single-pinhole ThAr exposure, the emission peaks are accurately located and the physical model parameters refined. With additional parameters from the science exposure FITS header, the model is finally adjusted to the ambient conditions of the observation and the raw data are rectified, extracted, and resampled to an equidistant wavelength grid with a kernel convolution interpolation. To account for instrument flexure at off-zenith positions of the telescope and the accompanying shift in wavelength and slit position, additional flexure compensation frames are typically acquired before the science exposure and the

appropriate calibration corrections performed automatically. A more detailed discussion on the achieved wavelength calibration accuracy is presented in Section 3.4.11. Again, the reader is referred to Modigliani et al. (2010) for a full description of all pipeline steps and to Bristow et al. (2010) for an extensive demonstration of the powerful physical model capabilities.

3.4 POST-PIPELINE REDUCTIONS

We implemented most of the additional calibration steps on the pipeline-reduced and rectified echelle orders. This offers the possibility of working on equidistant, rectangular pixel grids that are calibrated in wavelength and slit position, which simplifies the technical complexity. However, the rectification process with its kernel interpolation introduces covariances that, if not properly modeled, potentially lead to inconsistent error estimates and thus to a vitiation of the spectral information content. With this in mind, we paid particular attention to accurately quantifying uncertainties related to choosing post-pipeline corrections in order to achieve the highest possible data quality on the one hand, and a well characterized data structure with focus on reproducibility and manageability on the other hand.

3.4.1 *Error Map Adjustments*

A correct estimate of the uncertainties accompanying each observation and the subsequent reduction processes is crucial for any scientific analysis. We therefore carefully investigated each step of the error treatment and applied corrections to the pipeline implementation if necessary.

3.4.1.1 *Error Map Rescaling*

We analyzed the accuracy of the error propagation in the pipeline rectification process and we found the implementation of the error calculation in the ESO pipeline to be incorrect, although, surprisingly, it is correctly described in the manual. Based on the standard error estimate

$$\sigma_{tot}[ADU] = \frac{\sigma_{tot}[e^-]}{g} = \frac{\sqrt{gF + (\sigma_r[e^-])^2}}{g} = \sqrt{\frac{F}{g} + \left(\frac{\sigma_r[e^-]}{g}\right)^2}, \tag{11}$$

where F are the measured counts and σ_r is the readout noise (specified in the file header), we noticed that the pipeline end product lacks the correct treatment of the gain g, which is given in units of e^-/ADU (e^- ≡electrons). For data that is dominated by Poisson noise, the rectified errors differ by one factor of the gain from the correct value, whereas in

readout-noise-limited cases an additional gain dependent deviation occurs. After extensive testing, we implemented a scaling that leads to the correct error form via

$$\sigma_c = \frac{\sigma_p \sqrt{\frac{F}{g} + \frac{\sigma_r^2}{g^2} + \frac{\sigma_{r,B}^2}{g^2}}}{g\sqrt{\frac{F}{g} + \sigma_r^2 + \sigma_{r,B}^2}}, \tag{12}$$

where σ_p is the incorrect error computed by the pipeline and σ_c the error after correction. The third term under both square roots of Equation (12) originates from the bias subtraction that is applied by the pipeline right before the rectification and takes into account the noise level $\sigma_{r,B}$ of the master bias frame. However, because of the irreversibility of the kernel convolution during the rectification process, this remains only an approximate correction. This incorrect error calculation implementation is an issue that affects all wavelengths and thus at least in cases for which $\sigma_r^2 \ll gF$, produces a constant deviation from the correct error estimates, which translates into a systematic S/N bias.

3.4.1.2 *Rebinning Corrections*

Because the ESO pipeline implements a simple *resampling* of the pixel information from the raw to the rectified frame (with a simplistic Gaussian error propagation of flux uncertainties and readout noise), the output grid does not encode the correct information about the resampled pixel sizes. Here, we propose a different implementation that includes a *rebinning* of the raw grid, where the input fluxes are internally redistributed during the rectification and, hence, the associated errors rescaled according to the output pixel size, so that the raw-frame S/N per wavelength unit is preserved in the rectified frame (modulo covariances of the interpolation convolution, see Section 3.4.1.3).

We emphasize this resampling issue, because X-SHOOTER's dispersion relation varies by a factor of two in the covered wavelength ranges of the UVB and VIS arms. In both arms, it typically starts at 0.1 Å pix^{-1} in the blue and ends at 0.2 Å pix^{-1} at redder wavelengths, with an almost linear increase in between. The average instrumental dispersion of each order is given in Col. 5 of Table 3.

During rectification, the pipeline interpolates the dispersion-variable input signal to an output grid of user-specified constant dispersion. This interpolation is a basic resampling that does not account for the spectrally variable pixel size in the raw frame, but simply interpolates the detected counts to the desired output grid and applies a Gaussian propagation to the associated errors, irrespective of the size of the light collecting area at a given wavelength. This leads to a conservation of pixel values (intensities) and a S/N scaling, which is independent of the chosen output dispersion. In fact, the measured counts on the raw images represent fluxes and already constitute an implicit integration (over the wavelength range and slit coordinate dimension covered by each pixel). Thus, since spectroscopy is typically interested in (differential) distribution functions, the input pixel sizes need to be traced and propagated accordingly to the error map. While these considerations theoretically also hold for the cross-dispersed dimension, any change in

pixel size between raw and rectified spectrum essentially corresponds to a change in spectral dispersion, as X-SHOOTER's cross-dispersed pixel size ($\sim 0.16''$/pixel) remains almost constant for all orders in the UVB and VIS arm.

To measure the input pixel size, we constructed an artificial raw frame with a constant count level and rectified it with the keyword *rectify-conserve-flux=TRUE* (default *FALSE*)[5]. When normalized by the input count level, the pixel values β in the obtained rectified spectrum represent the relative output pixel size with respect to the true pixel size on the raw frame, i.e.,

$$\beta = \frac{A_o}{A_i}, \tag{13}$$

where $A_{i,o}$ are raw (input) and rectified (output) pixel sizes. Dividing each pixel of the rectified error map by $\sqrt{\beta}$ finally yields an error spectrum with properly propagated information on the true light collecting area at each spectral position and ensures a conservation of the raw-frame S/N.

3.4.1.3 *Covariance Considerations*

In addition to the variable pixel size, covariance of the spectral data in the rectified images is another effect that has to be properly taken into account if an accurate estimate of the measurement uncertainties in later analysis steps is desired. Pixel correlations are introduced by the kernel convolution process as part of the rectification procedure and the particular covariance contributions vary from pixel to pixel. To quantify the covariance we rectified a homogeneous noise frame (using the default kernel shape and size) and compared the standard deviations of the fluxes in the input and rectified frame. The standard deviation after rectification is lower by a factor of 1.22, which translates into an average correlation length of 1.5 input pixels or $1.5 \times \beta$ output pixels (for an explanation of β see Equation 13), respectively. Thus, the noise level inside the flux frame is underestimated and any further S/N calculations require the consideration of *both* the flux and variance frame. We also stress that any subsequent analysis step needs to correct for the effective number of independent pixels N_{eff} when computing a reduced χ^2 of any feature involving N output pixels, which can be approximated by $N_{eff} \approx N/(1.5 \times \beta)$. Although originally intended to be accessible for the user (Horrobin et al. 2008), the per-pixel covariance matrices are not output by the ESO pipeline and thus this piece of information is irreversibly lost and cannot be recovered from the data easily.

3.4.2 *Illumination Background and Pick-up Noise Subtraction*

Once the two-dimensional wavelength and slit mappings are known, the previously constructed global background frame (see Section 3.2.2) can be rectified in the same way as the associated science frame. This is accomplished by copying the science header to

5 Using the pipeline with either option (*rectify-conserve-flux=TRUE* or *FALSE*) does not treat the flux and variance values consistently.

the background model, so that both frames are pipeline-reduced with the same physical model parameters. This ensures a correct error treatment, since the error maps for both the science and the background frame are computed during the rectification (consisting of read-out noise and Poisson error), rescaled based on the corrections of Section 3.4.1, and can thus be propagated accordingly during the subtraction. While the fluxes are simply subtracted from each other, the errors of both frames are summed in quadrature, i.e.,

$$\sigma_{tot} = \sqrt{\sigma_s^2 + \sigma_b^2}, \tag{14}$$

where σ_s and σ_b are the rectified errors of the science frame and background frame, respectively.

3.4.3 *Bad Pixel Interpolation*

Since the bad pixel flagging and correction (based on the master bad pixel map computed during the master bias creation) did not work reliably with the X-SHOOTER pipeline v1.5.0 for our data set, we developed a routine that reliably flags bad pixels first, and then fits over the affected science regions to reconstruct the object signal. For reasons of technical simplicity (orthogonality of the $\lambda - slit$—coordinate system), we correct for bad pixels on the rectified spectra, which requires that the bad pixel information on the raw frame be accurately traced through the rectification process.

In a first step a master bad pixel map is created. It is based on two median stacks of *linearity* flat fields (homogeneously illuminated frames), each set with its own exposure time. Both stacks are normalized by their respective exposure times and then divided by each other, resulting in a frame in which pixels with a strong non-linear response show significant deviations from unity. For each pixel in this ratio frame the local median and standard deviation in a box with a side length of 25 pixels are computed. A $4\,\sigma$ detection threshold is applied to flag outliers, which are considered to be bad pixels and whose values are set to one in the master bad pixel map. Accordingly, good pixels are set to zero.

By appropriately updating all necessary header information, the master bad pixel map is rectified and extracted in exactly the same way as the science frames, ensuring that the information on the bad pixel positions is accurately traced and matches the two-dimensional mapping $(x, y \rightarrow slit, \lambda)$ of the science exposure. The kernel convolution interpolation that is applied during the rectification introduces pixel correlations (see Section 3.4.1.3) that map the original binary distribution of pixel values $\{0, 1\}$ in the master bad pixel map onto the full range of $[0, 1]$. We define the badness b of a pixel as how much the rectified bad pixel map deviates from zero and refer to this badness map whenever we want to check the quality of the pixels in the rectified science output.

In order to correct the science observation for artifacts introduced by non-linear pixels, each wavelength bin of the science flux frame is fitted separately with cubic b-splines[6]

6 IDL source code: http://www.sdss3.org/svn/repo/idlutils/tags/v5_5_5/pro/bspline/bspline_fit.pro

along the cross-dispersed direction on the rectified output (see Figure 9). The break points for the spline fit are defined only at pixels where $b \leqslant 0.1$ and pixels with $b > 0.1$ are excluded from the fit. Finally, a weighted linear combination r of the uncorrected data d and the corresponding fit f is computed,

$$r = (1 - b)\, d + bf, \tag{15}$$

however, only for pixel values for which $b \leqslant 0.25$. If $b > 0.25$ the comprised count value is considered to be too uncertain and the corresponding value of the spline fit is taken instead, because we encountered cases in which some pixels systematically showed count values $< -10^3$ after rectification (and bias subtraction), even though the corresponding raw signal was similar to the bias offset level. Such artifical outliers can dominate the linear combination even for $b \approx 1$ and, thus, we decided to introduce a threshold in b above which the corresponding flux values are ignored. We note that both the spline break point threshold and the linear combination threshold were adjusted on an empirical basis and work reliably for different kinds of illuminations and profile shapes.

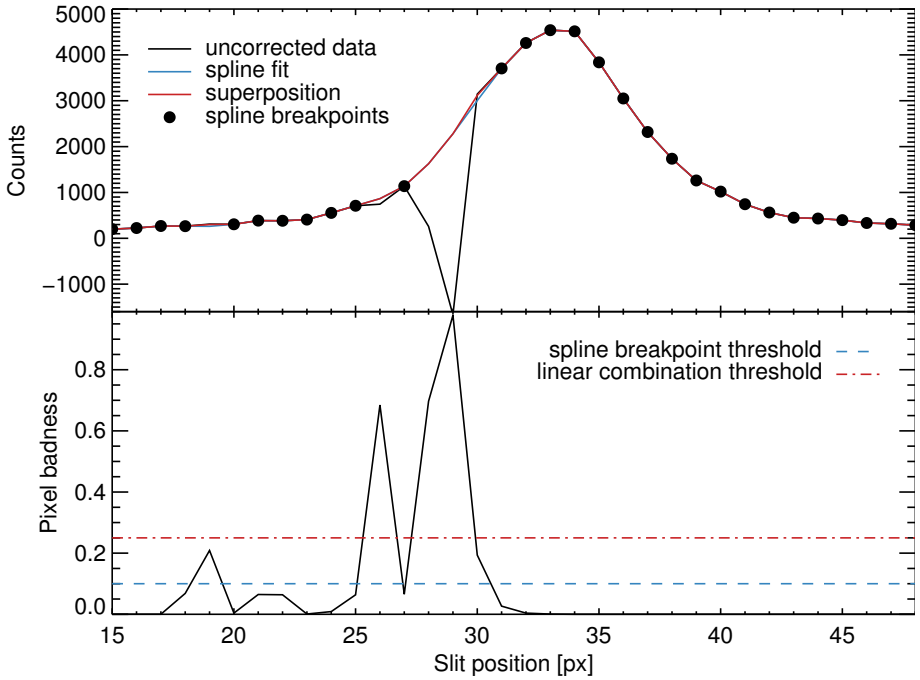

Figure 9: Cut through rectified echelle order five of GD71 (VIS), which is intersected by two adjacent bad columns on the raw frame. The top panel shows the uncorrected point spread function (black curve), the weighted spline fit (blue curve) and the weighted linear combination of both (red curve). The solid circles show the grid locations that are used as break points for the spline fit. The weighting factors are based on the pixel badness as depicted in the bottom panel. The thresholds for the spline break points (blue dashed line) and the weighted linear combination (red dash-dotted line) are overplotted.

Choosing splines for the reconstruction of bad pixel affected signals has the advantage that no further information on the spatial point spread function (PSF) of the data is re-

quired. However, there is a risk that the original light distribution may not be optimally recovered. We found our method to be robust for reasonably concentrated bad pixel regions ($\lesssim 3$ pix), which is the case for all our data. To illustrate the general performance of our correction method, we show a before and after comparison in Figure 10 for a section of echelle order five of GD71 (VIS), which is intersected by two bad columns on the raw frame ($x = 853, 854$). The imprints of the bad pixels are significantly reduced; however, we still recommend inspecting problematic detector regions manually with the help of the rectified master bad pixel map and updating the correction function as necessary.

3.4.4 *Flat Fielding*

Flat fielding is the next step that is applied to the bad pixel corrected data. As we want to correct only for pixel-to-pixel quantum efficiency variations, the global shape of the flat field spectral energy distribution, which generally needs to be considered temporally variable (changes in temperature/voltage of the flat lamp), should be removed first, as otherwise it would be imprinted into the sensitivity function of the instrument. In this case, all frames would need to be reduced with the same flat field image that was used for the standard star. Since our data set contains flat field images for every night, but only one acceptable flux standard star observation (GD71 in the night of November 7th), such a necessity represents an undesired limitation. The implementation of the X-SHOOTER pipeline, which flat fields the raw frames without any further treatment of the flat lamp exposure (i.e., without removing the SED of the lamp), except for a median stack and general wavelength-independent renormalization of the counts is therefore considered inappropriate. This implementation also means that any potential line emission signals from the flat lamp are implicitly contained in the final flux-calibrated science spectrum.

3.4.4.1 *Quantification of Flat Field Systematics*

Since we want to have the possibility of using one sensitivity function for our entire data set on the one hand, but always use the flat field images closest in time to our respective science frames on the other hand, we implemented a flat fielding approach that is based on the rectified version of each image. This treatment allows for a simple and robust elimination of the arc lamp's spectral response by fitting a smooth polynomial along the spectral direction. The drawback of this method, however, is related to the order in which additive and multiplicative steps are executed: ideally, the kernel convolution interpolation should be applied *after* each raw pixel is flat fielded with its individual response. If rectified, such a raw-frame-based flat fielding implementation yields a flat fielded signal f_{raw} and its associated noise model σ_{raw} that are given by

$$f_{raw} = \frac{\sum_i \frac{c_i}{r_i} w_i}{\sum_i w_i}, \quad \sigma_{raw} = \sqrt{\frac{\sum_i \left(\frac{\sqrt{c_i}}{r_i}\right)^2 w_i^2}{\sum_i w_i^2}}, \tag{16}$$

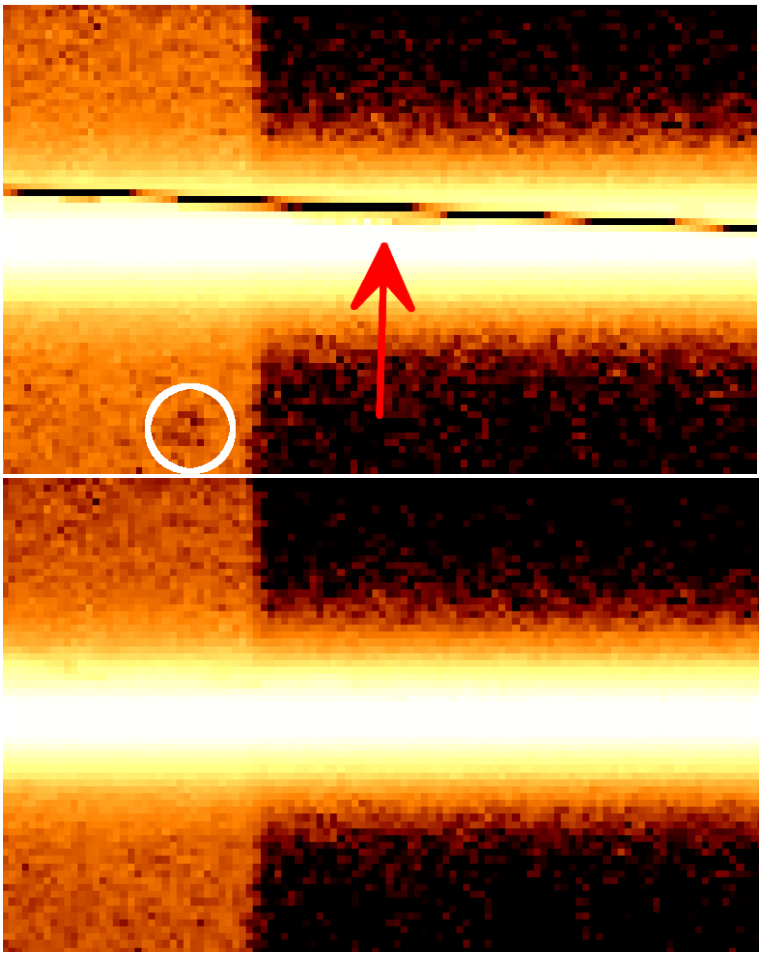

Figure 10: Zoomed-in section of the rectified echelle order five of GD71 (VIS) before (top) and after (bottom) application of the bad pixel interpolation. The artifacts of the bad columns 853 and 854 in the raw frame are visible as a dark stripe intersecting the illuminated echelle order. The area of reduced counts below the diagonal bad pixel stripe (indicated by the red arrow) is a consequence of the CRH rejection explained in Section 3.3.2. The cold spot at the lower left of the shown CCD section (marked by the white circle) is also reasonably corrected by our algorithm. The spectral dispersion direction runs horizontally along the x-axis. The plotted wavelength range is roughly 10 Å and the size along the cross-dispersed direction is ~4″. A vertical slice through these spectra is shown in Figure 9.

where c_i are the raw pixel counts on which the convolution is performed, w_i their respective kernel weights, and r_i the individual raw pixel responses as determined from the flat field measurements. In this simplified error estimation the only considered error component is Poisson noise and the flat fielding is assumed to be free of errors.

In our approach, however, the kernel interpolation is applied before the flat fielding, implying that the rectified pixel grid is flat fielded only with the kernel weighted average response, i.e.,

$$f_{rec} = \frac{\sum_i c_i w_i}{\sum_i w_i} \left(\frac{\sum_i r_i w_i}{\sum_i w_i} \right)^{-1}, \quad \sigma_{rec} = \sqrt{\frac{\sum_i c_i w_i^2}{\sum_i w_i^2}} \left(\frac{\sum_i w_i r_i}{\sum_i w_i} \right)^{-1}, \tag{17}$$

which produces slightly different results than Equation (16). To quantify the introduced numerical inaccuracy, we implemented both formulas in a one-dimensional Monte Carlo simulation with typical values for counts, kernel weights, and responses and compared their results. Figure 11 shows both f_{rec}/f_{raw} and $\sigma_{rec}/\sigma_{raw}$ for 10^5 realizations.

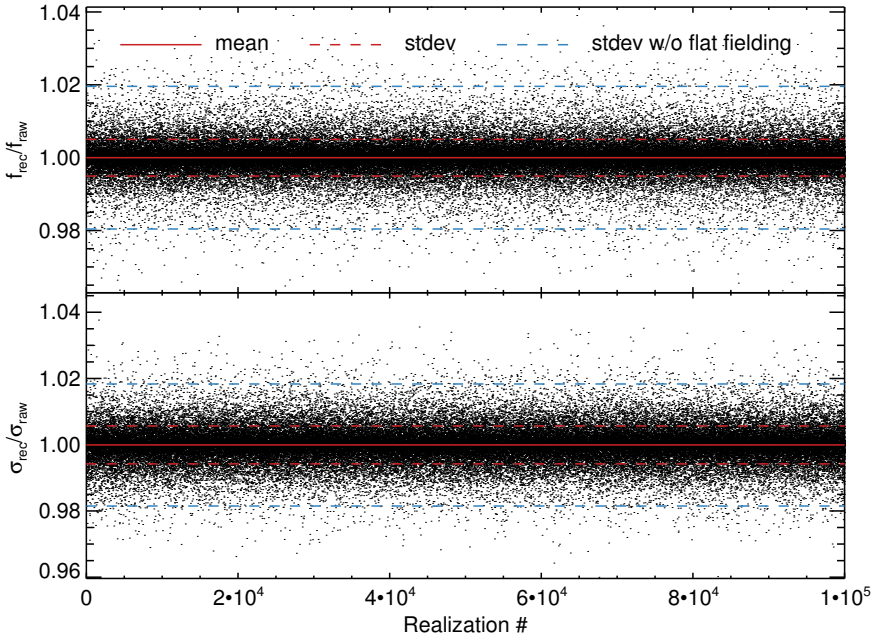

Figure 11: Ratios of 10^5 realizations of Equations (16) and (17). The interpolation is performed with a Lanczos kernel for random locations inside the inner $\pm 3\,\sigma$ of a Gaussian emission line with a FWHM of 3.5 pixels (assuming Poisson noise). The pixel responses are modeled with a normal distribution with $\mu = 1$ and $\sigma = 0.02$. In both panels (top: flux ratios, bottom: error ratios) the solid red line shows the ensemble mean, the dashed red line its standard deviation, and the blue dashed line the standard deviation when the data are rectified but flat fielding is not applied afterwards.

As input parameters for our simulation we selected values reflecting a typical X-SHOOTER observation: a one-dimensional Gaussian emission line with a FWHM of 3.5 pixels and a

central count level of 10^4 with an underlying continuum of 10^3 counts. The exact count values for the grid were determined with a random number generator and a Poisson noise model was assumed. In addition, the individual pixel responses were drawn from a normal distribution with $\mu = 1$ and $\sigma = 0.02$, the latter ones resembling a conservative upper limit on the expected pixel-to-pixel quantum efficiency variations. The rectification process was modeled with a standard Lanczos kernel with five lobes (Duchon 1979) and the count distribution was resampled with the kernel convolution at random grid locations inside the inner $\pm 3\,\sigma$ of the emission line.

Flat fielding the convolved output grid (see Equation 17) results in a $1\,\sigma$ uncertainty of 0.4% with respect to the accurate scenario of flat fielding the input grid before resampling (Equation 16). This is lower than the Poisson noise of a single pixel of a typically illuminated flat field frame ($\sim$1%). By contrast, omitting the flat fielding yields a $1\,\sigma$ deviation of 2.0%, which corresponds to the input response dispersion. The relative accuracy of the errors behaves in a similar way, with a $1\,\sigma$ deviation of 0.5% when flat fielding the resampled output grid and 1.7% if no flat fielding is applied at all.

Choosing a flat count distribution of 10^4 counts instead of an emission line profile for the input grid shows a deviation of only 0.03% for the fluxes and 0.5% for the errors. In both scenarios, this accuracy level is sufficient for all our purposes and thereby justifies implementing the flat fielding procedure on the rectified spectra.

3.4.4.2 *Removal of Flat Lamp Emission Lines*

In addition, working on rectified spectra also offers the possibility of easily removing emission lines of the flat field quartz lamp, which typically occur in the high energy range of the UVB arm. The sodium D2-lamp that is used to flat field the four bluest orders of the UVB arm of X-SHOOTER shows a multiplicity of emissions lines with a typical strength of one to five percent with respect to the underlying continuum. Not removing them from the quartz lamp SED, will imprint their inverse profiles in the science frame as additional, artificial absorption features.

In our flat fielding implementation we first create a median stack of five flat field images, which is then wavelength calibrated and rectified in the same way as the science exposure. Subsequently, the bad pixels of the master flat are corrected as described in Section 3.4.3. The quartz lamp's spectral continuum and the response of the instrument are removed by row-wise fitting one-dimensional twelfth-order CHEBYSHEV polynomials along the spectral dispersion direction. The impact of possible emission lines is removed by applying a $5\,\sigma$ clipping, together with a second fitting iteration. Normalizing by the continuum fit yields an intermediate solution that already carries direct information on the pixel-to-pixel variations, but still includes line signals, which can be removed by dividing each wavelength bin by its median value (see the two upper panels in Figure 12). The obtained quantum efficiency variations and the additional line emission signal are plotted in the third panel from the top in Figure 12. The necessity of correcting for quartz-lamp emission lines becomes obvious in the bottom panel in Figure 12, where we show the impact of such emission lines on the flat fielded SED of the spectrophotometric standard

star BD+174708. If the correction for quartz-lamp emission lines is omitted, the stellar spectrum systematically deviates on a five percent level from the data that were correctly flat fielded. This might lead to unexpected effects that are difficult to control if spectral features are located close to the emission features of the D2-lamp.

3.4.5 *Illumination Correction*

To achieve a relative flux calibration uncertainty of less than five percent for extended objects, we need to account for systematic illumination inhomogeneities along the slit. After the extraction and rectification process, the resulting slit illumination function is a combination of the instrument's imaging characteristics and the pipeline's ability to accurately trace and set extraction apertures around the curved echelle orders.

To measure the illumination function of X-SHOOTER we use dedicated sky flat fields that were taken in addition to the regular calibration runs of the instrument (C. Martayan, private communication). The optical light path of a sky image should be similar to the ones of scientific observations except for instrumental flexure, which is unique to every observation and depends on telescope pointing and time (see Section 3.4.11). By contrast, when the flat field quartz lamps are built into the instrument, we expect a different illumination pattern, rendering the quartz flats less useful to model the cross-dispersed illumination function of X-SHOOTER in science operation mode. The requirements imposed on the sky observations are a high S/N level, accurately compensated flexure, and no significant input signal gradient along the slit length of 11″. Sky flat fields are only taken on special request, with the implication that we have only one set of suitable observations for our entire data set.

For two different slit widths in each instrument arm (UVB: 0.5″, 5.0″; VIS: 0.4″, 5.0″), we rectified a sequence of five sky observations with their own flexure-compensated wavelength solution. Subsequently, the output was corrected for bad pixels and flat fielded (see Sections 3.4.3 and 3.4.4). We then normalized all cross-dispersed bins with respect to a weighted average of the central four rows, eliminating line emission and instrumental response. The resulting spectra consist of illumination inhomogeneities and observational noise in the (slit, λ) space. The noise level was reduced by taking a weighted average using the corresponding error frames over the set of five exposures. The illumination function can then be fitted with a high-order two-dimensional polynomial, yielding a smooth surface that follows any systematic gradients in the illumination pattern. Since each slit size has its own impact on the illumination function through different slit edge inhomogeneities and diffraction patterns, the above steps have to be executed separately for each slit size used. The left panel of Figure 13 shows one example of the illumination surface for echelle order three of the VIS arm for a 0.4″ wide slit. The maximum amplitude of the illumination variations is on the order of $\pm 2.0\%$ on a cross-dispersed length scale of ~ 5 pixels. Furthermore, there are additional long-scale variations of comparable amplitude that produce smooth illumination gradients along both the entire slit length and the full spectral range.

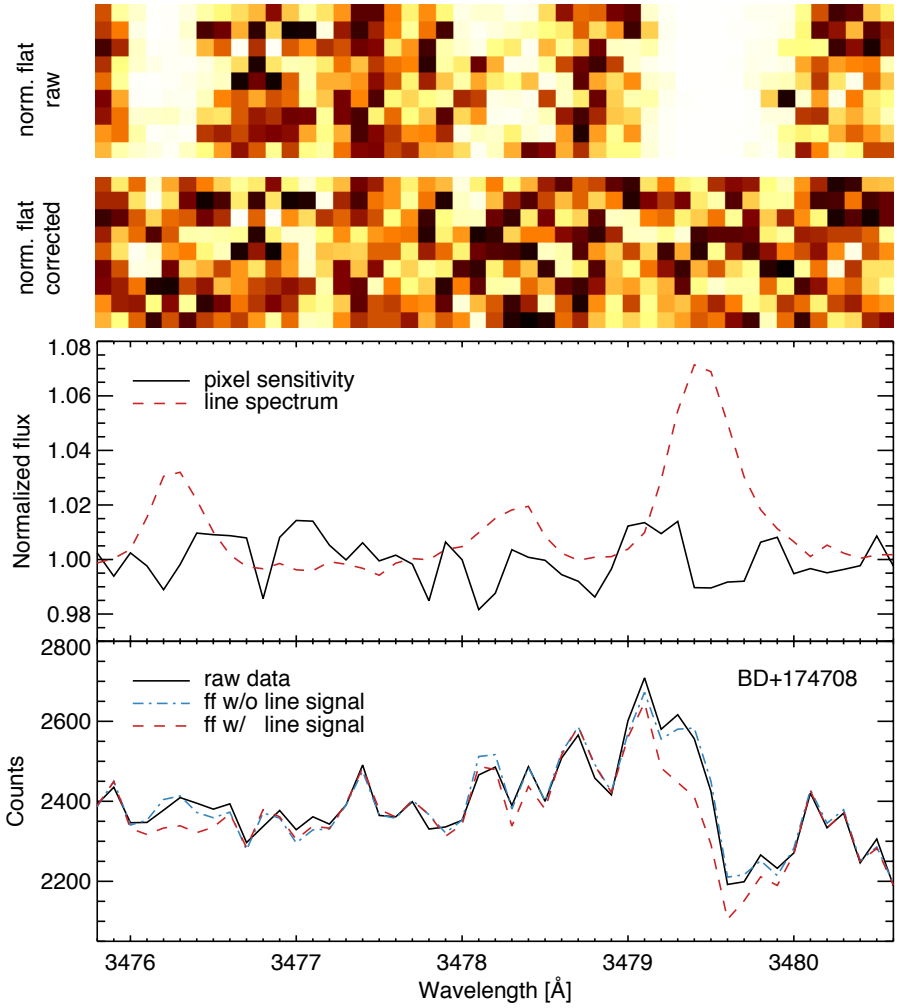

Figure 12: UVB flat field performance analysis. The top panel shows a zoomed-in section of the continuum-normalized SED of the D2 flat field lamp (echelle order four). The line emission is removed with an additional median along the cross-dispersed direction (second panel). In the third panel, we show the pixel-to-pixel quantum efficiency variations (solid black curve) at the central slit position and the corresponding line emission spectrum (dashed red curve). The bottom panel shows the SED of the spectrophotometric standard star BD+174708 without flat fielding (solid black curve), flat fielded with the continuum-normalized D2 lamp SED (dashed red curve), and flat fielded with its emission-line-free counterpart (dot-dashed blue curve). The wavelength scales of the four panels are aligned so that the positions of the emission lines are the same for images and plots.

For the narrow slit setup, the above mentioned numbers are typical amplitudes for any echelle order on both tested instrument arms. For the 5.0″ wide slit, we find that the small-scale fluctuations are considerably decreased and only the larger scale gradients among both cross-dispersed and spectral direction remain (see right panel of Figure 13). Thus, small-scale variations may be caused by slit edge inhomogeneities, as those will have a much greater fractional impact on smaller slit widths, and/or moving dust aberrations. To distinguish between static or temporally varying systematics, additional calibration frames would be required.

In general, the observed illumination inhomogeneities are of rather small amplitude, yet, in order to achieve a relative systematic flux calibration uncertainty below a few percent, a proper illumination correction is recommended.

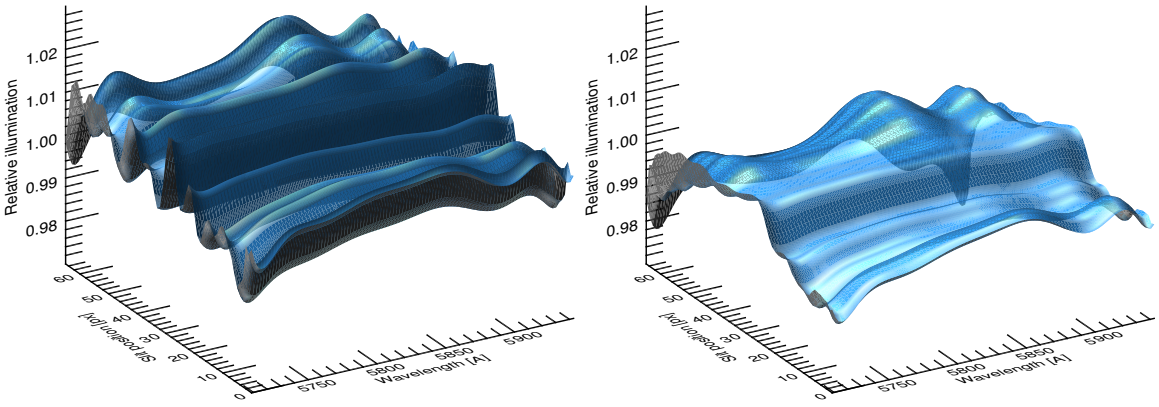

Figure 13: Two-dimensional illumination surfaces of echelle order three of the VIS arm for a 0.4″ slit (left) and a 5.0″ slit (right). The x-axis corresponds to the spectral dispersion direction, the y-axis to the cross-dispersed direction. The relative illumination is plotted on the z-axis. The maximum impact of the inhomogeneities is on the order of ±2.0%. The blue highlights and shadows were introduced to facilitate the visualization of the three-dimensional structure.

3.4.6 *Nodding*

Measurements conducted in *NOD* mode typically consist of two (or multiples of two) observations of the same target, between which the telescope pointing is slightly offset so that the object is imaged onto different slit positions for each observation. By co-adding the frames in the correct way, the sky signal is naturally removed, circumventing the need for a tedious sky modeling process. Yet, for the nodding technique to work accurately the sky signal needs to stay constant between the individual exposures, rendering this mode practically useless for any observations performed in twilight (e.g., standard star observations, see Section 3.4.7) when the sky signal might vary up to 20% within ten minutes.

The X-SHOOTER pipeline features a built-in treatment of nodded data, in which the co-addition is performed for the raw frames, yielding a rectified combined output. Never-

theless, the calibration steps presented in here are not applicable to these kinds of data in the strict sense, as multiplicative corrections are not commutable with summations, i.e.,

$$\sum_i \frac{F_i}{S_i} \neq \frac{\sum_i F_i}{\sum_i S_i}, \tag{18}$$

where F_i are the detected counts and S_i arbitrary correction factors of the pixels of interest. A similar reasoning was already presented in Section 3.4.4, where we describe how the kernel convolution of the rectification affects the accuracy of the flat fielding process.

We resolve this by rectifying and calibrating each sequential frame independently. All post-pipeline steps described in Sections 3.4.1 to 3.4.5 are applied to each frame and the co-addition is performed order-by-order for the calibrated spectra. For this, we read out the header keyword *HIERARCH ESO SEQ CUMOFF Y* of two subsequent frames A and B and compute the overall nodding offset. Dividing this offset (in arcseconds) by the scaling factor in the cross-dispersed direction ($0.16''$ pix^{-1} for unbinned data) should ideally yield an integer value, as only then can a direct match on pixel-scale level for the overlay of the two frames be achieved and an additional interpolation avoided. The co-added output flux, F_{AB}, then becomes

$$F_{AB} = F_A + F_{B_s} - (F_B + F_{A_s}), \tag{19}$$

where $F_{A,B}$ are the fluxes in the respective frames and s describes a shift by the nodding offset along the cross-dispersed direction. Since the overlapping part of the output spectrum then contains the sum of two exposures, the obtained counts in that region are divided by two to ensure a proper absolute flux calibration. The same scaling is applied to the propagated errors.

3.4.7 *Sky Subtraction for Point-like Objects*

This section describes the sky spectrum subtraction[7] in UVB and VIS arm spectra for point-like objects. We apply this treatment to the spectrophotometric standard star in our data set.

3.4.7.1 *General Considerations and removal of Artifacts*

In order to compute proper sensitivity functions required for the flux calibration of our data set, the spectrophotometric standard star signals need to be sky-subtracted. With X-SHOOTER, the standard star observations are usually performed either at the beginning or at the end of the night, often in twilight conditions. Since the default observation mode for these kinds of calibration data is either *OFFSET* or *NOD*, the sky spectrum to be subtracted is usually taken five to ten minutes after the stellar spectrum, depending on the exposure time of the respective standard star. Hence, without proper scaling of the sky

7 Throughout this work we refer to the sky spectrum as any spectrum that remains in the slit after subtraction of the primary science target spectrum. This includes any telluric spectrum, but also any other spectrum of an underlying background component

level during twilight conditions, the resulting subtraction typically results in a wavelength dependent under- or over-subtraction of up to 15%, depending on the twilight conditions.

The alternative built-in sky subtraction approach of the X-SHOOTER pipeline (v1.5.0), which defines two sky windows on each side of the science object and models the sky background with two-dimensional BEZIER splines without any additional sky frame, is better suited for twilight data. However, we found that this method produces unreliable results for some of our tested standard star spectra, in particular for regions where CRH residuals are found or at wavelengths of strong atmospheric absorption or emission. Since a careful adjustment of the involved fitting parameters did not eliminate the observed sky residuals, we decided not to use any of the pipeline methods.

To keep the technical complexity manageable, we implemented an order-by-order sky subtraction on the rectified spectra. For this, two sky window regions of nine pixels in spatial extent are defined at either slit end. Since residuals of CRHs and bad pixels are likely to compromise the sky signal, a proper treatment is necessary. As v1.5.0 of the X-SHOOTER pipeline does not propagate CRH positions into the quality control map, we require an algorithm that finds and flags any remaining residuals automatically. For this, at a given slit position, each pixel value is compared to a boxcar median (width: 50 pixels) running along the spectral dispersion direction and a $\kappa-\sigma$ clipping with $\kappa = 4$ and σ comprising the central 68% of the values inside the median box is applied to flag potential outliers. This procedure likewise flags CRHs and sky emission lines in narrow slit setups, requiring an additional step to reliably distinguish between both. In order to do that, we make use of the expected symmetry profile of the emission lines: Each pixel flagged in the first run is compared against the median of the same wavelength bin of the opposite sky window. The same $\kappa-\sigma$ clipping is applied, however, for this step with $\kappa=6$. Only if both conditions are fulfilled is the pixel considered a true outlier with respect to the underlying sky signal and its value is replaced with the above described spectral boxcar median. Both κ values have been selected empirically and were tested successfully in wide and narrow slit setups.

3.4.7.2 *Spline Modeling of the Background Spectrum*

With all outliers removed from the sky windows, the sky signal needs to be interpolated to the slit positions covered by the star. Fitting each wavelength bin individually along the cross-dispersed direction with a low-order polynomial offers a simple and robust means to handle line emission and absorption accurately once the spectrum is properly rectified. The caveat of this method, however, is its sensitivity to noise, as the spectral correlation length is set to zero by definition. Locally minimizing the residuals inside the sky windows for each bin can therefore lead to an increase in the bin-to-bin scatter outside the sky windows (and within the PSF aperture), as the noise level of each column is considered separately. To circumvent this problem we adopted the above mentioned spline fit approach along the spectral dispersion direction and implemented it to work on rectified spectra.

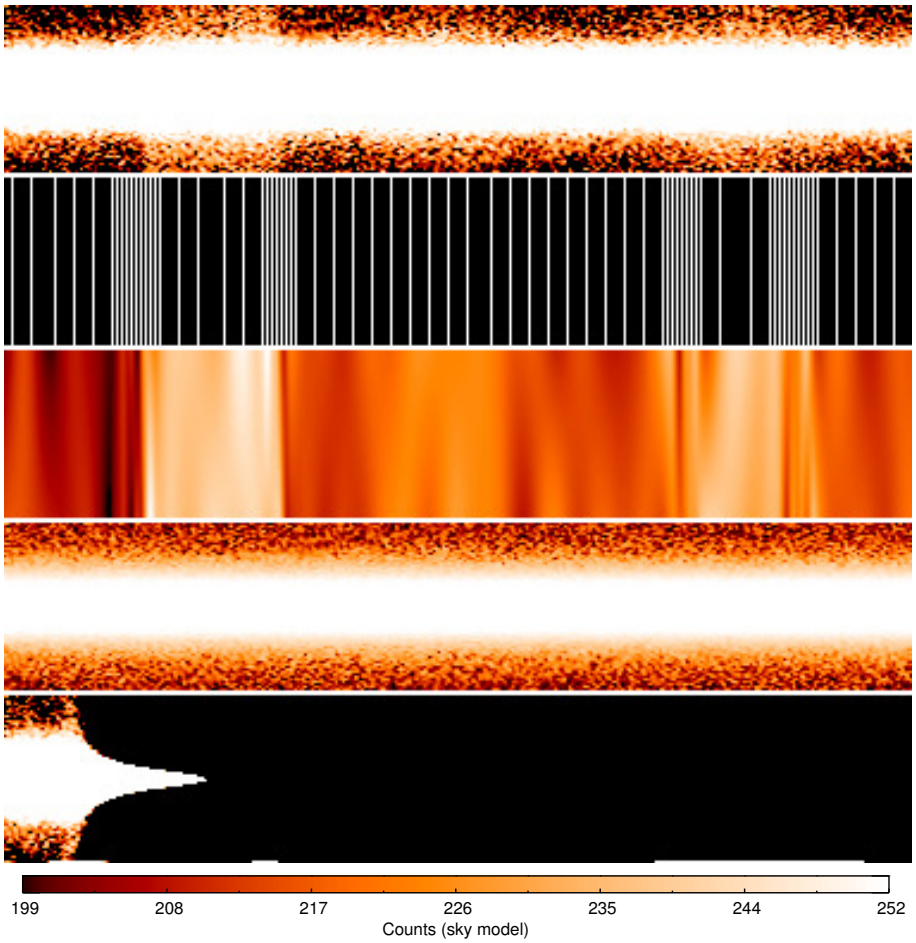

Figure 14: Sky subtraction sequence for GD71. The top panel shows a rectified spectrum of GD71 with an additional sky component. The break point distribution that forms the basis for the fits to the sky spectrum is shown in the second panel, while the corresponding sky model, based on two separate spline fits at either side of the stellar PSF and an additional interpolation along the cross-dispersed direction, is shown in the third panel. The final sky-subtracted spectrum of GD71 is presented in the fourth panel. For comparison, the fifth panel shows the corresponding result obtained with the X-SHOOTER pipeline, which failed to produce an acceptable solution for the shown wavelength range (7742 Å to 7770 Å) and other parts of the spectrum. The color scaling of the sky model is illustrated in the bar at the bottom.

The benefit of spline fits is their ability to model signals that show small, long-scale (sky continuum convolved with instrumental response) and large, short-scale gradients (line emission, atmospheric absorption windows) at the same time. This offers the ability to efficiently reduce the impact of noise, which is achieved by adjusting the break point density (i.e., denser sampling on strong gradients, sparser sampling on smoother gradients), with which the polynomial pieces are connected, so that the distances between the individual break points reflect the underlying gradient of the sky signal. For this, two step sizes are used: 1) if no features are detected the step width is set to 8 pixels, and 2) in regions with strong signal gradients (positive and negative) a step width of 2 pixels is applied, i.e., every other pixel is used as break point for the spline fit. As we want to adjust the fitting function to be variable on small scales only where the sky signal itself shows strong variations and, in turn, keep it smooth at all other wavelengths a careful discrimination between actual signal gradients and noise fluctuations has to be made (see Figure 14).

For this task, we first calculate a variance-weighted average of all pixels contained in the two sky windows along the cross-dispersed direction, resulting in an average sky spectrum (and its standard deviation) which is then further smoothed in spectral dispersion direction by a boxcar average with box size 5 to reduce bin-to-bin fluctuations. The resulting spectrum is convolved with a LAPLACE-like kernel of the form $\begin{pmatrix}1 & 0 & -2 & 0 & 1\end{pmatrix}$, yielding the second derivative L over a spectral correlation length of five pixels to further suppress pixel-to-pixel variations. The corresponding errors are propagated accordingly (yielding σ_L). Zero crossings of the Laplace-convolved spectrum depict large gradient changes if the neighboring values have a point-symmetric shape with respect to the zero crossing with a large absolute value. For the $i-th$ pixel of the sky spectrum, S, to be flagged as a position with a strong spectral gradient (e.g., transition from continuum to line or vice versa), the surrounding pixel values have to fulfill all three of the following criteria:

	positive gradient	negative gradient
1.	$\sum_{k=i-5}^{i-3} L_k > \kappa \cdot \sqrt{\sum_{k=i-5}^{i-3} \sigma_{L,k}^2}$	$\sum_{k=i-5}^{i-3} L_k < -\kappa \cdot \sqrt{\sum_{k=i-5}^{i-3} \sigma_{L,k}^2}$
2.	$\sum_{k=i+2}^{i+4} L_k < -\kappa \cdot \sqrt{\sum_{k=i+2}^{i+4} \sigma_{L,k}^2}$	$\sum_{k=i+2}^{i+4} L_k > \kappa \cdot \sqrt{\sum_{k=i+2}^{i+4} \sigma_{L,k}^2}$
3.	$\sum_{k=i-5}^{i-3} S_k < \sum_{k=i+2}^{i+4} S_k$	$\sum_{k=i-5}^{i-3} S_k > \sum_{k=i+2}^{i+4} S_k$

The left set of equations has to be fulfilled in case of a positive sky gradient, the right set has to hold if a negative gradient is to be flagged. By comparing averages over the intervals $[i-5, i-3]$ and $[i+2, i+4]$ we ensure that the impact of small-scale variations is degraded with respect to the true gradients inherent in the sky signal. We carefully adjusted the sensitivity parameter κ under the premise that even very faint lines or blended features are accurately flagged. As a side effect, the requirement to include very faint lines leads to

a significant flagging of noise spikes, thereby potentially lowering the spectral correlation length of the sky model at wavelengths without features and, hence, resulting in a slightly noisier fit. After detailed experimentation, we found $\kappa = 0.3$ to work well even for long exposed twilight data with many emission and absorption features in the red part of the VIS arm. If the S/N of the average sky spectrum drops below one, then we set $\kappa = 0.8$, which further minimizes the impact of noise, as no spectral features are expected in such a low S/N environment. In general, the above mentioned criteria have been carefully tested and optimized for many different observational setups and S/N scenarios and should therefore be widely applicable.

With all sky features flagged, seven break points with a stepping of two pixels are symmetrically distributed around each flagged position, while checking and correcting for possible overlaps within this distribution. Each interspace between the flagged positions is then filled up with break points with a stepping of eight pixels if the median number of counts within this space is > 30 and a stepping of 20 pixels if the median number of counts is < 30. Increasing the step size when only a few sky photons are detected enforces a smoother sky model and makes the approach more robust in low S/N scenarios. The threshold number has been empirically determined and performs well for all tested observations. Overall, this implementation yields a break point distribution whose spacing is adjusted to the spectral gradient of the sky signal (see Figure 14).

For the actual sky model, we take the weighted average for both sky windows (along the cross-dispersed direction) at every wavelength sampling point, as computed before, and then fit the obtained sky spectrum in the lower and upper sky window independently along the spectral direction. To further suppress noise artifacts, we additionally smooth the sky signal (before fitting) along the spectral direction with a boxcar median (21 pixels box size) inside those wavelength ranges where the break point stepping is 20 pixels. Since an accurate error propagation for spline fits can be cumbersome (Silverman 1985), we implemented a Monte Carlo approach, which simulates and fits each sky window 200 times with cubic splines based on the break point distribution, accounting for the noise level inside the sky windows. To decrease the impact of individual pixel values within the computed break point sample, we shift the global break point distribution by half the distance between each break point pair and repeat the Monte Carlo simulation. The final solution is the average (including its standard deviation) of the 400 fit realizations. Based on the obtained mean values and standard deviations the two models on either side of the stellar PSF are then linearly interpolated to all slit positions for each wavelength bin. This interpolation is again implemented as a Monte Carlo simulation, with 200 random realizations accounting for the $1\,\sigma$ errors of the spline fits, yielding a two-dimensional sky model with consistently estimated uncertainties that can be propagated into the total error budget.

Allowing for a gradient during the linear interpolation along the cross-dispersed direction is necessary for two independent reasons: 1) if the spectrum is obtained during twilight the sky can show intrinsic gradients, even along the relatively short slit length of $11''$ and 2) residuals from the inter-order scattered-light subtraction (see Section 3.2.2) might show up as an additional gradient component, which can then be removed by sub-

tracting a properly adjusted sky surface. To illustrate this sequence of steps, Figure 14 shows a part of the VIS spectrum for star GD71 before and after sky subtraction, together with the used break points and the obtained sky model.

To provide the user with additional quality control possibilities, the software outputs the break point mask, the sky model, and a sky subtraction residual image as separate *FITS* files so that any fitting parameter can be adjusted conveniently if desired.

3.4.8 *Sky Subtraction for GC Spectra*

For each GC, the sequence of observations contains at least one dedicated sky observation. All sky frames were taken with same instrumental setup as the respective GC frames, and thus can be directly subtracted, once both kinds of data have been flux calibrated and the individual orders merged into a final spectrum (see Section 3.4.10 for a detailed description of the flux calibration and the merging process). For GCs that have multiple sky frames available, we first compute the average sky spectrum and its respective error map. The subtraction is performed for all science frames in the same way, and the errors are propagated accordingly. It should be noted however, that this treatment implicitly assumes a constant sky count level throughout the sequence of frames. While this is certainly a valid approximation for the sky continuum flux, which is typically stable on a $\lesssim$ 2%-level under photometric conditions, individual emission lines that form in different parts of the atmopshere (especially OH lines) can vary significantly on a timescale of minutes (e.g., Patat 2003), and thus residuals at the respective line wavlengths have to be expected. This issue is often addressed by scaling the emission lines in the sky spectrum to the amplitudes of their counterparts in the science spectra, either purely numerically or with physically motivated correlations between certain families of lines (Noll et al. 2014).

Sky subtraction residuals are a non-critical issue for velocity dispersion measurements in the UVB / VIS spectral range, since the overall number of sky lines is low in this wavelength regime. We therefore undertake no further effort to improve the accuracy of the subtraction process. It should be noted, however, that a more sophisticated approach is required for detailed abundance measurements and if the NIR data is included in the analysis.

3.4.9 *Optimal Extraction of Point-like Objects*

Extracting a one-dimensional spectrum out of two-dimensional data is a complex but mandatory task for all point-like objects (Horne 1986; Cushing et al. 2004). Although the globular clusters in our data set are well resolved with X-SHOOTER , the sensitivity functions required for absolute flux measurements rely on accurate observations of point-like standard stars[8].

8 The presented extraction approach was designed to be applied to our spectrophotometric standard star observations. However, there is no limitation on the applicability to any other point-like object.

The goal of our optimal extraction technique is to balance the requirements of limiting the propagation of background noise on the one hand, and the extraction of the maximum amount of information on the stellar SED on the other hand. Hence, the cross-dispersed PSF needs to be properly modeled so that the threshold between signal and noise can be accurately estimated.

Our optimal extraction routine integrates the counts and their associated errors (from the error map) of each wavelength bin over an extraction aperture that maximizes its integrated S/N and determines the associated flux losses in the wings from the model PSF. Because of the principal lack of through-slit images, additional slit losses (occurring when the light rays pass through the slit) can only be estimated from the one-dimensional cross-dispersed signal that is imaged onto the detector.

This technique is, in principle, similar to the optimal extraction routine of Horne (1986) which is designed to iteratively find the best source profile fit along the spectral direction from data affected by noise and cosmic ray hits. Our approach is insofar different as we model the source profile along the cross-dispersed direction and propagate the full variance of the data *and* the uncertainty of the profile fit, while the Horne technique does not account for the r.m.s. of its profile fit in each iteration. With our prior knowledge of the full spatial light distribution along the slit for the entire wavelength range and its uncertainty propagated into the variance frame (including cosmic ray hits and CCD cosmetics, see Sects. 3.4.2 and 3.4.3), we can *directly* determine the optimal extraction aperture which maximizes the S/N ratio of the extracted spectrum. In the following, we explain this in more detail.

3.4.9.1 *Modeling the Cross-dispersed PSF*

In order to obtain crude, but robust estimates for the cross-dispersed PSF in each echelle order even for low S/N data, we spectrally average over 10 Å around the blaze wavelength of each order and normalize the peak of the count level to unity. A skewed Moffat profile (Moffat 1969) is fitted with a LEVENBERG-MARQUARDT least-squares method (IDL implementation by Markwardt 2009) to the resulting one-dimensional PSF. The Moffat profile is preferred over a Gaussian shape as the X-SHOOTER cross-dispersed PSF shows relatively pronounced wings, which cannot be reproduced with Gaussian. The exact parametrization is of the form

$$\mathrm{PSF} = \frac{a_1}{(u^2+1)^{a_4}}(1 + \mathcal{P}(a_5 u + a_6 u^2 + a_7 u^3)), \tag{20}$$

with $u = (y - a_2)\, a_3^{-1}$ and y being the slit coordinate. The asymmetry term, $\mathcal{P}(\dots)$, becomes necessary especially for good seeing conditions, when the optical distortions of the instrument become significant. Figure 15 shows such a scenario for one observation of the flux standard BD+174708, with a measured FHWM of $0.68''$ at a central wavelength of $\lambda_c = 7100$ Å, where both the symmetric and skewed best-fit models are overplotted. In general, we find significant symmetry deviations for seeing values corresponding to a FWHM $\lesssim 0.8''$. The penalty factor $\mathcal{P} \in [0, 1]$ weights the expansion term and is introduced

for low S/N data, because the additional asymmetry parameters might lead to unconstrained fitting parameters and divergent PSF models. In the first fitting run $\mathcal{P}$ is fixed at 1 and only orders with an averaged S/N > 100 are fitted and a best-fit PSF model is obtained.

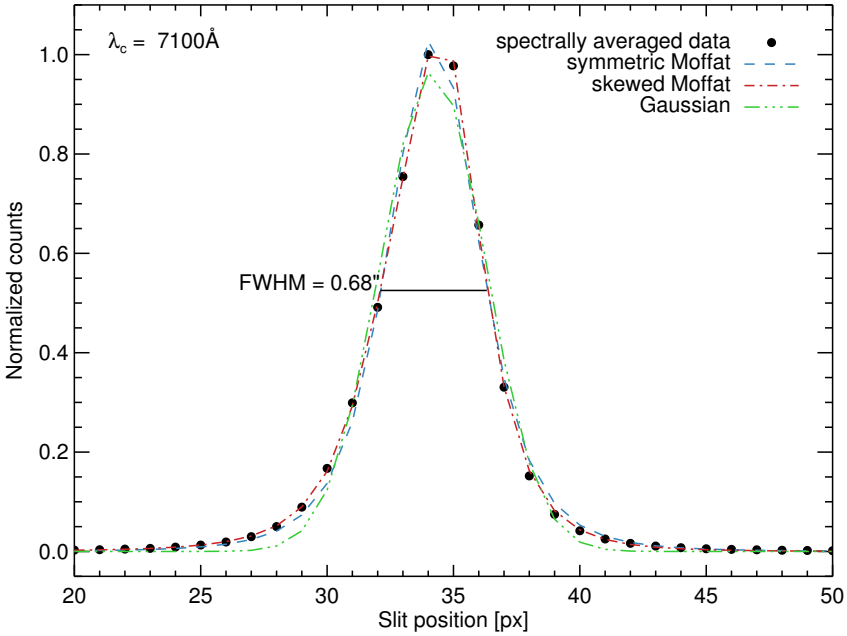

Figure 15: Cross-dispersed X-SHOOTER PSF and its best-fit models for the flux standard star BD+174708 in echelle order eight of the VIS arm ($\lambda_c = 7100$ Å). The fit to the spectrally averaged data (black circles) is considerably improved if a skewness term is added to the Moffat profile (dash-dotted red curve) as compared to its symmetric counterpart (dashed blue curve). The measured FWHM is 4.22 pix = 0.68″, whereas the DIMM seeing is indicated as 0.52″. The best-fit Gaussian is overplotted with a green dash-dotted line for comparison.

The resulting model parameters at the blaze wavelengths of each order with a S/N > 100 serve as initial guesses for additional fits at other wavelength ranges. The necessity for multiple PSF models within one echelle order arises from the wavelength-dependent seeing and the instrumental distortions that show commensurable variations on a 3% level within each order. In total, each order is sampled at ten equidistant spectral positions, using a boxcar average along the spectral direction to suppress noise. Averaging the data in such boxes with typical sizes of 100 − 400 pixels is complex, since, in case of a broken atmospheric dispersion correction (ADC) unit and/or poor wavelength calibration, the PSF centroid position is a function of wavelength, with typical shifts of 1−2 pixels from one order edge to the other[9]. A spectral average of such a drifting PSF potentially leads to an artificial widening of the PSF. Therefore, we first trace the centroid position along each

9 For proper wavelength calibrations, the centroid drift is typically stable at a 0.1 pixel level, which corresponds to the internal accuracy of the rectification process.

order by boxcar averaging over ten adjacent wavelength bins (i.e., with negligible centroid shifts within such a box) and fit the resulting spatial profile with a symmetric Moffat function of fixed width. This setup is chosen for reasons of execution speed, technical simplicity and robustness, and does not affect the accuracy of the derived information content. The symmetric profile (first term of Equation 20) is preferred for this task, as the parameters of its asymmetric counterpart have been shown to exhibit degeneracies and, hence, discontinuities can be observed if only a single parameter (centroid) is considered.

Once the centroid drifting function is known, the data are copied to a new array and by linear interpolation relocated to a new grid that is centered around the above fitted centroid trace. As this grid is now free from centroid shifts, the necessary boxcar averages can be computed without any further considerations, yielding a data set with ten PSFs at equidistant spectral positions per order. If the integrated signal-to-noise S_i is below 20, no fit to the data is performed at all and the model PSF is taken from the next sampling point where a model could be properly estimated. For sampling points with $S_i > 20$, $\mathcal{P}$ in Equation (20) is adjusted to the quality of the data by comparing it to a threshold signal-to-noise S_t above which the data are typically good enough to perform an unpenalized ($\mathcal{P} = 1$), i.e., asymmetric fit.

First, all parameters in Equation (20) are fitted simultaneously at fixed $\mathcal{P} = 1$, whereas in a second run, if $S_i < S_t$, the asymmetry parameters are kept fixed at the values of the first fit, the penalty factor is set to $\mathcal{P} = (S_i/S_t)^2$, and only the symmetric Moffat profile parameters are updated. With the choice of $S_t = 100$ we find that this method produces robust results for both low S/N data, where the actual shape of the PSF is not well constrained and the symmetric Moffat parameters is the only information that can be reliably extracted, as well as for high S/N data, where significant deviations from symmetry can be accurately modeled. In cases where all boxcar averages show $S/N < 20$, the PSF is modeled with the penalized approach at the sampling point with the highest S/N, and subsequently copied to all other wavelength positions.

The cross-dispersed range that is used for the PSF fit depends on the mode of observation. For *STARE* data, all pixels are included in the fit, whereas in *NOD* mode, the negative ghost PSFs at the slit edges need to be excluded, as they would otherwise affect the quality of the fit in the wings of the central PSF. Our truncation limits on the fitting region are based on two estimates: 1) the optimal extraction aperture (within which the integrated S/N is maximized) and 2) the zero-crossings of the averaged data (transition between central, positive PSF and negative PSFs at the slit edges). We take the mean value of both and round the result to the nearest integer. This choice performs reliably well, even in cases of bad seeing ($> 2''$) and small nodding offsets where the wings of the central PSF are substantially affected by their negative counterparts. As a further stability constraint for the convergence of the fit we impose additional boundary conditions and set the outermost four pixels at both slit ends to zero for *STARE* data, while this margin is increased to 15 pixels for *NOD* mode observations, for which the combined cross-dispersed dimension of the slit is significantly larger.

In order to increase the numerical accuracy when estimating the flux losses accompanying the optimal extraction, the obtained PSF models are computed on a grid that is

oversampled ten times with respect to the original cross-dispersed resolution and subsequently propagated to all other wavelengths by fitting a second-order one-dimensional polynomial along the spectral direction for all slit positions. The choice of the polynomial order is supported by the smooth FWHM vs. λ trend, as shown in the bottom panel of Figure 16, which typically shows a minimum around the blaze wavelength. The resulting wavelength-dependent PSF model contains all the necessary information on the PSF shape variability and is then back-transformed to the coordinate system of the original data (i.e., reintroducing the PSF's centroid drift) in order to be used for the object extraction.

3.4.9.2 *Target Signal Extraction and Flux Loss Determination*

The optimal extraction is performed by integrating each data bin along the slit dimension to its maximum S/N aperture, and correcting for the clipped counts by extracting the flux fraction of the truncated regions from the corresponding analytic model. The same technique is applied to the respective error frame, where the uncertainties of the clipped counts are estimated with a Poisson noise model, which we have found to be a conservative upper limit to the error of the profile fitting process as estimated by a dedicated Monte-Carlo simulation based on the covariance matrix of the model fit parameters. Figure 17 shows the computed extraction apertures and their corresponding flux losses for the star HD 38237 (spectral type A3) in echelle order 10 (UVB). While the extraction aperture function (top panel) shows discrete steps in integers of full pixels in addition to a fluctuation that is related to the combination of a non-centered centroid within a pixel and a symmetric extraction aperture around that centroid, the associated flux losses (bottom panel) pick up these discontinuities, but show an additional parabolic shape that is caused by the above mentioned wavelength dependence of the PSF. The amplitude of this systematic effect is three percent.

Estimating the flux losses due to the finite slit aperture requires an additional two-dimensional modeling of the PSF. As X-SHOOTER does not offer the possibility of acquiring through-slit images, we estimate the unaccessible second dimension from the cross-dispersed profile. For this, we use a LEVENBERG-MARQUARDT least-squares fit to construct a symmetric two-dimensional PSF that, if collapsed along the spectral dimension, fits the measured cross-dispersed data. This is superior to the Horne (1986) approach which does not provide a parametric solution of the cross-dispersed profile that could be used as a basis for the subsequent two-dimensional PSF model. Spherical symmetry is chosen as a prior, since we do not have any information about the potential occurrence of pre-slit skewness along the direction that becomes the spectral direction inside the spectrograph. The slit losses can then be estimated by setting an aperture resembling the long-slit around the PSF model. The aperture size is computed based on the information about the slit width from the file header. The slit loss estimation is performed for each order individually at the wavelengths shown in Col. 3 of Table 3 and the obtained values are then fitted globally with a third-order polynomial to obtain a smooth function for the entire spectral range of

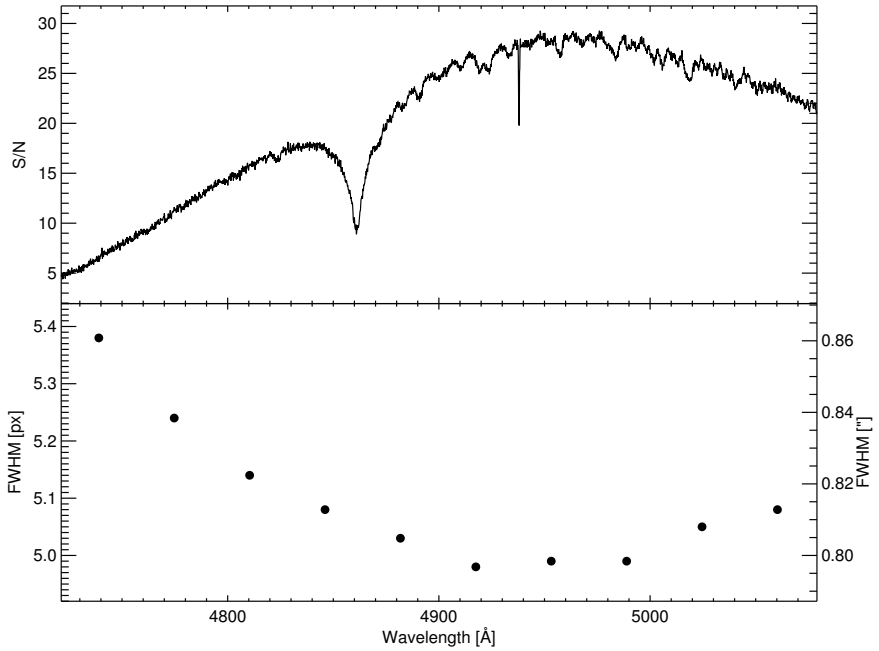

Figure 16: Optimally-extracted S/N spectrum (top panel) and measured FWHM (bottom panel) in echelle order 10 (UVB arm) for HD 38237. The downward S/N spike at 4938 Å arises from a cold spot on the CCD and demonstrates the quality of our optimal extraction procedure. The FWHM shows variations on a five percent level with a minimum close to the blaze wavelength.

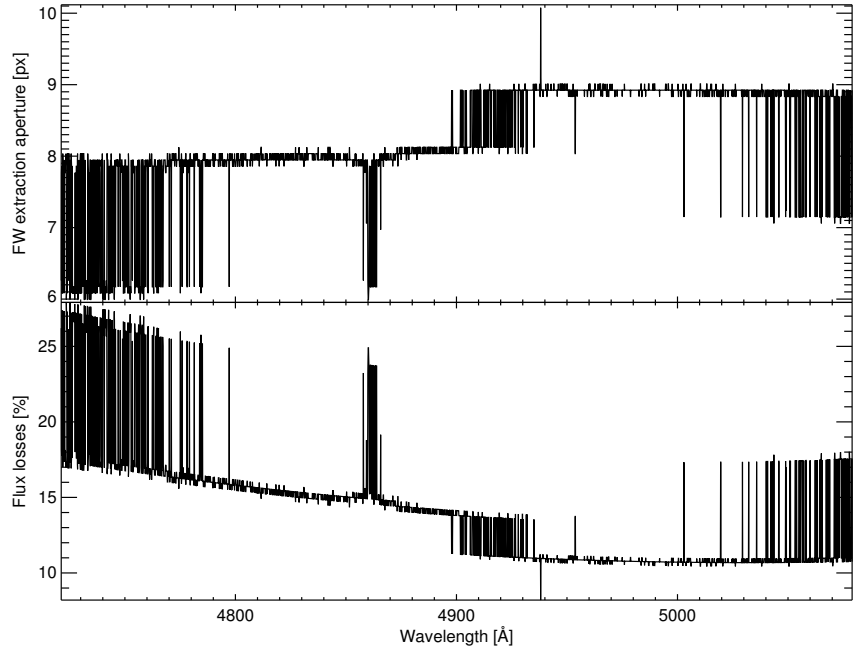

Figure 17: Full width optimal extraction apertures (top panel) and their associated flux losses (bottom panel) in echelle order 10 (UVB) for the star HD 38237. The extraction apertures resemble a discrete step function, as the S/N only changes at the transition between adjacent pixels. The corresponding flux losses follow this step function, but show an underlying smooth component that arises from the continuous PSF shape variation within the echelle order (see bottom panel of Figure 16).

the respective instrument arm. The fitting weights are based on the corresponding S/N values.

3.4.9.3 *Validation of Extraction Quality*

Optimally extracting the two-dimensional spectrum and correcting for both optimal extraction aperture flux losses and additional slit losses is mandatory if an accurate flux calibrated one-dimensional spectrum with a minimal noise component is required. To validate our approach and measure its accuracy, we reduced and compared a sequence of three observations of the same photometric standard star GD71 ($m_V = 13$) that were taken with similar exposure times (100 seconds) but different slit widths of 5.0″, 1.0″, and 0.5″. With a typical seeing of 1.0″ in all three measurements (UVB), we defined the 5.0″ slit size observation to be the reference case with negligible slit losses, and normalized the counts of the other two observations relative to this reference spectrum. Figure 18 shows the resulting flux ratios for both cases, where each observation has been optimally extracted (solid lines) and the individual echelle orders merged into one spectrum (for details on the merging process, see Section 3.4.10). For comparison, the conventional approach of collapsing the entire slit is overplotted as well (dashed lines). For the 1.0″ slit width (black dashed line), only about 65% of the overall flux at 4000 Å reaches the detector, whereas this number increases to approximately 72% at the red limit of the UVB arm (5850 Å). This trend correlates with the wavelength-dependent seeing, which is 1.05″ at the blue end and 0.75″ at the red end, according to the on-detector FWHM. When correcting for slit losses, the ratio reaches 98% between 3700 Å and 4200 Å, and slightly drops to 97% at the blue end and to 96% at the red end (black solid line). We believe that this residual curvature of the corrected flux may be caused by the ADC unit that almost perfectly corrects the PSF centroid position for wavelengths close to the zero-deviation wavelength (4050 Å for the UVB arm, see Vernet et al. 2011), but shows minor residuals for all other wavelengths. This scenario is supported by the orientation of the slit tilt angle, which was set to ∼25° relative to the parallactic angle for the presented observation, implying that any ADC imperfections might potentially introduce flux losses at the slit entrance. In addition to the smooth, global deviations from 100%, we find small systematic variations of $\lesssim 2-3\%$ between the blue end (typical $S/N \lesssim 10$) and the center ($S/N \gtrsim 20$) for some of the orders with wavelengths > 3500 Å, which imposes a S/N dependent limit on the absolute flux calibration as discussed in Section 3.4.10.

Decreasing the slit size to 0.5″ leads to a similar scenario; however, only ∼40% of the flux is captured by the detector (red dashed line in Figure 18). Applying the slit corrections lifts the ratio to 0.94 at the zero-deviation wavelength, with the same drop-offs at both sides as in the 1.0″ slit-width case (red solid line). For both the 0.5″ and 1.0″ slit widths, a slightly off-centered PSF within the slit caused by the limits of the VLT's pointing accuracy could be responsible for the observed systematic underestimation. However, this is purely speculative and cannot be examined in greater detail with the current data at hand.

The discontinuous peaks with amplitudes of $5-10\%$ bluewards of 3500 Å have been investigated carefully, but so far no satisfying explanation can be given. The spectral po-

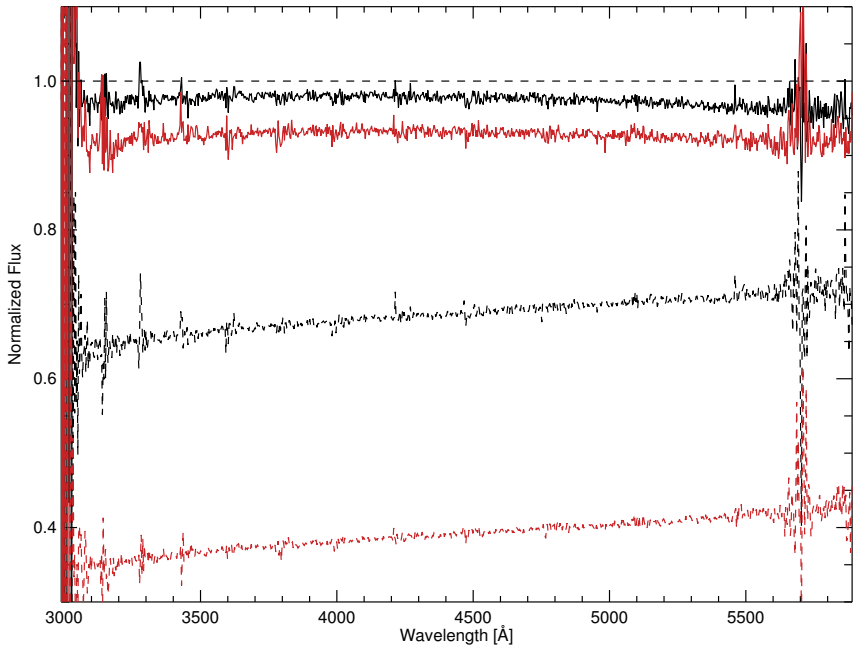

Figure 18: Normalized fluxes of GD71 in the UVB arm obtained with two different slit widths and two different extraction methods. The solid black (red) curve shows the optimally extracted and flux loss corrected data of the 1.0″ (0.5″) slit exposure, whereas the corresponding dashed curves show the conventional approach of collapsing the entire slit. All exposures have been normalized to the detected counts of a 5.0″ slit exposure, for which no significant flux losses have been measured. The data shown here are the merged result of all UVB orders. We note that the curves have been smoothed so that systematic trends can emerge.

sitions correspond to wavelengths right next to an order overlap, for which the blue part of the subsequent echelle order constitutes the only component of the merged spectrum. After extensive testing, we tend to rule out any residuals from additive effects, i.e., inter-order background subtraction or sky subtraction. A possible cause, however, could be related to the way we estimate the optimal extraction aperture, i.e., the cross-dispersed range over which the PSF is integrated to yield the counts with which the analytical model is rescaled (see Section 3.4.9.2). Utilizing an aperture within which the integrated S/N is maximized should represent a valid approach in theory, and so we speculate that our practical implementation might be too sensitive to noise in low S/N senarios. We will investigate this in more detail in the near future and hope to be able to resolve this issue. For the work presented here, this effect has no significance, since our standard star observation (performed with a 5″ slit) shows a S/N much higher than the regime in which above mentioned issue occurs.

It is interesting to note that the PSF shape at 5700 Å considerably opens up and returns back to normal size within a short spectral range ($\lesssim$ 100 Å). Since this wavelength range coincides with the spectral position of the transparency dip of the UVB/VIS dichroic element (see Section 3.4.10 for further details), we suspect that the PSF change happens before the slit (and outside the actual UVB/VIS spectrographs). A dedicated high S/N calibration sequence with various slit sizes in different observational scenarios (slit tilt angle, airmass, seeing) would be required to better quantify the instrumental PSF and its dependence on environmental parameters.

The wavelength-dependent increase in S/N of our optimal extraction method is shown in Figure 19. In the 1.0″ slit-width scenario, the median improvement is 1.51 (arithmetic mean 1.70), although it can be significantly higher in the blue part of the spectrum and at the order edges, where the overall instrumental response drops. For the 0.5″ slit, the median increase is 1.75 (arithmetic mean 1.93).

We note that the structure of the optimal extraction technique presented here can also be used to extract resolved or marginally resolved objects. In these cases, the Moffat light profile then needs to be replaced with a robust parametrization of the object's cross-dispersed light profile.

3.4.10 *Absolute Flux Calibration and Order Merging*

To flux-calibrate our UVB and VIS arm X-SHOOTER data, we compute the sensitivity functions based on optimally extracted spectrophotometric standard star spectra for each order individually. For this, we follow the scheme used by the *IRAF* tasks *standard*, *sensfunc*, and *calibrate*.

In this context it should be pointed out that the coverage of flux standard stars in our data set is not optimal. During the first visitor-mode run (four nights) no standard stars have been obtained. In the second visitor-mode run, four observations of BD+174708 and two observations of GD71V13.06 have been carried out. Both stars are HST standard stars and well characterized model spectra are available for either one (Hamuy et al. 1994; Vernet et al. 2010). Nevertheless, the usage of BD+174708 is strongly discouraged, as it

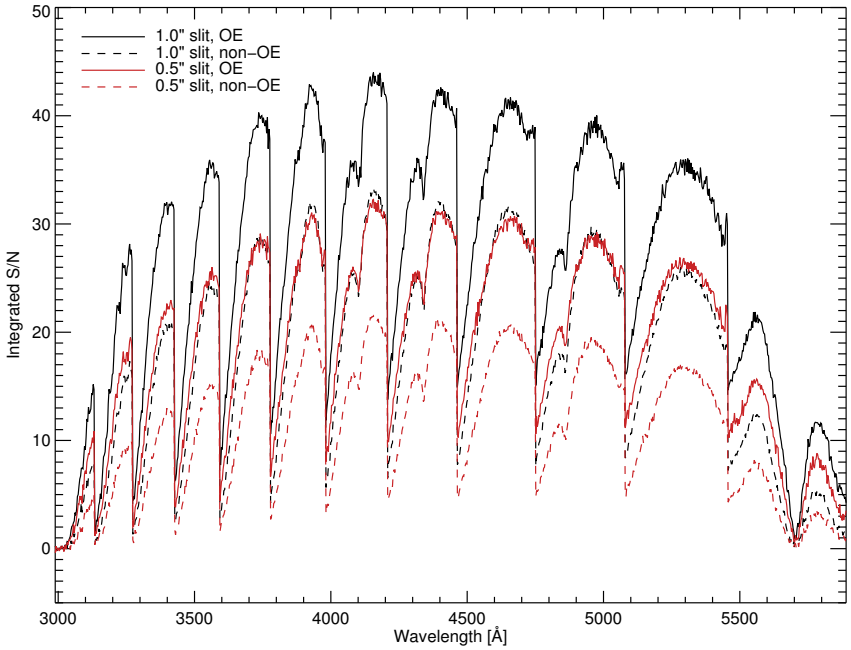

Figure 19: S/N curves of GD71 in the UVB arm obtained with two different slit widths and two different extraction methods (100 seconds exposure time). The solid black (red) curve shows the S/N of the optimally extracted 1.0″ (0.5″) slit-width data and the corresponding dashed curves show the conventional approach of collapsing the entire slit. We note that the curves have been smoothed so that systematic trends can emerge.

was discovered to be a spectroscopic binary (Bohlin & Landolt 2015) on the one hand, and it has a continuum entirely obscured due to line blanketing for $\lambda \lesssim 3,500$ Å on the other hand.

Moreover, the second observation of GD71V13.06 suffered from exceptionally bad seeing conditions ($\gtrsim 2.5$), and thus we decided to use the observation of GD71V13.06 on November 7th, 2009 as reference for all our data[10].

3.4.10.1 *Method*

In a first step, bandpasses that homogeneously sample the continuum of the respective standard star SED are defined. We carefully mask both stellar and telluric spectral features and use a generic bandpass width of 5 Å with a sampling step size of 5 Å if the continuum is well defined. As some echelle orders (e.g., VIS 14) are almost completely affected by atmospheric absorption, this task proved to be laborious and forced us to use significantly smaller and irregularly distributed bandpasses for certain wavelength ranges. This task was performed for both our standard stars (GD71V13.06, BD+174708) in both instrument arms (UVB, VIS) and the resulting bandpass samples are generally valid for these stars and can be used for any observation of that kind. Our bandpass selection for GD71V13.06 is indicated as a green baseline in the middle panel of Figure 20.

With the bandpasses defined, the standard star spectrum is integrated over all bandpasses and the resulting counts are stored in tabulated form together with the information on the bandpass location (central wavelength), bandpass width, and corresponding flux (at central wavelength) of a given model SED. For the latter, we use the pipeline-packaged models that are based on observations by Hamuy et al. (1994) and Vernet et al. (2010). They cover the entire wavelength from 3,000 Å to 25,000 Å at varying spectral resolutions; however, they need to be interpolated to a finer sampling to match the dispersion of our data. These tables are used as input for *IRAF sensfunc*, where separate sensitivity functions for each echelle order are computed including corrections for the effective airmass. As response fitting functions, we generally use cubic splines or Chebyshev polynomials, depending on the bandpass sampling of the respective order. The fit is manually cleaned from any outliers caused by bad pixel or CRH residuals and the function type and polynomial order are adjusted interactively if required. This process is performed iteratively with visual verification of convergence, as orders only weakly constrained by the bandpass selection react very sensitively to a change in the fitting parameters. We note that first correcting the science frame by the blaze function as derived from the flat lamp frame did not improve the quality of the final sensitivity function fit solution. By contrast, such a procedure would introduce additional complications, such as line emission in the flat lamp spectrum and a variation of the lamp's SED shape due to temporal voltage/temperature changes (see Section 3.4.4).

The subsequent merging process of the flux calibrated orders is performed with an error weighted average in the order-overlap regions and the errors are propagated accordingly.

10 During the service mode-run on February 9th, 2010 an additional observation of GD71V13.06 was performed, however for reasons of consistency we prefer to use the observation that is closer in time to the bulk of the GC spectra.

The same merging technique is also applied when the flux-calibrated results of the two instrument arms are to be merged into one global spectrum.

3.4.10.2 *Sensitivity Function Evaluation*

Table 3 shows an overview of relevant calibration parameters for our reference GD71V13.06 observation. The top panel of Figure 20 shows the resulting sensitivity functions in both arms. The functions are generally of parabolic shape, except for order 12 of the UVB arm. Instead of showing a typical response maximum at the blaze wavelength, this particular order features a pronounced dip close to the central wavelength of the echelle order. This effect is caused by a non-monotonous drop of the UVB/VIS dichroic transparency with local side maxima around 5,700 Å (compare the blue and yellow curves in Figure 3) and goes along with a PSF broadening in the cross-dispersed direction (see Section 3.4.9). When comparing observations with different time stamps, the dip positions and, hence, the associated sensitivity functions, turn out to be temporally variable, as the local maxima of the dichroic's transparency function are shifted along the dispersion axis (see inset in the top panel of Figure 20). While the instrumental throughput remained roughly constant within a time baseline of 24 hours in the shown case (solid green and dashed black curve), it varied by 20–30% within seven days (dot-dashed red curve). For other cases, we find a similarly high variation amplitude even within a single night. The true nature of this effect has yet to be unveiled and its impact quantified. Nevertheless, checking the ESO Ambient Condition Database[11] we speculate that ambient humidity might be responsible for the observed instrument behavior. On the respective nights, the humidity changed by a factor of three between the observation on February 17th, 2010 and the ones on February 10th/11th, 2010 while the temperature remained constant within 2°C.

3.4.10.3 *Absolute Flux Calibration Accuracy*

The middle panel of Figure 20 shows the flux-calibrated output of our spectrophotometric reference observation (solid black line). The S/N curve of the underlying data is above 50 per spectral bin, except for wavelengths $\lesssim 3200$ Å. To highlight any deviations from the used SED model (overplotted in red), we show the ratio spectrum between data and model in the bottom panel of Figure 20 (the propagated errors for this ratio are indicated by the blue band). For continuum regions, the systematic deviations between data and model are typically $\lesssim 1\%$, with very localized increases to $\lesssim 4\%$ at wavelengths where stellar features are present. Since atmospheric absorption bands occurring at wavelengths $\lesssim 3500$ Å and $\gtrsim 6900$ Å have not been corrected for, the sensitivity functions are only weakly constrained in the affected wavelength regions. From our experience of calibrating a significant number of different spectrophotometric standard star observations with different fitting functions and polynomial orders, we estimate that a conservative upper limit for the uncertainty in the sensitivity functions in extended atmospheric windows is 10%. At wavelengths $\lesssim 3050$ Å the obtained S/N in a typical standard star observation is too low to derive

11 http://archive.eso.org/asm/ambient-server

Order	Spectral order	Min. wavelength [Å]	Slit loss model wavelength [Å]	Max. wavelength [Å]	Avg. dispersion [Å/px]	Fitting function / polynomial order	No. of band-passes	RMS [$\times 10^{-2}$]	Remarks
				UVB					
1	24	2989	3125	3134	0.097	Spline3/4	8	0.44	atmospheric absorption, low S/N
2	23	3115	3260	3273	0.103	Spline3/4	10	0.50	atmospheric absorption
3	22	3253	3400	3425	0.109	Spline3/4	10	0.03	atmospheric absorption
4	21	3403	3550	3592	0.115	Chebyshev/8	9	0.02	
5	20	3568	3680	3777	0.122	Chebyshev/8	21	0.17	
6	19	3750	3920	3981	0.129	Spline3/4	9	0.07	H_ϵ, H_ζ, H_η
7	18	3951	4150	4208	0.137	Chebyshev/6	17	0.10	H_δ
8	17	4175	4370	4463	0.146	Chebyshev/8	28	0.18	H_γ
9	16	4427	4666	4751	0.155	Chebyshev/10	51	0.21	
10	15	4721	4970	5079	0.166	Chebyshev/12	44	0.14	H_β
11	14	5058	5300	5456	0.178	Chebyshev/15	80	0.19	
12_1	13	5446	5560	5693	0.196	Spline3/15	49	0.20	bluewards of dichroic dip
12_2	13	5693	5770	5893	0.184	Spline3/15	40	0.25	redwards of dichroic dip
				VIS					
1	30	5337	5480	5543	0.103	Spline3/8	36	1.85	dichroic variability, low S/N
2	29	5516	5640	5737	0.106	Spline3/8	40	0.15	dichroic variability
3	28	5709	5840	5945	0.111	Spline3/8	46	0.20	dichroic variability
4	27	5915	6050	6169	0.115	Spline3/8	46	0.15	
5	26	6136	6250	6411	0.120	Spline3/9	40	0.16	
6	25	6375	6525	6672	0.126	Spline3/6	32	0.12	H_α
7	24	6633	6800	6955	0.132	Chebyshev/9	48	0.22	atmospheric absorption window
8	23	6913	7100	7263	0.138	Chebyshev/9	53	0.30	atmospheric absorption window
9	22	7218	7420	7600	0.145	Spline3/6	53	0.18	atmospheric absorption window
10	21	7550	7770	7970	0.152	Spline3/8	60	0.28	atmospheric absorption window
11	20	7915	8150	8378	0.160	Spline3/6	50	0.27	atmospheric absorption window
12	19	8317	8600	8830	0.169	Spline3/6	61	0.26	
13	18	8762	9050	9329	0.179	Chebyshev/6	47	0.51	atmospheric absorption window
14	17	9258	9550	9810	0.193	Chebyshev/6	24	0.92	atmospheric absorption
15	16	9790	9980	10200	0.215	Spline3/10	53	1.22	low S/N

Table 3: Calibration parameters for the UVB and VIS arm of X-SHOOTER . The indices of the spectral orders as used in this work are given in Col. 1, whereas the corresponding true spectral numbers of the dispersive element are given in Col. 2. Column 3 shows the minimum wavelength of each order, Col. 4 the wavelength at which the slit losses are estimated (close to the blaze wavelengths) and Col. 5 shows the maximum wavelength per order. The average dispersion is given in Col. 6, although the dispersion is a function of both slit and wavelength coordinate in each order. Column 7 lists the fitting functions and polynomial orders used in the sensitivity function computation. The number of underlying integration bandpasses is presented in Col. 8. The resulting RMS are shown in Col. 9; however, we note that values < 0.1 and bandpass numbers $\lesssim 10$ are to be handled with care, as the fit is typically only weakly constrained in these cases. Finally, Col. 10 gives an overview of order-dependent features that might compromise the flux calibration accuracy.

a reliable sensitivity function and the flux calibration is limited by the low number of detected photons.

According to Bohlin (2000), the systematic model 1σ uncertainties for GD71 range from 4% at 1300 Å to 2% between 5000 Å and 10000 Å for the stellar continuum and 5% for the Balmer lines with respect to the adjacent continuum. Thus, the absolute flux calibration accuracy of well-exposed wide-slit X-SHOOTER observations will be mostly limited by model SED uncertainties as well as the photometric stability of the atmosphere. For narrow-slit spectra the uncertainties in the slit loss estimation (see Section 3.4.9) will dominate the systematic error budget with a conservative upper limit of 5% for 1.0″ slit widths and 10% for 0.5″. Moreover, spectral ranges of low S/N ($\lesssim$10, mostly the blue parts of each order) might show a further degradation of the flux calibration accuracy by $2-3$%, as illustrated in Figure 18. For all slit width setups we estimate that the absolute flux calibration is better than ~10% for the covered wavelength ranges of the UVB and VIS arm.

For demonstration purposes, we applied our reduction script to a sequence of stars with various spectral types. We chose objects observed as part of the ESO observing program 084.B-0869(A) (PI: S. Trager)[12], as they were taken with an instrumental setup that is similar to that of our data set in the UVB arm. As a consequence our reduction script can be executed automatically without any additional modifications. The flux-calibrated output for three different stars (spectral types: A3, F8, K3), all observed on November 26th, 2009 is presented in Figure 21. Each spectrum is a composition of two nodded frames, whose superposition has been optimally extracted and flux-calibrated against an observation of the spectrophotometric standard star GD 71 on the same night. We additionally corrected for the effective airmass of each observation. The S/N values are typically ~ 100 per spectral bin, except for wavelengths $\lesssim$ 3500 Å and at the dip of the dichroic response at ~ 5700 Å. Because of the effects explained above, the latter region in particular has to be treated with great care when quantitative resultes are required.

3.4.11 *Fine-tuning of the Wavelength Calibration*

Since X-SHOOTER is mounted at the Cassegrain focus of VLT, it suffers from flexure under its own weight of ~2.5 metric tons (D'Odorico et al. 2006). This effect is most pronounced for telescope pointings at large airmass and needs to be properly modeled and calibrated out if the full instrument potential is to be exploited.

3.4.11.1 *Wavelength Scale Update*

Regular multi-pinhole ThAr arc exposures, which form the basis of the wavelength calibration, are only taken ~1–2 times a week during daytime at zenith position, which means that extra frames have to be acquired to update the existing wavelength solution to the ambient parameters of the respective science exposures. For this reason, additional active flexure compensation (AFC) frames (short ThAr arc lamp exposures) are contemporaneously taken with each science observation, allowing for a line-shift measurement at the

12 The data were taken from the ESO data archive, accessible at http://archive.eso.org

current telescope orientation with respect to the zenith position. In this frame, however, there is only one valid reference line with which the shift that can be reliably modeled, as all other wavelength positions are subject to ADC corrections. This offset is then assumed to be a global shift of the wavelength solution of the respective arm. Although the instrument's spectral format is reported to be stable within ~1.5 pixels (Moehler et al. 2010; Vernet et al. 2011) during a typical night, we implemented a quality control check to validate the global accuracy of the wavelength calibration for each science exposure.

For this, we fit a set of 15 non-blended telluric lines in the VIS arm with a Gaussian profile and compare the obtained centroid wavelengths to their respective reference (air) wavelengths[13]. This procedure is performed individually for each cross-dispersed position within the slit, yielding for each telluric line both a median shift and a standard deviation (computed over all slit positions). Figure 22 shows an exemplary case for the O I "auroral green line" transition at 5577.339 Å (McLennan 1925a,b) for one of our observations of the globular cluster NGC 7099, performed with the 0.5″ wide slit. The difference between the median centroid wavelength of all fitted slit positions and the reference wavelength is −0.037 Å and thus more than three times larger than the intrinsic uncertainty of the fitting process (0.011 Å).

A global picture for the whole spectral range is presented in Figure 23, where the residuals for the entire set of 15 lines are plotted as a function of their respective wavelengths. Analyzing the weighted mean residual of all fitted wavelengths, we find it to be $\langle \Delta\lambda \rangle = -0.034$ Å, with an average uncertainty of $\langle \sigma \rangle = 0.022$ Å. This uncertainty can be interpreted as a conservative instrumental limit to the wavelength calibration, as — on average — individual lines cannot be modeled more accurately in this setup. The best linear fit is overplotted in red and shows a minor slope of $-3.84 \cdot 10^{-6}$. Despite its small amplitude, we want to emphasize that the bias on the residuals is observed in an optimal scenario in which the AFC measurements were conducted right before the corresonding science observation. As we have also encountered cases for which $|\langle \Delta\lambda \rangle| \gtrsim 0.05$ Å, we suspect that there may be undiscovered systematic effects that are not taken into account by the X-SHOOTER physical model and thus prevent a more accurate absolute wavelength calibration.

3.4.11.2 *Correcting for residual Flexure Compensation Drift*

To work around the issue of residual flexure compensation drift, we use the information provided by the axis intercept $\Delta\lambda_0$ and slope α of the fit to the residuals to de-bias the global wavelength solution. Since we want to avoid additional interpolation processes, we only change the wavelength grid by updating the appropriate header keywords. This is possible because of the linearity of the correction factor and the equidistance of the underlying wavelength grid. The corrected wavelength solution λ_c becomes

$$\lambda_c = (1 - \alpha)\lambda_u - \Delta\lambda_0, \tag{21}$$

13 as given by http://www.pa.uky.edu/~peter/atomic/

where λ_u are the nodes of the uncorrected wavelength grid. The new grid then has a new zero point *CRVAL1* and stepping *CDELT1*, and remains equidistant.

A demonstration of this correction procedure is illustrated in Figure 24, which shows mean wavelength residual (of all 15 sky lines) vs. airmass for the OB sequence of NGC 7099, consisting of observations with various telescope positions. One additional sky observation was performed and the AFC frame was taken only once at the beginning of the sequence (dashed red line; see also Table 1 and Figure 5 the sequence of observations). Each frame was integrated for ten minutes with an overhead time of approximately two minutes in between. The residuals of the uncorrected wavelength solutions (black) show a clear drift with airmass in addition to the above mentioned bias of the wavelength solution of the initial science observation (the first data point in Figure 24 corresponds to the mean value inferred from Figure 23). Correcting each science frame with its own correction factor based on Equation 21 reliably removes the observed wavelength shift and corrects the wavelength solution (blue), resulting in spectra whose wavelength calibration is only limited by X-SHOOTER's internal uncertainty of ~0.02 Å as described above.

Regrettably, a high-quality drift-correction is applicable exclusively to VIS arm data because this wavelength range contains a sufficiently high number of sky lines. By contrast, the sky line sampling in the UVB range is very poor and sky lines with sufficiently high S/N can only be obtained with exposures significantly longer than the ones utilized in our GC data set. The only prominent line that is visible in all our spectra is the auroral green line (~ 5577 Å). We therefore measure any potential wavelength drift in the UVB data against this line and assume the inferred value to be constant for the entire UVB spectral range. While this approach certainly approximates the required correction, the true shape of the drift function in the UVB arm remains to be studied in detail. For this, we propose to analyze a set of long exposed sky flats at various airmasses. In this case the wavelength-dependency can be constrained by using a larger set of lines in the analysis and different zenith angles can be used to search for correlations with the telescope pointing.

The NIR arm, however, should contain a sufficient number of usable sky lines so that the procedure described above should be applicable without great difficulties. The implementation and evaluation is intended for a future project.

It is important to note that a careful correction for residual wavelength drift is a crucial requirement for our GC data. We shall see in Section 5.7 that for some clusters the systemic radial velocities at opposite sides of the cluster center differ by $\sim 5\,\mathrm{km\,s^{-1}}$, which can be interpreted as a sign of ordered rotation within the GC. This velocity difference is on the same order as the observed wavelength drift (according to Figure 24 the drift from the first to the last scan is ~ 0.05 Å, which corresponds to a velocity difference of $\sim 2.5\,\mathrm{km\,s^{-1}}$ at a rest wavelength of 6000 Å), and so the residual flexure has to be carefully calibrated out before meaningful conclusions can be drawn. We therefore measure the residual flexure drift for our all GCs spectra ans apply the presented corrections by default.

The resulting wavelength accuracy of 0.02 Å, in combination with an absolute flux calibration uncertainty $\lesssim$ 10%, is expected to be sufficient for accurate kinematical measurements based on our GC spectra.

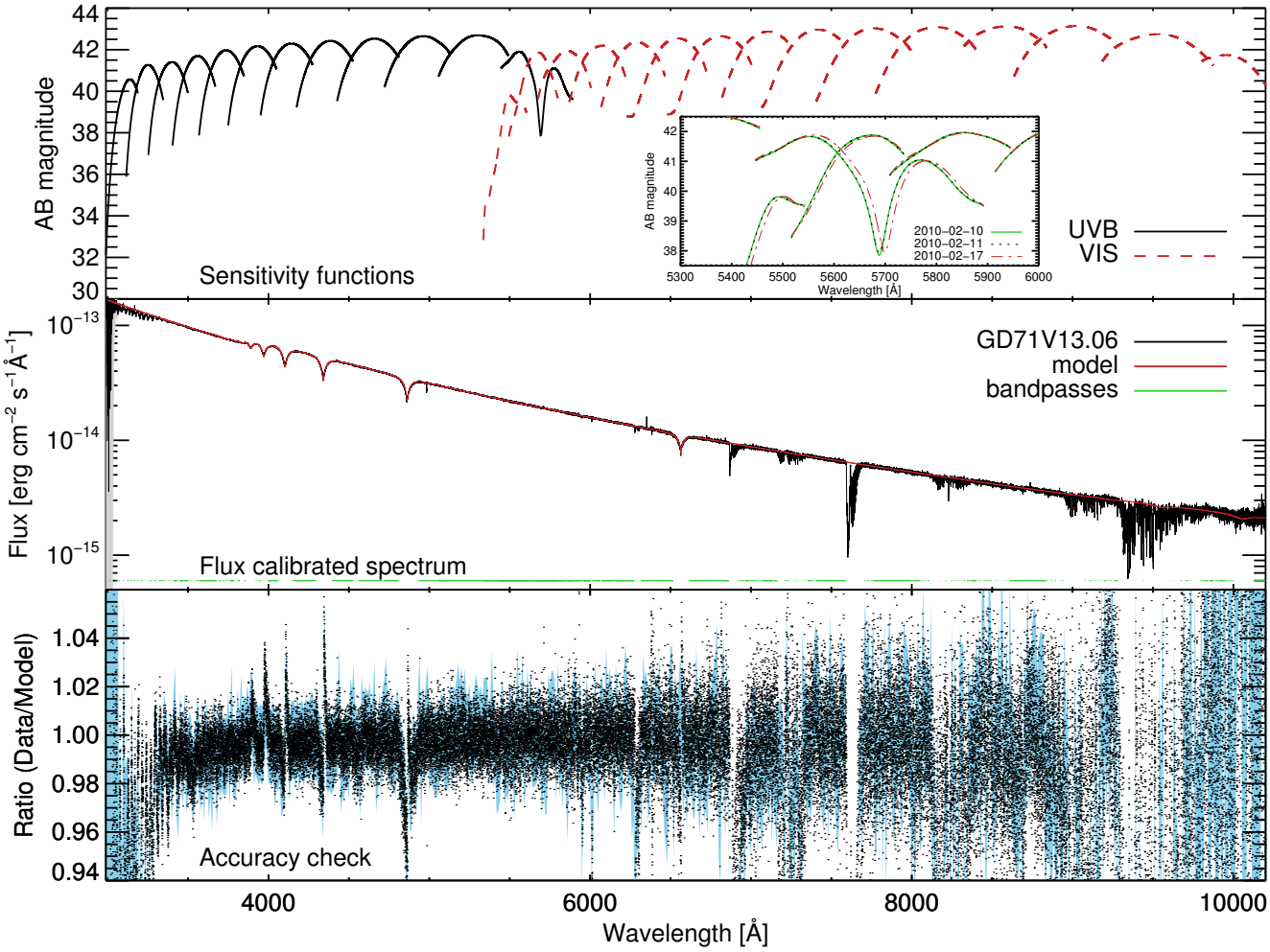

Figure 20: UVB and VIS sensitivity functions and the resulting flux-calibrated spectrum for GD71. The top panel shows the order-by-order sensitivity functions in AB magnitudes for both the UVB (solid black line) and VIS (dashed red line) arm, based on the observation on November 7th, 2009. The temporal variation of the instrumental throughput at the transition regime of the UVB/VIS dichroic is illustrated in the inset, where we show three different sets of sensitivity functions, obtained on three different nights in the relevant wavelength range. There, the solid green curve corresponds to the night in which NGC2808 has been observed in service-mode (February 10th, 2010), the dotted black line indicates the sensitivity function obtained 24 hours later, and the dot-dashed red curve depicts the sensitivity functions one week later. The middle panel shows the final flux-calibrated output for GD71 (solid black line), where all echelle orders of both instrumental arms have been merged into one spectrum. The underlying model SED is overplotted in red. The propagated observational 1σ uncertainties are indicated with a smoothed, symmetrical gray band around the mean values and are hardly visible for most of the spectral range. The bandpass selection used as input for the count integration is indicated in green at the bottom of the panel. Atmospheric absorption bands have not been corrected for. The ratio between model and data is shown in the bottom panel (black dots) and the propagated errors (assuming a 1.5% error for the model) are indicated with a smoothed, blue band. Systematic deviations are typically $\lesssim 1\%$, except for wavelength ranges covered by stellar features, where they can increase to $\lesssim 4\%$. We note that the flux-calibrated spectrum of GD71 is plotted with a very high resolution and so the electronic version of this plot is highly zoomable.

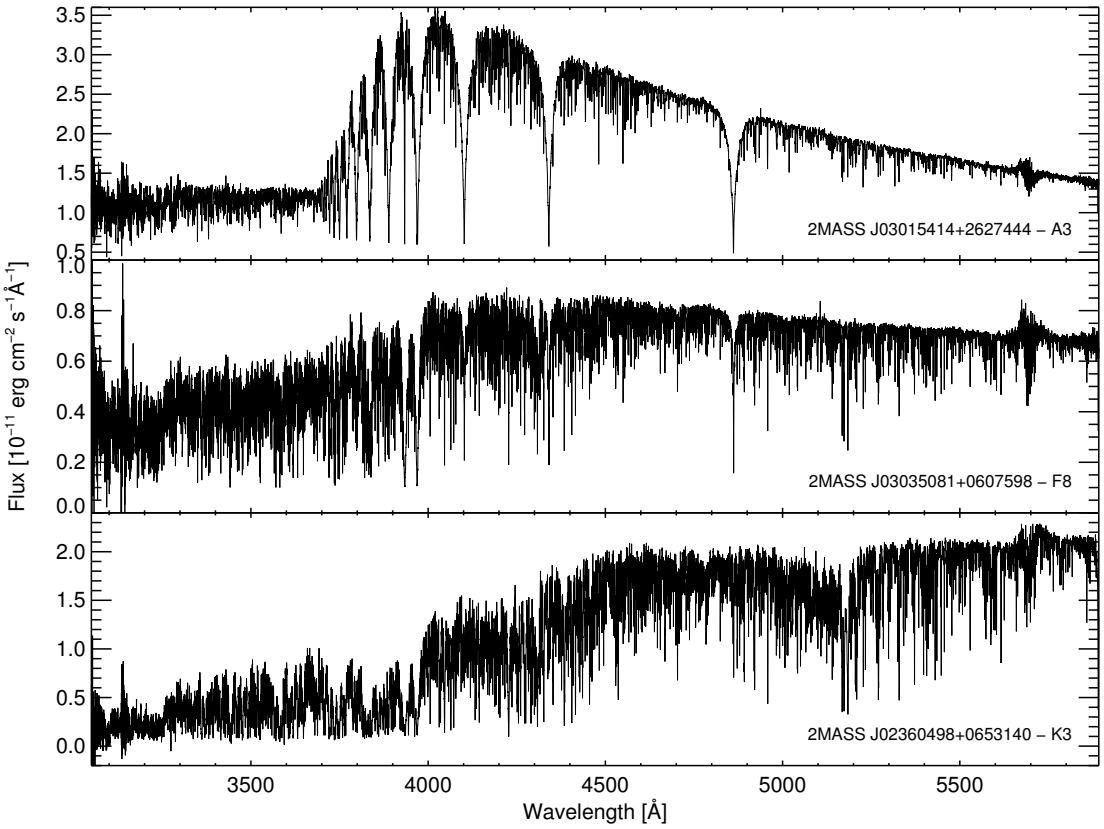

Figure 21: Stellar spectra from ESO observing program 084.B-0869(A). All stars were observed on November 26th, 2009 and automatically extracted with the prescriptions presented in this work. Each target was observed in *NOD* mode with a slit width of 0.5″. The underlying sensitivity functions were derived with the spectrophotometric standard star GD 71. The three panels cover the spectral type range from a hot star with spectral type A3 (*top panel*), to an intermediate-type star F8 (*middle panel*), to a cool giant star with a spectral type K3 (*bottom panel*).

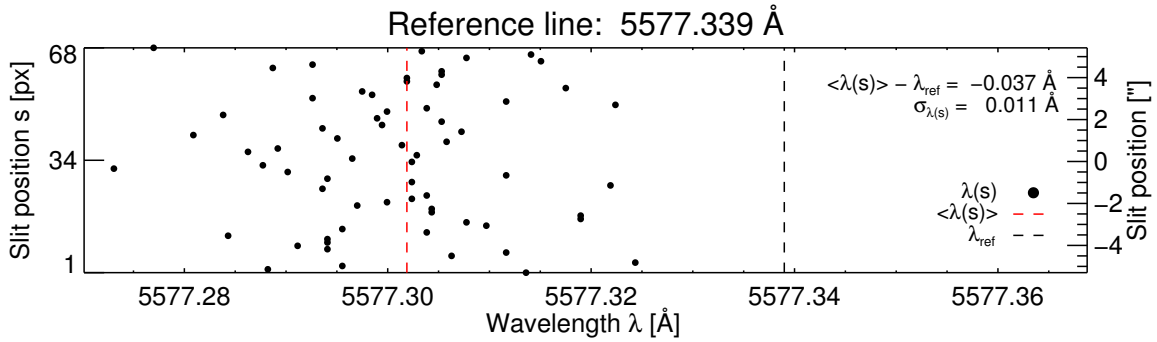

Figure 22: Gaussian centroid wavelengths as a function of slit position for the prominent O I line at 5577.339 Å. The median of all fitted wavelengths is shown with a vertical red dashed line, the corresponding air reference wavelength in dashed black. The difference between the measurement and reference is −0.037 Å and the standard deviation of the fitted values is 0.011 Å. The cross-dispersed direction corresponds to the y-axis, the spectral dispersion direction to the x-axis.

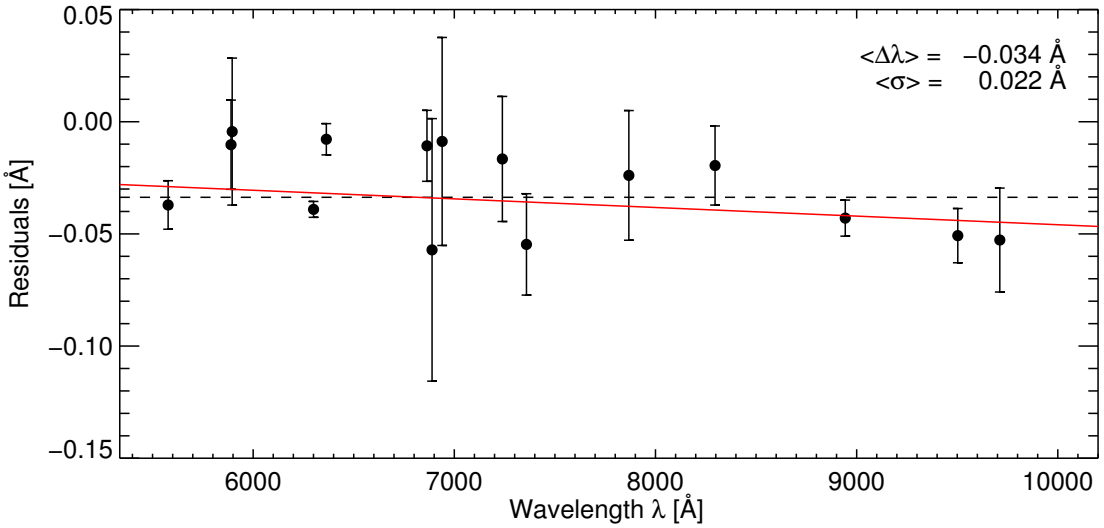

Figure 23: Wavelength residuals as a function of wavelength for 15 non-blended telluric lines. The individual data points and their uncertainties are derived as illustrated in Figure 22. The global weighted mean residual is −0.034 Å and is overplotted with a dashed black line. The error of the weighted mean is 0.022 Å. The best-fit straight line is overplotted in red.

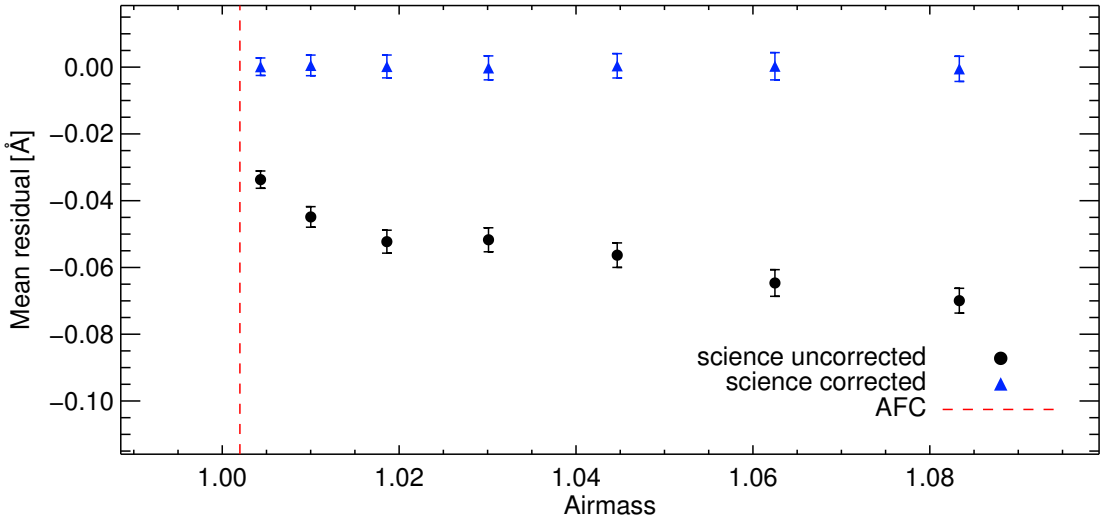

Figure 24: Mean wavelength residuals as a function of airmass for six observations of NGC 7099 and one additional sky frame. The black data points reflect the uncorrected weighted mean of all sky line residuals as explained in the text and shown in Figure 23. Correcting the wavelength solution of each observation by means of Equation (21) removes the bias (blue data points). The error bars illustrate the uncertainties of the weighted mean and represent the significance of the observed trend with airmass. The airmass at which the AFC measurement was performed is indicated with the dashed red line.

Part IV

SYNTHETIC SPECTRAL TEMPLATES

We use resolved Hubble Space Telescope photometry of our sample of eleven globular clusters in combination with stellar evolutionary models to convert for each cluster star the photometric data to the fundamental stellar parameters: the effective temperature $T_{\rm eff}$ and the surface gravity $\log g$. The utilized stellar evolutionary models represent the various stellar evolutionary phases that can be observed in an old stellar population and their application depends on the locus of a star in the color-magnitude diagram. All stars from the lower main sequence to the tip of the red giant branch are projected onto the best-fitting cluster isochrone from the literature. Blue straggler stars are modeled with isochrones of accordingly younger age and the horizontal branch population is synthesized with a specific model that statistically accounts for mass loss in the red giant phase. With $T_{\rm eff}$ and $\log g$ known for each photometrically resolved star, we select the appropriate stellar spectra from a synthetic spectral library and construct the luminosity-weighted composite spectrum. Applying this technique to all stars contained in the half-light radius of a cluster yields an instructive data set with which general statements about the contributions of the various evolutionary phases to the composite cluster spectrum can be made. For our velocity dispersion measurements we construct the synthetic composite spectra independently for each spatial bin in our observed spectra, which requires that the stellar contributions are modeled on a sub-arcsecond spatial resolution. The final spectra are eventually convolved with a model line spread function to match the instrumental resolution of our X-SHOOTER data and are subsequently used as templates in the velocity dispersion measurements.

4

CONSTRUCTION OF THE SYNTHETIC TEMPLATE SPECTRA

4.1 PREAMBLE

The dynamical masses $\mathcal{M}^{\rm dyn}$ for our sample of eleven GCs are measured with the Scalar Virial Theorem (e.g., Spitzer 1969; Binney & Tremaine 1987)

$$\mathcal{M}^{\rm dyn} \simeq 2.5\frac{3\,\sigma_0^2\,r_h}{G} \approx 1743\left(\frac{\sigma_0^2}{\rm km^2\,s^{-2}}\right)\left(\frac{r_h}{\rm pc}\right)M_\odot, \tag{22}$$

which requires as input the GC half-light radius r_h and the central velocity dispersion σ_0. While the former is taken from the catalogue of Galactic GCs by Harris (2010), the latter will be inferred from our observational data. This is accomplished by fitting a Doppler-broadened template spectrum to the observed one by means of a *penalized PiXel Fitting technique* (*pPXF*, Cappellari & Emsellem 2004). Due to the specific drift-scan mode of our observations (see Section 2.3), the integrated-light spectra typically comprise light of thousands of stars. This makes an accurate modeling of the template spectra necessary. For this, we use resolved *HST/ACS* photometry of our sample of GCs from the ACS Survey of Galactic globular clusters (Sarajedini et al. 2007), together with DARTMOUTH isochrones (Dotter et al. 2007) to determine the *effective temperature* $T_{\rm eff}$ and the logarithm of the *surface gravity* $\log g$ of each star contained in our scans. Based on these parameters, we assign to each star a synthetic spectrum taken from the PHOENIX synthetic stellar library (Husser et al. 2013) and subsequently construct the luminosity-weighted composite cluster spectrum, which is eventually used to measure the best-fit Doppler broadening. In order to perform accurate velocity dispersion measurements, we have to understand how the spectral features—in particular the line-width—in our observed integrated light spectra form, as only then the template can be properly constructed and used for the dispersion measurement. This includes four components, which we will briefly list here and then discuss in more detail below.

1) The atmosphere of each star leads to specific line shapes and strengths. While the elemental abundances in the atmosphere determine *which lines* potentially form, $T_{\rm eff}$ and $\log g$ are the dominant *broadening sources* of the lines through Doppler- and pressure broadening.

2) The *composite GC spectrum* is the sum over all individual stellar spectra ($\sim 10^5 - 10^6$), and the summation weights are given by the luminosities of the stars. The number of lines and their shapes are specific to the underlying stellar population (as parameterized by $T_{\rm eff}$, $\log g$, the metallicity [Fe/H], and the α-element abundance [α/Fe]).

3) The velocity dispersion, i.e., the random motions of the stars in the gravitational potential of the GC, leads to an additional Doppler-broadening that affects all spectral features in the composite spectrum.

4) The instrument with which the observations are performed imprints its own line spread function (LSF) with an associated broadening onto the integrated spectrum of the GC.

Consequently, velocity dispersion measurements with our data require that we first understand what kind of spectrum each cluster star emits, and, second, correctly model the contribution of each star to the synthetic composite spectrum of the GC. In a last step, we bring the resulting synthetic composite spectrum (hereafter "template") to X-SHOOTER's resolution so that any residual line-width deviation between template and observational data can be attributed to a Doppler-broadening caused by the random motions of the stars in the cluster potential. The details of the template construction process are covered in this chapter, whereas Chapter 5 deals with the actual velocity dispersion measurements. The dynamical mass estimates and resulting mass-to-light ratios will be presented and discussed in Chapter 6.

4.2 INTRODUCTION

In this Chapter we describe in detail how we construct the spectral templates that are used in our GC velocity dispersion measurements. Our sample of eleven GCs (see Section 2.3) is covered by deep *HST/ACS* and *HST/WFPC2* photometric observations, and these data sets will form the basis for the template construction process. The basic procedure can be explained in three steps.

First, we use isochrones to convert the photometric information into the stellar parameters $T_{\rm eff}$ and log g. For this, all stars are projected onto the respective best-fit isochrone. Populating an isochrone in this way yields the total luminosity with which each combination of $T_{\rm eff}$ and log g contributes to the composite cluster light. In a second step we retrieve for each combination of $T_{\rm eff}$ and log g a synthetic spectrum from a spectral library and scale the fluxes accordingly. The composite template spectrum is then obtained in a third step by summing over all contributing spectra and convolving the output to the instrumental resolution of X-SHOOTER . In order to achieve the best match between template and observation, this approach is applied for each slit position (i.e., cross-dispersed slit bin) individually. In this way we obtain a sub-arcsecond spatial resolution for the template.

The template construction description is organized as follows. We will give a short summary of the photometric data and the isochrones in Section 4.3. The utilized spectral library and associated restrictions are discussed in Section 4.4. The general mapping procedure of the photometric data onto the synthetic models is presented 4.5, and the obtained Hertzsprung-Russell-diagrams (HRDs) are discussed in 4.6. The application of the HRD data to the spectral library and the resulting composite spectra are presented Section 4.7. The modeling of the instrumental LSF is explained in Section 4.8. Finally, Sec-

tion 4.9 offers a description of how the drift-scan nature of our observations is taken into account in the construction process of the template spectra.

4.3 THE HST/ACS PHOTOMETRIC DATA AND DARTMOUTH ISOCHRONES

The drift-scan mode of our data set requires a detailed modeling of the template spectra that will be fed into the *pPXF* measurement. To minimize any biases related to the problem of template mismatch, we construct a composite template spectrum by considering each individual star contained in the scan. The deep photometry required for this task is taken from the photometric catalog of the ACS Survey of Galactic GCs by Sarajedini et al. (2007), who performed a consistent reduction of 65 GCs in *F606W* and *F814W* (located at $\sim 6,000$ Å and $\sim 8,000$ respectively; in the meanwhile the photometry has been updated to account for the marginal changes in the Wide Field Channel zero points presented by Bohlin (2007); we use the updated version). This survey was designed to provide a nearly complete star catalog for the central $2'$ of each cluster and uniform photometry with $S/N \gtrsim 10$ for stars as faint as $M_V \lesssim 10.7$ or $\mathcal{M} \gtrsim 0.2\,M_\odot$ (Sarajedini et al. 2007). Cross-comparing their GC sample with ours yields an overlap of ten GCs, which we list in Table 4. In addition, we found one additional cluster in our sample (NGC1904) that is covered by a *HST/WFPC2* snapshot program (Piotto et al. 2002) in *F439W* and *555W* (corresponding to $\sim 4,300$ Å and $5,400$ Å; We note that we use the data after they have been transformed to the B and V band, respectively). Although the *HST/ACS* data are generally significantly deeper, show a higher angular resolution, and cover a larger region of the GCs than the *HST/WFPC2* observations, the data available for NGC1904 should be sufficient to construct the template spectrum in a similarly robust way as for the other clusters. Unfortunately, Piotto et al. (2002) do not list the right ascensions and declinations for the individual stars in their reduced and publicly available catalogue, which renders these data useless if the drift-scan spectra are to be synthesized on a sub-arcsecond spatial accuracy. We therefore use the data provided by M. Frank (private communication), where the desired coordinates are listed. We note that the reduction quality is very similar to the data of Piotto et al. (2002).

Plotting the (apparent or absolute) magnitude against the flux-ratio of two different bandpasses yields information about both the overall luminosity and the approximate spectral distribution of the emitted energy of an astrophysical object. A plot of this kind is called color-magnitude diagram (CMD) and is widely used in many different astronomical fields, since observations with two different photometric filters are sufficient. The *HST/ACS* GC CMDs are remarkably rich in detail and immediately show a clear distinction of different evolutionary phases (see Figure 27). Yet, to quantify the physical parameters of the cluster's stellar population, detailed stellar evolution models are required. As mentioned in Section 1.2 we treat GCs as classical simple stellar populations, and thus rely on single isochrones to describe the distribution of stars in the CMD. Isochrone fit-

ting techniques typically yield ages t, abundances (metallicity [Fe/H] and α–element abundances [α/Fe]), distance modulii μ[1], and reddening values $E(6-8)$[2].

An isochrone is a theoretical curve that, for a given distance, predicts where stars of the same age and composition, but with initial different masses would appear in a CMD. An isochrone contains information in tabulated form about the stellar masses m, effective temperatures $T_{\rm eff}$, surface gravities log g, bolometric luminosities L_{bol}[3], and the fluxes in selected bandpasses of a given stellar population. For this, a synthetic population of stars with a range of initial masses is numerically evolved in time, and for each star the evoutionary track in the parameter space is recorded. An isochrone is defined as the curve that connects the points of equal age across the all evolutionary tracks, i.e., for all stars. It is clear that a detailed theoretical understanding of stellar evolution is required, in order to be able to provide this powerful tool. The shape of the isochrone very much depends on the input physics, and lately, due to significant increases in available computing power, sophisticated models could be implemented that greatly improved the accuracy even down to stellar masses of $0.1\,M_{\odot}$ (Girardi et al. 2000; Demarque et al. 2004; Pietrinferni et al. 2004, 2006; Yi et al. 2004; VandenBerg et al. 2006; Dotter et al. 2007).

An isochrone corresponding to an older age shows a fainter and redder main sequence turn-off (MSTO), as the more massive stars that are both bluer and brighter have already evolved off the main sequence (MS) and onto later stages, like the sub-giant phase (SG), red-giant branch (RGB), or have even died as a Type II supernova. This basic fact has been extensively used since its first systematic application by Demarque & Percy (1964) to age-date clusters and galaxies. Although there are several different groups that produce theoretical stellar evolution models, only the PADOVA isochrones (Girardi et al. 2000; Marigo et al. 2008) and the DARTMOUTH isochrones (Dotter et al. 2007) extend past the lower mass limit of the *HST/ACS* survey data *and* include photometric data on the *HST* photometric systems. Dotter et al. (2010, hereafter D10) have systematically fitted the DARTMOUTH isochrones to a subset of the *HST/ACS* GC data set and obtained a homogenous estimate on {t, [Fe/H], [α/Fe], μ, $E(6-8)$}. They used the comprehensive *McMaster catalogue of Milky Way Globular Clusters* (Harris 1996, revision 2003; current revision 2010) for an estimate of the initial values for {t, [Fe/H],[α/Fe],μ, $E(6-8)$} and then slightly varied the parameters until a good fit was obtained to the unevolved MS first, and to the RGB second. Again, the MSTO was used to determine the best-fit age of a given GC, although it should be noted that the uncertainties given by D10 only include random uncertainties due to the photometric scatter of the data, but neglect potential systematic age errors due to incomplete knowledge of chemical composition and incomplete treatment of the input physics, such as rotation and convection. D10 excluded several GCs in their analysis that are known to host multiple stellar populations, because a single age and metallicity determination would be insufficient to characterize the respective GC composite light. They

1 Since this work does not with surface brightnesses, we use μ exclusively for the distance modulus.

2 With $E(6-8)$ we mean $E(6-8) = (m_{F606W} - m_{F814W}) - (m_{F606W} - m_{F814W})_0$ for all clusters except NGC1904, for which we mean $E(6-8) = (m_B - m_V) - (m_B - m_V)_0$. The subscript 0 denotes the fluxes that would have been measured without the presence of interstellar dust. A more detailed explanation is given in Section 5.3.

3 Whenever we refer to the luminosity L we implicitly mean the bolometric luminosity, unless otherwise noted.

Name	[Fe/H]	[α/Fe]	μ	$E(6-8)$	t^{iso} [Gyr]	$\mathcal{M}^{HB}_{max}$	$\mathcal{M}^{HB}_{avg}$	$\sigma^{HB}_{\mathcal{M}}$	t^{BS} [Gyr]
NGC104	−0.7	0.2	13.30	0.023	12.75 ± 0.50	0.87	0.75	0.02	1,1.5,2,2.5,3.75,5,6.25,7.5,8.75,10,11
NGC288	−1.4	0.4	14.85	0.013	12.50 ± 0.50	0.82	0.79	0.10	1.5,2,2.5,3.75,5,6.25,7.5,8.75,10,11
NGC362	−1.3	0.2	14.80	0.023	11.50 ± 0.50	0.84	0.80	0.10	2,2.5,3.75,5,6.25,7.5,8.75,10
NGC1851*	−1.2 [a]	0.2 [b]	15.55 [a′]	0.023 [a′]	11.00 [c]	0.86	0.80	0.10	1.5,2,2.5,3.75,5,6.25,7.5,8.75
NGC1904*	−1.6 [a]	0.2 [d]	15.65 [a′]	0.03 [a′]	13.25 [e]	0.80	0.75	0.10	1.5,2,2.5,3.75,5,6.25,7.5,8.75,10,11.5
NGC2298†	−1.9	0.2	15.60 [a]	0.237	13.00 ± 1.00	0.80	0.78	0.10	1.5,2,2.5,3.75,5,6.25,7.5,8.75,10,11.5
NGC2808*,†	−1.1 [a]	0.2 [b]	15.45 [a]	0.165 [a]	12.50 [f]	0.83	0.65	0.15	1.5,2,2.5,3.75,5,6.25,7.5,8.75,10
NGC6656*,†	−1.7 [a]	0.2 [d]	13.70 [a′]	0.36 [a′]	13.25 [g]	0.80	0.70	0.10	1.5,2,2.5,3.75,5,6.25,7.5,8.75,10,11.5
NGC7078	−2.4	0.2	15.40	0.083	13.25 ± 1.00	0.79	0.77	0.10	1.5,2,2.5,3.75,5,6.25,7.5,8.75,10,11,12
NGC7089	−1.6	0.2	15.48	0.048	12.50 ± 0.75	0.81	0.75	0.20	1.5,2,2.5,3.75,5,6.25,7.5,8.75,10
NGC7099	−2.4	0.2	14.82	0.053	13.25 ± 1.00	0.79	0.77	0.10	1.5,2,2.5,3.75,5,6.25,7.5,8.75,10,11,12

Table 4: Cluster parameters used for the template construction. [Fe/H] denotes metallicity, [α/Fe], denotes the α-element abundance, μ is the distance modulus, $E(6-8)$ denotes the color excess due to foreground reddening, t^{iso} is the age of the best-fit isochrone (including MS,SG,RGB), $\mathcal{M}^{HB}_{max}$ ($\mathcal{M}^{HB}_{avg}$) is the maximal (average) stellar mass in the utilized horizontal branch (HB) model, $\sigma^{HB}_{\mathcal{M}}$ is the Gaussian dispersion of the parametrized mass loss in the HB model, and t^{BS} is the grid of ages used for the spectral synthesis of blue stragglers. ∗ denotes clusters that have not been analyzed by D10. † indicates clusters with known differential reddening. If not otherwise noted, the values for [Fe/H], [α/Fe], μ, $E(6-8)$, and t^{iso} are from D10. Other sources are: a) Harris (2010); a′ Harris (2010), adjusted to obtain the best visual fit; b) Carretta et al. (2011); c) Koleva et al. (2008), adjusted; d) Carney (1996); e) Kains et al. (2012), their CMD is consistent with 9 Gyr< t <15 Gyr; f) Carretta et al. (2010) give a value of 0.33, however since their values are generally higher than the ones of D10, we adopted a value of 0.2; g) Piotto et al. (2007); h) Davidge & Harris (1996), adjusted.

point out that it is even likely that in the *HST/ACS* survey additional GCs with (to-date) undetected multiple stellar populations exist. In this case, however, the separation between the populations needs to be either sufficiently small so that the multiple sequences overlap within the photometric errors, or differential reddening, where the reddening amplitude varies strongly as a function of the line-of-sight, prohibits a clear distinction between the populations. Table 4 lists their best-fit estimates for distances, reddening, chemical abundances, and ages. For clusters that are covered by our observations and are included the *HST/ACS* survey, but that were not included in the D10 analysis we obtained the according values from the literature (the corresponding references are given in the caption of Table 4).

We used the DARTMOUTH webform[4] to retrieve the respective isochrones based on the values given in Table 4. Suprisingly, a good match to the data could however only be obtained if the reddening correction $E(6-8)$ was applied only to the color axis, which, in turn, neglects any overall extinction along the magnitude axis and constitutes an incomplete treatment of the reddening correction. In combination with the fact that D10 do not specify which reddening law was applied to propagate the obtained reddening estimates to the full set of photometric filters, we have the impression that D10 applied $E(6-8)$ to

4 http://stellar.dartmouth.edu/~models/webtools.html; This work is solely based on DARTMOUTH isochrones. We note, however, that a repetition of the presented analysis with PADOVA isochrones could be used as consistency check.

colors, which in turn implies that the distance modulus μ is the only parameter that shifts the isochrone along the magnitude axis. It is evident that re-performing the full isochrone-fitting analysis is beyond the scope of this project, so we decided to use the values from D10 regardless of this potential blemish. For the clusters that are not included in their analysis we adopted the approach of using $E(6-8)$ as a shift along the color acis and μ as the exclusive shift along the magnitude dimension for reasons of consistency. We believe that the error introduced by this treatment is negligible for the purpose of projecting the photometric data onto the isochrones, because not accounting for extinction simply alters the distance modulus without changing the shape of the isochrone. In this context it is worth noting that the constructed template spectra will be eventually reddened to match the observations. In order to avoid similar ambiguities as mentioned above, we will describe this process in detail in Section 5.3.

The DARTMOUTH isochrones extend from the lower MS (LMS) up to the tip of the RGB, when helium-burning in the stellar core is ignited. As a consequence, all stars in an evolutionary phase inside these two limits can be consistently modeled with a single isochrone. In addition, all of our analyzed clusters show a distinct horizontal branch (HB) population, which for most clusters significantly contributes to the total flux. Thus, an explicit model for the HB stars is required. We use the *Synthetic HB Generator* offered on the DARTMOUTH webform that allows for the generation of a synthetic HB population (including the asymtotic giant branch, AGB) in a similar way to the standard isochrone. Input parameters are [Fe/H], $[\alpha/Fe]$, the total number of stars N of the population, the maximum allowed stellar mass in the population $\mathcal{M}_{max}$, the average stellar mass $\mathcal{M}_{avg}$, and the width of the Gaussian mass distribution $\sigma_{\mathcal{M}}$. $\mathcal{M}_{max}$ is constrained by the maximum stellar mass that still exists in the hydrogen-burning population, which corresponds to the tip of the RGB and typically is $\sim 0.8\,M_\odot$ for GCs with ages of ~ 12 Gyr. We adjusted $\mathcal{M}_{avg}$ and $\sigma_{\mathcal{M}}$ for each cluster individually until the best match between synthetic and observed HB populations in the CMD was obtained. We list the resulting values in Table 4. The synthetic HB[5] population is not a continous curve like an isochrone, but rather a set of individual points that are spread across a certain area in the CMD, each one representing an individual synthetic star. The spread is caused by the specific amount of mass loss that each star suffers on the RGB and is modeled statistically with a Gaussian distribution of width $\sigma_{\mathcal{M}}$. In this context, it is worth mentioning that the various observed HB morphologies have been a long-standing puzzle in astronomy, since theory predicts that the locii in the CMD should be predominantly determined by the metallicity. In consequence, two clusters with equal [Fe/H] are expected to show the same HB morphology, but observations reveal major differences in many cases (compare the CMDs of NGC288 and NGC362 in Figure 27; both clusters have similar metallicities but show very different HB morphologies). This effect is known as the *second parameter* phenomenon, and several additional cluster parameters have been put forward to explain the observed spread. These include the specific amount of mass loss on the RGB (Peterson 1982; Catelan 2000), stellar rotation (e.g., Mengel & Gross 1976), GC ellipticity (Norris 1983), age (Searle & Zinn 1978; Catelan

5 Whenever we refer to the HB population we mean HB and AGB stars, since the DARTMOUTH HB models include both phases.

& de Freitas Pacheco 1993; Dotter et al. 2010), GC density (Fusi Pecci et al. 1993), and helium abundance (Sandage & Wildey 1967; D'Antona et al. 2002). Recent results of Milone et al. (2014)suggest a combined effect of metallicity, age, and He abundance, such that [Fe/H] and age are responsible for the overall distance between HB and RGB (along the color-axis), whereas the extension of the HB to bluer colors arises from an internal star-to-star helium abundance spread, associated with multiple populations in the GCs. These results should be handled with care, however, since spectroscopic helium abundance measurements only exist for a few GCs. Thus, this puzzle is far from being resolved and a comprehensive picture is still missing. It should be noted that we did not undertake any attempt to explore this effect further in the work presented here. As a consequence, systematic uncertainties in the utilized synthetic HB models by D10 have to be expected that are not taken into account in our approach.

Apart from the HB, most clusters also a show an extended population of blue straggler stars (BSSs), which in the CMD reside in the space between the MSTO and the HB. Currently, there are two popular formation mechanisms for BSSs. One scenario is based on direct stellar collisions, in which two previously uncorrelated stars collide in a high-density environment like the cores of GCs. The other approach assumes that BSSs belong to binary systems, where mass is transfered from the companion onto the BSS (see Sills 2010 for a short summary on BSS formation). Any potential explanation must provide a mechanism that either delays the evolution of a higher-mass star, or increases the mass of a normal MS star such that it stays on the MS longer than its regularly evolving counterparts. It is interesting to note that the recent results of Leigh et al. (2011) suggest that mass transfer in binaries is the dominating formation channel in GCs, with direct collisions additionally enhancing the number of BSSs for some clusters. A common way to model the population of BSSs in the CMD is the use of isochrones with correspondingly younger ages (e.g., Simunovic et al. 2014). We therefore model all potential BSS candidates with a grid of isochrones spanning a range of ages. The oldest age is constrained by the age of the cluster, while the youngest age is chosen such that the corresponding curve in the CMD approaches the bulk of the HB population as close as possible without intersecting it (typically ~ 1 Gyr). The age stepping is $0.5 - 1.5$ Gyr, with smaller step sizes for younger ages. The exact ages that we used for the modeling are listed in Table 4.

4.4 THE PHOENIX SYNTHETIC SPECTRAL LIBRARY

The comparison between the spectrum of a composite astrophysical object and individual stellar spectra provided by spectral libraries is a powerful tool to draw conclusions about the stellar content of the object. This approach has been extensively applied for more than 100 years, when Scheiner (1899) first compared spectra of M31 and the Sun and noticed a surprising similarity, concluding that M31 was primarily composed of solar-type stars. Since then a lot of progress has been made in the compilation of spectral libraries. A good, however somewhat outdated overview of available libraries is given by Leitherer et al. (1996) and another short summary is presented by Cassisi & Salaris (2013).

For the task of synthesizing observed spectra with theoretical models, one in principle has two options. Using *empirical spectral libraries* bears the great advantage of naturally incorporating real-world physics into the synthesis. Consequently, line strengths and shapes in the library spectra should match the observed features to a high degree. Furthermore, instrumentational systematics like the exact shape of the LSF as a function of wavelength are automatically accounted for if the library was generated with the same instrument as the science data. Drawbacks of empirical libraries, however, are typically related to the limited spectral resolution and wavelength coverage (both determined by the instrument with which the data were obtained) and possibilities to circumvent this issue generally involve significant amounts of observing time and different instruments. In particular the latter point usually implicates that the library's consistency might be severely compromised. Moreover, systematic errors in abundance measurements have to be expected, because the true chemical compositions of the stars in the library are usually not known exactly. In addition, the covered stellar parameter space of the library can be insufficient and thus the available sampling of $T_{\rm eff}$, log g, [Fe/H], and $[\alpha/\mathrm{Fe}]$ does not meet the requirements imposed by the scientific object of interest. In these cases, a direct comparison between library and observed data is not possible and necessitates additional efforts. Popular examples for empirical specral libraries in the optical wavelength regime with resolutions $1,000 \leqslant R \leqslant 10,000$ are the MILES library (Sánchez-Blázquez et al. 2006; Falcón-Barroso et al. 2011), the STELIB library (Le Borgne et al. 2003), and the ELODIE library (Prugniel & Soubiran 2001, 2004).

The above mentioned advantages and disadvantages are essentially reversed for *synthetic spectral libraries*. Their spectral accuracy is determined by the completeness of the utilized atomic (and molecular) line list on the one hand, and by the understanding of the line broadening effects and the numerical treatment on the other hand. As with all scientific simulations, a compromise between model accuracy and computation time has to be taken. In case of stellar atmospheres this translates into choosing between plane-parallel or spherically symmetric modeling of the atmopshere's geometry, and between local thermodynamic equilibrium (LTE) or non-LTE (NLTE) treatment of the physical processes. Conversely, synthetic libraries have the advantage that the wavelength coverage and spectral resolution can be adjusted as needed, and the sampling of stellar parameters and elemental abundances can be customized to fit the desired purposes. A very popular set of synthetic model atmospheres is based on the ATLAS code (Kurucz 1969, 1970, 1979). Its newer revisions have been used extensively to compute various spectral libraries (e.g., Murphy & Meiksin 2004; Rodríguez-Merino et al. 2005).

In this work we will make us of the PHOENIX library (Husser et al. 2013) for the spectral synthesis. It is a high-resolution synthetic spectral library based on the stellar atmosphere code PHOENIX, which is a combination of two codes that were originally developed to treat cool stars on the one hand (Allard 1990), and the expanding ejecta of novae and supernovae on the other hand (Hauschildt 1991).

PHOENIX offers a consistent treatment for atmospheres of stars on the MS up to the RGB by using a special mixture between LTE and NLTE physics and spherical geometry for the entire range of considered stellar parameters. While plane-parallel atmospheres

parameter	range	$\text{step}_{\text{orig}}$	$\text{step}_{\text{interp}}$
T_{eff} [K]	[2,300, 7,000]	100	100
	[7,000, 12,000]	200	100
log g [cm/s^2]	[0.0, 6.0]	0.5	0.5
[Fe/H]	[-4.0, -2.0]	1.0	0.1
	[-2.0, 1.0]	0.5	0.1
[α/Fe]†	[-0.2, 1.2]	0.2	0.2

Table 5: Parameter space coverage of the PHOENIX spectral library. The values are taken from Husser et al. (2013), except for the last column, which lists the step size of the interpolated grid. † $[\alpha/\text{Fe}] \neq 0.0$ is only available for $3500\,\text{K} \leqslant T_{\text{eff}} \leqslant 8000\,\text{K}$.

are usually accurate enough for stars near the MS, whose atmospheres are physically thin compared to the size of the star, atmopsheres of giant and super-giant stars require a spherical geometry to produce accurate fluxes in the synthetic spectra. Hauschildt et al. (1999a,b) find that for $T_{\text{eff}} \leqslant 10,000$ K plane-parallel atmospheres are sufficient for gravities $\log g \geqslant 3.5$, and recommend spherical geometry for $0.0 \leqslant \log g \leqslant 3.5$ and $T_{\text{eff}} \leqslant 6,800$K. The current PHOENIX library, however, uses spherical symmetry for *all* atmospheres to provide a homogenous model grid through all evolutionary phases (Husser et al. 2013). Furthermore, the PHOENIX library generally assumes LTE, where the mean free path of particles is much smaller than the temperature scale height (a characteristic distance over which the temperature varies). Thus, the particles see an almost constant kinetic temperature between subsequent collisions. In an NLTE treatment the populations of certain energy levels of selected atoms are allowed to deviate from their LTE value. It should be noted that the PHOENIX code implements a NLTE treatment for $T_{\text{eff}} \geqslant 4,000$ to model special line profiles for Li I, Na I, K I, Ca I, and Ca II. For a deeper understanding of the physics of stellar atmospheres we refer the interested reader to the comprehensive introduction by Hubeny (1997).

The wavelength coverage of the PHOENIX library reaches from 500 Å to 5.5 µm with a resolving power $R \approx 500,000$ in the wavelength range between 3,000 Å and 10,000 Å. The available samplings of T_{eff}, log g, [Fe/H], and [α/Fe] are listed in Table 5 (columns 1-3).

Despite its great parameter coverage we had to overcome a number of limitations in the synthesis process. These include:

1) We round the effective temperatures predicted by the DARTMOUTH models to the nearest integer multiple of 100 K. Thus, for $T_{\text{eff}} \geqslant 7,000$ K, where the intrinsic PHOENIX temperature stepping is 200 K, we need to interpolate the T_{eff}-grid to fill in the missing data. This is achieved by linearly interpolating the spectra of two adjacent temperature sampling points to the desired T_{eff}-value. This interpolation is perfomed for each wavelength bin individually and finally yields a homogenous T_{eff}-sampling from 2,300 K to 12,000 K.

2) We utilize a metallicity sampling based on integer multiples of 0.1 dex for the DARTMOUTH isochrones (see Table 4). Since the PHOENIX library is tabulated with a step size of

0.5 dex, an additional interpolation along the [Fe/H]-grid is required. The actual implementation is similar to the interpolation along the T_{eff}-grid: adjacent PHOENIX metallicity sampling points are linearly interpolated for each wavelength bin, yielding a uniform [Fe/H]-stepping of 0.1 dex.

3) The PHOENIX temperature grid ends at $T_{eff} \leqslant 12,000\,K$. As a consequence, we have to model all stars with hotter atmospheres with $T_{eff} = 12,000\,K$. We note that an extension of the PHOENIX library up to $T_{eff} \leqslant 25,000\,K$ is planned (Husser et al. 2013), but not yet available. Until then, a certain fraction of hot HB stars cannot be modeled properly.

4) Non-solar α-abundances, i.e., $[\alpha/Fe] \neq 0.0$, are only available for $3,500\,K \leqslant T_{eff} \leqslant 8,000\,K$. This implies that all spectra with $T_{eff} \notin [3500\,K, 8000\,K]$ are modeled with scaled-solar abundances, i.e., $[\alpha/Fe] = 0.0$.

Tweaking the parameter space of the PHOENIX library in this way yields a uniform and reasonably consistent grid of stellar spectra for the GC spectral synthesis. The final sampling is listed in column four of Table 5.

4.5 TRANSFORMATIONS OF THE PHOTOMETRIC DATA

Projecting each cluster star in the CMD onto an appropriate isochrone corresponds to a transformation from the observed parameters $\{m_{F606W}, m_{F606W-F814W}\}$ to the more physical stellar parameters $\{T_{eff}, \log g\}$. This transformation is required to select for each star the correct synthetic spectrum from the PHOENIX library, so that an appropriate composite template spectrum can be constructed. Although the spectral synthesis will be eventually performed locally for each slit position (i.e., on a sub-arcsecond scale), the transformation of the photometric data to the corresponding set of stellar parameters is based on the global cluster CMD (i.e., all stars covered by the photometric observation). This is owed to the fact that the global distribution of cluster stars constrains the locii of the various evolutionary phases much more robustly than partial subsets, and thus the mapping will be much more accurate.

We start by using the global *HST/ACS* CMD (containing all stars) and manually set color cuts that divide the CMD into two regions. One closed polygonal chain is drawn around all potential HB and AGB stars and another one around all stars from the lower MS up to the tip of the RGB. Since all clusters in our sample show a very distinct HB population, defining the HB/AGB polygon is rather straight-forward and caution has only to be exercised in the region where the AGB approaches the RGB. To disentangle between the two, we overplotted the synthetic HB population and used their distribution as a proxy for the expected locii of the HB/AGB in the overlapping region. The color cuts were then adjusted such that they approximately followed the synthetic population in this part of the CMD. The procedure is illustrated in Figure 25, where we show the CMD of NGC104 and overplot the two polygonal chains (solid black lines) used to disentange between HB/AGB and MS/RGB. The synthetic HB population is plotted with cyan diamonds, and all stars that are eventually contained in the HB/AGB polygon are highlighted with magenta open squares. Nevertheless, it should be mentioned that this treatment suffers from a certain degree of ambiguity because the exact choice for the cuts is somewhat arbitrary. On the

other hand, the AGB typically contains very few stars and for most clusters it is well separated from the RGB. Thus, the net effect of a potential wrong classification is expected to be low.

Figure 25 also illustrates that the synthetic HB population is usually confined to a relatively narrow band in the CMD, whereas the observed population shows a larger spread towards brighter luminosities than could be explained by the photometric errors alone (the photometric errors in this part of the CMD are almost neglible). Although this discrepancy is not very pronounced for NGC104, it is much more apparent for other clusters in our sample (compare e.g., NGC1851 or NGC2808 in Figure 27). A mismatch of this kind can be either be caused by systematic problems in the HB model ($\equiv$ model population too faint; given the above described uncertainties related to the second parameter phenomenon, we suspect that this is the dominant effect) and / or by foreground stars that were not properly removed from the *HST/ACS* data ($\equiv$ observed data too bright; less likely given the high reduction quality of the *HST/ACS* data). Unfortunately we cannot correct for either effect because, first, the synthetic HB model does not offer a sufficiently large parameter space (e.g., helium abundance variations) to explore whether a similarly large spread in the model can be obtained, and, second, any potential foreground star will also be contained in our drift-scan data. Thus, a cleaning of the respective stars from the CMD would indeed remove them from the resulting template spectrum, but the stars would still be contained in the observational data, and hence the removal would become meaningless. We therefore set the cuts sufficiently wide so that all potential HB candidates are included in the polygon and model all of them as a regular part of the HB population (see below for the actual mapping onto the theoretical models).

The polygon that embraces all stars from the LMS to the tip of the RGB is chosen with special attention paid to the MSTO and SG, in order to carefully mask out potential BSS candidates. We note that the actual choice (within reasonable limits) does not affect the results critically since the width of the polygon will be refined in a subsequent step. The BSS polygon is limited mostly by the MS/RGB and HB/AGB polygonal chains, and additionally by the youngest utilized isochrone on the blue side of the CMD (see Figure 27). It should be noted that similar to the MS/RGB polygon the exact choice is only preliminary and will be adjusted later.

All stars that are not contained in any of the polygons will be excluded from the subsequent analysis, and thus will have no contribution to the final template spectrum. These include predominantly white dwarfs (at the lower left of the CMD) and a small fraction of MS stars, which reside outside the respective polygon due to uncertainties in the photometric measurement. The luminosities of theses objects are intrinsically very low, implying that their impact on the composite spectrum is neglible and their exclusion should not produce any significant bias.

The mapping process of the observational data onto the theoretical curves slightly depends on the evolutionary phase because different isochrones/models are used for different parts of the CMD (see Section 4.3). The exact implementations will be explained below:

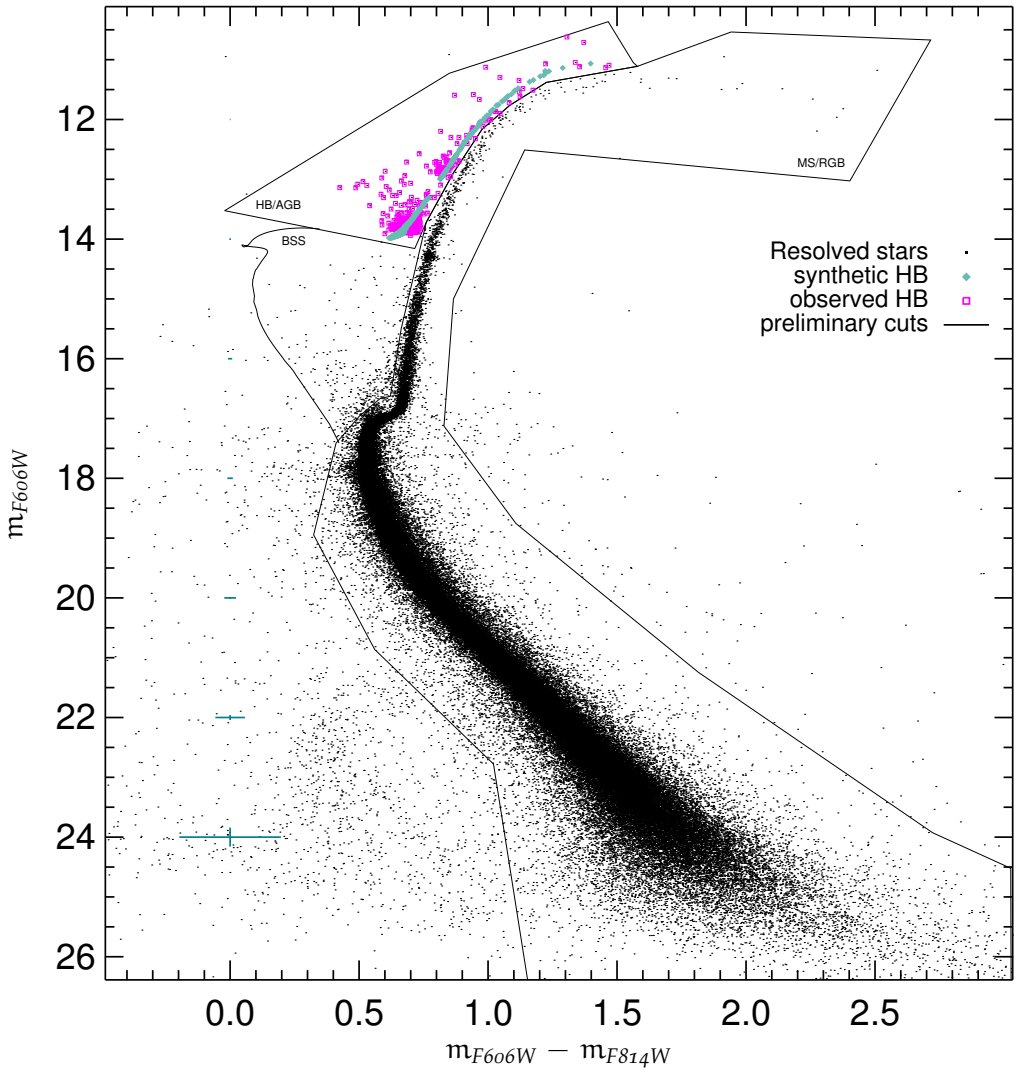

Figure 25: CMD of NGC104 based on *F606W* and *F814W* photometry from *HST/ACS* observations by Sarajedini et al. (2007). The overplotted cuts (solid black lines) are used to distinguish between the various evolutionary phases. The synthetic HB stars are overplotted with cyan diamonds. All observed stars contained in the HB/AGB polygon are highlighted with magenta open squares. Typical photometric errors at various magnitudes are indicated by turquois crosses on the left-hand-side of the plot. For $m_{F606W} \lesssim 20$ these are usually smaller than the utilized line-width.

MS, SG, RGB. The MS, SG phase, and RGB are modeled concurrently with a single isochrone based on the parameters given in Table 4 (columns 2-6). The isochrone is resampled to a $\sim 5\times$ finer grid in color-magnitude-space and the corresponding stellar parameters are linearly interpolated accordingly. We apply a magnitude cut and project all stars with $m_{F606W} < 26$ that are enclosed by the polygonal chain onto the isochrone. For this we compute for each observed star $\star_i$ the Euclidean distances to all isochrone bins iso_j, i.e.,

$$d_{ij} = \left((x_{\star_i} - x_{\mathrm{iso}_j})^2 + (y_{\star_i} - y_{\mathrm{iso}_j})^2\right)^{1/2}, \tag{23}$$

where $x \equiv m_{F606W} - m_{F814W}$ and $y \equiv m_{F606W}$ denote the axes of the utilized CMDs. Information is stored about the mapping $\mathrm{iso}_{j'} \leftrightarrow \star_i$, where $\mathrm{iso}_{j'}$ is the isochrone bin for which this distance is minimal (i.e., the closest model point the observed star). This mapping, however, needs to be refined, as at this step all stars enclosed by the polygon would be considered, independent of their actual distance to the isochrone, and thus the result would strongly depend on the a-priori choice of the cuts. In order to obtain a distribution of stars with a consistently estimated width around the model curve we apply a $\kappa - \sigma$ clipping, i.e., we perform a masking based on the distances between observed data and model. Since an isochrone is a curved line in the two-dimensional CMD, with varying orientation angle $\alpha = \alpha(x, y)$ with respect to the ordinate, all stars $\star_i$ belonging to an isochrone bin iso_j (as computed by Equation 23) will be confined in a band with an inclination angle $\frac{\pi}{2} + \alpha_j$ (see Figure 26 for a sketch; the band containing the stars is indicated by the red arrow). In order to measure the scatter of the observed data about a particular isochrone bin iso_j along the perpendicular direction of the isochrone's orientation (i.e., along the normal of the isochrone), we perform a rotation of the observed data based on the bin's orientation angle. This corresponds to a coordinate transformation from x, y to a coordinate system that is perpendicular to each isochrone bin, and thus the scatter in the resulting system will be one-dimensional.

Let $\{\star\}_j$ be the set of stars populating isochrone bin iso_j, then the photometry of each star $\star_i \in \{\star\}_j$ with $\star_i = (x_{\star_i}, y_{\star_i})$ is rotated via

$$\begin{pmatrix} x'_{\star_i} \\ y'_{\star_i} \end{pmatrix} = \begin{pmatrix} \cos\alpha_j & -\sin\alpha_j \\ \sin\alpha_j & \cos\alpha_j \end{pmatrix} \begin{pmatrix} x_{\star_i} - x_{\mathrm{iso}_j} \\ y_{\star_i} - y_{\mathrm{iso}_j} \end{pmatrix}, \tag{24}$$

and we analyze the distribution of $\{x'_\star\}_j$ (the $y'_{\star,i}$ are determined by the length of an isochrone bin in the CMD and thus are neglibly small if the isochrone is resampled to a sufficiently small stepping). For most parts of the CMD $x'_{\star_i} \simeq x_{\star_i} - x_{\mathrm{iso}_j}$, because the isochrone runs almost along the vertical direction for the MS and RGB phases and thus $\alpha \approx 0$. Any scatter of the photometric data then corresponds solely to scatter along the color dimension. At the MSTO and along the SG phase, however, the isochrone changes its orientation significantly and scatter along the magnitude dimension becomes more significant.

Since the distribution of $\{x'_\star\}_j$ about the central value is expected to be asymmetrical due to unresolved binaries and / or an overall mismatch between the isochrone and the data,

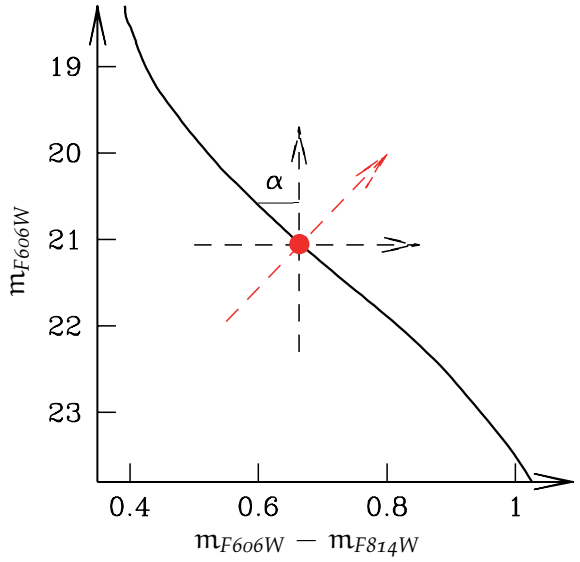

Figure 26: Sketch indicating the isochrone orientation angle α. The isochrone runs from the bottom right to the top left. The red circle indicates an isochrone bin and the angle α is measured against the ordinate. All stars that will be potentially projected onto the bin are confined in band whose orientation is indicated by the red arrow. Note that the amplitude of the shown angle is slightly misleading, since the isochrone is almost vertical in this part of the CMD. Image Credits: A. Pasquali.

we do not compute a standard deviation of all $x \in \{x'_\star\}_j$, but rather the asymmetrical limits enclosing 68% of all stars around the median value $\left\langle \{x'_\star\}_j \right\rangle$, yielding $\sigma_\downarrow$ and $\sigma_\uparrow$. Some isochrone bins (especially on the RGB of some clusters), however, might be either empty or only sparsely populated by stars. These low numbers can lead to a considerable bin-to-bin scatter of $\left\langle \{x'_\star\}_j \right\rangle$, $\sigma_\downarrow$, $\sigma_\uparrow$ and we account for this numerical instability by applying a median boxcar smoothing to these three quantities (box size = 5 bins; empty bins are ignored in the smoothing). Finally, we choose $\kappa = 6$ for the clipping and only consider stars $\star_i$ with

$$\left\langle \{x'_\star\}_j \right\rangle - \kappa\sigma_\downarrow < x'_{\star_i} < \left\langle \{x'_\star\}_j \right\rangle + \kappa\sigma_\uparrow \tag{25}$$

to be true members of isochrone bin iso_j. All stars that lie outside these limits are removed from the set $\{x'_\star\}_j$. The rotation and subsequent clipping is eventually applied to all isochrone bins, yielding a specific number of member stars for each bin. When the obtained limits $\left\langle \{x'_\star\}_j \right\rangle - \kappa\sigma_\downarrow$, $\left\langle \{x'_\star\}_j \right\rangle + \kappa\sigma_\downarrow$ are transformed back to the true color-magnitude-space (by means of the inverse of Equation 23), they depict the width of the scatter about the isochrone in both magnitude and color dimension. In a last step we apply magnitude cuts that split the isochrone into different parts, each representative for a different evolutionary phase. We distinguish between lower main sequence (LMS), upper main sequence (UMS), main sequence turn-off (MSTO), sub-giant phase (SG), and red giant branch (RGB). This differentiation becomes important in a later step of our analysis when we compare the spectra of different phases to one another (see Section 4.7). It should

be noted that the exact choice of the applied cuts is to some extent arbitrary, in particular the distinction between LMS and UMS, and UMS and MSTO, respectively. Although the cuts approximate the different phases in the CMD reasonably well, any quantitative conclusions have to be drawn with care.

BSS. The CMD region of the blue straggler stars is defined by three components: the youngest isochrone used in the BSS modeling process (see Table 4) as a limit on the blue side, $\left\langle \{x'_\star\}_j \right\rangle - \kappa\sigma_\downarrow$ (transformed back to color-magnitude-space) as red limit, and the HB polygon as an upper luminosity limit (see Figure 25). The stars confined in this area are treated in a similar way as described above for the MS,SG, and RGB, with the only difference that the area is sampled with number of isochrones (see Table 4 for the utilized ages). Consequently, the distances between stars and isochrone bins d_{ij} (see Equation 23) are computed for each isochrone independently, and the closest bin among all isochrones is used to infer the stellar parameters.

HB. Although the model HB population is not represented by a continous curve in the CMD, the mapping process is very similar to the other two cases: For each observed star the closest theoretical model star is found and its parameters used for the stellar model. It should be noted, however, that for some clusters even the best-fit synthetic HB population shows a systematic displacement relative the observed population, such that the model typically is too faint and / or too red. We speculate that this offset is likely caused by incomplete physics in the HB model atmospheres related to the second parameter phenomenon. Since the amplitude of the offset is comparably small, we correct for the displacement by shifting the theoretical data until the bulks of the model and observed HB populations align. The tabulated model parameters (T_{eff}, $\log g$, L_{bol}), however, remain unaltered, since we have no plausible way to estimate how the shift translates into a correction for these parameters. Nevertheless, the applied shift is necessary, as it ensures that the observed HB population is not projected onto only a few, very bright members of the theoretical population (which align well with the observation due to their exceptionally large spread). Hence, despite the mismatch in the CMD, the utilized HB model is still considered to be a good representation of the observed population, and the intrinsic spread of the stellar parameters (as given by the width of the model population) is fully exploited. We note that this treatment potentially leads to an underestimation of the total HB flux (because the theoretical data are shifted in the CMD, but T_{eff}, $\log g$, and L_{bol} remain unaltered), yet, given the lack of a better HB representation, we see no other way to correct for it.

In a last step, any stars that were so far unregarded due to their particular position between HB polygon and youngest BSS isochrone are either considered to be HB or BSS members, depending on their distance to the closest model star/bin, and the stellar parameters are inferred correspondingly. The final mapping results are presented in Figure 27, where we show the *HST/ACS* CMDs for our sample of eleven GCs and color-code the various phases and their member stars. All stars that are projected onto the main isochrone

are color-coded with light orange (LMS), brown (UMS), light purple (MSTO), light green (SG), and dark green (RGB; see the first color bar in Figure 27). The main isochrone is overplotted with a solid curve, while the BSS isochrones are plotted with dashed curves. The isochrone ages are color-coded as indicated by the second color bar (young ages are plotted in yellow, intermediate ages in blue, and old ages are plotted in red). BSSs are plotted with a star symbol, and their color indicates on which isochrone (i.e., what age) they are projected. The synthetic HB population is plotted with cyan diamonds, while the observed HB stars are overplotted with magenta open squares. The shift direction of the synthetic HB is indicated by a black arrow, where the arrow head denotes the position *after* the shift (the arrow is only plotted if a shift was required). It should be noted that the plotted uncertainty bands around the main isochrone (solid black lines; obtained by back-transforming the limits of Equation 25 by means of the inverse of Equation 23) have been strongly smoothed for reasons of visibility, and therefore do not resemble the actual bands which are used for the mapping. As a consequence, stars that are included in the mapping and thus color-coded, can be found outside the error bands.

When comparing the various CMDs presented in Figure 27, we find that our presented mapping procedure produces mostly consistent results across our sample, inspite of significant differences in the distribution of stars in the CMDs (compare e.g., the CMDs of NGC7089 and NGC7099: the MS widths, the number of BSSs and the HB morphology are vastly different for these two clusters). Nevertheless, it is evident that this our approach implicates a number of uncertainties that we want to briefly discuss below.

1) Unresolved binaries along the MS, which manifest themselves as an additional concentration in the CMD located above and to the right of the true MS, are treated in the same way as single stars, despite the fact that both deviate from the isochrone for different reasons. The presented mapping procedure implicitly assumes photometric uncertainties to be the only cause for the observed scatter around the theoretical model, and we account for this uncertainty by allowing for a finite width around the isochrone. Within this band, each star is then mapped onto the respectively closest isochrone bin. While the closest bin (based on the Euclidean distance as given by Equation 23) is certainly a suitable choice for stars whose deviation is caused by random photometric scatter, unresolved binaries show deviations from the isochrone in a preferred way, the particular direction depending on the mass ratio of the two stars. An unresolved binary consisting of two equal-mass stars (and therefore equal luminosity and color) will be shifted purely vertically by $-2.5 \cdot \log 2 \approx -0.75$ because its composite surface temperature remains the same, while the total luminosity is doubled. With varying mass ratio a second shift component along the color dimension (towards redder colors) is introduced, since the atmosphere of the hotter component is blended with the contribution of the cooler companion. Unfortunately, the distribution of binary mass ratios in GCs cannot be generally predicted (see Hut et al. 1992 for a comprehensive overview), as it depends on both the primordial distribution and the dynamical evolution of the cluster. This information, however, would be required to accurately account for binaries in the mapping procedure, and thus we

undertake no further attempt to correct for this issue. It should be emphasized that this treatment does not imply that binaries are excluded entirely from the analysis. It merely implies that the direction along which they are projected on the theoretical model is similar to that of single stars, and thus inappropriate for these objects. Their inclusion in the analysis is ensured by allowing for assymetric bands around the isochrone (see Equation 25). An illustrative example is the MS of NGC288, a GC with a known pronounced binary sequence (Bellazzini & Messineo 2000), which clearly shows a stronger scatter to redder colors than to bluer colors (relative to the main locus of the MS; see Figure 27). Yet, the number of excluded stars is very similar on both sides of the MS, owing to the asymmetry in the $\kappa - \sigma$ clipping.

2) Multiple stellar populations with distinct differences in age and / or chemistry are not taken into account by our mapping procedure, owing to the fact that we use a single isochrone for each cluster (excluding the BSS isochrones, which are used for a very small subset of stars and which only differ in age). Although this isochrone certainly reflects the average properties of the underlying populations reasonably well and can be used in a statistical way to derive the average stellar parameters for a cluster's composite population, a subset of stars might show significant devations due to systematically different ages and / or chemistries. This can be either in the form of additional distinct sequences that run parallel along the MS, SG, or RGB, or in the form of a general increase of scatter about the average locus of the distribution (e.g., Lee et al. 1999; Bedin et al. 2004; Milone et al. 2008; Han et al. 2009). Judging from the uncertainty bands in the CMDs presented in Figure 27 (solid black lines), the typical scatter about the isochrone is $\lesssim 1$ along the magnitude dimension and $\lesssim 0.2$ in color, and thus much smaller than the extent of the global distribution in the CMD (the stars span a typical range of ~ 14 magnitudes in luminosity and ~ 2 magnitudes in color). This suggests that the isochrone luminosities should represent reasonably robust estimates for the different phases, even if distinct differences between multiple populations are not accounted for (the expected differences of two populations that differ by $\sim 250\,\mathrm{Myr}$ at an absolute age of $\sim 12\,\mathrm{Gyr}$ is on the order of a few hundreths of a magnitude (Milone et al. 2009), and thus hardly detectable). The influence of the different populations onto spectral features in the composite spectrum, however, is hardly predictable, since it depends on the overall number of member stars of each population, and the actual differences in age and chemistry between the populations. While the overall continuum shape and strength should be approximately the same for all stars that are mapped onto the same isochrone bin, irrespective to which population of stars they belong (since they are confined within a rather narrow band, and thus, all have roughly the same temperature and surface gravity), individual line strengths might show major deviations, depending on the actual chemistry of each star. Consequently, this implies that the overall shape of an observed spectrum should be well reproduced by a template based on our mapping technique, whereas a higher uncertainty and even systematic deviations must be expected for the reproduction of certain individual lines. Indeed, these abundance variations (primarily in light elements) have been measured spectroscopically in a number of GCs (see Gratton et al. 2004 for a comprehensive review on light element

abundance variations) and are widely quoted as one of the evidences for multiple populations. It is thus highly likely that signatures of this kind are also contained in our data, and deviations for certain lines have to be expected in the template. This topic will be further discussed in Section 5.3, where a comparison between the templates spectra and the observational data is presented.

In this context it should be noted, however, that our data can in principle be used to infer contraints on the existence of multiple stellar populations: using stellar templates with different chemistries and varying their relative contributions, it should be possible to constrain both the relative contribution of each population and its chemical abundances. The fact that the relative constributions in the synthesis can always be cross-checked with the observed distribution of stars in the CMD constitutes a major advantage over approaches that exclusively utilize either photometry or spectroscopy. The significance of the constraints might be even improved by applying the analysis to each spatial bin of our spectra individually, as, due to available *HST/ACS* photometry, we can exactly assess which stars in the CMD are responsible for the observed spectrum. Any differences in the relative contributions of different stellar populations between two slit positions, as measured by spectroscopy, should always be consistent with the distribution of stars in the CMD that contribute to the composite spectrum. Detailed elemental abundance measurements are planned for a future project and an implementation of the described idea seems worth to be considered. Furthermore, it should be noted that the signatures of multiple populations in a CMD are partly degenerate with the signature of unresolved binaries, since both effects can produce additional sequences that are hardly distinguishable.

3) Differential reddening is an additional source of scatter along both dimensions in a CMD. Although the reddening values are small for most of the clusters in our sample ($E(6-8) \lesssim 0.05$; see Table 4), three clusters (NGC2298, NGC2808, and NGC6656) are known to be significantly affected by differential reddening ($E(6-8) \gtrsim 0.2$). This effect should result in an approximately symmetric scatter about the average locus in the CMD ($E(6-8)$ is expected to vary randomly across the field-of-view), and thus is automatically accounted for in the mapping process by accordingly larger uncertainty bands. Nevertheless, if an accurate spectral synthesis on a per-slit-bin-resolution ($\sim 0.16''$) is desired (e.g., for chemical abundance gradient measurements) it seems worthwile to use accurate reddening maps, if available, as only then the contributions of each star to the composite spectrum will be precisely estimated. For the velocity dispersion measurements presented in this work, where we compare the observed spectra and templates over the full spectral range, which covers thousands of spectral lines, we think it is justified to omit this cumbersome correction.

4) For some clusters no clear allocation to a distinct evolutionary phase can be made for stars that occupy the area in the CMD between RGB and HB/AGB, since all three models for the HB, RGB, and BSS overlap in this region (e.g., some bright BSSs in NGC7078 and NGC2808; compare Figure 27). It therefore has to be expected that individual stars in this area suffer from an incorrect mapping and are erroneously mapped onto a model that is

not appropriate for their stage of stellar evolution. As a consequence, the overall luminosity of the respective template spectrum will be slightly misestimated, however—and this is even more important—the spectral features in the composite template should remain mostly unchanged, as all stars in a given phase have roughly the same stellar parameters, and thus including or excluding individual stars should not change the average stellar parameters of the respective template dramatically. Nevertheless, a more sophisticated technique, where the mapping is performed based on a maximum-likelihood approach, is certainly worth to be considered, but remains without application in the work presented here.

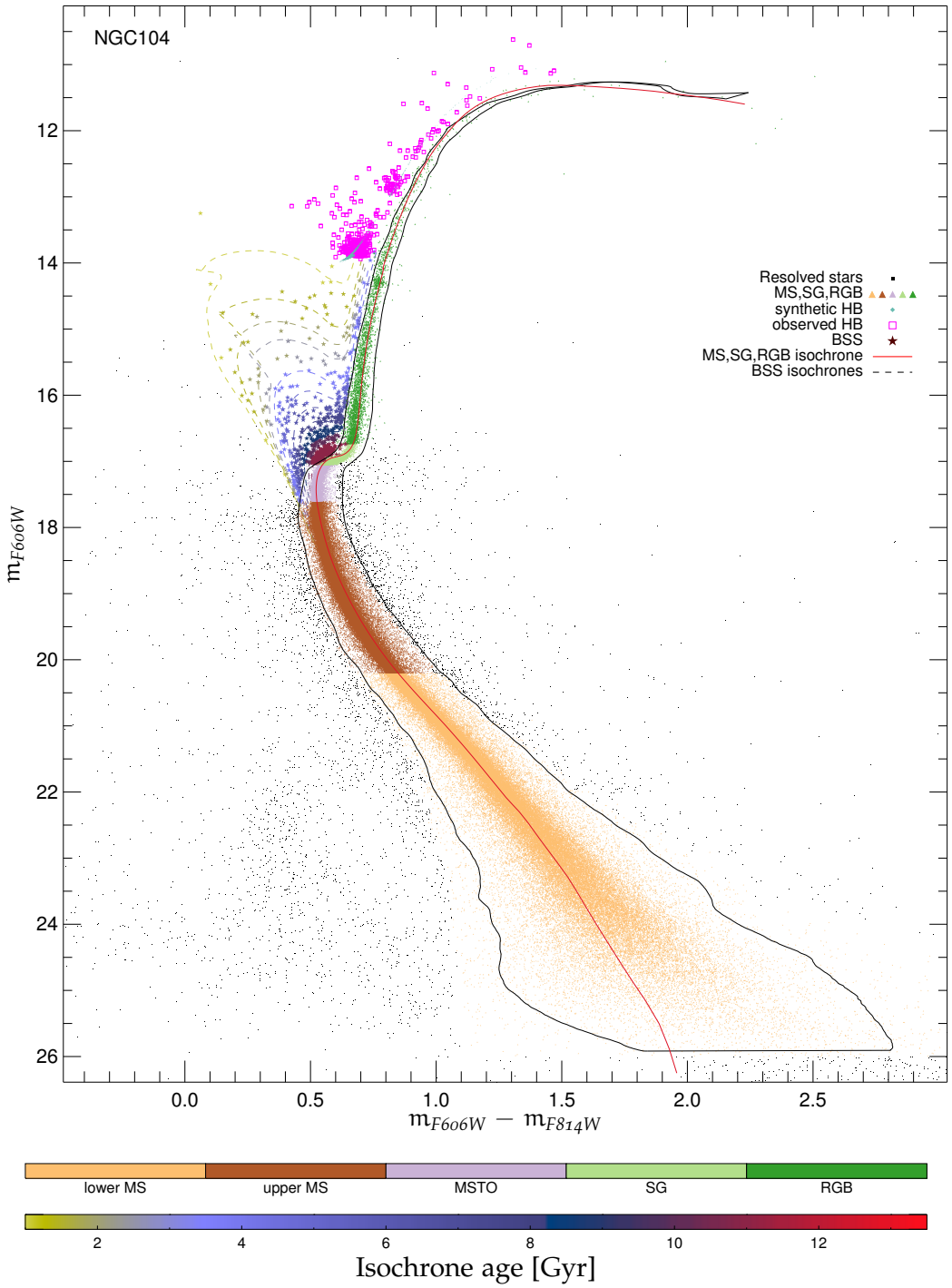

Figure 27: CMD of NGC104 based on *F606W* and *F814W* photometry from *HST/ACS* observations by Sarajedini et al. (2007). All stars that are projected onto the main isochrone are color-coded with light orange (LMS), brown (UMS), light purple (MSTO), light green (SG), and dark green (RGB; see the first color bar). The main cluster isochrone is overplotted with a solid curve, while the (accordingly younger) isochrones used to model the BSS population are plotted with dashed lines. The isochrone ages are color-coded as indicated by the second color bar (young ages are plotted in yellow, intermediate ages in blue, and old ages are plotted in red). BSSs are plotted with star symbols, and their color indicates on which isochrone (i.e., what age) they are projected. The synthetic HB population is plotted with cyan diamonds, while the observed HB stars are overplotted with magenta open squares. The shift direction of the synthetic HB is indicated by a black arrow, where the arrow head denotes the position after the shift (the arrow is only plotted if a shift was necessary). The plotted uncertainty bands around the main isochrone (solid black lines) have been obtained by transforming the limits of Equation 25 back to color-magnitude space. They have been strongly smoothed to enhance the clearness of the plot. As a consequence, stars that are included in the mapping and thus color-coded, can be found outside the error bands.

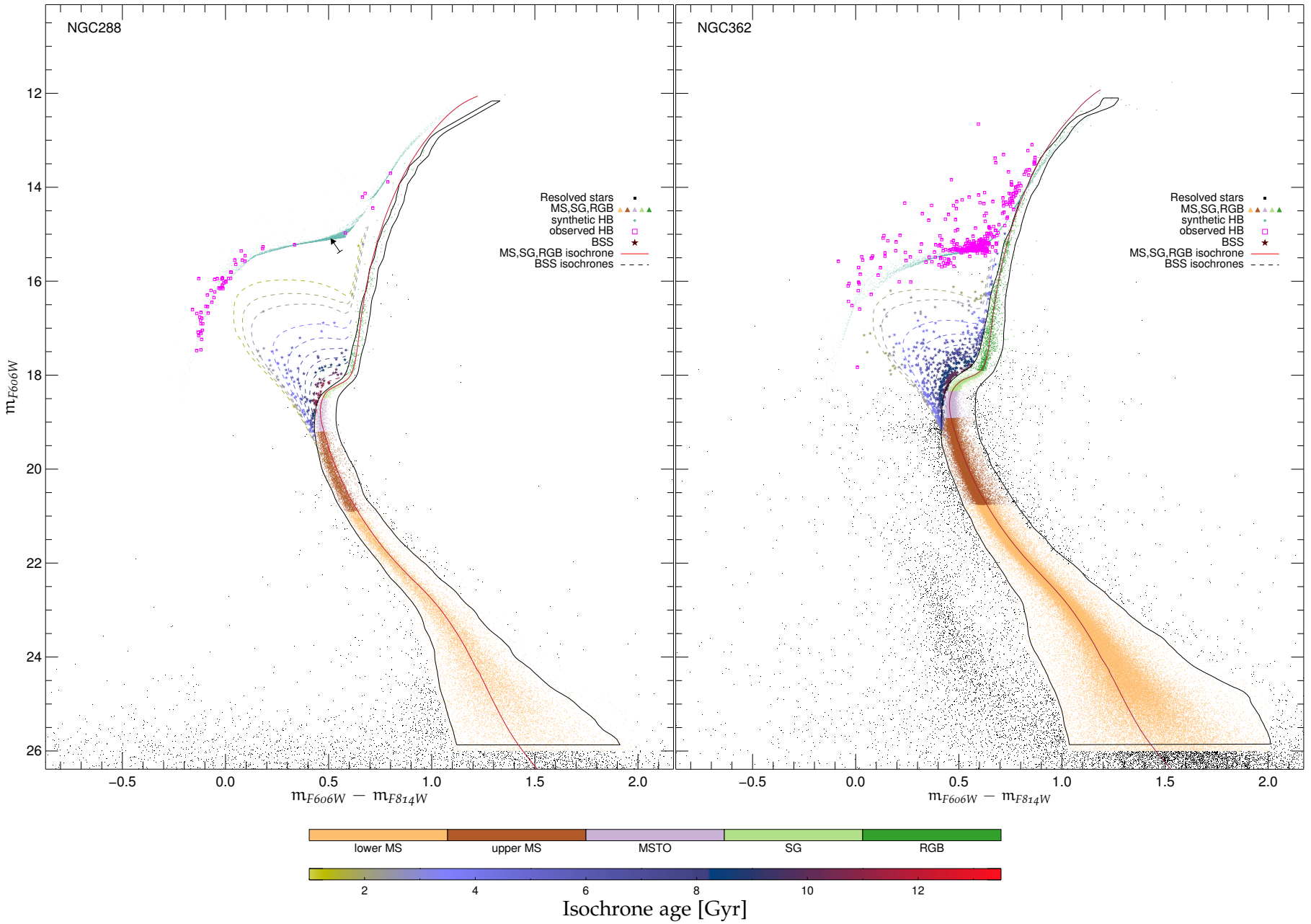

Figure 27 – Cont.: CMDs of NGC288 and NGC362.

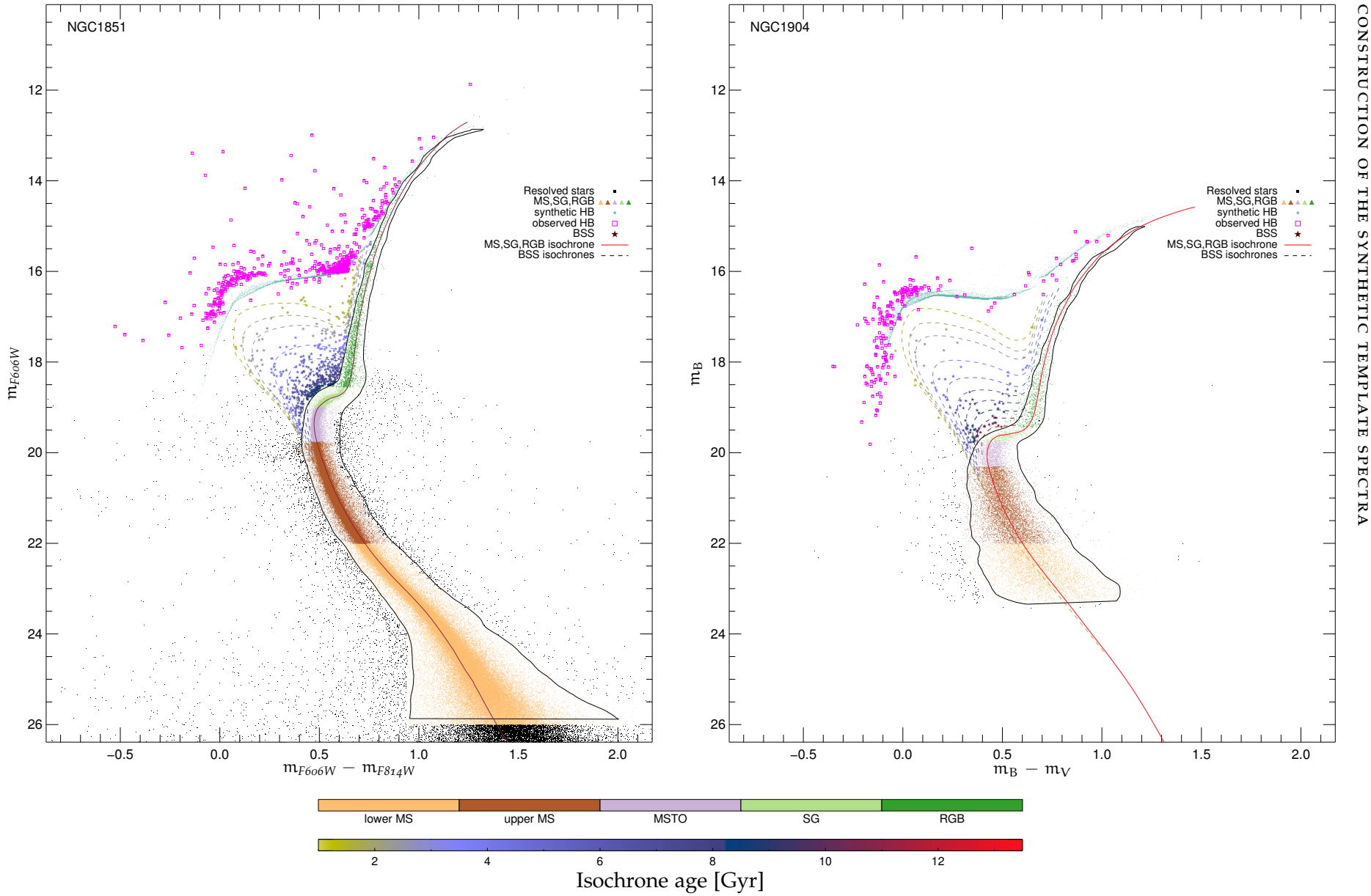

Figure 27 – Cont.: CMDs of NGC1851 and NGC1904. Note the different filters for NGC1904.

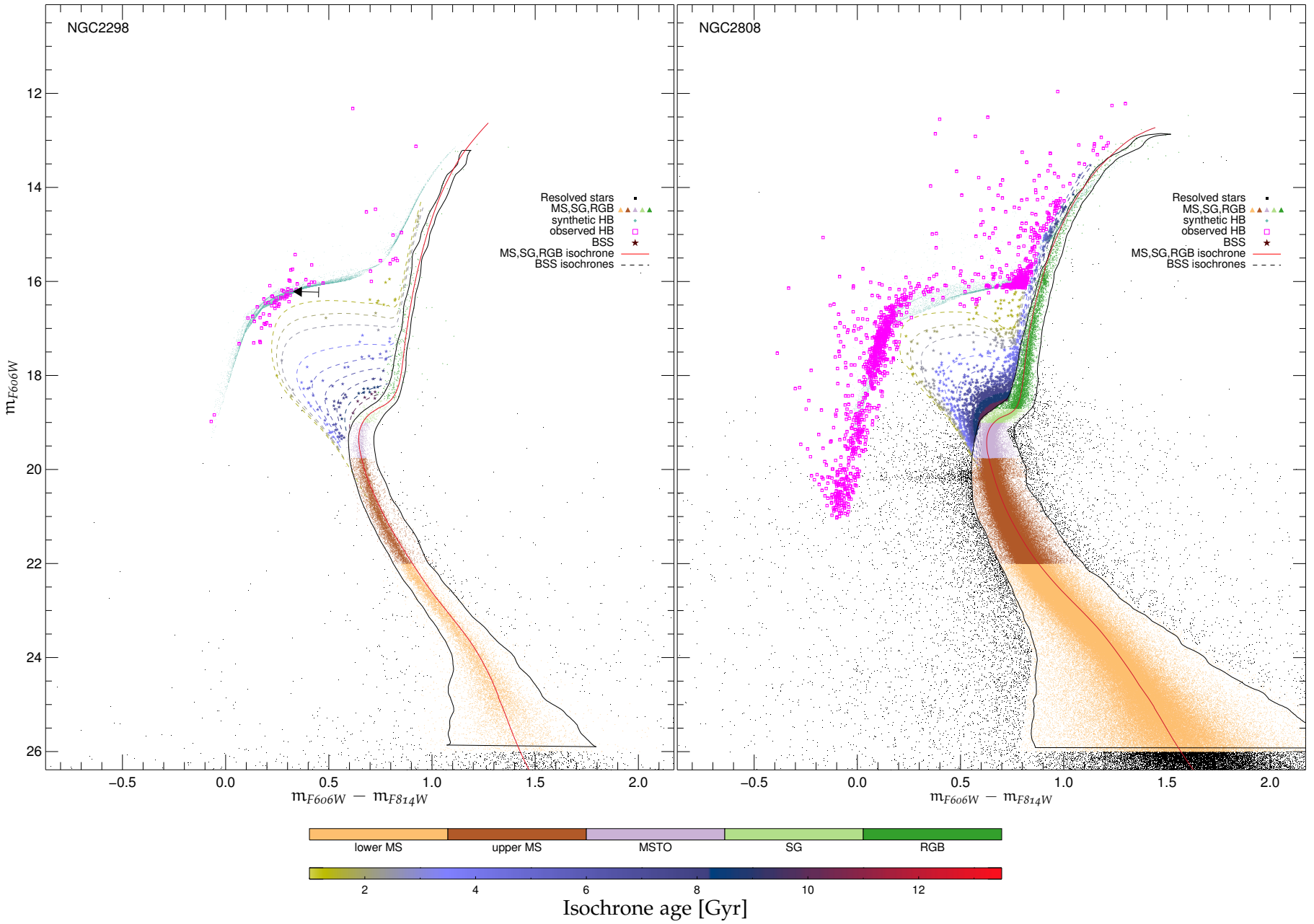

Figure 27 – Cont.: CMDs of NGC2298 and NGC2808.

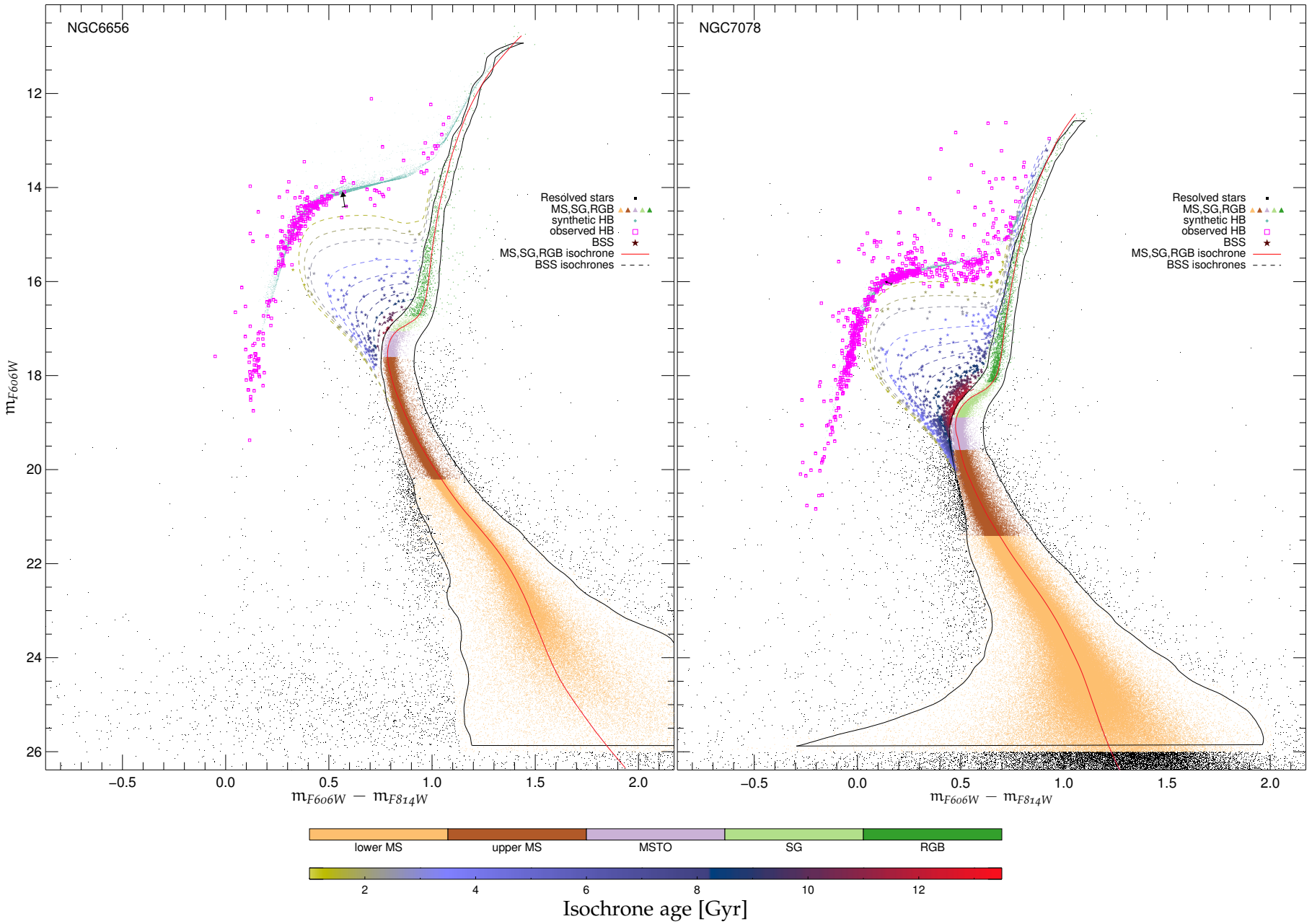

Figure 27 – Cont.: CMDs of NGC6656 and NGC7078.

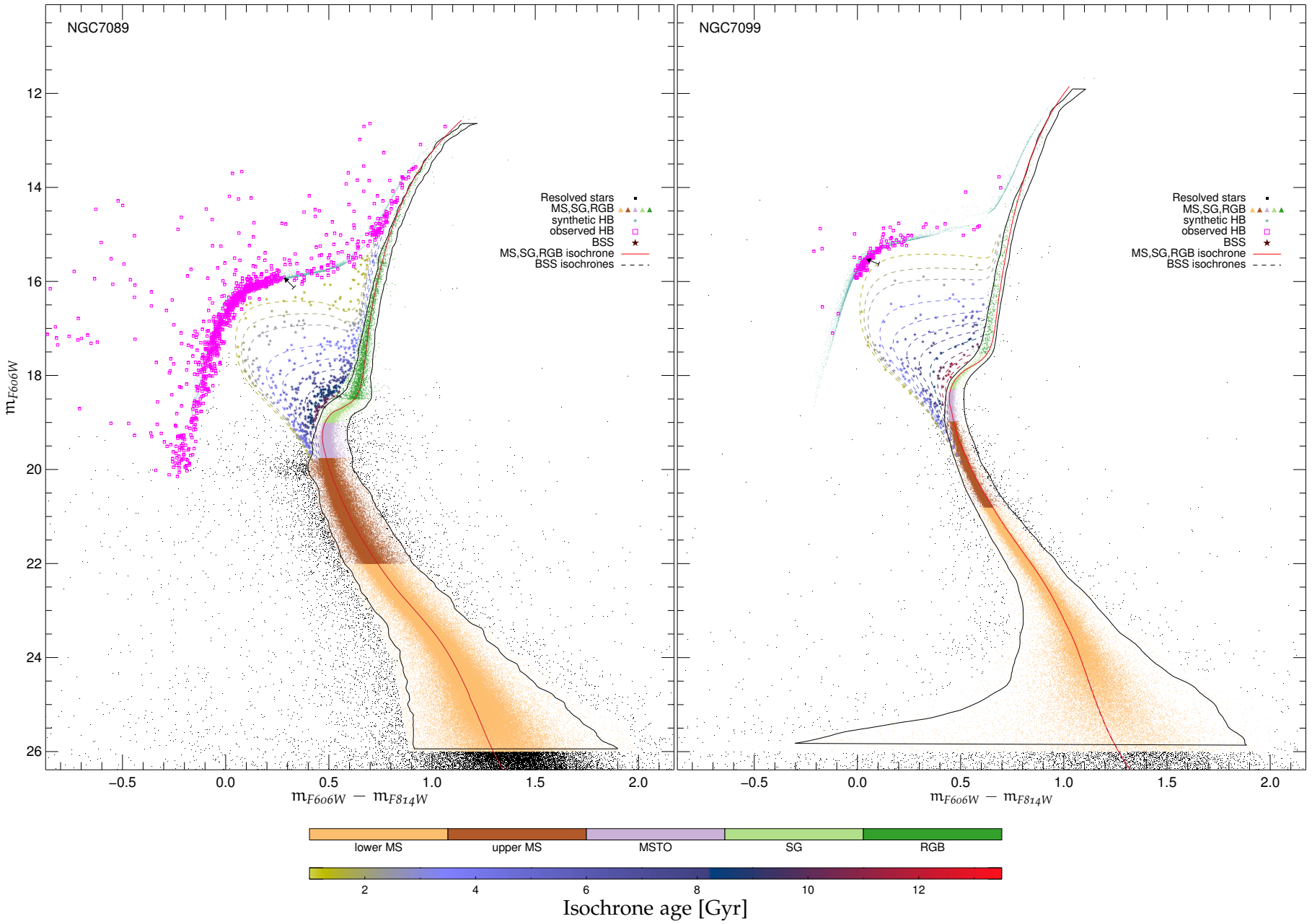

Figure 27 – Cont.: CMDs of NGC7089 and NGC7099.

4.6 HERTZSPRUNG-RUSSELL-DIAGRAMS OF GLOBULAR CLUSTERS

By mapping each star onto an appropriate model we can consistently transform the photometric data $\{m_{F606W}, m_{F606W-F814W}\}$ into the stellar parameters $\{T_{eff}, \log g\}$, which, in combination with [Fe/H] and $[\alpha/Fe]$ will be used to determine the stellar composition of our drift-scanned spectra. A diagram in which the surface gravity $\log g$ is plotted against the effective temperature T_{eff} is an alternative form of the *Hertzsprung-Russel-Diagram*[6] (HRD), which was first shown by Hertzsprung (1911) and later used independently by Russell (1913) to discriminate between *dwarf* and *giant* stars. They were among the first to notice that stellar formation and evolution imposes tight correlations between the various stellar parameters and thus observed stars occupy only very distinct locii in these diagrams (in this respect a CMD can be considered a special form of a HRD as well).

The application of the mapping procedure explained in Section 4.5 to the photometric data yields a distribution of stars in the HRD, with an underlying binning that reflects the bin sizes of the utilized isochrones / HB models. For the subsequent spectral synthesis, it is necessary to rebin the HRD to match the parameter stepping of the PHOENIX library ($\Delta T_{eff} = 100\,K$, $\Delta \log g = 0.5\,cm\,s^{-1}$). We implemented the rebinning with a two-dimensional histogram, whose bin sizes were adjusted to the required values. The obtained number density distribution $dN/(dT_{eff}\, d\log g)$ depends on various parameters, like the cluster's present day mass function (which itself is a function of the dynamical evolution of the cluster, with mass segregation leading to a preferred evopaporation of low-mass stars), the completeness of the photometric observation, the occurence of mass transfer onto BSS, the mass loss on the RGB, and probably additional effects that are not mentioned here.

Panel twelve of Figure 28 shows the stellar number density as a function of T_{eff} and $\log g$ (i.e., the number-weighted HRD) for NGC7078 within its half-light radius r_h[7]. The number of stars per bin is indicated by the color scale, running from $\sim 10^3$ (red) to less than one (blue). We note that for reasons of clarity we logarithmically rebinned the histogram along the T_{eff}-axis for the plots shown in Figure 28, and thus fractional values below unity can occur. In this way the dynamic range of the plot along the temperature-dimension is significantly increased and the detailed shape of the distribution for low temperatures is better visible. We also note that for the plots presented in Figure 28 the bin size along the gravity-axis has been reduced and is $d\log g = 0.05$. i.e., $10\times$ the PHOENIX resolution.

Panel twelve indicates that HB, BSS, and the tip of the RGB contain only very few stars (typically $\leqslant 10$ per bin). On the RGB this number slightly increases with increasing surface gravity and approaches ~ 100 per bin on the SG branch. The large majority of stars, however, occupies the narrow band of the MS, with a maximum number of ~ 3300 being located at $\log T_{eff} \approx 3.65$ (which, according to the utilized isochrone, corresponds to a mass of $m \approx 0.4\,M_\odot$). The drop-off to even lower temperatures is most likely a combination of

6 In this work we use Hertzsprung-Russel-Diagram and the $\{T_{eff}, \log g\}$-plane interchangeably

7 The half-light radius was chosen to obtain a well-sampled spatial average on the one hand, and to simplify the comparison between different clusters on the other hand.

photometric incompleteness and a possible decrease of the MF towards even lower $T_{\rm eff}$ (and thus even lower stellar masses). In this context it is interesting to note that Pasquali et al. (2004) find the characteristic mass m_c in a log-normal parametrization of NGC7078's MF, i.e.,

$$\frac{dN}{d\log(m)} = A - \left[\frac{\log(m/m_c)}{\sqrt{2}\sigma}\right]^2, \tag{26}$$

to be $m_c \approx 0.3\,M_\odot$, which is consistent with the distribution of stars in our number-weighted HRD, given the lack of completeness correction in the utilized data. We note in passing that our isochrone-mapping approach could—at least theoretically–be used to derive mass functions as well. For this, however, a detailed knowledge of the photometric completeness of the *HST/ACS* is fundamental. In the work presented here, we aim at modeling the spectral composition of our drift-scan spectra and thus we concentrate on those parts of the HRD that contribute most to the observed flux. As $L/L_\odot \propto (M/M_\odot)^3$ for MS stars in this mass range (Salaris & Cassisi 2005), the lower MS with its low-mass stars does not contribute significantly to the total flux and it is justified that no incompleteness correction is applied.

This assumption is further supported by the distribution of stars in the luminosity-weighted HRD, in which the number of stars per bin is multiplied by the stellar luminosity as predicted by the respective model, i.e. for the i-th temperature bin and the j-th gravity bin we obtain

$$\frac{dL_{ij}}{dT_{\rm eff,i}\ d\log\ g_j} = \frac{dN_{ij}}{dT_{\rm eff,i}\ d\log\ g_j} \times L^\star_{ij}, \tag{27}$$

where $L^\star_{ij}$ are the stellar luminosities for the $\{T_{{\rm eff}\,i}, \log\ g_j\}$-bin as predicted by the isochrones / synthetic HB-model. The luminosity-weighted HRD ($\equiv$ luminosity density as a function of $T_{\rm eff}$ and $\log\ g$) is a more useful representation of a cluster's stellar population since the weights now correspond to a directly observable quantity. Panels one to eleven of Figure 28 show the luminosity-weighted HRDs of our sample of eleven GCs and the total luminosity per $\{T_{{\rm eff}\,i}, \log\ g_j\}$-bin is color-coded as indicated by the color bar below the figure. Common to all clusters, the luminosity function in the HRD can be characterized qualitatively by showing almost neglible values for the LMS, followed by a gradual increase up to the MSTo. The luminosity along the SG phase is slightly reduced and rises again along the RGB. The local flux maximum at the MSTO arises from the multiplication of a high number of stars (see panel twelve) with an intermediate luminosity at this particular evolutionary phase. Although stars on the SG branch are intrinsically brighter (and cooler), their number density is decreasing too rapidly and so the overall luminosity weights gradually decrease. By contrast, RGB stars, although even less abundant, have individual luminosities that overcompensate for their low number and thus they dominate the overall light of the cluster (the luminosities per bin are comparable to the ones at the MSTO, however the RGB occupies more bins in the HRD). Towards the tip of the RGB the stochastic flux variations between adjacent bins become considerable. It is worth noting that some bins are entirely empty despite the relatively large area sampled for each GC (inside its half-light radius). This scatter is the combined effect of the very low number of

RGB stars and the high luminosity that each of these stars emits. In this region of the HRD, non-empty bins are typically occupied by single stars only, however these giants can emit $\sim 10^3\,L_\odot$ and thus account for a significant fraction of the cluster's total light budget. Due to the shape of the mass function (MF), however, the specific number density of these stars approaches zero close to the tip of the RGB and thus one naturally expects the luminosity weighted data to scatter between zero (empty bin) and its maximum values (bin occupied by a single giant star). As our drift-scans sample relatively small fractions of a GC's area on the sky, we have to pay particular attention to the exact (projected) position of each star within the cluster in order to model the stellar population correctly. The impact of individual bright stars on the composite spectrum will be further discussed in Chapter 5. Stars on the HB are comparable in number to stars on the RGB, however they are hotter on the one hand, but less luminous on the other hand. It is therefore expected that they do not dominate the clusters' total light, yet contribute substantially to the blue part of the composite light. The individual luminosities per bin for the BSS population are comparable to the ones for the lower MS, although the BSSs typically occupy more bins, which in turn produces a higher flux output. A more quantitative analysis of the individual contributions to the composite GC spectrum will be presented in the next section.

4.7 SYNTHETIC COMPOSITE SPECTRA

While the descriptions presented in Section 4.6 are merely a qualitative, yet instructive characterization of the different flux contributions, a quantitative analysis requires a detailed consideration of the various spectral shapes associated with the different evolutionary phases. While indeed the RGB is typically the dominant component in the total bolometric luminosity of a GC, its quantitative contribution depends on the spectral range of interest. According to Wien's law (e.g., Carroll & Ostlie 1996), the SED of a cool RGB star with $T_{\rm eff} \sim 4,000\,K$ peaks at $\sim 7,200\,Å$, MSTO stars with typical temperatures of $\sim 6,500\,K$ have their maximum intensity at $\sim 4500\,Å$, and hot HB members with $T_{\rm eff} \sim 10,000\,K$ produce their peak at $\sim 2,900\,Å$[8]. Thus, each part of the HRD not only contributes with its specific luminosity weight, but distributes this weight according to the spectral shape of the corresponding spectrum. In order to compute the synthetic composite spectrum for the eleven GCs presented here, we draw for each $\{T_{\rm eff}, \log\, g\}$-bin the appropriate PHOENIX spectrum and scale it to the overall flux level as determined by the luminosity weight of the respective bin. PHOENIX spectra are already flux-calibrated, which requires that each spectrum is first scaled to the solar bolometric luminosity before it can be multiplied by the corresponding luminosity from the HRD. This is achieved by normalizing the spectrum relative to its total flux and then multiplying it by $L_\odot$, i.e.,

$$F_\lambda^{out} = \frac{F_\lambda^{in}}{\sum_\lambda F_\lambda^{in}} \times L_\odot, \tag{28}$$

8 It should be noted that the deviation of a stellar atmosphere from an ideal black body can be significant, and hence the validity of Wien's law for stars is only approximate

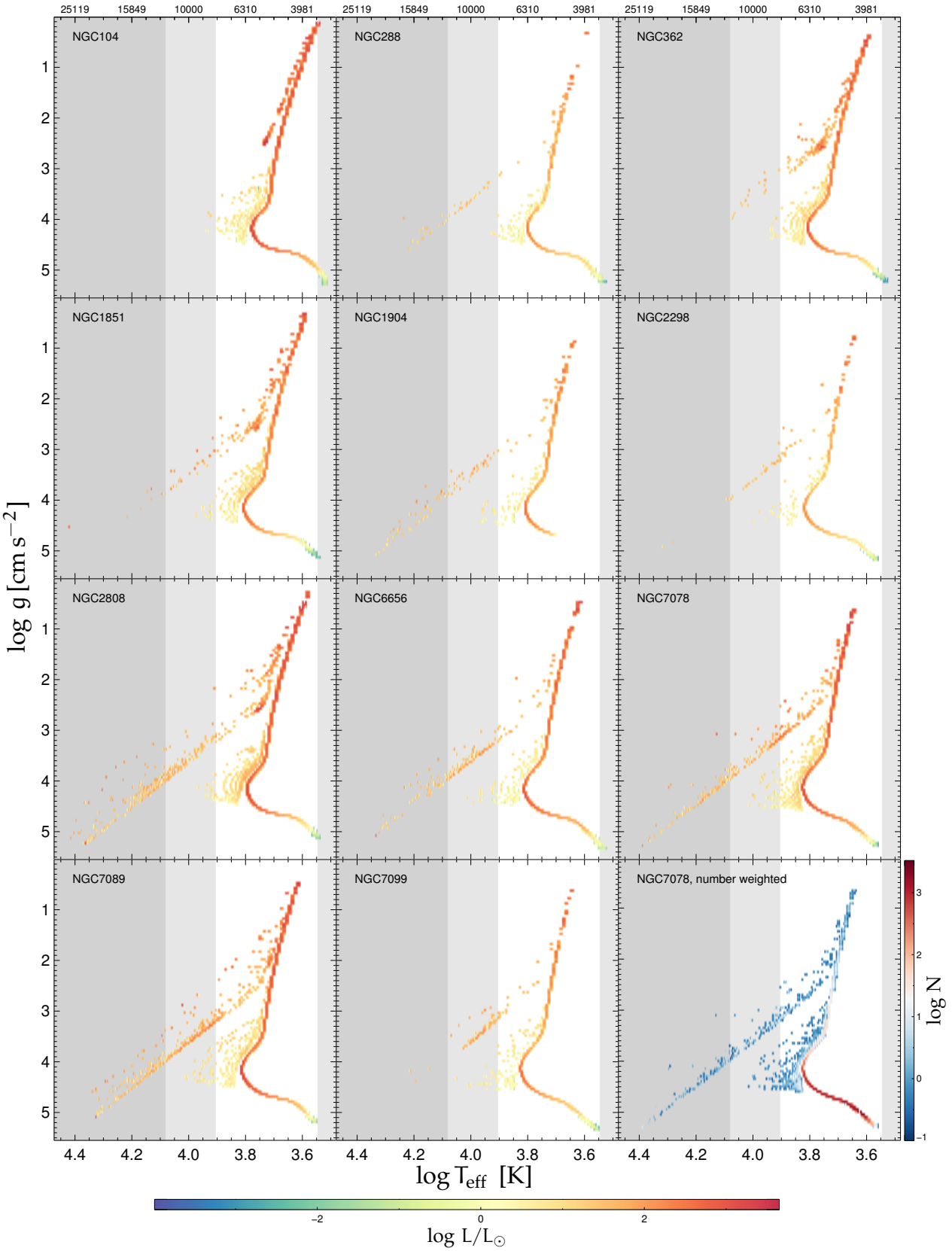

Figure 28: Panels one to eleven: luminosity-weighted HRDs for our sample of eleven GCs. Panel twelve: number-weighted HRD for NGC7078. The color-coding indicates the weights of each $\{T_{\rm eff}, \log g\}$-bin (see horizontal color bar for the luminosity-weighted HRDs and vertical color bar for the number-weighted HRD, respectively). The photometric data underlying the HRDs are the CMDs plotted in Figure 27. The plotted bin sizes are $dT_{\rm eff} = 100\,K$ and $d\log g = 0.05$, respectively. Effective temperatures for which no α-enhanced PHOENIX spectra are available are shaded with light grey. The region with $T_{\rm eff} > 12,000\,K$ is shaded with dark gray. Here, no PHOENIX spectra are available and stars in this area need to be modeled with $T_{\rm eff} = 12,000\,K$. We note that the HRDs have been logarithmically rebinned along the $T_{\rm eff}$-axis for visibility reasons.

where $F_\lambda^{in,out}$ denote the fluxes in each spectral bin. A spectrum scaled in this way can be multiplied by the respective luminosity weight without any further considerations. Constructing a luminosity-weighted spectrum for all $\{T_{eff}, \log\ g\}$-bins and integrating over the HRD eventually yields the synthetic composite spectrum.

The total synthetic composite spectra (integrated over the complete HRDs) for our sample of eleven GCs are plotted in in Figure 29 (black curves). The contributions of the individual evolutionary phases, obtained by integrating the HRD over the respective subregions that correspond to the individual phases in the CMDs (see Figure 27), are overplotted with various colors. It should be noted that the total composite spectrum of each cluster has been normalized so that $\max\left\{F_\lambda^{tot}\right\} = 1$. Furthermore, the flux of each wavelength bin in the total composite spectrum always corresponds the sum of the flux of all individual phases.

For most clusters the RGB dominates the entire spectral range between 3,000 Å and 10,000 Å. For NGC1851, NGC1904, NGC2808, and NGC7089, however, the HB contribution can be stronger than the RGB component for $\lambda \leqslant 4,000$ Å. The LMS generally shows a similar continuum shape as the RGB, although the overall flux level is lower by a factor $10^{-2} - 10^{-3}$. This is expected as they both share roughly similar effective temperatures, but differ significantly in log g (and thus the total luminosity). For most clusters, the HB is the second dominant component in the global spectrum, with UMS and MSTO coming next in the ranking order. The SG phase and BSSs are typically less luminous and the LMS generally is the faintest component in the composite spectra. NGC6656 is an exception to this ordering, as both MS components are significantly enhanced and the UMS is even the second strongest contributor. NGC288 shows a similar tendency, although less pronounced. The last panel of Figure 29 is a close-up of the spectral region between 3,800 Å and 4,000 Å for NGC6656 and nicely illustrates how the actual composition of the total spectrum depends on the spectral lines of interest. The wings of the three prominent Balmer lines H_ϵ ($\lambda\lambda$ 3970), H_ζ ($\lambda\lambda$ 3888), H_η ($\lambda\lambda$ 3835) are mostly produced by the hot HB population, while the cores rather reflect the line shapes of the UMS and RGB. The Ca II doublet ($\lambda\lambda$ 3935, $\lambda\lambda$ 3968) is almost inexistent in the HB spectrum, but it is stronger than the Balmer series for the UMS and RGB. This is expected, as Ca II is generally the strongest for G-type stars (which roughly corresponds to the spectral type around the MSTO), whereas the strength of the Balmer series correlates with the effective temperature, and thus is expected to be most pronounced for BSS and HB members (Gray & Corbally 2009). Quantitatively decoding the contributions of the various evolutionary phases to the full set of spectral lines would require a comprehensive statistical analysis, which is beyond the scope of this thesis. Nevertheless, with the presented estimates for the relative strengths of each phase such an analysis seems possible and worthwhile to be pursued in a subsequent project.

To provide the reader with practical numbers, we convolved the spectra shown in Figure 29 with the U, B, V, R, I filters of the Johnson-Cousins system (Johnson & Morgan 1953;

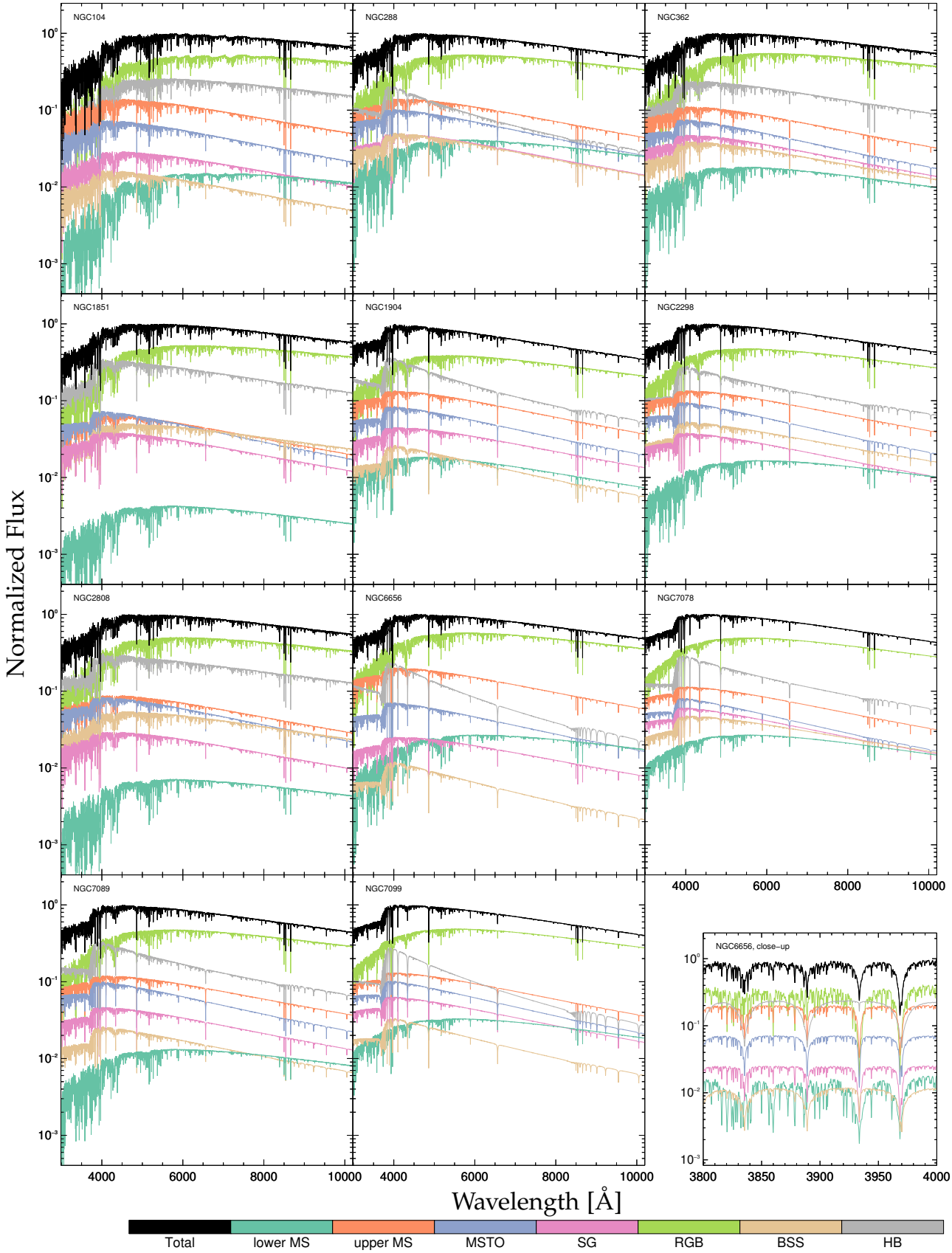

Figure 29: Synthetic composite spectra of our sample of eleven GCs, integrated over the respective half-light radius. The cumulative spectra, integrated over the full HRDs, are plotted in black and the contributions of the individual evolutionary phases are overplotted with various colors (as indicated by the color bar on the bottom). The spectra have been normalized so that the maximum flux in each cumulative spectrum corresponds to one. The spectral range and resolution correspond to the ones of X-SHOOTER's UVB and VIS arms. Panel twelve shows a close-up of the spectral range $3,800\,\text{Å} - 4,000\,\text{Å}$ for NGC6656 and illustrates the impact of the individual evolutionary phases on the formation of different spectral features.

Cousins 1974), and computed the relative flux contributions of the evolutionary phases to the total flux for each filter, i.e.,

$$\frac{\int F_{phase,\lambda}\, T_\lambda\, d\lambda}{\int F_{tot,\lambda}\, T_\lambda\, d\lambda}, \tag{29}$$

where $F_{phase,\lambda}$ and $F_{tot,\lambda}$ denote the spectral fluxes of a single evolutionary phase and the total composite spectrum, respectively, and T_λ is the transmission function of the filter. The obtained values are listed in Table 6. We also computed the luminosity-weighted averages for the stellar parameters T_{eff} and $\log g$ for each evolutionary phase, and present them in Table 7.

As a consistency check we plot the average effective temperature of stars at the MSTO as a function of [Fe/H] (taken from Harris 2010) in Figure 30. The evident linear trend is reassuring, as it corresponds to the well-known anti-correlation between metallicity and temperature (e.g., Sparke & Gallagher 2007): metals increase the opacity of a stellar atmosphere and thus metal-rich stars are both fainter and redder. In this context it should be noted that the values presented in Table 7 are merely meant to give a realistic overview of the range of stellar parameters occuring in Galactic GCs. These average values, obtained by integrating over the half-light radius, are not used in our analysis, since we construct the template on a per-slit-bin basis and thus consider the stellar parameters of each contributing star individually.

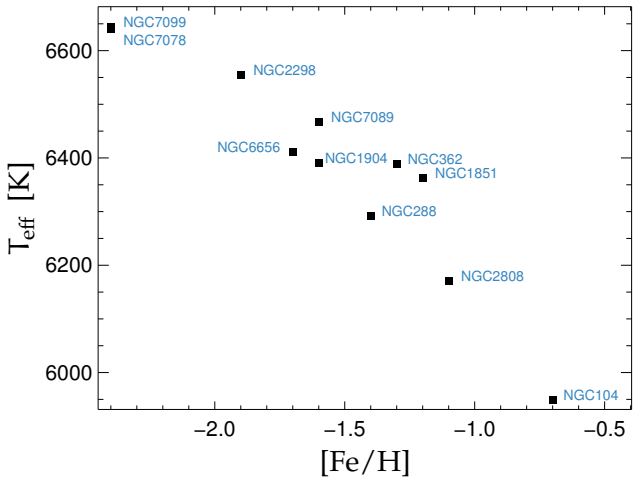

Figure 30: Average effective temperature of stars at the MSTO versus average metallicity from Harris (2010).

The results listed in Table 6 show that, independently of cluster metallicity, the RGB typically contributes between ~ 30% (U) and ~ 65% (I), while the HB influence ranges from almost ~ 40% (U; NGC1851) down to ~ 5% (I; NGC6656).

The contributions for BSS and SG are $\lesssim$ 5%, MSTO $\lesssim$ 10% (with the exception of NGC6656 for which the fraction is $\lesssim$ 25%), and UMS $\lesssim$ 15%. It is interesting to note that these contributions typically decrease by a factor of two from the U to the I band,

GC	Filter	LMS	UMS	MSTO	SG	RGB	BSS	HB
NGC104	U	0.7	24.3	14.2	5.1	27.6	2.8	25.2
	B	1.1	17.7	9.7	3.7	39.0	2.1	26.6
	V	1.3	13.5	6.7	2.8	47.8	1.5	26.4
	R	1.6	11.2	5.2	2.3	52.9	1.2	25.6
	I	1.7	9.3	4.1	1.9	57.8	0.9	24.3
NGC2808	U	0.5	13.1	12.6	4.3	29.8	6.2	33.6
	B	0.6	9.9	9.4	3.3	38.6	5.8	32.4
	V	0.7	8.2	7.1	2.7	49.3	5.3	26.7
	R	0.8	7.1	5.9	2.4	54.1	4.9	24.9
	I	0.8	6.2	4.9	2.1	57.5	4.6	23.8
NGC1851	U	0.3	10.4	11.2	6.0	28.3	5.9	38.0
	B	0.4	7.4	8.2	4.4	37.3	5.4	37.0
	V	0.4	5.8	5.8	3.5	49.9	4.9	29.7
	R	0.4	4.9	4.7	3.0	56.0	4.6	26.4
	I	0.4	4.2	3.8	2.5	60.6	4.3	24.1
NGC362	U	1.7	17.1	10.7	7.0	32.2	5.0	26.3
	B	1.7	12.6	8.4	5.4	41.5	4.3	26.2
	V	1.8	9.7	5.9	4.1	53.3	3.4	21.7
	R	1.9	8.3	4.8	3.5	59.1	3.0	19.5
	I	1.9	7.1	4.0	3.0	63.6	2.6	17.8
NGC288	U	3.0	19.0	13.4	6.5	32.8	5.9	19.3
	B	3.4	15.1	10.9	5.3	41.4	5.3	18.7
	V	4.1	13.1	8.6	4.4	53.9	4.3	11.5
	R	4.7	11.7	7.4	3.9	59.9	3.8	8.7
	I	5.0	10.5	6.3	3.4	64.6	3.3	6.9
NGC7089	U	0.9	16.0	12.4	6.0	32.5	2.8	29.5
	B	1.0	12.6	10.2	4.9	38.3	2.6	30.4
	V	1.4	11.3	8.2	4.2	50.8	2.2	22.0
	R	1.6	10.4	7.0	3.8	56.8	1.9	18.5
	I	1.7	9.5	6.0	3.4	61.4	1.7	16.2
NGC1904	U	2.1	17.3	9.9	5.5	30.6	2.6	31.9
	B	1.9	14.3	8.7	4.8	35.0	2.6	32.7
	V	2.1	13.5	7.7	4.6	46.5	2.2	23.3
	R	2.2	12.7	7.1	4.5	52.2	2.0	19.3
	I	2.2	11.9	6.4	4.2	56.8	1.8	16.6
NGC6656	U	1.6	26.6	8.7	3.3	38.4	1.2	20.3
	B	2.0	21.2	7.2	2.7	45.7	1.2	20.0
	V	2.7	18.0	5.7	2.3	59.1	0.8	11.4
	R	3.1	16.0	4.8	2.1	65.4	0.7	8.0
	I	3.4	14.2	4.1	1.9	70.1	0.5	5.8
NGC2298	U	1.2	18.0	11.2	4.8	37.0	5.5	22.3
	B	1.3	14.0	9.4	3.9	40.5	5.3	25.6
	V	1.7	12.3	7.5	3.3	50.9	4.6	19.6
	R	2.0	11.3	6.4	3.0	55.8	4.3	17.2
	I	2.2	10.3	5.6	2.7	59.6	4.0	15.7
NGC7099	U	2.9	16.8	11.3	7.4	39.2	3.2	19.2
	B	2.9	13.2	9.8	6.3	42.4	3.1	22.3
	V	3.6	11.9	8.1	5.5	54.1	2.4	14.3
	R	4.1	11.0	7.0	5.0	60.3	2.0	10.6
	I	4.4	10.0	6.1	4.5	65.2	1.7	8.0
NGC7078	U	2.4	14.5	8.8	7.0	39.3	4.9	23.0
	B	2.4	11.4	7.7	6.0	42.7	4.7	25.2
	V	2.9	10.1	6.2	5.1	52.7	4.3	18.8
	R	3.1	9.1	5.3	4.5	57.8	4.1	16.0
	I	3.3	8.3	4.5	4.0	61.8	3.9	14.2

Table 6: Flux contribution per evolutionary phase. All values are given in percent. The ranking order is from the highest (top; $[Fe/H] = -0.7$) to lowest (bottom;$[Fe/H] = -2.4$) metallicity.

GC	LMS		UMS		MSTO		SG		RGB		BSS		HB	
	$\langle T_{eff} \rangle$	$\langle \log g \rangle$	$\langle T_{eff} \rangle$	$\langle \log g \rangle$	$\langle T_{eff} \rangle$	$\langle \log g \rangle$	$\langle T_{eff} \rangle$	$\langle \log g \rangle$	$\langle T_{eff} \rangle$	$\langle \log g \rangle$	$\langle T_{eff} \rangle$	$\langle \log g \rangle$	$\langle T_{eff} \rangle$	$\langle \log g \rangle$
NGC104	4181	4.73	5592	4.47	5949	4.15	5573	3.90	4242	2.50	5920	3.82	4766	2.19
NGC2808	4584	4.72	5833	4.47	6170	4.16	5748	3.84	4512	2.53	5405	3.57	7261	3.96
NGC1851	4683	4.72	5968	4.47	6363	4.17	5866	3.82	4403	2.35	5431	3.52	6370	3.13
NGC362	4899	4.71	6063	4.45	6388	4.17	6016	3.89	4497	2.42	5952	3.80	5670	2.58
NGC288	4687	4.73	5920	4.48	6292	4.21	6007	3.93	4591	2.38	6131	3.93	9704	3.86
NGC7089	4644	4.77	5990	4.51	6467	4.20	6088	3.87	4710	2.49	6345	3.74	8572	3.88
NGC1904	5488	4.64	6175	4.41	6391	4.15	5967	3.84	4891	2.64	6683	3.94	9979	3.93
NGC6656	4552	4.81	6091	4.46	6410	4.08	5908	3.77	4693	2.48	7055	4.05	11015	4.23
NGC2298	4700	4.80	6118	4.49	6555	4.16	6161	3.85	4820	2.40	6090	3.73	7089	3.38
NGC7099	4955	4.80	6220	4.48	6643	4.19	6246	3.85	4858	2.34	7077	4.00	8717	3.39
NGC7078	5000	4.79	6202	4.49	6641	4.20	6275	3.86	4861	2.38	5936	3.73	8081	3.74

Table 7: Average stellar parameters T_{eff} [K] and $\log g$ [$cm\,s^{-2}$] per evolutionary phase. The values denote luminosity-weighted averages over all stars in the respective phase.

owing to the comparably hot stellar atmospheres in these evolutionary stages. The LMS shows contributions between $\sim$ 1% and 5 $\sim$ %, and has the highest impact in the I band due to its cool atmospheres. We do not provide any errors on the presented numbers, since a meaningful assessment of the uncertainties would require a more comprehensive treatment of the photometric data. These uncertainties could be possibly computed by using a grid of different ischrones spanning a suitable range in age, metallicity and α-abundance. Each cluster should then be mapped onto each isochrone separately, or, if the cluster is suspected to harbor multiple stellar populations, simultaneously onto a number of appropriately chosen isochrones reflecting the properties of the underlying populations. The uncertainties on the luminosity weights would then follow from the scatter of the assigned values between the different models and can be propagated in the resulting composite spectrum with Monte Carlo methods. Furthermore, a sophisticated approach to deal with stars in binary systems (e.g., like the one presented by Ji & Bregman 2013, who fit the distribution of MS stars in the CMD with multiple models) would be required to obtain a better accuracy especially for the MS contributions, and, lastly, a detailed correction for differential reddening would be desirable. Nevertheless, the templates and the resulting flux fractions presented here are based on actual star counts and supposed to reflect the stellar populations in our sample of GCs to a degree that is unmatched in previous velocity dispersion measurements, where typically only single templates of single RGB stars are used.

In Figure 31 we plot the BSS fraction against the combined fraction of all MS stars (LMS + UMS + MSTO). The plot sugggests a linear anti-correlation, such that low MS contributions lead to a relative enhancement in BSS flux. Interestingly, combinations of a low MS fraction and a low BSS (lower triangle in Figure 31) are avoided, however two clusters (NGC2298 and NGC288) are found in the upper triangle, thus showing an excess of BSS light with respect to the hypothetical anti-correlation found for the other clusters

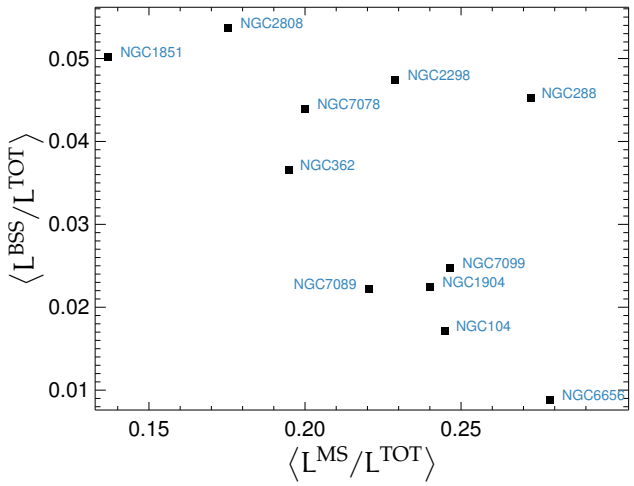

Figure 31: BSS flux contribution versus combined MS (LMS + UMS + MSTO) contribution. The plotted values are the average contributions over all filters (U, B, V, R, I).

in our sample. Any conclusions, however, remain speculative, since the plotted data are likely affected by a number of different systematics that have not yet been accounted for. In particular, the photometric incompleteness of the *HST/ACS* data increases with decreasing stellar luminosity, and, hence, it should be greater for MS members than for BSS. Additionally, we expect the incompleteness to show a dependence on stellar density (i.e., crowding, where faint stars are blended with bright stars), and thus it should correlate with both radial distance from the cluster's center and angular extent of the cluster on the sky. More compact clusters should therefore be biased against small MS flux contributions and NGC1851 (highest central stellar density $\rho_0 \approx 10^{5.1}\,L_\odot\,pc^{-3}$ and smallest angular diameter on the sky in our sample, values taken from Harris 2010) might be potentially affected by this observational bias. This speculation is further supported by the direction of the two outliers,i.e., enhanced MS contribution at fixed BSS flux: both NGC288 ($\rho_0 \approx 10^2\,L_\odot\,pc^{-3}$) and NGC2298 ($\rho_0 \approx 10^3\,L_\odot\,pc^{-3}$) have central densities that are significantly smaller than the sample average ($\rho_0 \approx 10^{4.5}\,L_\odot\,pc^{-3}$), and thus we expect a higher detection rate of faint objects for these clusters. On the other hand, NGC104 and NGC7099 ($\rho_0 \approx 10^5\,L_\odot\,pc^{-3}$) show similarly high MS contributions as NGC288 and NGC2298, but significantly lower BSS flux fractions, and so the picture remains inclusive. This topic will need to be addressed in a follow-up investigation.

Figure 32 shows the dependence of the MS and HB contributions in the B-band on the clusters' half-light radius. In both panels there are indications for linear correlations, however caution has to be exercised again for any interpretation, since the same systematics as explained above for Figure 31 apply. The left panel of Figure 32 suggests an increase of the MS flux fraction with increasing cluster size, with three potential outliers (NGC362, NGC1904, and NGC7099), which show a relative enhancement of MS contribution to the total flux. Surprisingly, the lower triangle of the plot remains empty. If the linear correlation is real, this seems unexpected as the MS contribution should rather be underestimated

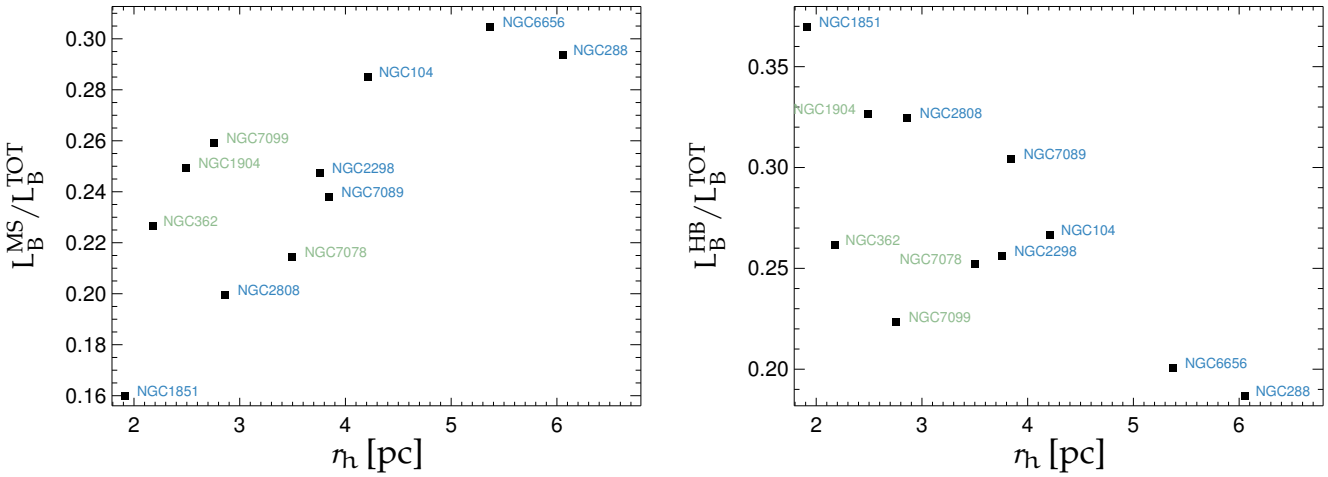

Figure 32: *Left:* B-band flux fraction of MS stars (LMS + UMS + MSO) versus GC half-light radius. *Right:* B-band flux fraction of the HB population versus GC half-light radius. The names of core-collapsed clusters are highlighted in green (NGC362, NGC1904, NGC7078, NGC7099). Information about core-collapse and half-light radii are taken from Harris (2010).

for small radii. Interestingly, all three outliers (as well as NGC7078) from the hypothetical linear sequence have undergone core collapse at least once in their lifetimes (see Harris 2010, and references therein) and thus their structural parameters and / or stellar populations might be different from pre-core-collapse clusters. Yet, this would not explain why NGC7078 falls in line almost perfectly with the other clusters, despite being very similar to NGC7099 (similar central densities, central concentrations, and projected half-light radii on the sky, however $m_V^{NGC7078} = 6.2$, $m_V^{NGC7099} = 7.2$, and $L_V^{NGC7078} \approx 5\, L_V^{NGC7099}$; thus, NGC7099 is expected to suffer from a greater photometric incompleteness and the MS flux contribution should be accordingly lower). Furthermore, NGC1904 is the only cluster in our sample for which the significantly less deep *HST/WFPC2* data have been used to compute the luminosity weights. Supported by the MS cut-off as shown in panel 5 of Figure 28, we would expect this cluster to show a depletion rather than an enhancement in MS luminosity, although it has to be said that its MSTO and UMS (contributing most to the total MS flux) are still well sampled by the observational data. Since any argument put forward, however, is merely speculative, meaningful conclusions can only be drawn if observational biases are properly addressed and the sample size extended. At least the latter can be possibly achieved without significant additional expenses, as the *HST/ACS* GC data set comprises a total of 65 clusters (Sarajedini et al. 2007). Since our code is also ready to handle *HST/WFPC2* observations, the snapshot data set of Piotto et al. (2002) with a total of 74 GCs can be potentially included as well, although any incompleteness issues are expected to be more significant for these observations. The interpretation of the right panel of Figure 32, where we plot the HB flux contribution as function of half-light radius, has to be viewed in the same context. Similar to the left panel, all clusters

that deviate significantly from the hypothetical linear trend are core-collapse clusters and the direction of scatter seems counter-intuitive if photometric incompleteness is the only cause for the observed trend. If both the suggested negative correlation between HB flux and cluster size and the positive correlation between MS contribution and cluster size, respectively, still hold after incompleteness issues have been properly accounted for and more clusters included in the analysis, then detailed numerical studies seem to be the tool of choice to address this intriguing relation, which could hint at previously undetected effects in a cluster's internal and / or external dynamical evolution.

Despite all uncertainties inherent to the values presented in Table 6, they should still be readily usable in a number of different astrophysical applications. As stated above, many integrated-light velocity dispersion measurements in the past relied on an exclusive usage of RGB-type templates, implying that the specific line-shape (as determined by $T_{\rm eff}$ and log g) of cool giants is used as reference to compute the Doppler-broadening of the entire stellar population. Although it may be true that many of these studies have used the Calcium II triplet at $\lambda \approx 8500$ Å, where the RGB component dominates the composite spectrum, our analysis suggests that in this band still $\sim 40\%$ is emitted by significantly hotter and denser stars with considerably broader lines (compare panel twelve in Figure 29). Consequently, in dispersion measurements of extragalactic GCs, for which the stellar population cannot be resolved into individual stars, the flux fractions presented in Table 6 can be used to improve the quality of the reference template spectrum, by combining a set of appropriately scaled spectra reflecting the various evolutionary phases (with stellar parameters similar to the ones presented in Table 7). A potential second application is related to extragalactic GCs for which only the brightest stars can still be individually resolved. If the fluxes of the RGB and potentially of the HB are known, the values given in Table 6 can be used to roughly estimate the flux contributions of the remaining phases. We plan to extend Table 6 to include GCs spanning more ages and chemical compositions in the near future. Additionally, when the photometric incompleteness of each cluster is properly accounted for, individual values will become more meaningful and the table can be used to analyze the relative flux contributions for previously undetected correlations in a statistical way.

4.8 A MODEL FOR X-SHOOTER'S LINE SPREAD FUNCTION

Measuring the velocity dispersion based on the Doppler-broadening of spectral lines of integrated-light spectra requires a detailed understanding of the instrumental line spread function (LSF). It is important that the line width of the template spectrum resembles that of the hypothetical non-velocity broadened data as close as possible, so that any measured broadening component can be attributed to the motion of stars in the GC. By contrast, dispersion estimates based on the radial velocity distribution of individual, resolved stars are free from any systematics arising from potential deficits in the modeling of the LSF (both instrumentally and physically due to the atmosphere of a template star), as only the centroid of a line (or of a number of lines) is used to derive the radial velocity shift of the observed data. In Sections 4.5 – 4.7 we have presented the approach with which

we model the integrated-light composite spectra of our sample of eleven GCs, with detailed focus paid to a realistic consideration of the underlying stellar populations. This section will cover the effects that X-SHOOTER's finite resolution has on the measured spectral line-widths. Since we do not use observed X-SHOOTER spectra as spectral templates in the velocity dispersion measurements, it becomes necessary to bring the synthetic templates from R$\sim$100,000 (PHOENIX resolution) to R$\sim$10,000 (X-SHOOTER resolution). In this context it should be noted that at the X-SHOOTER dispersion of ~ 0.15 Å/px, a typical GC velocity dispersion of $\sim 5\,\mathrm{km\,s^{-1}}$ corresponds to ~ 1 pixel. It therefore becomes clear that a simplistic resampling of the template spectra is not sufficient, as higher-order effects (e.g., non-Gaussian shape of the LSF, λ-dependence of the resolution) need to be included in the modeling process if a sub-pixel accuracy is desired.

To assess X-SHOOTER's spectral resolution we use ThAr-frames that were taken in regular slit mode and with the same slit sizes as our science observations. A ThAr lamp spectrum is typically characterized by a high number of lines ($\gtrsim 1/$Å) with well-defined laboratory wavelengths. These lines are mostly unresolved even at $R \lesssim 150,000$ (Murphy et al. 2007) and cover the entire spectral range of the two X-SHOOTER arms studied here, i.e., 3,000 Å–10,000 Å. This justifies the approximation that at R$\sim$ 10,000 any line-broadening in the ThAr frame is caused solely by X-SHOOTER's optics, and thus the line shapes in the rectified frame can be used straightforwardly to measure the instrumental LSF. In this context it should be noted that this treatment implicitly assumes that the resolutions of both the ThAr and the GC frames is slit-limited. In slit-limited observations the slit width is smaller than the spatial extent of the light-emitting source and thus the diffraction at the slit is the predominant cause for the measured line width on the detector. Given the typical seeings and utilized slit widths in our GC observations ($\sim 1''$ seeing vs. $0.5''/0.4''$ slit widths; see Section 2.3) in combination with the applied drift-scan mode, where each star in the scan is homogenously moved across the slit, the resolution of our integrated GC spectra is expected to deviate only insignificantly from a perfect slit-limited observation. The ThAr frame, on the other hand, is expected to show no deviation, because the ThAr arc lamp homogenously illuminates the slit.

As the UVB and VIS data that are used for the velocity dispersion measurements are technically coming from two different instruments, with different detectors, optics, and slit sizes (UVB: $0.5''$, VIS: $0.4''$) we measure the LSF for each arm individually. The template spectrum is then split into two parts, according to the spectral ranges of the two instrumental arms, and each part is degraded to X-SHOOTER's respective spectral resolution separately. The subsequent re-merging of the two components is performed in the same way as for the observational data (see Section 3.4.10).

In a first step the ThAr frame being closest in time to our data set is reduced, rectified, and "flux-calibrated" (i.e., corrected for the instrumental response) similar to the GC frames. This ensures that the spectral resolution is the same for the ThAr frame and the science frames. For the line-width measurements we collapse the spectrum along the cross-dispersed direction and propagate the errors accordingly, i.e., sum them in quadrature. This increases the S/N and enhances the quality of the extracted line fit parameters. By visual inspection we browsed through the resulting spectrum and selected in each

arm ~ 500 lines that showed no signature of line-blend contamination, i.e., that showed no deviation from a symmetric shape. In this context it should be noted, however, that most of the ThAr lines are actually blends even at $R \sim 150,000$ (Murphy et al. 2007). Nevertheless, given the fact that they are still unresolved at such high spectral resolution, they are viable candidates to be included in our sample, as the approximation to assign the measured line-width exclusively to instrumental broadening seems valid. For the LSF measurement we parametrize the line profile in a similar way as the PSF (see Section 3.4.9). This is owed to the fact that a simple Gaussian profile does not represent the LSF appropriately and a sub-pixel accuracy for the dispersion measurement is required. The exact parametrization is of the form

$$\mathrm{LSF} = a_1 + a_4\, e^{-0.5u^2}\,(1 + a_5 u^2) + a_6\,\lambda, \tag{30}$$

with $u = (\lambda - a_2)/a_3$, i.e., we use a standard Gaussian and expand the profile to allow for additional kurtosis (the actual instrumental PSF shows negative excess kurtosis). Since a_3 and a_5 exhibit a certain amount of degeneracy (they both control the width of the line profile), we fix the kurtosis term to be

$$a_5(\lambda) = 4.201 \cdot 10^{-2} + \frac{5.726 \cdot 10^{-5}}{\text{Å}} \cdot \lambda, \tag{31}$$

and only fit the Gaussian width a_3. These parametrization of a_5 has been found after extensive tests and describe the overall increase of the kurtosis with increasing wavelength. An example comparison between a ThAr line at $\lambda = 3967.4$ (black curve), the best-fit Gaussian (blue), and the line model as described by Equation 30 (red) is shown in Figure 33.

To construct a λ-dependent LSF model, we analyze all lines included in our list and then fit the obtained $a_3(\lambda)$ with a low-order Chebyshev polynomial. For this, we apply a $\kappa - \sigma$ clipping ($\kappa = 6$) to remove outliers first. These are expected, since blended lines are probably still contained in the utilized line list. The obtained values for a_3 (after clipping; black circles) and the Chebyshev-fit (red line) are shown in Figure 34 for the UVB arm.

With $a_3(\lambda)$ and $a_5(\lambda)$ known, we can construct the LSF for all wavelengths at which the template spectrum is tabulated, i.e., Equation 30 is evaluated for all wavelength bins individually. Since the LSF kernel is not constant in wavelength space, a convolution in Fourier space is not possible and multiplications and summations have to be performed directly in pixel space. In our IDL code this convolution takes $\sim 10 - 100$ s per PHOENIX spectrum, and, with 68 slit positions in each scan, adds up to a considerable amount of time.

In a last step, the degraded template spectra need to be transformed to air wavelengths, as only then a comparison with the observational data is possible. We use the transformation given by Morton (1991), i.e.,

$$\begin{aligned}\lambda_{air} = \lambda_{vac}(1.0 + 2.735182 \cdot 10^{-4} + \\ + 131.4182/\lambda_{vac}^2 + 2.76249 \cdot 10^8/\lambda_{vac}^4)^{-1},\end{aligned} \tag{32}$$

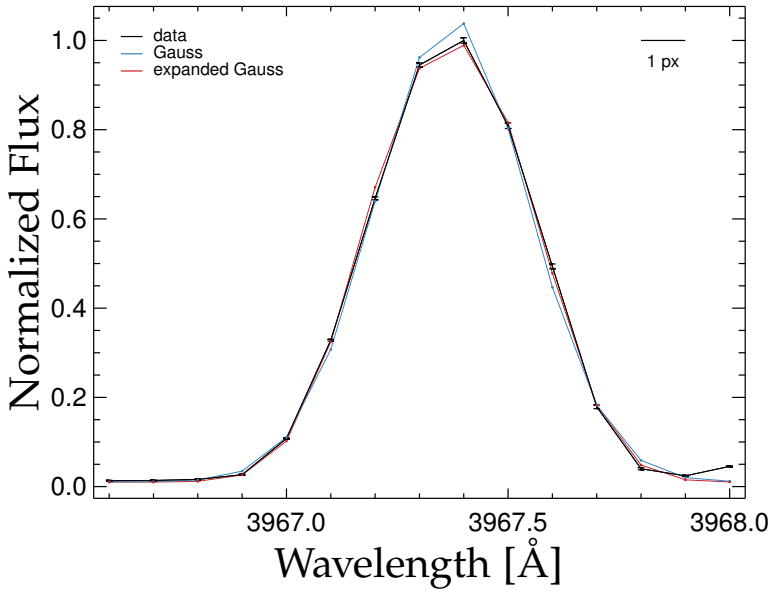

Figure 33: ThAr line at $\lambda = 3967.4$ (black curve). The best-fit Gaussian is plotted in blue and the best-fit line model as parametrized by Equation 30 is plotted in red. The measurement uncertainties of the data are indicated with error bars. We note that the flux increase at the red end of the plotted wavelength range is due to a second line, which was not included in the fit.

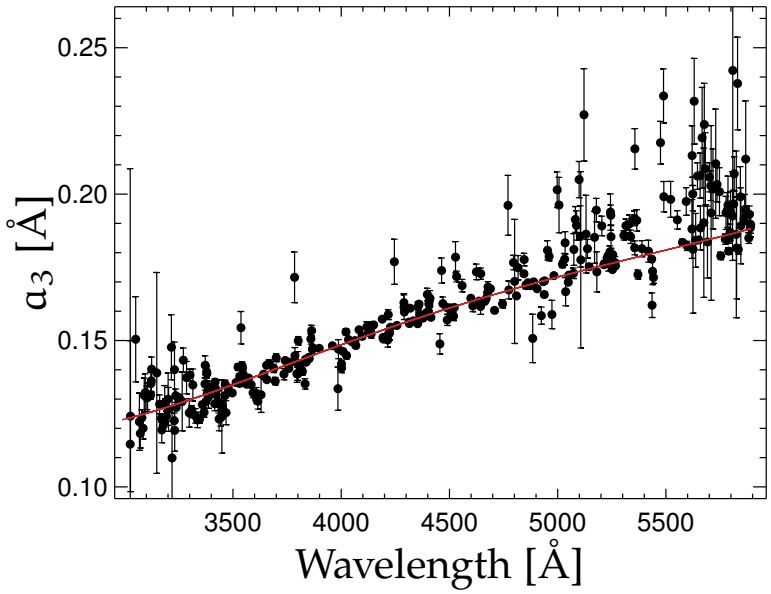

Figure 34: Gaussian width a_3 (from Equation 30) as a function of wavelength for X-SHOOTER's UVB arm (black circles with error bars). The low-order Chebyshev fit is indicated in red. The increase of scatter at $\sim 5,500$ Å is mainly due to a decrease of the instrumental response. Positive outliers are likely to be caused by blended lines.

which is a commonly utilized parametrization and also used, e.g., by the SDSS project.

We note that the procedure described here is performed independently for the two instrumental arms. For this, the synthetic templates are first divided into two parts, reflecting the respective instrumental arms. Once both parts are degraded to X-SHOOTER's resolution, they are re-merged in the default way (see Section 3.4.10), i.e. based on a weighted average. Since the resolutions of the UVB and VIS arm are somewhat different in the overlapping wavelength range, we use an error map of an actual GC observation as input for the weighted average. In this way, we reproduce best the relative contributions of each arm to the resulting merged spectrum, and thus recover the combined LSF in the overlapping region as accurately as possible. It should be noted, however, that this becomes only important if the dichroic variability is calibrated out and the full spectral range used in the analysis. In the work presented here, we do not correct for the problems associated with the UVB/VIS dichroic and mask out the affected region. The proposed weighting thus does not affect the velocity dispersion measurements presented in this work.

4.9 MODELING THE STELLAR CONTRIBUTIONS IN THE DRIFT-SCAN SPECTRA

In Sections 4.6 and 4.7 we constructed the HRDs and the resulting synthetic composite spectra for all stars contained within the half-light radius of a GC. The half-light radius

was chosen as an instructive example and to increase the intercomparability within our sample. For our drift-scan spectra, however, the presented approach needs to be slightly modified, so that it accounts for the true area covered by each scan. This is accomplished by determinig the flux contributions that each star in the GC has to each spatial slit bin in our drift-scans. To illustrate this approach we sketch the geometrical setup of one drift-scan in Figure 35. The start pointing of the scan is denoted $\mathrm{R.A.}_0$, Dec_0 (green cross symbol) and corresponds to the center of the slit. The spatial extent of the slit ($0.5''/0.4'' \times 11''$) is indicated by the green-shaded area and the black arrow denotes the direction along which the slit is moved during integration (which corresponds to the R.A.-axis). The area covered by the scan is indicated by the black rectangle. The vertical extent of the scan $\Delta\,\mathrm{Dec}$ corresponds to the X-shooter's slit length and is $11''$. The horizontal size $\Delta\,\mathrm{R.A.}$ is the product of the drift-scan velocity $\delta\,\mathrm{R.A.}$ and the exposure time t_{exp}, i.e.,

$$\Delta\,\mathrm{R.A.} = \delta\,\mathrm{R.A.} \cdot t_{exp}, \tag{33}$$

which implies that, to first-order approximation, all stars with

$$\mathrm{Dec}_\star \in [\mathrm{Dec}_0 - \Delta\,\mathrm{Dec}/2, \mathrm{Dec}_0 + \Delta\,\mathrm{Dec}/2] \quad \text{and} \quad \mathrm{R.A.}_\star \in [\mathrm{R.A.}_0, \mathrm{R.A.}_0 + \Delta\mathrm{R.A.}] \tag{34}$$

are contained in the scan. In our data, the vertical ($\equiv$ cross-dispersed) dimension $\Delta\,\mathrm{Dec}$ is subdivided into 68 bins, which corresponds to a step size $= 0.16''/\mathrm{px}$. These bins are indicated with small tick marks on the left-hand side of the plot (one slit bin is highlighted by shading it with diagonal lines). The star symbols in Figure 35 denote the relative *HST/ACS* positions of the 500 brightest stars in the third scan of NGC7089[9]. Color and size of a symbol indicate the *F606W*-magnitude of the respective star (brighter stars have lighter colors and larger symbols). We model stars as one-dimensional objects and the vertical extent of a star is parametrized with a Moffat profile (see Equation 20) based on the seeing Fwhm as extracted from the Fits header. Each star is thus modeled with the same profile shape and any seeing variations during the integration of one scan are neglected. The resulting cumulative light distribution within the scanned area is color-coded in red, with darker colors implying higher fluxes. The apparent "flatness" of most light profiles in Figure 35 (i.e, the same shading over the entire length of the profile) is caused by the limited dynamic range of the color-coding, since the fluxes are *linearly* scaled. This instructively illustrates that the total light budget is dominated by only a small number of stars. The one-dimensional treatment for the stars is justified, since the drift-scan mode integrates all fluxes along the R.A.-dimension in any case (this axis later becomes the dispersion axis). The integrated fluxes at each slit position are shown in the right panel of Figure 35 and correspond to the cross-dispersed profile that is later measured in the spectrum. Furthermore, Figure 35 illustrates that stars outside the slit also contribute flux to the drift-scan spectrum because of atmospheric seeing.

9 this scan is used as a working example. We note that the presented setup and explanations are valid for all our drift-scan observations

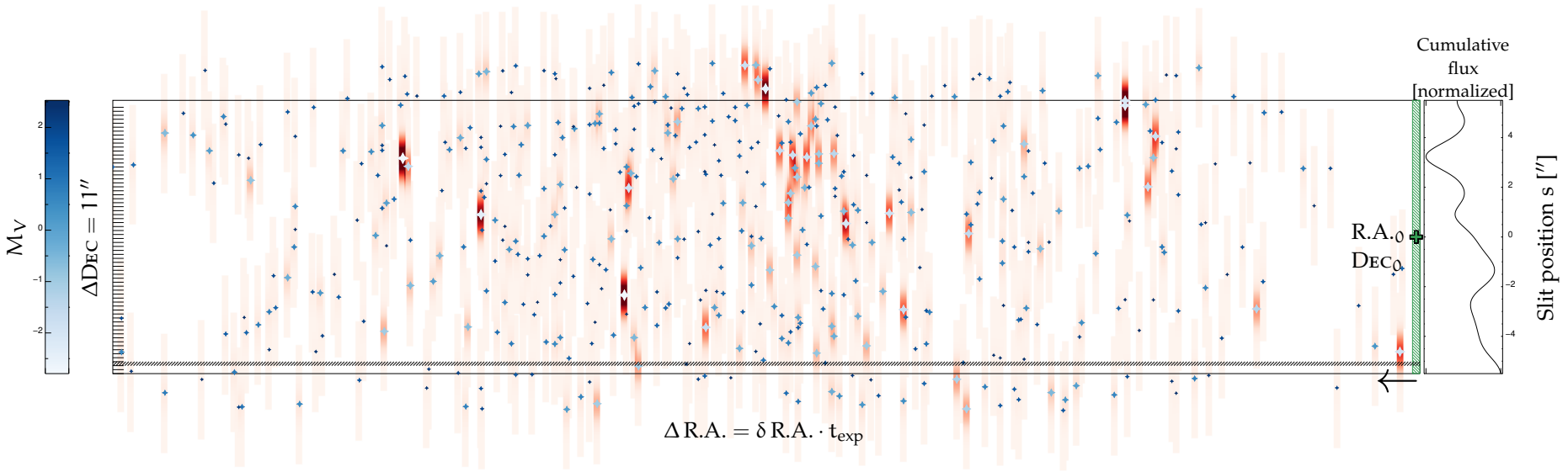

Figure 35: Sketch of the geometrical setup of a drift-scan observation. The coordinates of the start of the observation are denoted R.A.$_0$, DEC$_0$ (green cross symbol) and correspond to the slit center. The spatial extent of the slit ($0.5''/0.4'' \times 11''$) is indicated by the green-shaded area and the black arrow denotes the direction along which the slit is moved during integration. The area covered by the scan is indicated by the black rectangle and covers $11''$ along the DEC-dimension and $\delta\,\text{R.A.} \cdot t_{exp}$ along the R.A.-dimension ($\delta\,\text{R.A.} \equiv$ drift-scan speed; $t_{exp} \equiv$ exposure time). Overplotted with star symbols are the relative *HST/ACS* positions of the 500 brightest stars in the third scan of NGC7089 (this scan also covers the cluster center, which is at slit position $s \approx 4''$). This corresponds to $\sim 5\%$ of all stars contained in the actual scan. The luminosity of a star (as measured by its *F606W*-magnitude) is indicated by the symbol's size and color (see blue color bar; brighter stars are plotted with lighter colors and larger symbols). The individual stellar profiles are modeled with one-dimensional Moffat profiles (see Equation 20), and the resulting linearly-scaled light distribution produced by all 500 stars is indicated with red (higher fluxes are indicated with darker colors; we note that for reasons of claritity the individual light profiles are plotted with a finite width). The cross-dispersed dimension is subdivided into 68 bins, which is the sampling determined by the instrument/pipeline. The resulting flux contributions to one particular slit bin (an example bin is highlighted as the band filled with black diagonal lines) are given by the respective color scales of the profiles in the intersecting region. The right panel shows the cumulative flux distribution if the area is integrated over the R.A.-dimension and corresponds to the flux profile that is measured along the cross-dispersed direction of the spectrum. We note that the aspect ratio of the plot is slightly misleading, because typically $\Delta\,\text{R.A.} \gtrsim 10\,\Delta\,\text{DEC}$.

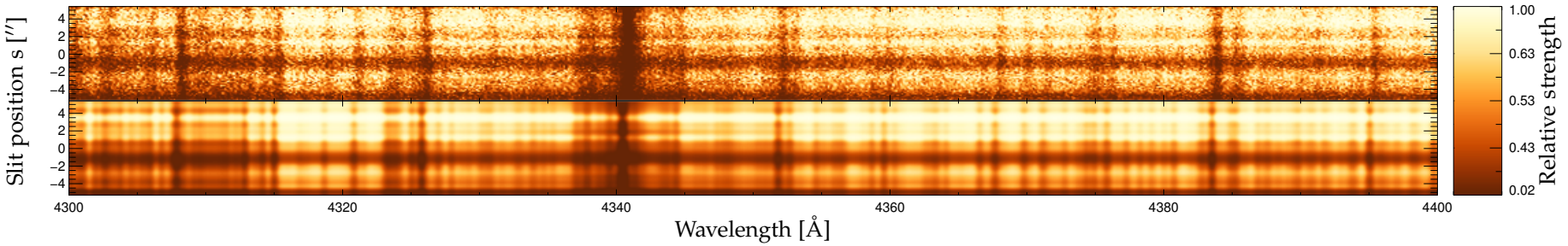

Figure 36: Two-dimensional spectra comparison between observation (top) and template (bottom) for the third drift-scan of NGC7089. The spectra are plotted as a function of wavelength (x-axis; range $4,300\,\text{Å} - 4,370\,\text{Å}$) and slit coordinate (y-axis, range $\pm 5.5''$ with respect to the telecope pointing). The relative flux intensities are indicated by the color coding (see color bar). The template spectrum has been degraded to X-SHOOTER's resolution (see Section 4.8) and converted to air wavelengths. The apparent shift in wavelength between observation and template is caused by the systemic radial velocity of the GC.

In order to obtain the template spectrum for one drift-scan observation, the HRD is constructed individually for each of the 68 slit bins by considering only stars whose flux profile is non-zero at the respective slit position. The HRD luminosity function at slit position s then becomes

$$\frac{dL_{ij}^{s}}{dT_{\mathrm{eff},i}\ d\log\ g_j} = \frac{dN_{ij}^{s}}{dT_{\mathrm{eff},i}\ d\log\ g_j} \times L_{ij}^{\star} \times \sum_i f_{\star_i}^{s}. \tag{35}$$

Here, $f_{\star_i}^{s}$ is the flux contribution of star i to slit position s, i.e.,

$$f_{\star_i}^{s} = \frac{\int_{s}^{s+0.16''} ds\ \mathrm{PSF}_{\star_i}}{\int_{-\mathrm{inf}}^{+\mathrm{inf}} ds\ \mathrm{PSF}_{\star_i}} \tag{36}$$

and the summation in Equation 35 is performed over all stars that contribute (i.e., for which $f_{\star_i}^{s} \neq 0$). As explained above, the PSF is modeled with a symmetric Moffat profile and is the same for all stars. It is worth noting that typically $\sim 10^3$ stars contribute to a single slit bin. Yet, due to the specific shape of the luminosity function, the brightest star accounts for $\sim 10-50\%$ of the total flux in the bin. Moreover, in a typical setup of our observations, a slit of $\sim 0.5''$ covers a single star only for $\sim 1-10\,\mathrm{s}$, and thus any effects that take place on comparable time scales (e.g., pointing uncertainties, seeing variations) might lead to potential differences between individual stars. We will discuss them further below.

The final template spectrum for one drift-scan is constructed as explained in Section 4.7, with the only difference that the underlying HRDs are specific to each slit bin. The top panel of Figure 37 shows a comparison between the synthetic (dot-dashed blue curve) and observed (solid black curve) cross-dispersed profiles for the example drift scan of Figure 35 (the profiles have been obtained by computing the spectral median for each slit bin).

The overall match of the two profiles is already acceptable and individual peaks are mostly reproduced at the correct position. Nevertheless, the synthetic template is, first, slightly shifted with respect to the observed profile and, second, shows different relative ratios between maxima and minima. Judging from our entire data set, the shift typically has an amplitude of $\sim 0''-2''$ and shows no slit dependence, i.e., the shift is constant across the length of the slit. It is interesting to note, however, that some observations show an additional differential shift component, i.e., certain peaks are shifted more strongly than others. It is difficult to assess the true causes for this peculiar effect, but we speculate that the constant offset is likely caused by an overall uncertainty in VLT's and / or HST's pointing precision. The additional differential component could hint at a temporal instability of the pointing accuracy. Strong winds could cause tail motions of the VLT, and as individual stars are captured by the slit only for a few seconds this could cause a random displacement for each star. Another explanation could be related to uncertainties in the drift direction, such that the resulting scan was not entirely aligned with the

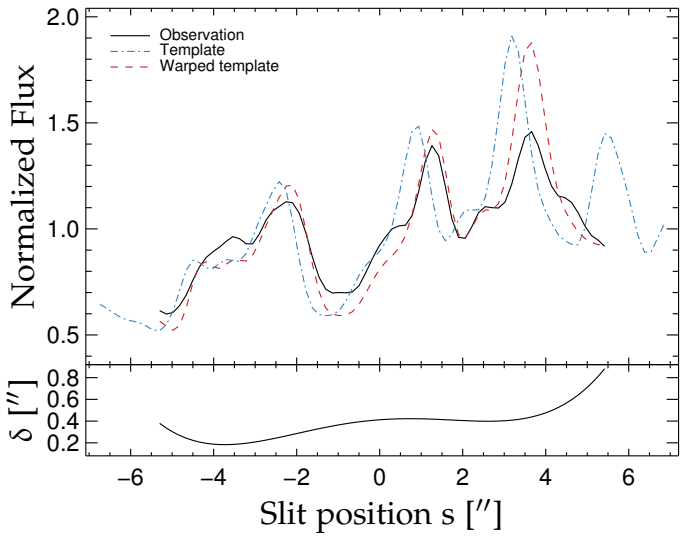

Figure 37: *Top*: Cross-dispersed flux profiles of the example scan of NGC7089. The observed profile is plotted with a solid black curve and the constructed template profile is overplotted with a dot-dashed blue curve. After correcting for the differential shift, the template spectrum aligns acceptably with the observation (dashed red curve). *Bottom*: Fitted differential shift between observation and template.

R.A.-dimension. This scenario would naturally lead to a differential offset relative to the reference HST positions, as stars at the end of the observation (i.e., at the end of the scanned area) would be more strongly displaced than stars at the start. We note, however, that our suggested explanations are merely speculative and cannot be distinctly confirmed or rejected with the data at hand, because the file headers do not contain any information about the true drift direction or the final pointing of the telescope. Independent of the true cause, it is evident that the offset has to be corrected for. Otherwise our analysis might suffer from significant template mismatch which can occur if an observed bright star (peak in the observed cross-dispersed profile; presumably a cool RGB star with low log g) is correlated with diffuse cluster light in the template (minimum in the synthetic cross-dispersed profile; presumably caused by UMS and MSTO stars, which are both hotter and denser than the RGB star) or vice-versa. This scenario would entirely vitiate our careful template construction and introduce potential biases due to systematic discrepancies between observation and template. We therefore address this issue by "warping" the template slit coordinate, i.e., we fit a differential displacement to each slit position of the template to align the template cross-dispersed profiles with its observed counterpart. The fitted displacements are modeled with a low-order Chebyshev polynomial to account for the differential component in the offset. In mathematical terms, the flux $F(s_i)$ at slit bin s_i is shifted to the position $s_i + \delta s_i$, i.e.,

$$F(s'_i) = F(s_i + \delta s_i), \tag{37}$$

where the displacement δs_i is allowed to vary smoothly with slit position. Since the resulting slit grid s'_i is inhomogenously spaced, we need to resample the shifted profile to the same slit positions on which the observed data are defined. This is achieved with a linear interpolation. The obtained warped profile for the example scan of NGC7089 is plotted with a dashed red curve in the top panel of Figure 37 and the utilized displacement function $\delta(s)$ is shown in the bottom panel. Despite the satisfactory alignment the between observed and synthetic profiles we would like to point out the following implications of the warping procedure:

1) The quality of the shift correction increases with the number of strong features in the cross-dispersed profile that can be used for the cross-match, and, thus varies from scan to scan. The achieved match as illustrated in Figure 37 can be considered average for our data set.

2) The offset between template and observation requires the template to be constructed well beyond the limits given by the slit edges, as only then a reliable shift correction is possible. This enables us to shift template stars into the slit that, based on their HST coordinates, would intrinsically not be included (and vice-versa, i.e., moving them out although their astrometry would suggest to include them in the synthesis). This is the reason why the unwarped template profile in Figure 37 (dot-dashed blue curve) extends past the limits of the observational profile.

3) Our correction implies that all stars with the same declination in the *HST/ACS* astrometry are shifted in the same way, indepent of their right ascension (which is equivalent to a time coordinate, since we scanned along R.A. at fixed Dec; compare Figure 35). This might be a proper assumption for the constant component of the displacement and would account for static pointing residuals between our observations and the *HST/ACS* data. In this context it should be noted that *HST/ACS* 's absolute astrometry is expected to be accurate at the 0.2″ level (Koekemoer et al. 2006) and is typically limited by the astrometry of the guide star. VLT's pointing uncertainty is given to be 2″[10] and an additional tracking uncertainty of 0.1″ over 30 minutes is expected. This tracking uncertainty could—at least partly—be responsible for the observed differential shift, since it is a time-variable effect that (randomly) displaces each star along the slit dimension during the integration of the drift-scan (displacements along the perpendicular dimension can be neglected since they will be integrated over by the drift-scan in any case). In this scenario, our suggested treatment of warping the final templates would not entirely account for the true displacements of each star, as it corrects only the luminosity-weighted average shift of each slit position (which is primarily determined by displacements of the brightest stars contained in the scan). As our observations contain luminosity-weighted spectra as well (and thus will be dominated by the brightest stars as well), this seems to be an acceptable approximation and we make no further efforts to correct for the observed offset beyond what is presented

10 see the document describing the requirements for scientific instruments on the VLT; https://www.eso.org/sci/facilities/paranal/instruments/visfocus/doc/VLT-SPE-ESO-10000-2723_is1.pdf

in this work. We note that the field-of-view distortions of *HST/ACS* can be ruled out as a possible cause. Borncamp et al. (2015) recently reassessed the quality of the geometric distortion correction for *HST/ACS* and found the exisiting correction (which is underlying the data that we utilize in our analysis) to be accurate at least at the $\sim$ 0.15 pixels level. Given the *HST/ACS* plate scale of $\sim$ 0.05″/px, any expected residual distortion is thus neglible.

Even if the template profile is corrected for the differential shift along the cross-dispersed dimension, Figure 37 indicates that the synthetic profile still has a slightly different shape than the X-SHOOTER observation. The most prominent feature is doubtlessly the relative amplitude difference between the two peaks at $\sim$ 1″ and $\sim$ 3.5″. While the observed spectrum shows approximately equally strong peaks, the $s = 3.5''$ peak is almost twice as bright in the synthetic template (with respect to the underlying profile). A certain discrepancy has to be expected, as the template construction process is based on several steps, each of which exhibits its own uncertainties and thus might affect the accuracy of the final template. The mapping process, where all stars are projected onto an appropriately chosen isochrone, certainly bears the highest risk for the introduction of systematical errors. Photometric erros in the *HST/ACS* data could potentially lead to an erroneous derivation of stellar parameters for some stars, by projecting them onto the wrong region of the model isochrone. Furthermore, the isochrone itself can predict inaccurate values, either because the utilized input physics is incomplete and / or because the specified parameters (age, chemical composition, distance modulus, reddening) are not appropriate for the respective stellar population. This certainly applies even more to GCs that host multiple stellar populations with distinct differences in age and / or metallicity, as we only use one isochrone to model the global cluster population. In addition, the flux calibration of the PHOENIX library could systematically deviate depending on the particular stellar atmosphere $\langle T_{\rm eff}, \log\ g \rangle$ of interest.

With this said, it is suprising that the difference in relative strength between the two peaks at $\sim$ 1″ and $\sim$ 3.5″ is already contained in the *HST/ACS* data themselves (i.e., without applying our mapping procedure), as shown by the right panel of Figure 35, where the integrated *F606W*-fluxes of the 500 brightest stars are plotted as a function of slit position. This indicates that—at least for this particular scan example of NGC7089—the mapping process itself is not the source for the discrepancies between template and X-SHOOTER spectra, because the fluxes underlying Figure 35 are based on directly measured *F606W*-magnitudes (with photometric errors much smaller than any of the uncertainties related to the mapping process). A potential systematical problem in the flux-calibration of our X-SHOOTER spectra seems implausible at this amplitude. In Section 3.4.5 we discussed the cross-dispersed illumination function and find typical variations of $\leqslant$ 5% along the slit length. Even if the applied illumination corrections are entirely off due to an incomplete understanding of the responsible effects, we would not expect differences as large as $\sim$ 30% (relative difference between template and observation for the peak at $s \approx 3.5''$). Seeing variations over the integration time of the drift scan appear implausible to explain the observed discrepancy as well. These are indeed expected, but the impact should be much

smaller than the observed differences (a reasonable estimate for seeing variations within the time lapse of one scan should be $\sim \pm 0.5''$). Conversely, seeing conditions that remove 50% of the star's profile peak would significantly broaden the wings of the PSF, which, however, is not observed, as Figure 37 suggests an approximately equal width of the two peaks at $\sim 1''$ and $\sim 3.5''$ in our X-SHOOTER spectrum. Contamination by foreground stars is expected to be a (minor) issue for some of the GCs in our sample, but this effect should rather operate in the opposite direction: As we expect the *HST/ACS* data to be mostly cleaned from foreground stars, any additional stars captured in our drift scans should produce extra flux in the observed spectrum relative to the template. As a consequence, bright stars along the line of sight are expected to produce their characteristical imprint as additional peaks in the observational cross-dispersed profile, rather than in the template profile (the issue of foreground contamination will be further discussed in Section 5.5).

In due consideration of any additional effect that might influence the strengths of the peaks, we speculate that at least one of the stars that contribute to the $s \approx 3.5''$ peak is variable. This might either be due to intrinsic stellar variability, as expected for a considerable fraction of red giants (e.g., Mira variables) and HB stars (RR-Lyraes), or due to a spatially unresolved eclipsing binary system. Irrespective of this discrepancy's true nature, we undertake no further effort to correct for the differences in relative strength, and thus only perform the above explained shift correction along the slit-dimension (which, except for the required interpolation, leaves the fluxes unchanged). We note in passing that any residual difference in the continuum flux levels between template and observation will be naturally accounted for in the velocity dispersion measuerement (see Section 5.5). Therefore, a different scale between template and observation does not affect the quality of the derived kinematical parameters.

We computed the shift correction functions for all scans in our data and corrected the respective template spectra accordingly. In Figure 36 we show for our example scan of NGC7089 a comparison between observation (top panel) and corrected template (bottom) in the wavelength range $4,300\,\text{Å} - 4,370\,\text{Å}$ for all 68 slit bins. Both spectra have been histogram-normalized to increase the dynamic range of the figure (see color bar). The presented template spectrum has been degraded to X-SHOOTER's resolution and converted to air wavelengths (see Section 4.8). We emphasize the remarkable match quality.

Spectra of this type will be used in Chapter 5 to determine a cluster's radial velocity (line shift between observation and template in Figure 36) and its velocity dispersion (line broadening in the observed spectrum relative to the template). This analysis will be performed individually for each slit position s.

Part V

VELOCITY DISPERSIONS

We measure the velocity dispersion and radial velocity of each globular cluster at different distances from its center. The velocity dispersion profiles obtained in this way exhibit distinct fluctuations that are not expected from theoretical models and are, therefore, explored in detail. A possible cause for these fluctuations could be related to a general template mismatch, which, however, can be ruled out, as the typical match quality between template and observation along both dimensions (i.e., spatial and spectral) is good. Our analysis suggests that the brightest stars in a scan (i.e., either foreground stars or stars in the cluster) can contribute up to $\sim$ 50% to a scan's integrated spectrum, and thus may bias the inferred kinematic cluster properties at their position. In fact, their spectra may show kinematic imprints of rotation and / or an additional radial velocity component due to a binary companion or previous interaction with a binary. These factors can influence our measurements in a way consistent with the observed fluctuations. We illustrate a possible way to minimize the impact of these bright stars in order to recover the smooth cluster kinematics. Follow-up numerical simulations may be used in conjunction with the derived velocity dispersion curves to constrain the radial mass profile of the globular clusters. The radial velocity profile shows indication of ordered rotation for some clusters, which may be used as an additional constraint for their dynamical modeling.

5

VELOCITY DISPERSION MEASUREMENTS WITH PPXF

The velocity dispersion σ is the statistical dispersion of the individual stellar velocities about the mean systemic velocity in the ensemble. It is defined as

$$\sigma = \sqrt{\langle v_i^2 \rangle - \langle v_i \rangle^2}, \tag{38}$$

where v_i are the individual stellar velocities and $\langle\rangle$ denote average values. In spectral observations, however, only the projected dispersion along the line-of-sight σ_{LOS} can be directly measured. Unfortunately, the transformation between the true velocity dispersion σ and σ_{LOS} is complicated and requires detailed knowledge of the phase space distribution of the stars, which itself is a function of various dynamical parameters. The core of the problem is related to the fact that at any point x in the GC[1], the measured velocity dispersion σ_{LOS} is not only determined by the spread in velocities around $\langle v(x) \rangle$, but also by the variation of the mean velocity along the line-of-sight. The exact mathematical formulation of the problem can be found in Binney & Tremaine (1987, Chapter 4) and the general way out of this dilemma is the assumption of a certain dynamical model for the GC. Based on this model, the theoretically predicted kinematic parameters, i.e., $\langle v(x) \rangle$ and $\sigma(x)$, can be projected along a dimension that corresponds to the line-of-sight of the observation, thereby facilitating a one-to-one comparison between the observed σ_{LOS} and the model predictions. The utilized models can be either analytic or in the form of N-body representations and are of fundamental importance to infer dynamical properties from the measured line-of-sight velocity dispersion. In this context it should be noted that one way to break possible degeneracies between different models is offered by the measurement of higher order velocity moments. In this case, not only the mean value and the symmetric dispersion are measured, but also higher moments like skewness or kurtosis. Evidently, this requires the data to be of sufficiently high S/N on the one hand, and the LSF to be properly sampled on the other hand. Our kinematic measurements cannot constrain these higher orders and so we will exclusively focus on the measurement of the symmetric broadening. Furthermore, we emphasize that we do not explore the implications that our measured values have for different dynamical models. An analysis of this kind is intended for a subsequent project, in which we plan to run a set of N-body simulations with a variety of initial conditions to constrain the mass profiles for our sample of GCs. Here, we will use Equation 22 (taken from Spitzer 1969, 1987) to estimate the dynamical masses based on the central line-of-sight velocity dispersions. This equation implicitly assumes a dynamically relaxed cluster, spherical symmetry, and isotropic stellar orbits, i.e,

$$\sigma_{tot}^2 = \sigma_r^2 + \sigma_\phi^2 + \sigma_\theta^2 = 3\,\sigma_r^2. \tag{39}$$

1 It should be noted that this problem is not restricted to GCs, but a general issue for all dynamical systems that are observed in projection.

We note that whenever we refer to the velocity dispersion σ, we implicitly mean the line-of-sight velocity dispersion $\sigma_{\rm LOS}$, but for the sake of simplicitly we shall drop the subscript from here on.

This Chapter is organized as follows. Section 5.1 describes the logarithmic rebinning of the spectra, which offers a direct translation between wavelengths and velocities. In Section 5.2 we present the mathematical formulation of the velocity dispersion measurement. The impact of Galactic extinction on our observations is discussed in Section 5.3 and a general assessment of the match quality between the synthetic templates and the observed spectra is presented in 5.4. In Section 5.5 we describe the mode of operation with which we measure the dispersion in our drift-scan spectra. The results will be presented in Section 5.6, where a detailed discussion of the observed features in the dispersion profiles is given. In Section 5.7 we briefly discuss how ordered rotation needs to be removed if a velocity dispersion integrated over the central core region is desired. The obtained core-integrated values are presented in Section 5.8. In Section 5.9 we summarize the findings for each cluster in our sample. In Chapter 6.2 we utilize the central velocity dispersions to estimate the dynamical masses.

5.1 LOGARITHMIC REBINNING OF THE SPECTRA

If a spectral line with rest wavelength λ_0 is measured at wavelength λ', then the shift $\Delta\lambda \equiv \lambda' - \lambda_0$ is connected to the radial-velocity inducing this line-shift via

$$\frac{\lambda - \lambda_0}{\lambda_0} \equiv \frac{\Delta\lambda}{\lambda_0} = \left(\frac{1 + \frac{v_r}{c}}{1 - \frac{v_r}{c}}\right)^{1/2} - 1 \approx \frac{v_r}{c}. \tag{40}$$

The approximation in the last steps holds for $v_r \ll c$, which is well satisfied for all GCs. An object is *blue-shifted* (*red-shifted*) if $\Delta\lambda < 0$ ($\Delta\lambda > 0$), and, thus $v_r < 0$ ($v_r > 0$). According to Equation 40, the amplitude of the line-shift $\Delta\lambda$ depends on the wavelength of the spectral feature (at fixed v_r) and thus a Doppler-shifted spectrum is altered in a λ-dependent way. This circumstantial fact can be avoided if the logarithms of the wavelengths are considered. Adding plus one and then taking the natural logarithm of Equation 40 yields

$$\ln\lambda - \ln\lambda_0 = \frac{1}{2}\ln\left(\frac{1 + \frac{v_r}{c}}{1 - \frac{v_r}{c}}\right) \approx \ln\left(1 + \frac{v_r}{c}\right). \tag{41}$$

Hence, the shift $\Delta\ln\lambda \equiv \ln\lambda - \ln\lambda_0$ is independent of λ and only depends on v_r. Therefore, a logarithmic spectrum of a moving star preserves its intrinsic pattern (i.e., distances between spectral features) and is merely moved along the $\ln\lambda$-axis with fixed stepping. This also implies that any velocity broadening likewise affects all spectral features, i.e. the Gaussian width (in $\ln\lambda$-space) of the velocity dispersion kernel is the same everywhere. Thus, any fitting technique that compares the observed spectrum to a broadened template spectrum to find the best-fit broadening kernel will computationally greatly benefit from the possibility of performing the necessary convolution in Fourier-space, instead of

having to compute a separate kernel for each wavelength (which would be the case in λ-space).

The logarithmic rebinning of our spectra is performed with the routine *LOG_REBIN*, which is delivered with *pPXF*. It makes the zero-order assumption that the linear spectrum is constant within each individual pixel. During rebinning, the counts are redistributed onto a new grid which is non-uniform in linear wavelength space, but equidistant $\ln\lambda$-space. Error propagation is performed based on the variances, i.e., the squared error map is logarithmically rebinned and the square root is taken of the resulting spectrum. This is, however, only an approximate treatment of the error propagation as it does not consider correlations between adjacent pixels, which are introduced by the rebinning. Thus, any χ^2 of a fit will not be accurate in a strict statistical sense and care has to be applied if meaningful measurement uncertainties are to be inferred. Since the error maps, as returned by the pipeline, do not encode information about the correlation introduced by the rectification in the first place anyway (see Section 3.4.1.3), we did not undertake further steps to correct for the additional correlation of the logarithmic rebinning process. Logarithmically rebinning the spectrum yields the *velocity scale* dv, which corresponds to the pixel size of the logarithmically binned spectrum in velocity space. For our data set this is $dv = 5.1\,\mathrm{km\,s^{-1}\,px^{-1}}$.

5.2 MATHEMATICAL FORMULATION OF THE SPECTRUM-FITTING TECHNIQUE

In this work we use the penalized Pixel-Fitting technique (*pPXF*) of CE04 to extract the stellar kinematics from our integrated spectra. *pPXF* applies the maximum penalized likelihood formalism (e.g., Merritt 1997) to the scenario in which the line-of-sight velocity distribution (LOSVD) can be properly parametrized and was originally designed to measure the kinematics of galaxies. The actual implementation, however, is independent of the nature of the stellar system (as long as the LOSVD can be expressed in parametric form), and so we can apply it to the GC spectra without any modifications.

In order to make the reader familiar with this algorithm, we will briefly outline its general setup based on the description given in CE04. For a more detailed presentation of its mode of operation, we refer the reader to the original publication and additionally to the manual that is included in the code package.[2]

To recover the LOSVD $\mathcal{L}(v)$ of stars from an observed GC spectrum $G(x)$, one first needs to parametrize its impact on the shape of the spectral features in the integrated GC spectrum. The standard parametrization is of the form (e.g., van der Marel & Franx 1993; Gerhard 1993)

$$\mathcal{L}(v) = \frac{e^{-0.5u^2}}{\sigma\sqrt{2\pi}}\left(1 + \sum_{m=3}^{M} h_m H_m(v)\right), \tag{42}$$

where $u = (v - V)/\sigma$ (V is the GC's systemic velocity and σ the velocity dispersion) and H_m are the Hermite polynomials. This is a higher-order expansion of a Gaussian profile

2 The source code can be retrieved from http://www-astro.physics.ox.ac.uk/~mxc/software/#ppxf.

with which it is possible to model complex kinematic profiles arising from multiple components (e.g., random motions in a galactic bulge superimposed onto a rotating disk). A model GC spectrum $G_{\rm mod}(x)$ is constructed by taking a suitably selected template spectrum and rebinning it to $\ln\lambda$-space, i.e., $x = \ln\lambda$. This template is convolved with $\mathcal{L}(v)$ and the best-fit parameters of the LOSVD are estimated by minimizing the χ^2, which is a measure for the agreement between $G_{\rm mod}(x)$ and $G(x)$ and defined as

$$\chi^2 = \sum_{n=1}^{N} r_n^2, \tag{43}$$

where we have assumed that $n = 1..N$ spectral pixels have been included in the comparison. The residuals r_n are computed via

$$r_n = \frac{G_{\rm mod}(x_n) - G(x_n)}{\Delta G(x_n)}, \tag{44}$$

where $\Delta G(x_n)$ is the measurement error in the n-th pixel. In the general case of fitting multiple templates simultaneously to the observed data (which is actually the more common case; we will also make use of this feature in Section 5.5), the construction of the GC model spectrum can be written as

$$G_{\rm mod}(x) = \sum_{k=1}^{K} w_k \, (B * T_k)(x) + \sum_{l=0}^{L} b_l \, \mathcal{P}_l \qquad w_k \geqslant 0, \tag{45}$$

where T_k are spectra from a template library containing K stellar spectra, $B(x) = \mathcal{L}(cx)$ is the broadening kernel (c is the speed of light and needed to convert between v and $\ln\lambda$), and $*$ denotes convolution. The $\mathcal{P}_l$ are Legendre polynomials of order l and used to correct any residual large-scale differences in shape between model and observed spectrum. As can be seen, the final model is a linear combination of a set of broadened templates and w_k are the respective template weights.

The true strength of *pPXF*, however, is its incorporation of a penalty function in the computation of the residuals, i.e., it allows to vary all Hermite-parameters freely to reproduce the details of the actual profile when the S/N is high, but forces the solution to a Gaussian shape if the S/N is low. This becomes necessary, since typically σ and h_4 in Equation 42 are strongly correlated. As a result, the derived parameters are not unbiased anymore, i.e., when performing a Monte-Carlo simulation with known input values, they do not scatter symmetrically around the true values, but show a bias into a specific direction (although the overall χ^2 remains the same). This usually happens in a scenario with low S/N and small velocity dispersion, since then the data are both noisy and undersampled. With undersampling we mean that the typical length scale of the signal to be measured (e.g., velocity dispersion) is only $\sim$1 px and thus hardly reconstructable in an accurate and unbiased way. The idea of a penalized treatment is to fit all parameters $(V, \sigma, h_3, \ldots, h_M)$ simultaneously, but to add an adjustable penalty term to the χ^2 so that the solution is

biased towards a Gaussian shape when $h_3, \dots, h_M$ are unconstrained due to a low S/N of the data. The penalized χ^2_p is defined as

$$\chi^2_p = \chi^2 + \alpha \mathcal{P}, \tag{46}$$

where the penalty function $\mathcal{P}$ is a term describing the integrated square deviation of the line profile $\mathcal{L}(v)$ from its best-fitting Gaussian $\mathcal{G}(v)$, i.e.,

$$\mathcal{D}^2 = \frac{\int_{-\infty}^{+\infty} (\mathcal{L}(v) - \mathcal{G}(v))^2 \, dv}{\int_{-\infty}^{+\infty} \mathcal{G}(v)^2 \, dv}. \tag{47}$$

The penalty factor α is responsible for the applied level of penalty in case of deviations from Gaussianity and should scale with the χ^2 of the fit, i.e., higher penalties in low S/N scenarios for which χ^2 is larger. van der Marel & Franx (1993) showed that in case of a Gauss-Hermite parametrization of the LOSVD (see Equation 42) $\mathcal{D}^2$ can be well approximated by the weights of the Hermite polynomials, i.e.,

$$\mathcal{D}^2 \approx \sum_{m=3}^{M} h_m^2, \tag{48}$$

which implies that one could in principle set the penalty $\mathcal{P} = \mathcal{D}^2$ and use Equation 46 as the goodness of fit estimate. This, however, is not desirable because, first, one would still need a way to automatically adjust α according to the S/N of the data, and, second, evaluating χ^2 is computationally much less efficient than minimizing the residuals r_n. CE04 therefore suggest to use the penalized residuals

$$r'_n = r_n + \beta \, \mathrm{Var}(r) \, \mathcal{D}, \tag{49}$$

where the variance $\mathrm{Var}(r)$ is given via

$$\mathrm{Var}(r) = \frac{1}{N} \sum_{n=1}^{N} r_n^2. \tag{50}$$

According to Equation 49, a deviation $\mathcal{D}$ of the LOSVD from Gaussianity is only accepted as an improvement of the fit, if it is able to decrease the variance $\mathrm{Var}(r)$ accordingly at the same time. Furthermore, it can be shown that in this case the penalty factor $\alpha = \beta^2 \chi^2$ and thus scales in the desired way. This treatment ensures that meaningful results can still be inferred if both the S/N and velocity dispersion are low.

In addition to the overall mode of operation of *pPXF* we want to highlight some additional features that this algorithm offers. It is not only capable of fitting *additive* Legendre polynomials to compensate for potential differences in the continuum shape between model and observation (see Equation 45), but it also allows for the possibility of including

multiplicative polynomials, without affecting the quality of the derived parameters of $\mathcal{L}(v)$. Furthermore, recent versions of *pPXF* facilitate the usage of multiple kinematic components, i.e., different sets of templates $T_{k,i}$ are convolved with different LOSVDs $\mathcal{L}(v)_i$. We will make use of this feature in Section 5.5.

For a more detailed explanation of the *pPXF* algorithm and additional benchmark tests we refer the reader to the original publication of CE04 and the references therein.

5.3 REDDENING CORRECTIONS

If a comparison of the continuum shapes between observed and template spectra is desired, Galactic extinction due to dust in the inter-stellar medium (ISM) has to be taken into account first. The necessary correction can be implemented either by removing the influence of the extinction on the observed spectrum, or by artificially applying the consequences of extinction to the template spectrum. For reasons of consistency, we decided to take the latter approach and left the observational data unaltered.

In order to minimize confusion of the reader that can potentially arise if the corresponding terminology is not well defined, we want to present a short overview of the parameters connected to Galactic extinction and the resulting reddening.

Dust grains (mainly silicates and carbon) in the ISM, which make up about 1% of the ISM's total mass, with diameters $\leqslant 1\mu m$ efficiently scatter and absorb radiation at wavelengths less than their own dimension (e.g., Sparke & Gallagher 2007). The wavelength-dependent *extinction* A_λ describes the difference between the observed flux m_λ and the emitted flux $m_{\lambda,0}$ in magnitudes,

$$m_\lambda = m_{\lambda,0} + A_\lambda, \tag{51}$$

where $m_{\lambda,0} = M_\lambda + \mu$ is the apparent magnitude that would be measured if distance were the only factor reducing the observed flux (M_λ is the absolute magnitude and μ is the distance modulus). A_λ varies roughly as $\lambda^{-1.5}$ from $3,000 - 23,000$ Å (see e.g., Cardelli et al. 1989; Fitzpatrick 1999). Thus, a spectrum's blue part is differentially scattered and absorbed more strongly, which in turn results in an apparent *reddening* of the measured light. This feature can be expressed by the *color excess* between two filters B and V, which is defined as

$$E(B-V) = A_B - A_V = (B-V) - (B-V)_0, \tag{52}$$

where $(B-V)$ is the measured color, and $(B-V)_0$ the intrinsically emitted color. We note that we use reddening and color excess interchangeably. The *normalized extinction* $1/R_V$ measures the steepness of the extinction curve via

$$R_V = \frac{A_V}{E(B-V)}, \tag{53}$$

and thus connects the overall level of extinction A_V to the change in color $E(B-V)$. Throughout this work we adopted $R_V = 3.1$, which represents a widely-used average

value for the diffuse ISM (Schultz & Wiemer 1975; Sneden et al. 1978; Savage & Mathis 1979). To propagate the extinction in one filter A_V (as measured by $E(B-V)$ and assuming $R_V = 3.1$) to all other wavelengths in our spectra A_λ, we used the parametrization given by Cardelli et al. (1989), which is of the form

$$\frac{A_\lambda}{A_V} = a(\lambda^{-1}) + \frac{b(\lambda^{-1})}{R_V}. \tag{54}$$

The parameters a, b are seventh-order polynomials for the considered wavelength range. Their exact values and further details on their derivation can be found in Cardelli et al. (1989).

For the reddening estimates of our GC sample we normalized both templates and observations such that the median flux between 7,800 Å and 8200 Å was set to unity, i.e.,

$$\left\langle \left\{ F(\lambda) \,|\, \lambda \in [7,800\text{Å}, 8200\text{Å}]) \right\} \right\rangle = 1. \tag{55}$$

The extinction curves for the GCs have been obtained by using the color excesses $E(B-V)$ given by Harris (2010) and $R_V = 3.1$ as initial values for Equation 54 and then fitting the artificially reddened template against the uncorrected observation. To improve the robustness of this fit, we first constructed the luminosity-weighted average spectrum for each cluster, by integrating all drift-scan spectra along the cross-dispersed dimension and co-adding the results. The resulting spectrum corresponds to the luminosity-weighted average within the area covered by the drift scans, which for most clusters is well approximated by the region enclosed by the GC half-light radius r_h. The resulting average spectra are shown in Figure 38 (black curves). The respective template spectra, which have been integrated in the same way, are overplotted in blue (without extinction correction) and red (with extinction correction). The obtained best-fit reddening values $E(B-V)$[3] are given in the bottom right corner of each panel. Since telluric absorption bands in the observational data have not been corrected for in the reduction process, the respective wavelength ranges have been excluded from the fit (denoted by gray bands). In addition, the overlapping range between UVB and VIS, which is affected by a variable throughput of the dichroic (see Section 3.4.10), has been masked out as well.

The obtained reddening values have to be interpreted with care because they might suffer from a number of systematics. A first argument relates to the fact that the obtained $E(B-V)$ are merely average values for the area covered by the drift-scans. In our data set, however, NGC2298, NGC2808, and NGC6656 are subject to differential reddening (Harris 2010), where the extinction amplitude varies strongly with position, and thus an average value seems insufficient to characterize the GC. A second argument, which potentially affects all clusters in our sample, is given by the issue of a general template mismatch: any intrinsic difference in slope between observation and template eventually implies that the fitted reddening curve will be systematically biased, because it will automatically compensate for this mismatch by adjusting E(B-V) accordingly. These differences might be expected for various reasons. Firstly, the observational and template spectral data are

3 We note that we mean $E(B-V)$ and not $E(6-8)$ here.

flux-calibrated independently, which can lead to inconsistencies in the continuum slopes. This can be either due to an inaccurately determined effective temperature of the model SED that is used for the flux standard star and / or a systematic deviation for the PHOENIX spectra due to an incomplete modeling of the involved physics (in addition, the PHOENIX library does not offer atmospheres with $T_{eff} > 12,000\,K$, which biases the modeled spectrum to redder fluxes). Secondly, the observed drift-scans might contain contributions of bright foreground stars that alter the shape of the observed spectra, but are not included in the template. Thirdly, any inconsistencies introduced in the CMD-mapping process (see Section 4.5) will directly affect the shape of the template, either by using non-appropriate isochrones or by an inconsistent projection technique. These explanations imply that the exact $E(B-V)$ values of our analysis have to be handled with care and likely do not represent the true extinction amplitude. Nevertheless, the results presented in Figure 38 demonstrate that the substantial differences between uncorrected templates (blue) and observed data (black) can, at least partly, be explained by foreground extinction in the Galaxy. This is an important consistency check for the presented template construction process and indicates that the obtained templates indeed represent a reasonable approximation to the observed spectra.

In this context we want to note that any residual continuum deviation after the reddening correction will be accounted for by fitting additive and multiplicative polynomials with *pPXF* (see Section 5.2; in particular Equation 45). Therefore, the true cause for the residual difference is subordinate as long as individual spectral features are sufficiently well reproduced in the template spectrum.

5.4 ASSESSMENT OF THE TEMPLATE MATCH QUALITY

In this Section we want to present a qualitative assessment of the match between template and observation. A detailed and quantitative comparison covering the full spectral range would require in-depth chemical abundance determinations, which is beyond the scope of this work and planned for a subsequent project.

Figure 38 reveals that the template match is best for NGC104. Template and observation are well aligned over almost the entire spectral range, with major deviations only found in telluric absorption windows and the wavelength region between 5,350 Å and 5,950 Å, where the UVB/VIS beam splitter suffers from a temporal instability in the throughput (see Section 3.4.10). As these deviations are expected and will be addressed in a revised and extended data reduction procedure, we will not discuss them further in this work. The only significant deviation outside these spectral windows is the minor bump at ~ 6,820 Å that is contained in the observed data, but not well reproduced by the template. The fact, that this potential overestimation of flux is common to all clusters in our sample with respect their corresponding template could hint at a systematic problem in the flux-calibration. We therefore carefully checked the related calibration steps (see Section 3.4.10 for a detailed description of the flux calibration), but we could not find any peculiarities that might potentially be responsible for the bump (the usage of the terminology *bump* relates to the fact that both bluewards and redwards of the feature the data are nicely

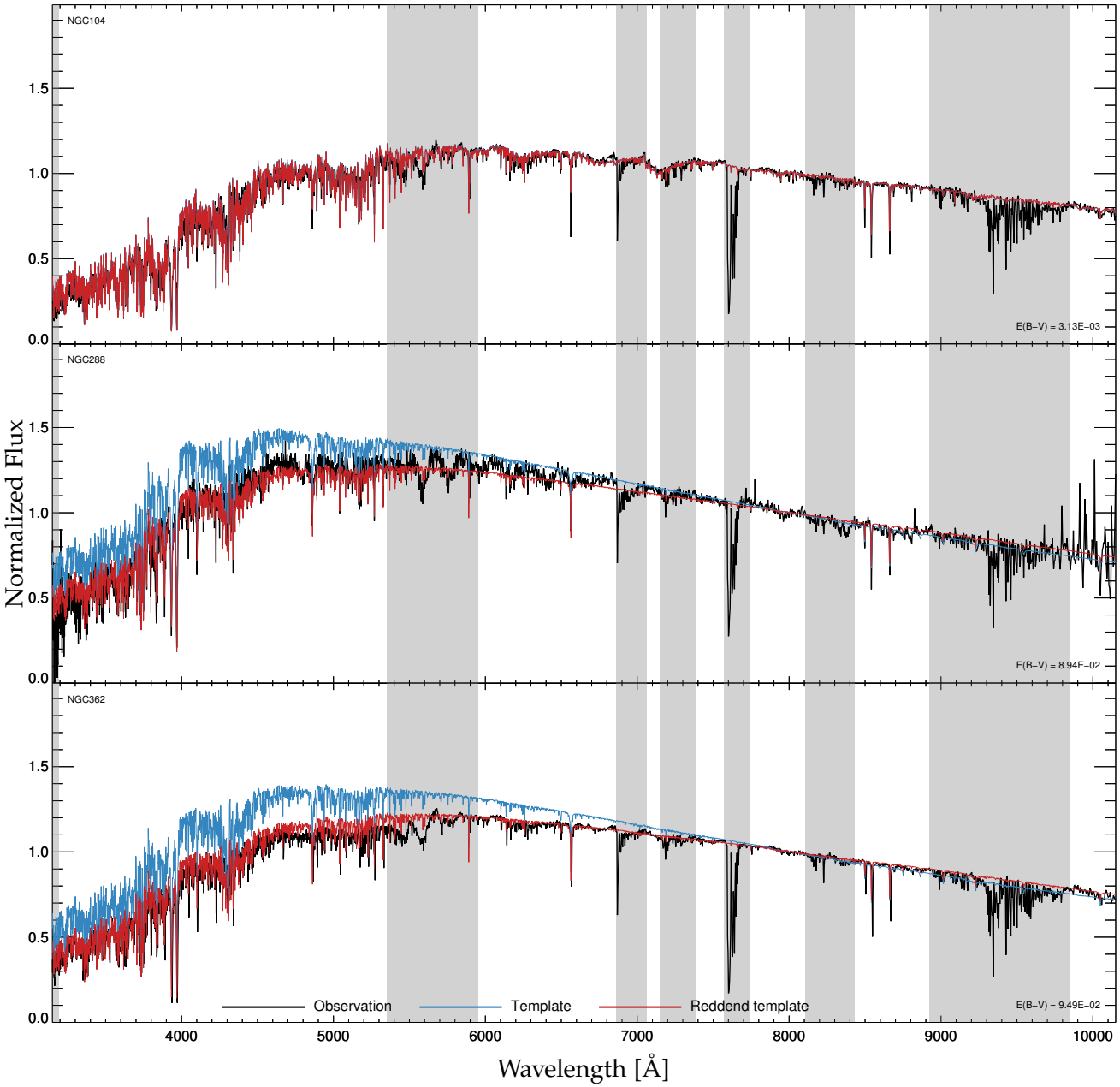

Figure 38: Cumulative spectra for our sample of eleven GCs. For each cluster, the black curve is the sum over all flux-calibrated observational drift-scans after sky subtraction and represents an estimate to the luminosity-weighted average spectrum within the GC half-light radius r_h. The corresponding template spectrum is plotted in blue (before reddening correction) and red (after reddening correction). The obtained best-fit reddening values $E(B-V)$ are given in the bottom right corner of each panel. Telluric absorption bands (gray-shaded regions) have not been accounted for in the reduction process and they have been masked out for the reddening estimates and the velocity dispersion measurements. The region between 5,350 Å and 5,950 Å has been excluded in the analysis due to the dichroic throughput instability. All spectra have been normalized so that the median flux in the range 7,800 Å – 8,200 Å corresponds to unity. The Figure is continued on the two subsequent pages.

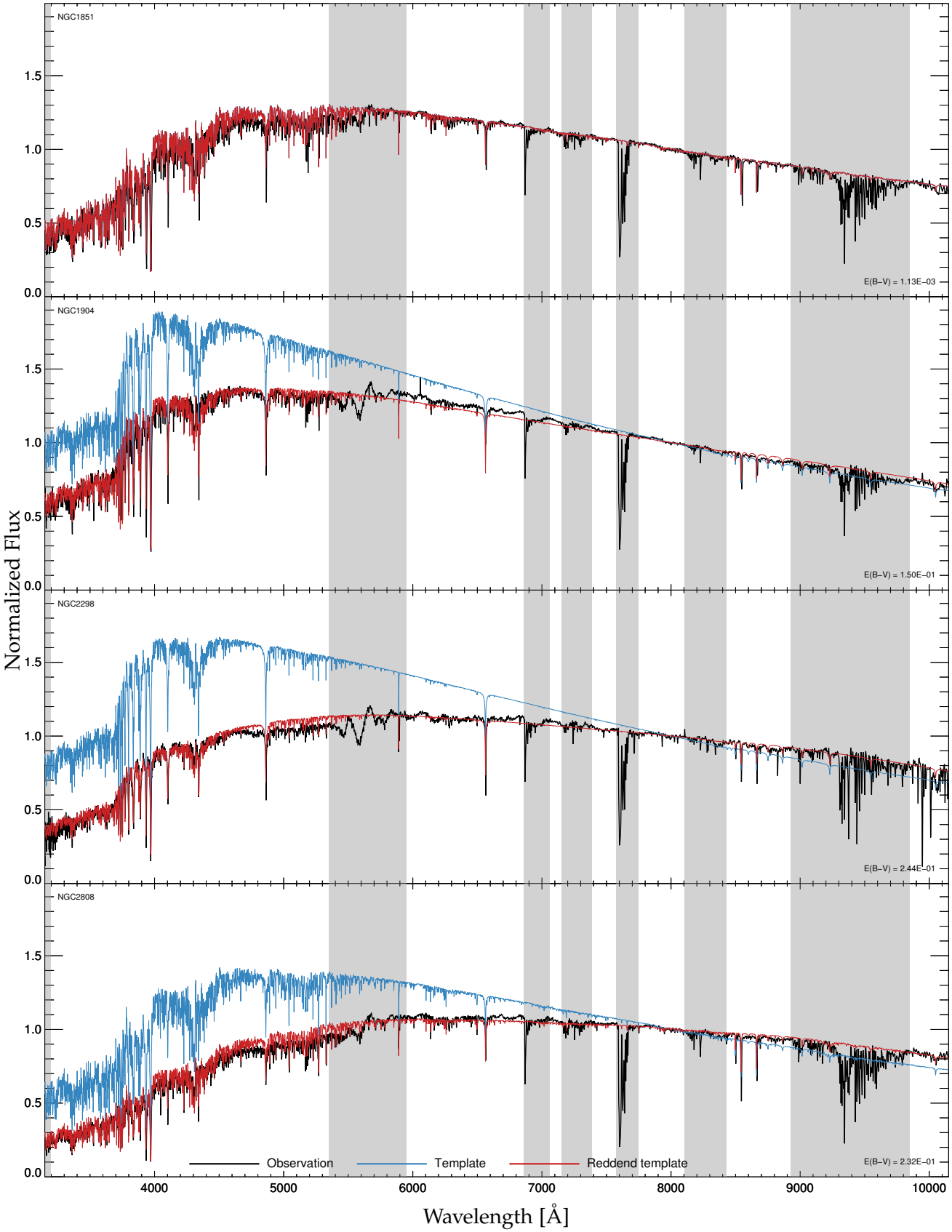

Figure 38 – Cont.

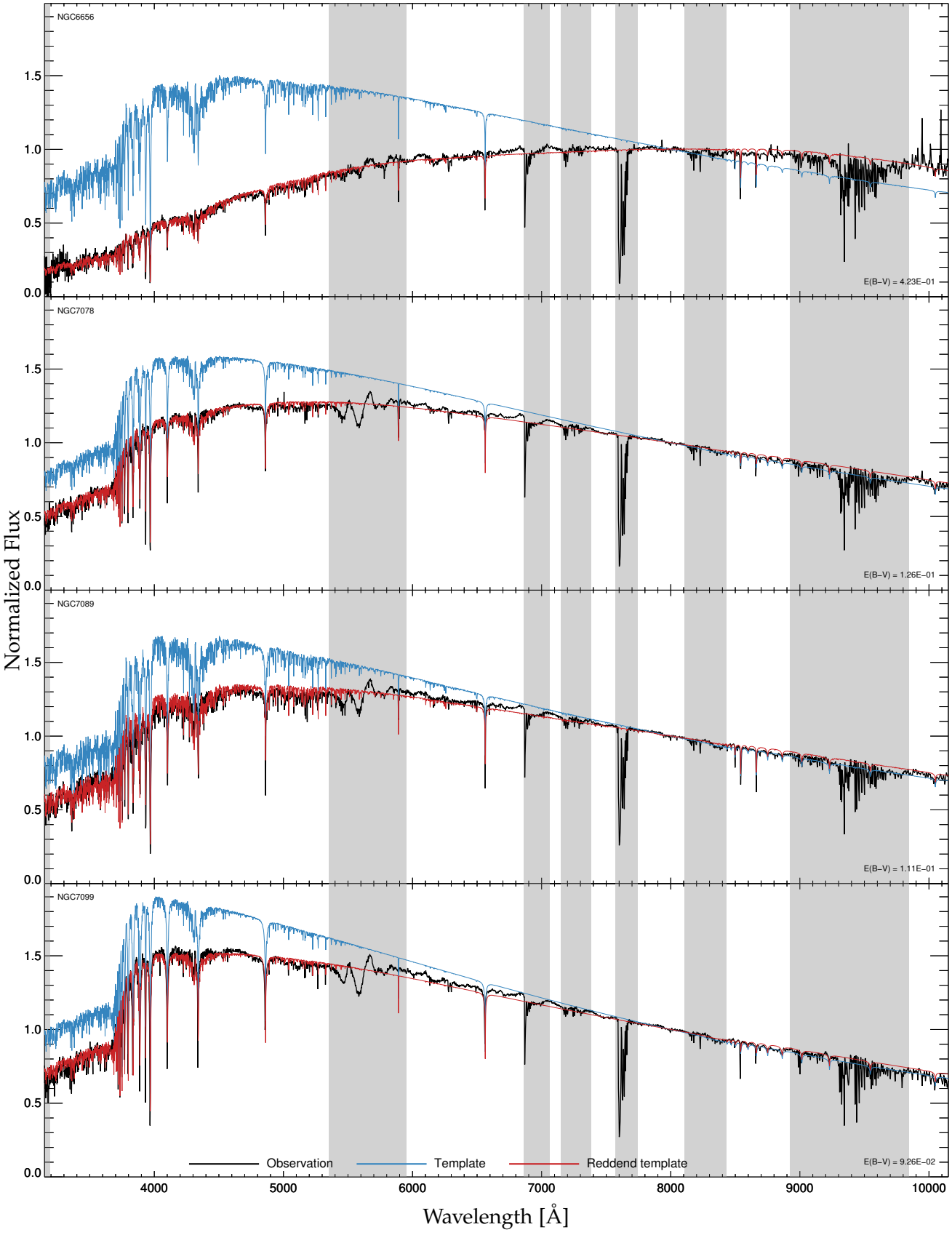

Figure 38 – Cont.

matched by the template, and thus if the template is considered the reference spectrum, the feature sticks out as an enhancement of flux. Nevertheless, an erroneous depletion of flux in the template could equally well explain the observed deviation). Furthermore, we could not reproduce a similar feature when applying the same sensitivity function to an additional flux standard star, and therefore conclude that issues in the flux calibration are unlikely to be the cause of the observed flux bump. This conclusion is supported by the fact that the shape of the bump differs from cluster to cluster (e.g., NGC6656 and NGC288 only show mildly pronounced features), which is unexpected if the flux-calibration, where the same sensitivity function is applied to all GCs in our sample, is responsible. It should be noted that there is a prominent sky line located at $\lambda\lambda\,6864$, right before the atmospheric absorption trough. As sky lines are variable on a $\sim 2-3\%$ level over the time scale of one drift-scan, we do expect residuals in the sky subtraction, since we do not differentially scale the emission lines in the sky frame to match those in the GC spectrum. These residuals, however, should be distributed symmetrically around zero, thus producing over- and undersubtraction artifacts with equal probability. By contrast, the flux overestimation observed for all GCs is, firstly, much broader than an individual emission line, and, secondly, always positive with respect to the underlying template spectrum. Sky subtraction issues can thus be ruled out as a possible cause for the observed feature.

Under the hypothesis that systematic problems in the data reduction are generally not considered to be responsible (this statement, however, has to be handled with care), the obvious explanation for the observed deviation is a difference in chemical composition and / or the stellar atmosphere physics between observation and template.

In order to identify the vast number of features in the GC composite spectra (see Figure 38) a detailed element abundance analysis is crucial, which, however will not be presented here and is planned for a subsequent project. Yet, to give a qualitative overview of possible candidate features that might be responsible for the bump, we show a sequence of eight characterstic dwarf-spectra (from O to M spectral type) between $3,500$ Å and $7,000$ Å in Figure 39, five additional spectra from G to M in the range $3,800$ Å $-$ $5,600$ Å in Figure 40 (both figures taken from Gray & Corbally 2009), and three M dwarf spectra in the range $5,200,$ Å $-$ $9,000$ Å in Figure 41 (taken from Lowrance et al. 2002). In the spectral region of interest ($\sim 6,500$ Å $-$ $7,000$ Å) dominant absorption features can only be seen for K and M stars, for which the atmospheric temperatures are sufficiently cool that molecules can form. Titanium oxide (TiO) certainly has the greatest influence on the spectral shape for these stars, as it forms strong absorptions bands in the entire visual wavelength range such that nearly no continuum emission can be identified. Nevertheless, the actual position of the bump feature is incompatible with TiO (which is rather responsible for the decline redwards of $\sim 7,000$ Å). Calcium hydrate (CaH) is a second molecule that strongly contributes to the absorption bands bluewards of $\sim 7,000$ Å in cool stars (see Figure 41), but, as for TiO, the absorption is maximal where the bump in the GC composite spectrum is located, and thus CaH can be ruled out as a possible explanation as well.

The only objects whose spectrum naturally reproduce the flux maximum observed at $\geqslant 6,800$ Å in our GC composite spectra are carbon stars, for which we show some exem-

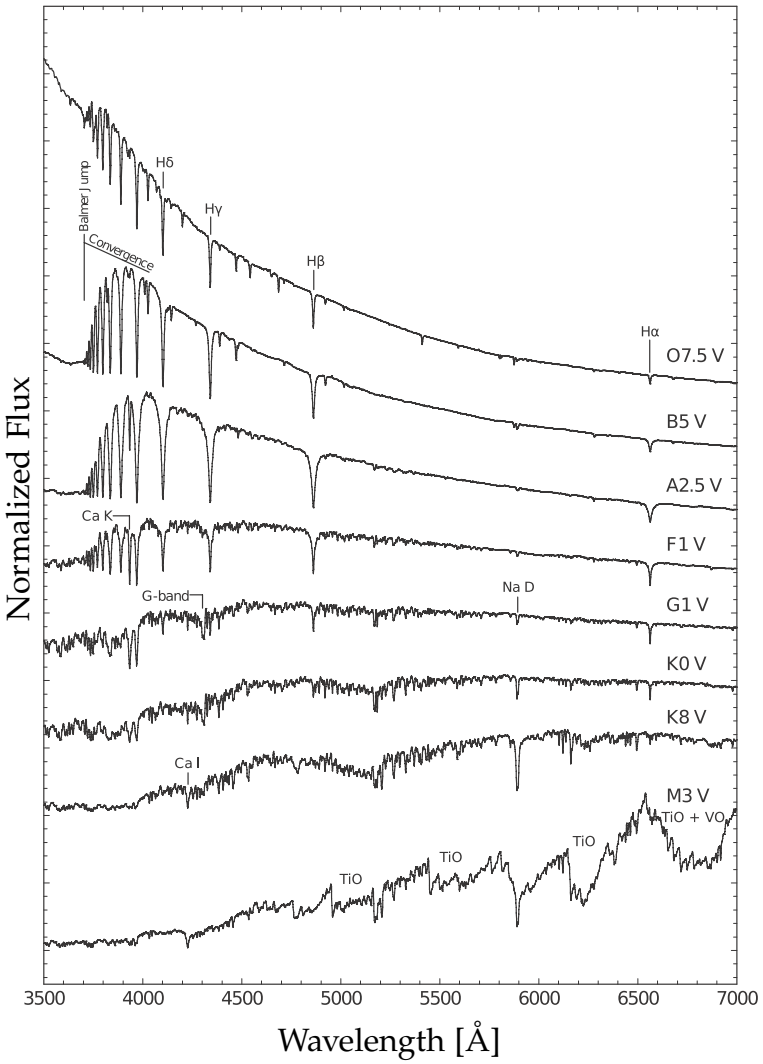

Figure 39: Characteristic spectra of eight different MS dwarfs, ranging from O- to M-type in the wavelength range $3,500\,\text{Å} - 7,000\,\text{Å}$. The most prominent spectral features are labeled. The hydrogen lines (Hα at 6563 Å to the Balmer jump at 3646 Å) increase in strength from O to A, then decrease. The two blended D lines of Na I increase downward. The H and K doublet of ionized calcium at 3968 Å and 3933 Å are strongest in G stars. The G-band (mainly due to the CH molecule) is neglible in types earlier than F, and then starts to strengthen toward the cooler types. TiO bands dominate in M-type spectra, but are almost entirely absent in earlier types. The spectra have been normalized at a common wavelength and separated by an arbitray offset for clarity. Figure taken from Gray & Corbally (2009).

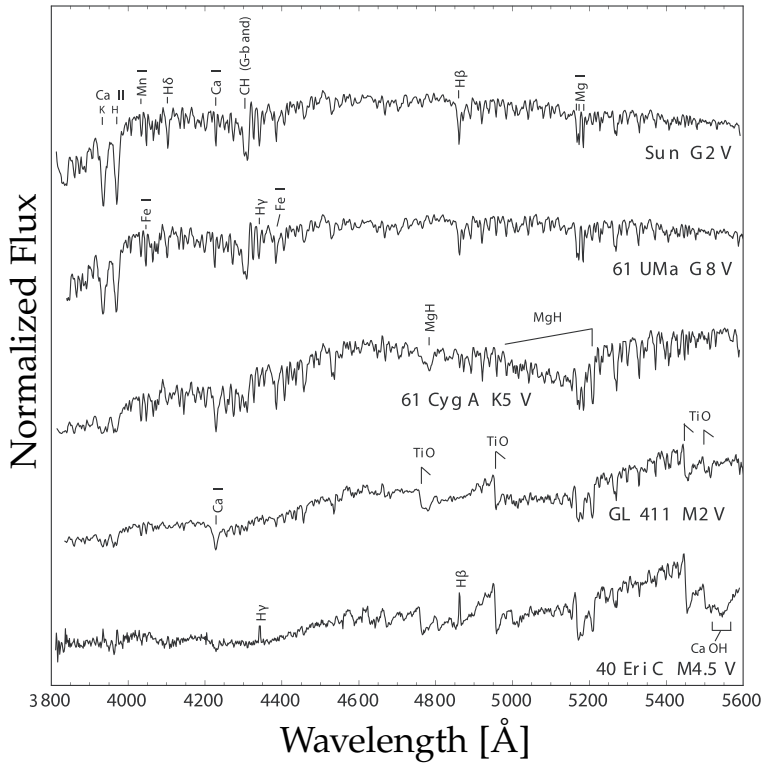

Figure 40: Characteristic spectra for MS stars from G to M in the wavelength range 3,800 Å – 5,600 Å. The most prominent spectral features are labeled. MgH absorption is strongest in K stars. TiO and CaOH strengthen toward later types. The bottom star radiates hydrogen emission lines from its chromosphere, caused by magnetic activity. The spectra have been normalized at a common wavelength and separated by an arbitray offset for clarity. Figure taken from Gray & Corbally (2009).

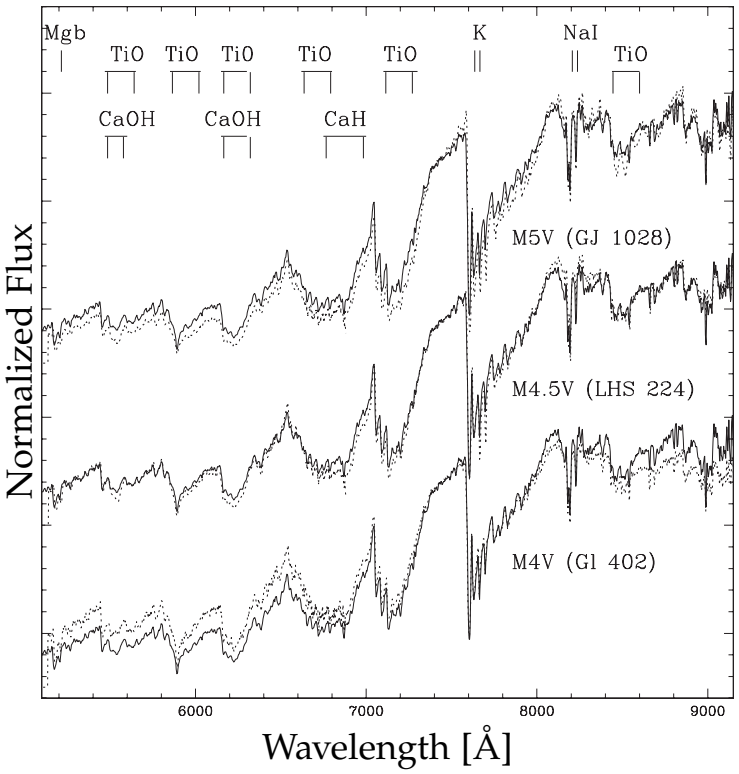

Figure 41: Characteristic M dwarf spectra in the wavelength range $5,200\,\text{Å} - 9,000\,\text{Å}$. The entire spectral range is dominated by strong TiO, CaOH, and CaH absorption bands. Of particular interest is the band head at $\sim 7,000\,\text{Å}$. This is too red to be responsible for the observed bump at $\sim 6,800\,\text{Å}$ in the composite spectra of our GCs (see Figure 38). Figure taken from Lowrance et al. (2002).

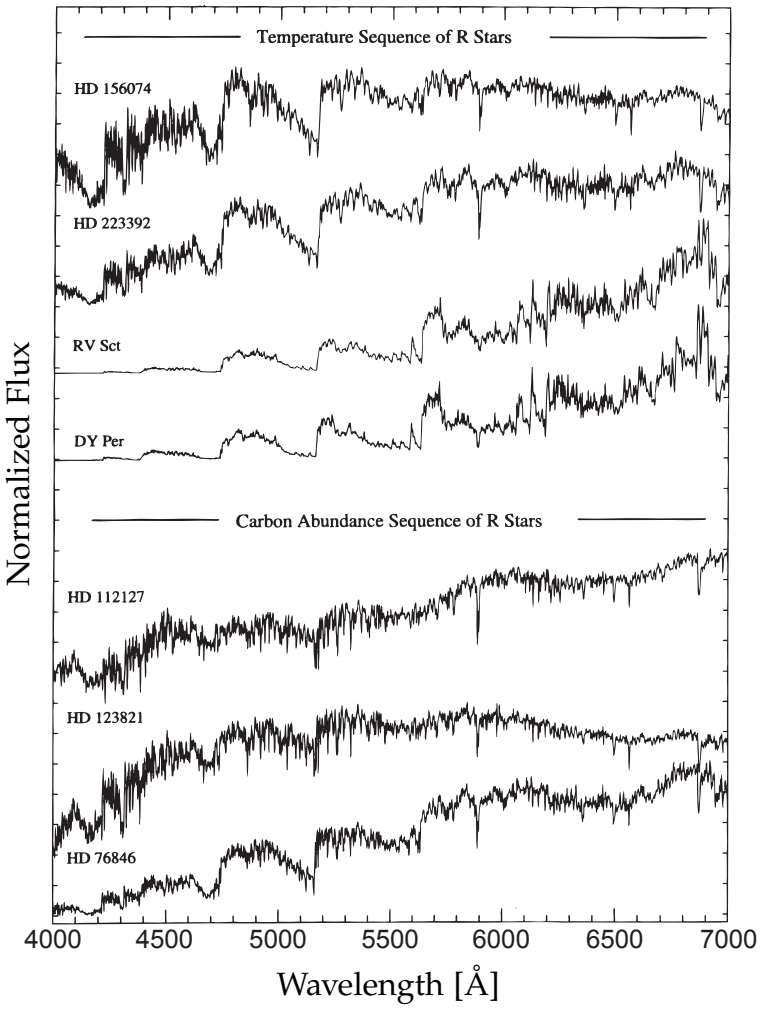

Figure 42: Characteristic carbon star spectra in the wavelength range $4,000\,\text{Å} - 7,000\,\text{Å}$. The first four spectra are ordered by surface temperature, ranging from hottest (top) to coolest (bottom). The three bottom spectra are ordered by carbon abundance (increasing from top to bottom). The local maximum at $\sim 6,800\,\text{Å}$ naturally aligns with the observed bump at $\sim 6,800\,\text{Å}$ in the composite spectra of our GCs (see Figure 38). Figure taken from Barnbaum et al. (1996).

plary spectra in Figure 42 (taken from Barnbaum et al. 1996). Carbon stars are late-type stars whose atmospheres contain more carbon than oxygen. After forming carbon monoxide (CO) in the upper layers of the star, the excess of available carbon atoms forms additional carbon compounds which lead to the strongly pronounced red color of the star. Most of the flux with $\lambda \leqslant 4,000$ Å is almost entirely suppressed, and molecules such as C_2, CN, and CH strongly obscure the continuum from 4,000 Å to 10,000 Å (in fact, it is predominantly CN that contributes to the total absorption in the relevant wavelength range, see Boyer et al. 1975; Barnbaum et al. 1996). Since the ISM (out of which the stars are formed) is everywhere oxygen- rather than carbon-rich, the inversion of the C/O ratio in carbon stars has to be caused either by *internal* stellar evolution or some *external* process, i.e., through environmental interaction (Barnbaum et al. 1996). Currently, there are two accepted formation scenarios for carbon stars (e.g., McClure 1985; Wallerstein & Knapp 1998). In the internal scenario, the abundance of carbon is thought to be a product of helium-shell burning at the end of the AGB phase, and, through the third dredge-up (e.g., rotational mixing), is brought to the stellar surface. By contrast, the external mechanism involves mass transfer in a binary system of a white dwarf and a red giant (or red dwarf). The mass transfer, however, happened in the past, when the today's white dwarf was still in its AGB phase and produced an overabundance of carbon through the internal stellar evolution scenario described above. The star presently observed to be a red giant accreted the carbon-rich material (which was lost through strong stellar winds by its companion) when it was still on the MS, and thus the excess of carbon observed in its atmosphere today was not produced internally in this star. There are individual, known carbon stars in Galactic GCs (e.g., Côté et al. 1997; Sharina et al. 2012), however their discoveries were rather serendipitous and thus a robust estimate for their true number is not available. In this context it should be noted that Indahl & Pessev (2014) systematically searched GC CMDs for potential carbon stars and found a total of 128 candidate stars in the Harris catalogue (containing 157 GCs). These, however, are only candidates and follow-up observations are required both to determine their true nature and to confirm their GC membership. This perspective at least indicates that the spectral imprint of carbon stars could be contained in the composite spectrum of their host GC. In this scenario, however, the strength of the bump should vary along the cross-dispersed direction, since we would not expect carbon stars to be homogeneously distributed in the GC. A first preliminary analysis rather indicates a constant strength of the feature at all scan positions and so the suggestion to use carbon stars as a possible explanation for the observed feature remains speculative.

If, however, the bump feature is attributed to a CN absorption at $\sim 6,500$ Å in general, without the explicit need for one or more carbon stars in the GC population, then the required relative overabundance of C relative to O needs to be explained in an alternative way. In this context it is worth mentioning that, based on deep spectroscopy of individual MS stars, Harbeck et al. (2003) have found a bimodal CN abundance distribution for NGC104. Their measurement is based on the widely-used spectral indices defined at $\lambda\lambda\,3883$ and $\lambda\lambda\,4215$ (Norris & Freeman 1979; Norris et al. 1981), but unfortunately no predictions for the expected absorption strengths at redder wavelengths are given. The au-

thors argue that, contrary to internal stellar evolutionary processes (MS stars in GCs with masses $\leqslant 0.8\,M_\odot$ do not have deep convective envelopes and, as a consequence, processed material is not brought up to the surface easily), binarity combined with pollution by AGB stars—similar to the external formation scenario for carbon stars (see above)—is likely to be one of the causes to explain the observed abundance distribution. A third scenario is also presented, in which the CN abundance bimodality results from self-enrichment during the star formation episode of NGC104, i.e., from exploded high-mass stars that enriched the remaining ISM with metals. This, however, would imply an abundance variation not only for light elements, and thus does not naturally explain the observed lack of variations in the heavy elements (Cannon et al. 1998). In order to shed new light on this topic we propose to perform a dedicated analysis of the $\lambda\lambda\,3883$ and $\lambda\lambda\,4215$ indices for our composite GC spectra and check the obtained results for consistency with the observed absorption strength at $\sim 6,500\,\text{Å} - 7,000\,\text{Å}$. In addition, as our spectra are taken at varying distance from the respective cluster center, the spatial dependance of the absorption strength might further help to distinguish between different formation scenarios. We note that the integrated-light spectrum of the globular cluster NGC6528 in the work of Puzia et al. (2002, their Figure 5) shows a similar bump at $\sim 6,800$ Å, but the feature remains uncommented. Nevertheless, the mere existence favors the idea of a true chemical cause over a residual artifact from an imperfect flux calibration, and is likely connected to the topic of multiple stellar populations (Richer et al. 2013 claimed evidence for up to four distinctly different main sequences; see Section 1.2). We note that at least two other clusters in our sample, NGC288 and NGC362, are known to exhibit an inhomogeneous CN distribution as well (Smith & Langland-Shula 2009) and so it seems worthwhile to repeat the spectral synthesis with appropriately scaled C and O abundances. The synthetic spectra offered by Gustafsson et al. (2008), which are based on the code *MARCS* and explicitly span a wide range in C/N and C/O ratios might be preferred to further explore the implications of carbon enhancement in the composite spectra of our GCs.

Evaluating the template match quality of the rest of our sample, we find that it is on average considerably worse than for NGC104. Almost all observed composite spectra show a depleted flux level at $\sim 5,100$ Å, which is caused by Magnesium monohydride (MgH; see Figure 40) in combination with the Mg*b* triplet. Additionally, we find major differences typically at $\sim 4,800$ Å and $\sim 6,300$ Å, which are likely due to TiO and / or CaOH (compare Figures 40 and 41). These deviations from the template spectra could be due to a wrong estimate of the utilized [α/Fe]-abundance in the synthesis process (all of these elements are considered α-elements). This is expected to a certain degree, since both the literature values are somehow uncertain and the values were rounded to multiples of 0.2 dex to agree with the sampling of the PHOENIX library. Yet, it seems that the observed spectra are systematically lower especially in the $\sim 5,100$ Å region (NGC288 forms an exception, but this could be due to an offset in the reddening estimate because the overall slope of the continuum for $\lambda \gtrsim 6,000$ Å does not really match either), which might hint at an incomplete physical treatment of the utilized template atmospheres. The fact that NGC104 is overall better reproduced in the template synthesis process might be connected to its higher metallicity: According to Figure 28 it contains nearly no stars with temper-

atures $\geqslant 8,000\,\mathrm{K}$, the limit above which we have to use scaled- solar [α/Fe]-abundances for the template construction (see Section 4.4 for details on this restriction). In turn, this implies that in all other clusters, there is a significant number of stars (or better, flux, as we are more concerned about the integrated light), which are synthesized with an underestimated [α/Fe]-abundance (the GCs in our sample all have $[\alpha/\mathrm{Fe}] \gtrsim 0.2$; compare Table 4). This almost exclusively affects hot HB stars (stars with $\leqslant 3,500\,\mathrm{K}$ also have to be modeled with scaled-solar [α/Fe], but they only insignificantly contribute to the overall flux) and one may argue against it that in A-type stars with $T \approx 10,000\,\mathrm{K}$ no significant metal lines are expected (compare Figure 39). In this context, however, it is worth mentioning that there is now considerable evidence that HB stars hotter than $\sim 11,500\,\mathrm{K}$ experience a dramatic enhancement of their photospheric heavy element abundances through radiative levitation (Landsman 1999; Grundahl et al. 1999). Under certain conditions, momentum from photons can be transferred onto ions in the lower stellar layers. As a consequence, some chemical elements are pushed upwards and cause overabundances in the outer atmospheric layers. This effect, however, is very selective on the nature of the element: the capability to absorb momentum from the stellar radiation field strongly depends on the element's ionization potential and a range between $\sim$ 10.5 eV and $\sim$ 13.6 eV is favored (Cassisi & Salaris 2013), which includes C, P, Cl, and Ca. The involved processes, however, are complex and for those elements with ionization energies between $\sim$ 13.6 and $\sim$ 18 eV, no general answer can be given whether or not these ions couple sufficiently strongly to the radiation field so that they can be levitated to the star's surface. Nevertheless, the following trends have been found (Behr et al. 1999, 2000; Behr 2003; Pace et al. 2006): the majority of HB stars hotter than $\sim 11,500\mathrm{K}$ show iron abundances $[\mathrm{Fe/H}] \gtrsim 0.0$, which, depending on the initial cluster metallicity, corresponds to enhancements by a factor of $30-300$. A factor of ~ 100 is found for Ti, and Ca is typically enhanced more modestly by a factor of 10. By contrast, Mg shows little, if any, enhancement. This selective coupling implies that a parametrization of the elemental abundances by [Fe/H] and [α/Fe] is probably insufficient to characterize a stellar atmosphere. As a consequence, detailed model atmosphere computations incorporating more realistic heavy element distributions would be required for the hot HB populations of almost all GCs in our sample to estimate the influence of radiative levitation on the composite spectrum. In addition, there is now comprehensive evidence for light element abundance variations (see Gratton et al. 2004, for a review) within individual GCs, and so scaling the abundances of all α-elements by the same amount might not be an appropriate approximation in general for a cluster's stellar population.

Regardless of the shortcomings mentioned above, we point out that the computed templates already represent a remarkable match to the observational drift-scan data. We emphasize that the synthesized spectra shown in Figure 38 are no fit to the observed data, but were obtained by converting photometric data by means of stellar evolution (i.e., isochrones) into model spectra. Since all stars in a cluster have been modeled with the same chemistry it comes as no surprise that any potentially existing variations in the elemental abundances are not reproduced properly. Given the richness of detail that our data set offers, we will certainly pursue this intriguing topic in a subsequent project, where de-

tailed elemental abundances will be derived. For the purpose of comparing the templates with the observational spectra to measure the velocity dispersions for our sample of GCs, we apply no further modifications to the templates and correct for any residual slope difference by fitting additional long-scale polynomials (see Section 5.2).

5.5 SINGLE- AND MULTI-KINEMATIC COMPONENT MODES

Given the large number of parameters that can be adjusted in the *pPXF* code (see Section 5.2), we performed extensive test runs to measure the performance and evaluate the significance of the obtained results. We eventually decided to employ *pPXF* in two different ways, which both yield consistent, but slightly different outcomes. We will first present our motivation for the utilized approaches and then discuss the obtained results in Section 5.6.

1. *Single-component mode*: In this approach we first construct the cumulative template for each slit position. With cumulative template we mean the sum over all contributions of the various phases (i.e, similar to the spectra plotted in black in Figure 36. Each slit bin of the template is then fitted against the observed drift-scan spectrum using *pPXF* in the single-kinematic-component mode, i.e., $k = 1$ and only one $\mathcal{L}(v)$ is used (see Equation 45). After numerous test runs we decided to switch off the Hermite-expansion of the LOSVD entirely, as the usage of systemic velocity V and dispersion σ as the only parameters in $\mathcal{L}(v)$ yielded the most robust and consistent results. We include six additive and six multiplicative Legendre polynomials in the fit to correct for any difference in continuum shape. The initial values for (V, σ) are chosen as $(V_{r,0}, 3\,dv)$, where $V_{r,0}$ are the radial velocities from Harris (2010) to which we added the helio-centric velocity correction (as indicated by the respective header keyword of the X-SHOOTER frame), and $dv = 5.10\,km\,s^{-1}\,px^{-1}$ is the velocity scale of the logarithmically rebinned spectrum. CE04 suggest to oversample the template in case the expected velocity dispersion drops below $\sim 0.7\ dv \approx 3.6\,km\,s^{-1}$ for our data. This is not expected for the majority of clusters in our sample (with the exception of NGC288, which is listed with $2.9\,km\,s^{-1}$ in the Harris catalogue) and consequently we decided not to perform any oversampling[4]. This minimizes the computation time dramatically.

2. *Multi-component mode*: In this mode we essentially use the same fitting parameters as in the single-component mode, i.e., six additive and six multiplicative Legendre polynomials to account for deviations in the continuum shape and (V, σ) as the only parameters defining a LOSVD. Contrary to the single-component mode, however, we do not combine the contributions of the respective evolutionary phases into a cumulative template, but feed the individual phase templates into *pPXF* simultaneously (see Equation 45). The total number of templates is given by the number of individually modeled evolutionary phases (seven) plus one additional template resembling the brightest star at the slit posi-

4 We conducted dedicated fitting runs with oversampled templates in order to assess potential biases. In most, if not all, cases (including NGC288) we could not find significant deviations.

tion under study. This treatment is owed to the specific drift-scan mode: Individual stars can contribute up to $\sim 50\%$ of the total flux in a single slit bin, and thus dominate the observed spectrum. In these cases, a measurement of the velocity dispersion is accordingly more intricate, as the velocity-broadend spectrum of the diffuse bulk of GC stars will be strongly blended by the spectrum of the bright star. By definition, if stellar rotation is neglected, this single spectrum has no additional line-broadening (in addition to the line broadening mechanisms inside the stellar atmopshere) and we therefore expect that the velocity dispersion inferred from such a composite spectrum is correspondingly smaller. We address this issue by fitting two independent LOSVDs, one for the template of the bright star, $\mathcal{L}(v)_\star$, and one for the seven remaining templates, $\mathcal{L}(v)_\bigcirc$, which resemble the diffuse cluster light. According to Equation 45 the fitted model (without the additional Legendre polynomials) can be written as

$$G_{\rm mod}(x) = w_\star \left(B_\star * T_\star\right)(x) + \sum_{k=1}^{7} w_{k,\bigcirc} \left(B_\bigcirc * T_{k,\bigcirc}\right)(x), \tag{56}$$

where the sum includes all templates that are used to model the diffuse light component. Since we have detailed knowledge about all stars contributing to a particular slit position, we can infer the weight of the bright star template $w_\star$ from the *HST/ACS* photometry. For most slit positions, the brightest star contributes $\sim 10\% - 20\%$, but in some cases we find values $\gtrsim 50\%$ (see panel two of Figure 43 for the contribution of the brightest star as a function of slit position; this topic will be further discussed in Section 5.6). The template $T_\star$ for the brightest star is chosen according to its evolutionary phase, and in most cases it is a RGB template. We note, however, that we do not use a template that specifically matches $\{T_{\rm eff}, \log\ g\}$ of the brightest star, but take the average evolutionary phase template to which the respective star belongs and scale the total flux to the luminosity of the star. Evidently, this might not be a perfect fit for the particular star of interest, but we argue that any uncertainties introduced by this shortcoming are likely negligible. Nevertheless, we plan to include an accurate modeling of the brightest star in a revised analysis. When fitting the model spectrum $G_{\rm mod}(x)$ of Equation 56, we impose several boundary constraints for numerical stability reasons.

Firstly, the velocity broadening line profile for the bright star template $\mathcal{L}(v)_\star$ is kept fixed at zero velocity dispersion, but the radial velocity is allowed to vary freely within $\pm 15\,\mathrm{km\,s^{-1}}$ relative to the radial velocity of the diffuse component. This setup reflects that this template is used to model the contribution of an individual star, which is superimposed onto the diffuse light of the GC, and thus might be shifted in radial velocity with respect to the underlying cluster average. Enforcing zero velocity broadening for this template implicitly implies that we do not allow for any rotation of the brightest star, yet this constraint is numerically required to minimize potential degeneracies between the two fitted LOSVDs: Allowing *pPXF* to broaden the bright star template unboundedly may lead to scenarios where the necessary broadening is either entirely attributed to the bright star template or shared with varying amounts between the two kinematic components. As we are interested in a robust estimate of the velocity dispersion of the diffuse light

component, this is an undesired effect and fixing $\mathcal{L}(v)_\star$ to zero broadening has shown to decrease the numerical scatter.

Secondly, the individual weights of the diffuse light templates $w_{k,\bigcirc}$ are allowed to be re-determined by *pPXF* within specified boundaries, which we set to be 0.5 and 2. Thus, the relative contributions of the individual templates get re-weighted in the composite model, which potentially allows for an optimized χ^2. The specified boundaries reflect the fact that we have prior knowledge on the respective phase weights (as determined from the photometric *HST/ACS* data), however, they allow for minor variations about the values inferred in Chapter 4) to compensate for any systematic uncertainties introduced during template construction. These might originate from different treatments of the evolutionary phases: While MS, SG, and RGB are consistently modeled with the same isochrone, the HB is synthesized with a separate model, and, thus might suffer from systematical differences in the estimated overall luminosity. This may be particularly true for those clusters, where we had to specifically shift the model HB population to brighter luminosities to obtain a good match with the observed stars. Since we did not rescale the luminosity weights of the inferred stellar parameters accordingly, the shift of the model HB population might lead to a potential underestimation of the total HB contribution and thus the proposed re-weighting in the *pPXF* model construction becomes reasonable. Furthermore, allowing for a re-estimation of the template weights seems justified by a second argument: it was stated in Section 4.5 that for some GCs no clear allocation to a distinct evolutionary phase can be made for stars that occupy the area between RGB and HB in the CMD (see Figure 27), as the models for the HB, RGB, and BSS overlap in this region. It, therefore, has to be expected that individual stars in this area suffer from an incorrect mapping (this phenomenon was already discussed in Section 4.5). Nevertheless, the re-weighting process has to be performed with care in order to avoid unphysical scenarios in which the inferred best-fit weights are inconsistent with the distribution of stars in the *HST/ACS* CMDs. In addition, the unbounded fit is disfavored for a second reason: it bears the risk of yielding strongly degenerate results, as intrinsic differences in the line widths between the evolutionary phases might be misused as substitute for the required velocity broadening. In more detail, a relative overestimation of the HB template (with intrinsically broad lines due to both high temperature and relatively large surface gravity) leads to a systematically lower estimate for the GC velocity dispersion, because part of the required line broadening in the model spectrum is achieved by using a template with broader features, instead of using a spectrum with narrow lines and accounting for the necessary line-broadening with an appropriately chosen LOSVD. In mathematical terms, this can be explained by analyzing Equation 56: The line broadening in the model spectrum $G_{\mathrm{mod}}(x)$ results from an interplay between intrinsic line shape of the template spectrum $T_k(x)$ and the kinematic broadening kernel $B(x)$, which reflects the velocity dispersion of the cluster. Increasing the respective weight w_k of a broad-line template results in accordingly lower estimates for the LOSVD. Vice-versa, using an RGB-only template might lead to an overestimation of the velocity dispersion, since the required broadening is then entirely accounted for by external cluster kinematics and the contributions of any line-broadening mechanisms appearing internally in hot and dense stellar atmospheres are mostly neglected in the

wavelength range [Å]	remarks
$3,000 - 3,200$	low S/N
$5,350 - 5,950$	dichroic
$6,860 - 7,060$	telluric abs.
$7,150 - 7,385$	telluric abs.
$7,575 - 7,744$	telluric abs.
$8,104 - 8,427$	telluric abs.
$8,924 - 9,847$	telluric abs.

Table 8: Spectral regions masked from the *pPXF* fit. The first column lists the wavelength range, the second column denotes the reason why the range was excluded.

formation of the composite spectrum. The exact choice $0.5 \leqslant w_{k,\bigcirc} \leqslant 2$ has been made after a number of test runs and has been found to produce robust and meaningful results.

It is important to note that in both modes we do not include the full available spectral range in the fit. The masking becomes necessary for a number of reasons, which we will briefly summarize here.

1) We do not correct for telluric absorptions, and thus the observational data will contain strong absorption bands from which no information can be extracted. These bands can be found at wavelengths $\gtrsim 7000$ Å and are typically confined to regions with an extent of ~ 250 Å. The location of these bands is well-defined and constant in time, which allows a simple masking. To determine the atmospheric windows, we used the flux standard star observation with its pronounced continuum emission and selected all wavelengths that shows strong depletions in flux. We list the defined windows in Table 8.

2) Due to the temporal variability of the dichroic throughput we consider all wavelengths in the spectral overlapping region between UVB and VIS arm unreliable. This encompasses the spectral range $5,350$ Å $- 5,950$ Å.

3) The S/N in the bluest part of the UVB spectrum is typically very low, which might introduce biases in the fitted LOSVD. We thus decided to exclude all wavelengths bluewards $3,200$ Å to minimize this risk.

The masked regions are listed in Table 8 and furthermore indicated as gray-shaded regions in Figure 38.

5.6 KINEMATICS RESULTS

The fit of the template spectra to the observational data is performed independently for each slit bin (i.e., each pixel row in e.g. Figure 36), and yields a one-dimensional line-of-sight velocity dispersion profile σ as a function of radius. The final profile for NGC1851 (NGC1851 is used as showcase here, but all conclusions also apply to the other clusters in our sample) is shown in panel three of Figure 43 and contains many features that

were unexpected previous to the analysis. Consequently, Figure 43 contains a number of additional panels which we propose to consider in the interpretation of the observed features. Because parameter correlations play an important role in the subsequent analysis, all panels share a common x-axis, depicting the distance from the cluster center (note that the x-axis is given in four different units: [″] denotes the distance to the cluster center in arcseconds as given by the FITS header, $[r/r_h]$ gives the distance in units of half-light radii, $[r/r_c]$ is in units of core radii, and [pc] denotes the distance in parsec if the angular separation from the cluster center is converted via the distance modulus. The reference values for r_h and r_c have been taken from Harris (2010). The values of r_h are slightly different from the values that were used to set up our drift-scan observations and that are plotted Figure 6).

We will briefly describe each panel first and then present a detailed analysis of the obtained velocity dispersion estimates. A cluster-specific overview of the kinematics results for each GC is presented in Section 5.9.

5.6.1 *General Assessment*

Panel one (top) of Figure 43 contains the cross-dispersed light profiles of our observations (solid black curve) and the constructed templates (dashed red). The blue line is a fit to the minima of the observed light profile and will be used in a later step of the analysis. The second panel is split into two sub-panels. The top part shows the fitting-weights (blue and red curve) that are used to fit the obtained velocity dispersion profile of panel three with a smooth function, and will be explained later. The bottom part shows the relative flux contribution that the brightest star makes to the overall GC flux, i.e., $L_\star/(L_\star + L_\bigcirc) = L_\star/L_{tot}$, for each slit position. The third panel of Figure 43 shows our estimates for the velocity dispersion as a function of distance from the cluster center. The values obtained in single-component mode σ^{1T} (1T indicates that one template was used in the model construction) are plotted in blue (68%-confidence limits overplotted in light blue) and the values obtained in multi-component mode $\sigma^{8T}_\bigcirc$ (eight templates and two kinematic components) are plotted in red (error bands overplotted in light red). The smooth fit to the single-component mode data is plotted in purple (light purple error bands) and the fit to the multi-component mode is plotted in orange (light orange error bands). These fits will be discussed in more detail below. Panel four shows the obtained radial velocity profile v_r, however here three components are plotted. Red colors correspond to the values inferred by the single-component mode, blue colors depict the average radial velocity of the diffuse cluster component $v^{8T}_{r,\bigcirc}$ as determined by the multi-component mode, and the radial velocity of the bright star template $v^{8T}_{r,\star}$ is shown in green (also derived via the multi-component approach). Finally, panel five shows the reduced χ^2 of the *pPXF* fits for both the single-component mode (blue) and the multi-component mode (red). We note that whenever the *pPXF* fit yielded meaningful uncertainties we plot them as filled error bands in panels three and four. If no error estimate was output by *pPXF* (or an error that is much larger than the depicted plotting area), but still an estimate on the actual fitting parameter was obtained, we plot the respective value with a filled circle (without any

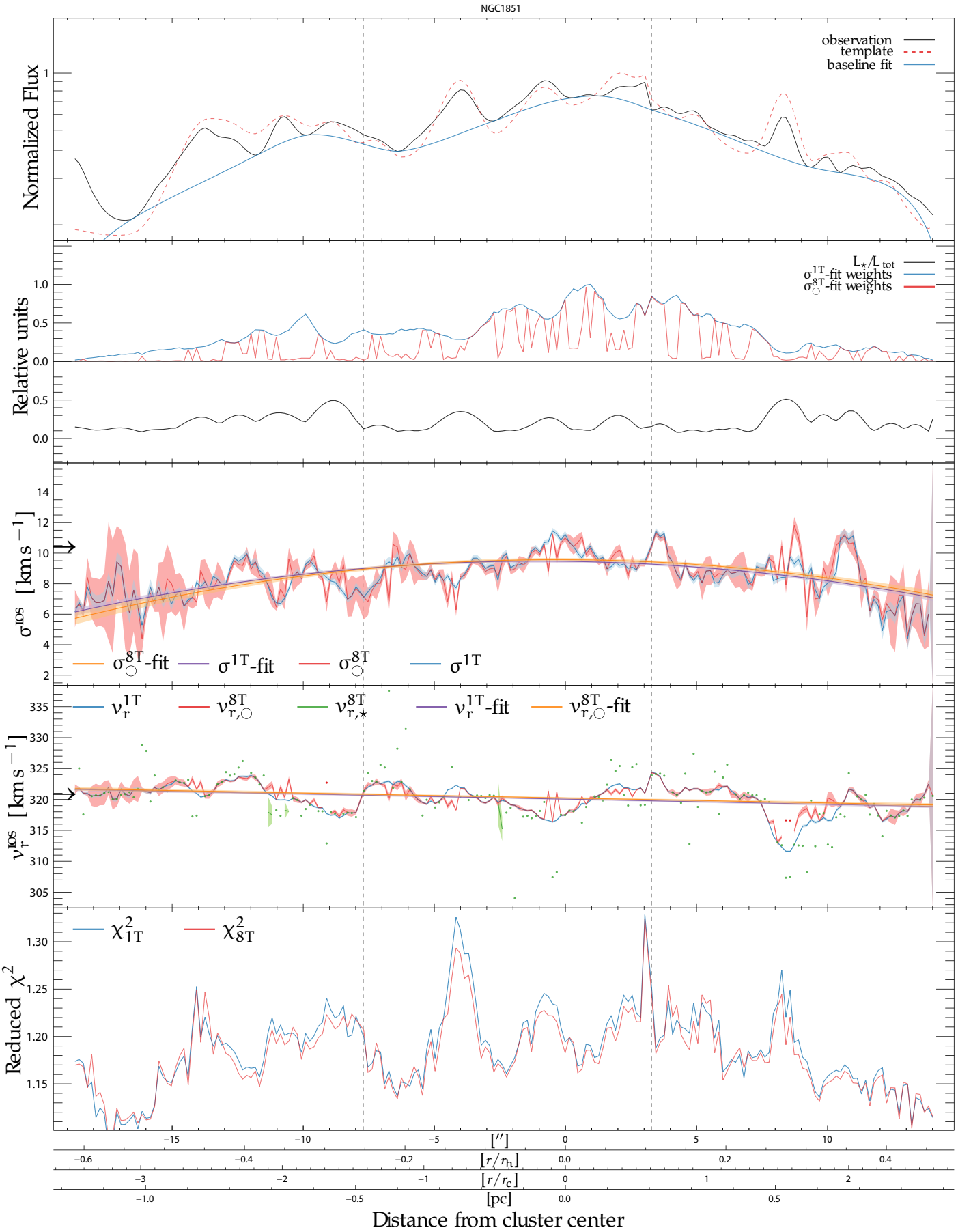

Figure 43: Luminosity and kinematics profiles for NGC1851. First (top) panel: cross-dispersed flux profiles. Second panel: fitting weights and flux contributions of the brightest stars. Third panel: velocity dispersion profile. Fourth panel: radial velocity profile. Fifth (bottom) panel: reduced χ^2 of the *pPXF* fits. A detailed explanation of the various plots is presented in Section 5.6.

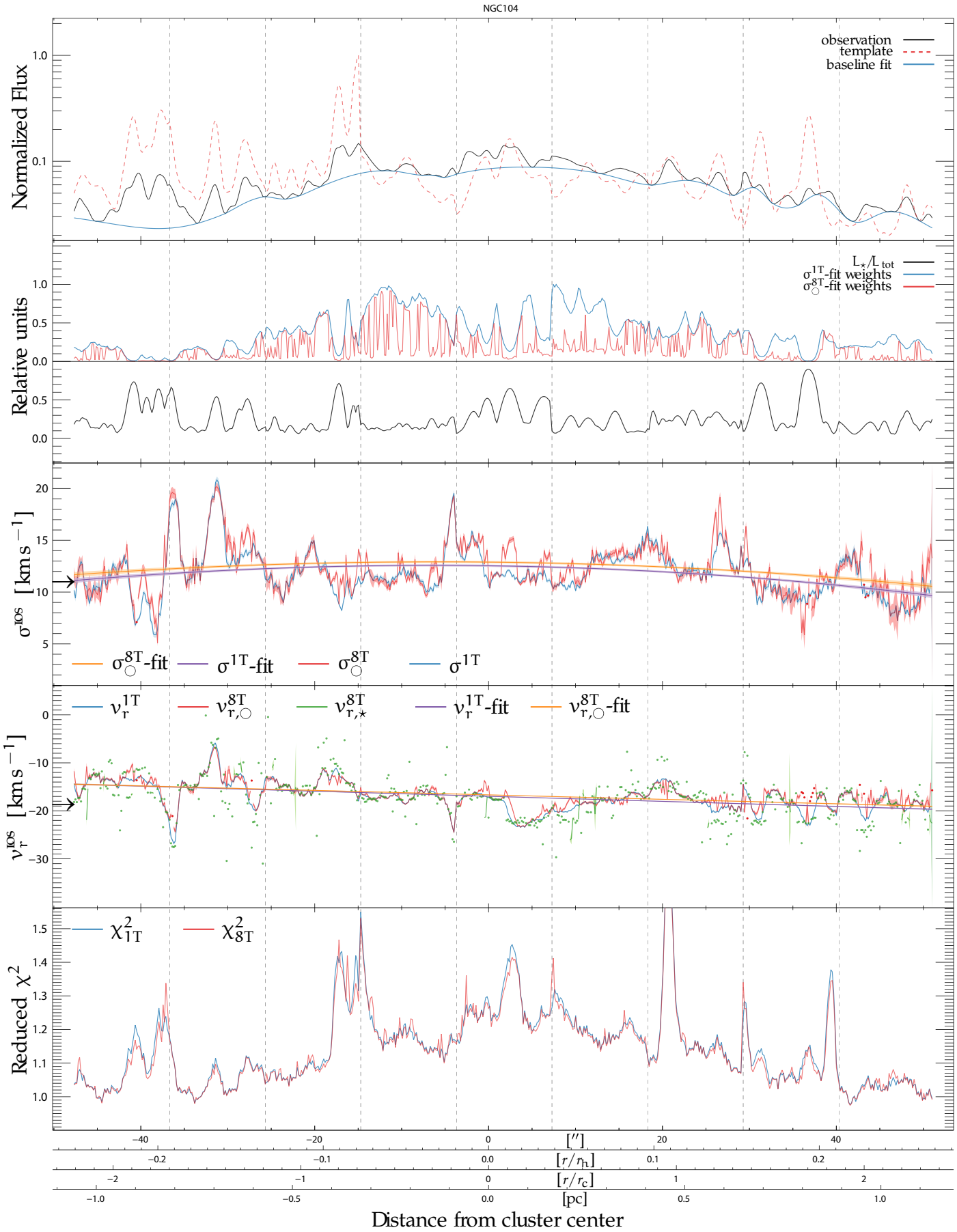

Figure 44: Same as Figure 43 but for NGC104.

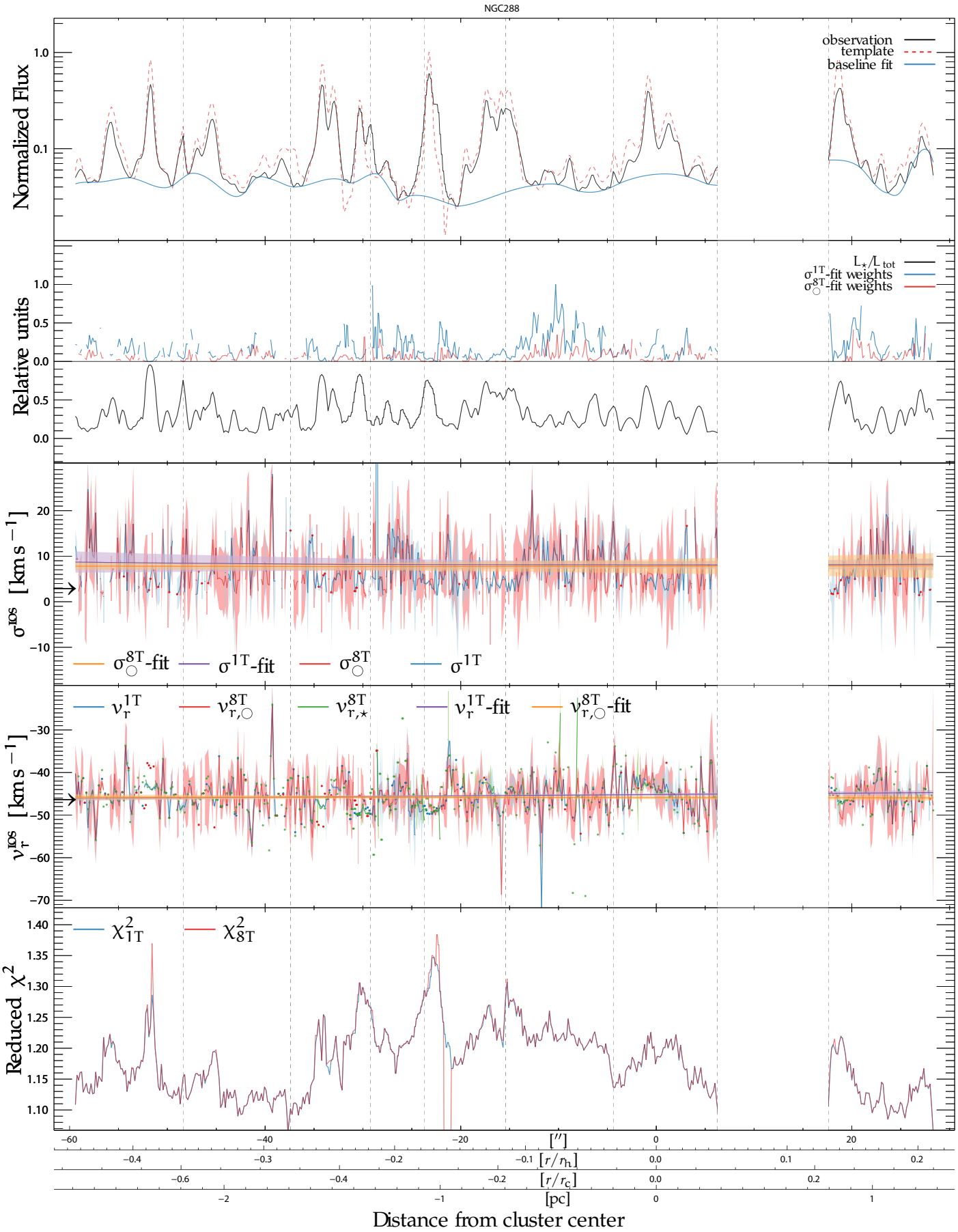

Figure 45: Same as Figure 43 but for NGC288.

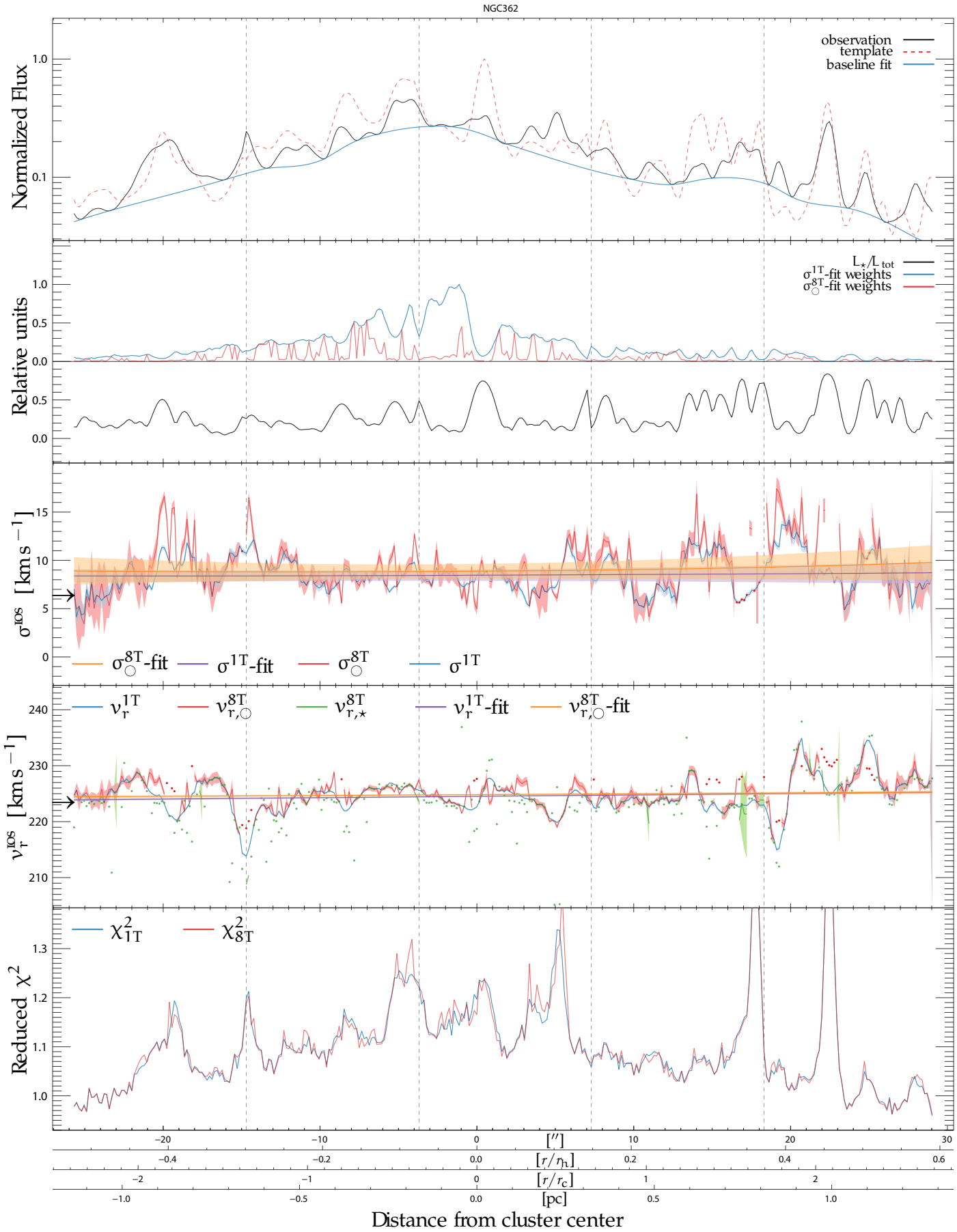

Figure 46: Same as Figure 43 but for NGC362.

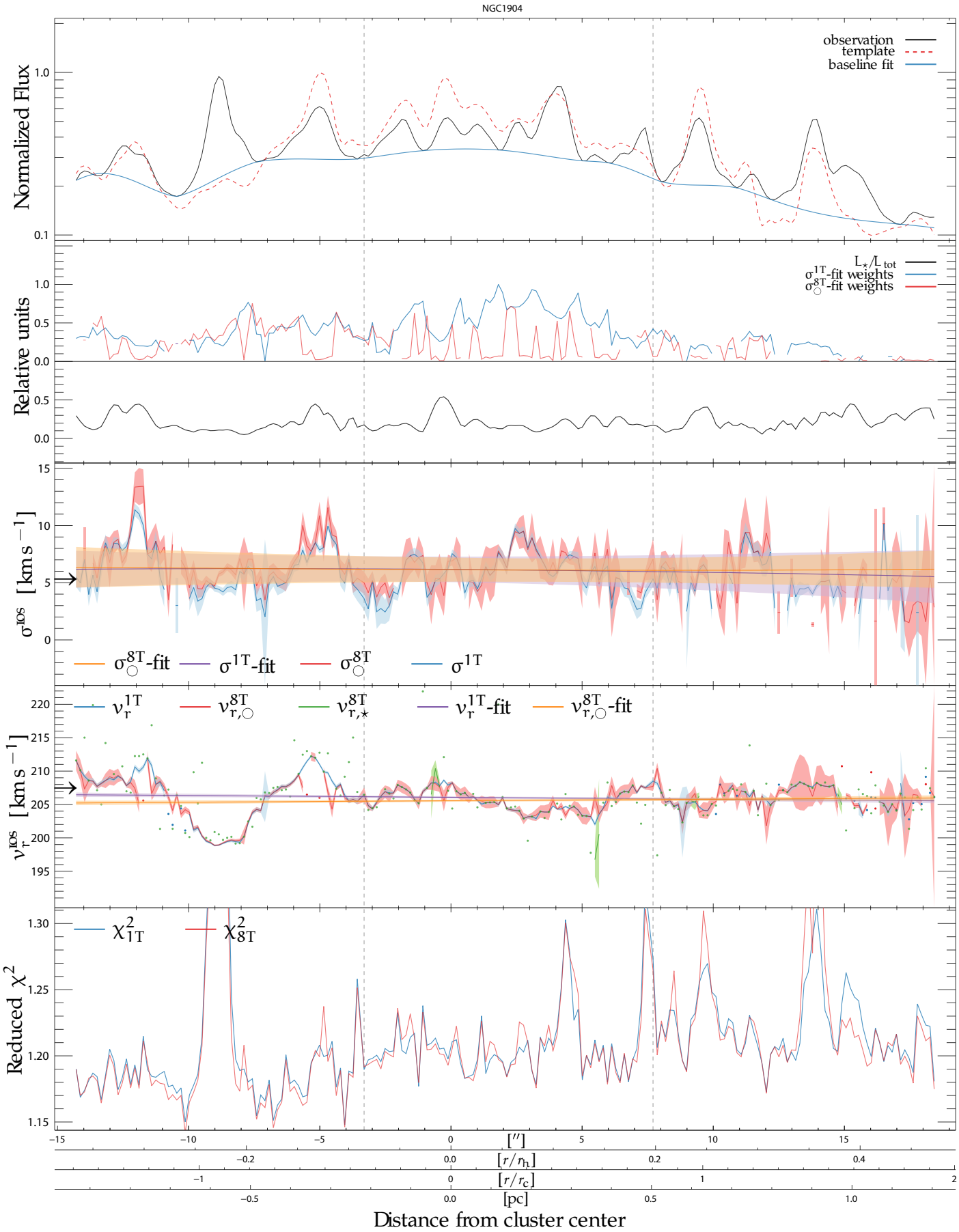

Figure 47: Same as Figure 43 but for NGC1904.

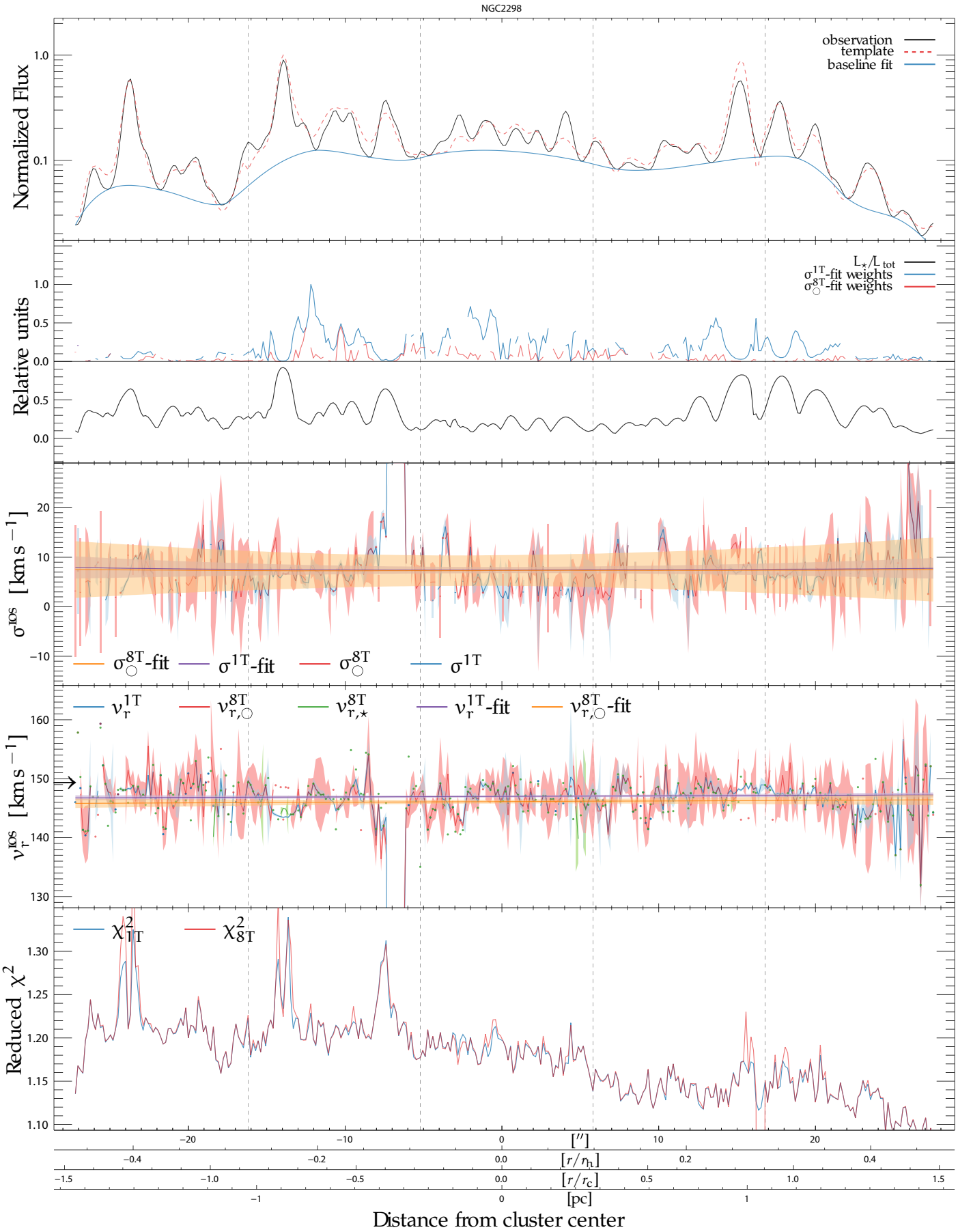

Figure 48: Same as Figure 43 but for NGC2298.

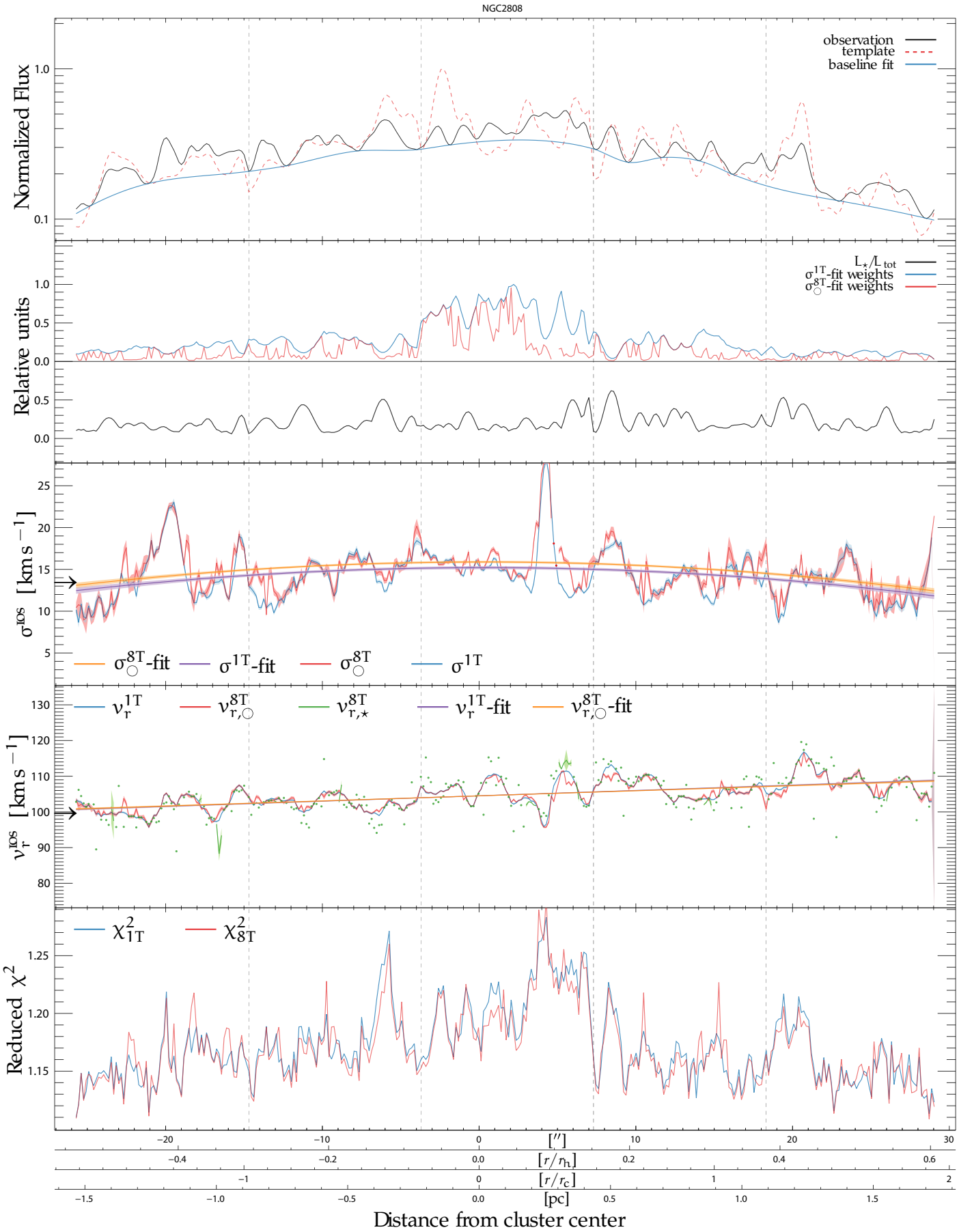

Figure 49: Same as Figure 43 but for NGC2808.

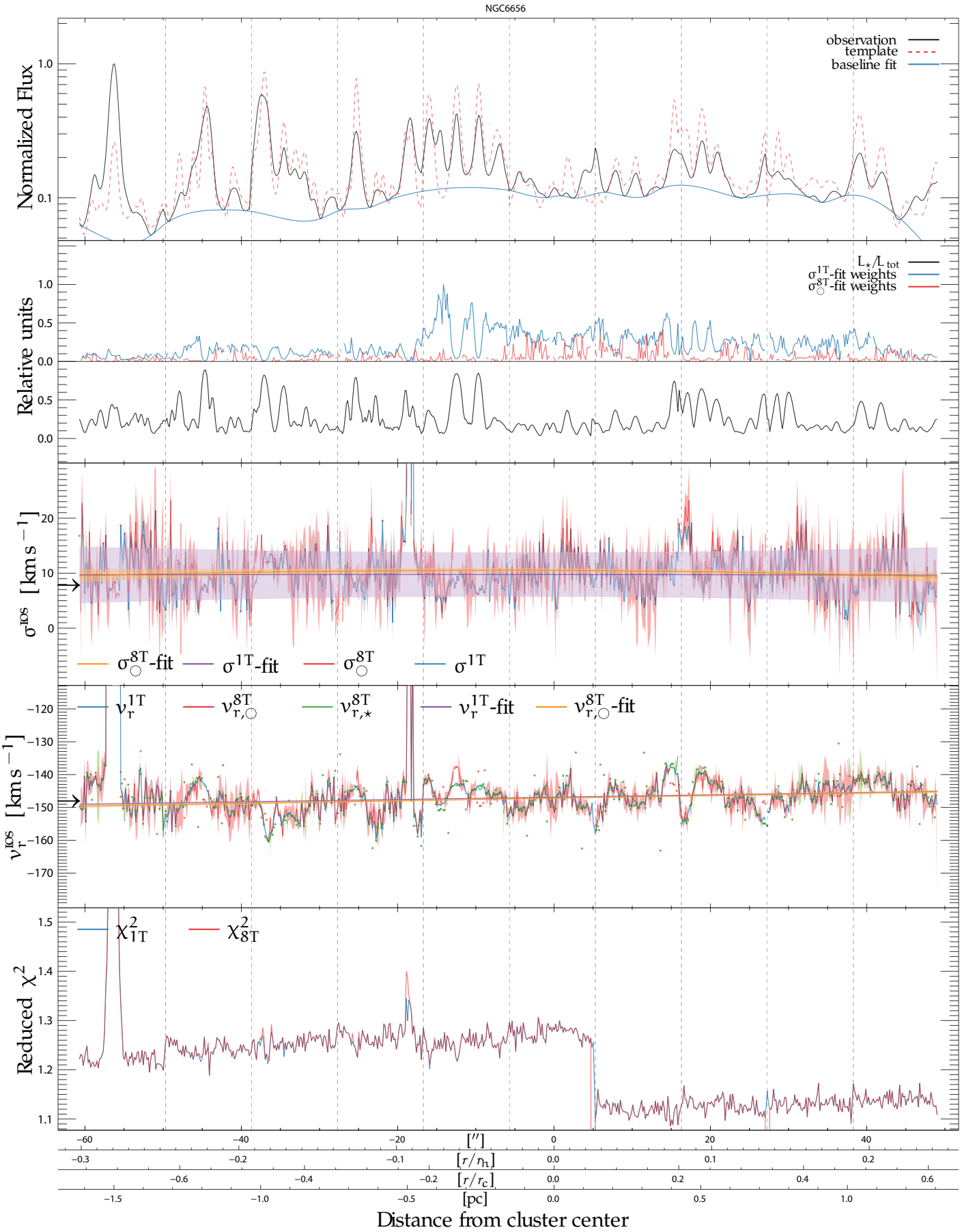

Figure 50: Same as Figure 43 but for NGC6656.

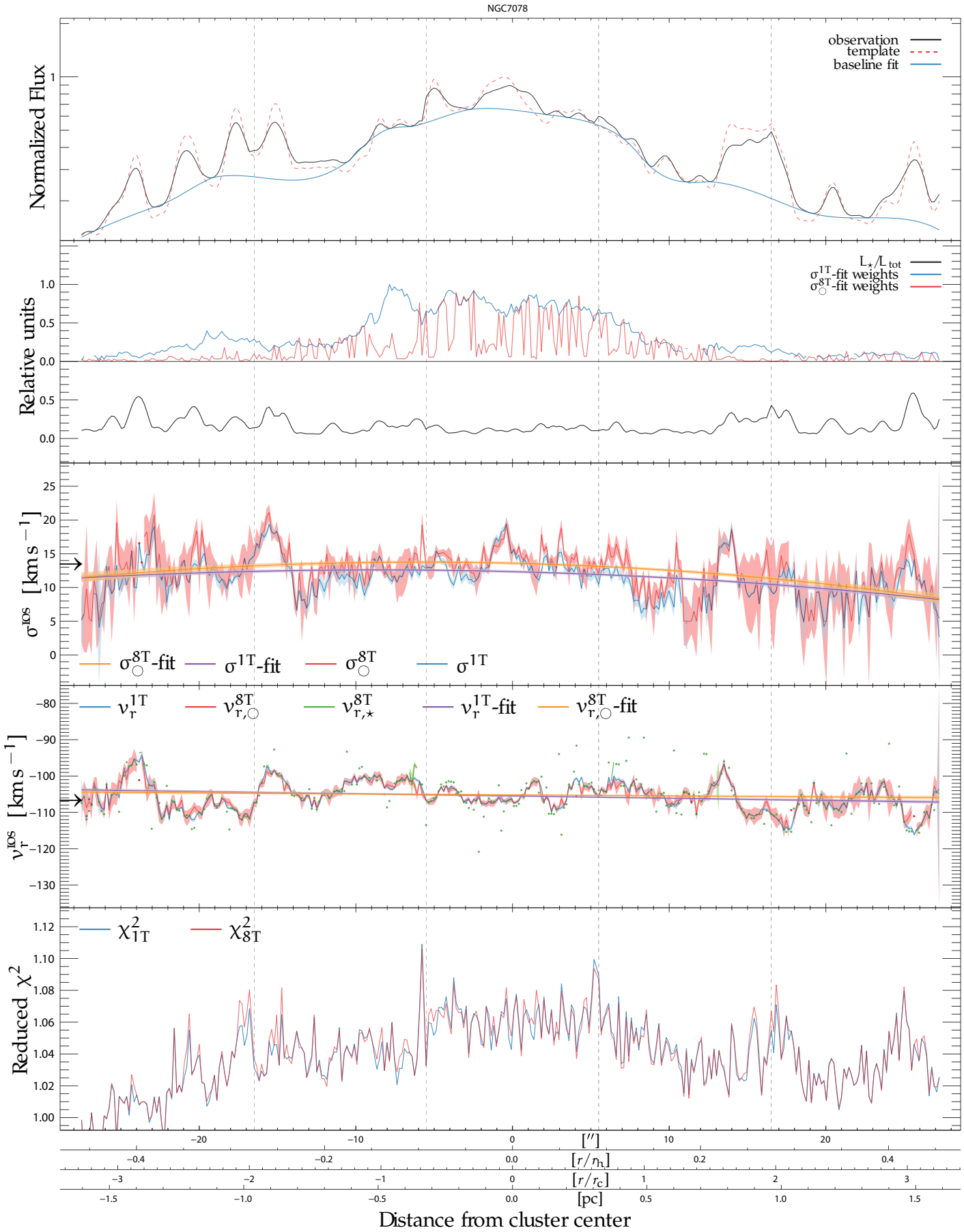

Figure 51: Same as Figure 43 but for NGC7078.

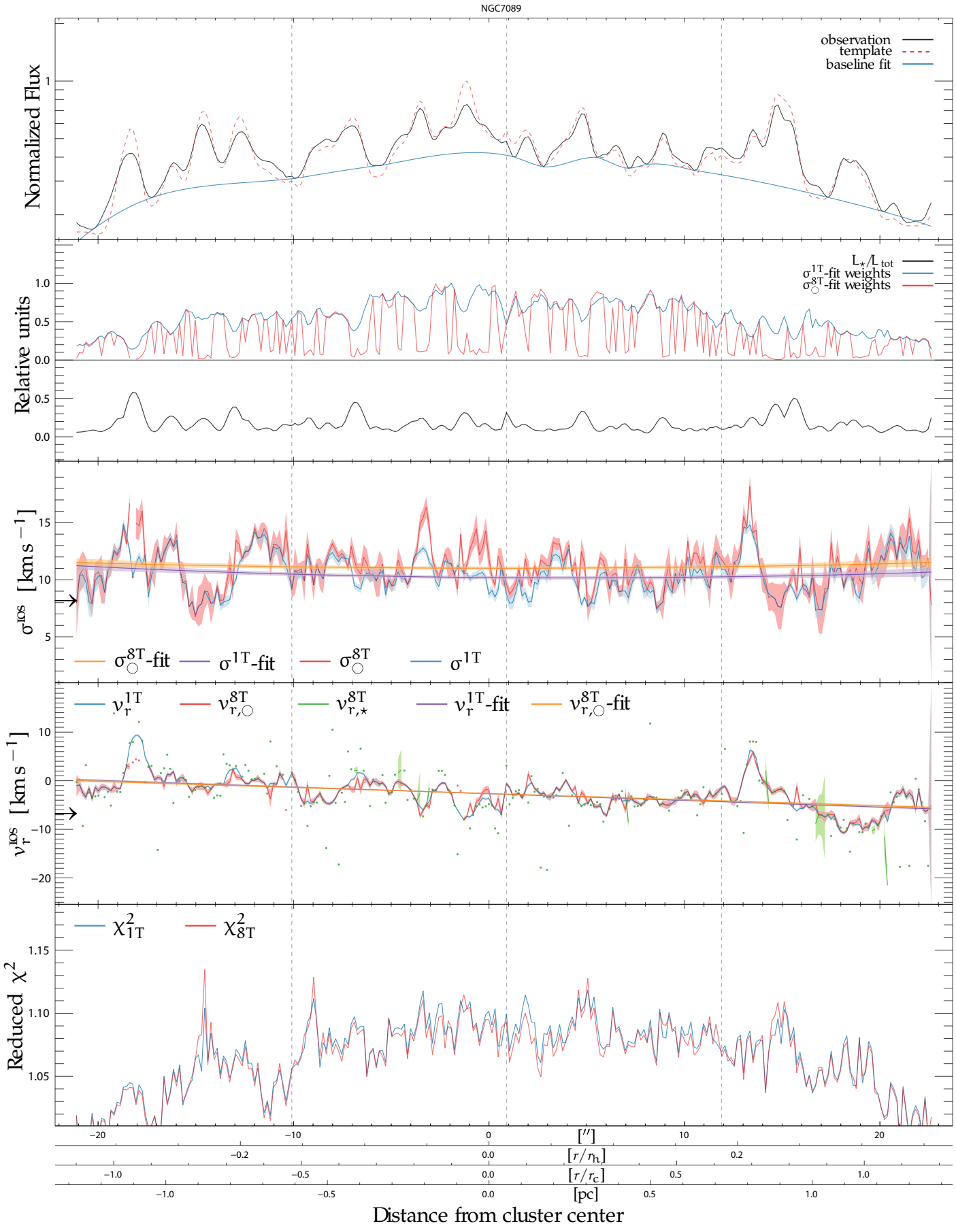

Figure 52: Same as Figure 43 but for NGC7089.

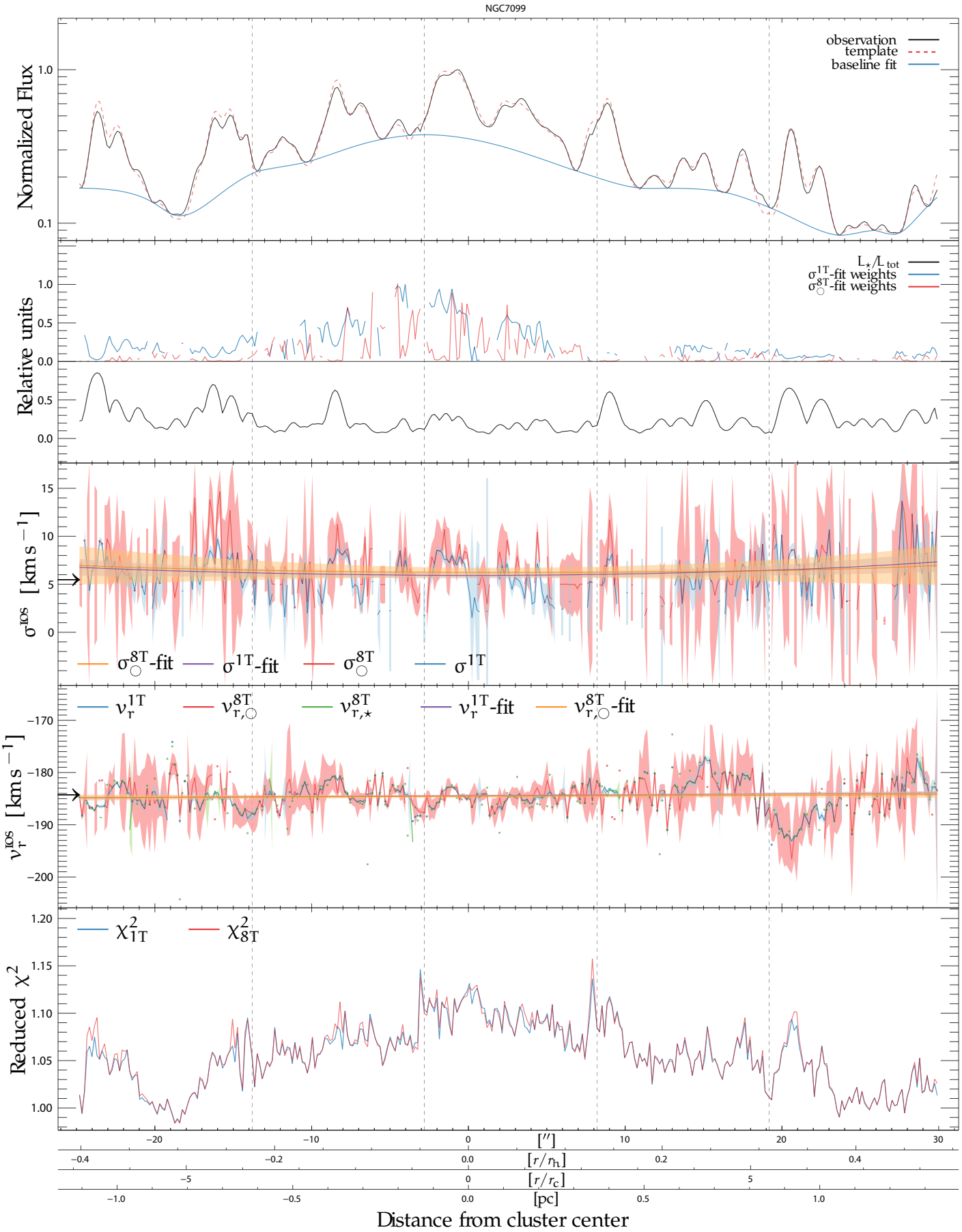

Figure 53: Same as Figure 43 but for NGC1851.

associated error band). This is mostly the case for the radial velocity of the bright star template $v_{r,\star}^{8T}$. If no convergence of the *pPXF* fit could be obtained, we do not plot any data and leave the respective slit position empty. Before we present a detailed analysis of the velocity dispersion profiles, we will give a brief and qualitative overview of the great amount of details seen in Figure 43.

For most clusters, the synthetic and observed cross-dispersed profiles (panel one) match very well on a global scale. With the shift correction applied (see Section 4.9), most features are reproduced at the correct positions and the relative strengths are approximately matched (Note the logarithmic scaling of the fluxes). NGC104 and to a lesser degree NGC2808 form an exception, as their match is considerably worse. We can only speculate about the true causes for this difference, since all clusters have been observed with the same observing strategy on the one hand, and the respective templates have been consistently constructed on the other hand. With NGC104 being the first target in the sequence of our observations (see Section 2.3) we presume that the drift-scan speed and / or drift-scan direction was not properly set for some or all of its scans. Since the observing strategy can be considered *experimental* (VLT does not allow for drift-scan observations in regular service-mode operation), deviations from the desired behavior have to be expected. We note that we have no means to reconstruct the actually covered scan area because the FITS headers contain neither information about the scan speed, nor about the telescope pointing at the end of the drift-scan observation. By contrast, NGC2808 is the only cluster in our sample for which the X-SHOOTER observations were conducted in service mode, and thus we had no possibility to verify the execution quality. We, therefore, suspect that similar arguments apply to this cluster as those pointed out for NGC104.

The relative contributions of the brightest stars at each slit position (panel two; black curve) correlate mostly with the peaks in the flux profile, which is expected if the star is bright not only in relative, but also in absolute terms.

Evaluating the velocity dispersion profiles (panel three), we find that for most clusters the central values are approximately compatible with the literature values (denoted by arrows on the left hand side of the panel and listed in column two of Table 9). Considering the global shape of the profile, it approximately peaks at the center of the cluster for most GCs, while some clusters in our sample show a rather flat distribution. This difference might be due to different core radii r_c of the GCs in our sample, and thus, despite the fact that our scans always cover approximately the same fraction of the half-light radius r_h, they still sample different parts of the luminosity (and mass) profile. For a detailed understanding of the global shape of the dispersion profiles, however, in-depth N-body simulations are inevitable, and so we will not investigate this topic further in this work. Superimposed onto the global shape of the dispersion profiles, we find distinct minima and maxima at all radii. The amplitude of these extrema is well above the significance limit of our measurement, if the confidence intervals of the *pPXF* fits are used as reference (these naturally only account for the random error component, but not the systematic). These features are seen for most, if not all clusters in our sample, and were unexpected previous to the analysis. The causes for these variations can be manifold and need to be understood if an interpretation of the velocity dispersion profile with respect to the underlying

GC kinematics is intended. It should be noted that the single-component approach (blue colors) and multi-component approach (red colors) do not produce significantly different results, except for a general increase in scatter for the latter. On the one hand this confirms the robustness of the data, on the other hand however, this indicates that the theoretical considerations that motivated the multi-component mode (see Section 5.5) could not be accounted for by our implementation. A detailed analysis of the observed features as well as potential explanations and their implications will be presented in the next section. Here we proceed with a short evaluation of the radial velocity profiles (panel four).

For most clusters the global profile can be approximated by a linear function, with systematic deviations to both smaller and larger radial velocities—similar to the features observed in the dispersion profiles. The slope of the underlying linear trend varies from cluster to cluster and could hint at ordered rotation taking in place in some of the GCs. Both utilized kinematic approaches do not differ significantly from each other. At some positions it can indeed be seen that the average radial velocity of the diffuse cluster component $v_{r,\bigcirc}^{8T}$ (red colors) and that of the brightest star $v_{r,\star}^{8T}$ (green colors) scatter approximately symmetrically about the cluster average value v_r^{1T} as inferred by the single-component approach. As the average radial velocity is a luminosity-weighted average of all contributing spectra, it will always be biased against the particular velocity of the brightest star, which is expected to show random motions in the cluster potential (statistically, this motion can be described by the velocity dispersion). This implicates that, first, random fluctuations about the global trend are expected, and, second, if the cluster kinematics are split up in two components, we expect that both components will scatter in opposite directions about the average value. A more detailed analysis and possible correlation with the velocity dispersion profile will be given below.

Panel five shows the reduced χ^2 of the *pPXF* fitting procedure. For most clusters $1 \lesssim \chi^2 \lesssim 1.5$, but we see distinct variations that may correlate with the S/N of the data (as depicted by the flux level in the cross-dispersed profile; panel one) and the flux contribution of the brightest star (panel two). Especially the latter case might indicate a template-mismatch problem, related to the fact that we model the brightest star with the average template of the evolutionary phase to which it belongs. It remains to be seen whether an exact treatment, i.e., using a template that accurately matches the inferred stellar parameters for the brightest star, diminishes the observed χ^2 variations.

5.6.2 *Detailed Considerations*

After the general descriptions given in the previous paragraph, we will explore here in more detail the variations in the velocity profiles. In this regard it is particularly important to consider the length scale on which these features appear and to cross-match this scale with other available information. In what follows, we present a comprehensive overview of effects that can potentially affect the measured velocity dispersion profile.

1) Considering the reduction process, a minor correlation between adjacent pixels is expected from the rectification process. As described in Section 3.4.1.3, the cross-dispersed

pixel size (i.e. arcsec/pixel) remains roughly constant throughout the full spectral range of the UVB / VIS arms, but the kernel convolution during rectification is expected to introduce bin-to-bin correlations on a $\sim 1-2$ bins scale. We did not perform dedicated measurements to quantify the exact amount of correlation along the cross-dispersed dimension, since we do not intend to derive the velocity dispersion profile on a per-pixel resolution ($\equiv 0.16''$). Furthermore, it should be noted that the extent of the observed extrema is on the order of ~ 10 pixels, and thus much larger than the expected correlation length of the rectification. Interestingly, this length scale corresponds to a typical PSF width at a seeing of $\sim 1''$, and we therefore believe that the observed variation of the dispersion profile is not an artifact, but truely contained in the observed spectra.

2) The typical length-scale of the variations suggests that the cause might be of stellar origin. In Section 5.5 we have already discussed one possible influence that individual bright stars might have on the composite drift-scan spectrum. We argued that the superposition of a non-rotating, very bright star onto the diffuse cluster light might potentially lower the inferred velocity dispersion, since in this case the observed composite spectrum will resemble that of a single star to a higher degree. To validate this scenario we compare the slit positions of the observed minima with the relative flux contribution of the brightest star to the cluster light, $L_\star/L_{tot}$, in the respective bin (panel one of Figure 43; black curve). The suggested scaling is indeed seen for some of the slit position, e.g., at $\sim -11''$ and $\sim -4''$ for NGC1851, or at $\sim -40''$, $\sim -18''$, $\sim 32''$, $\sim 37''$ for NGC104 (which will be used as a second showcase here): In these bins the contribution of the brightest star is significantly enhanced with respect to the respective cluster average, while at the same time the inferred velocity dispersion estimates are accordingly lower. The multi-component approach, however, which is designed to address this issue, does not yield better, if not worse, results in most cases. In some rare cases, e.g., for NGC2808 the negative amplitudes seem to be slightly less pronounced if the multi-component technique is used, but overall we have to state that the performance can not keep up with the single-template approach. This is especially true for the significance of the inferred kinematic parameters, since the random errors are considerably larger in the multi-component analysis for the majority of cases. This is partly expected, as the multi-component approach features a much higher number of fitting parameters, which in turn bears a higher risk of resulting in only marginally constrained (or even totally unconstrained) best-fit values. Yet, the intended goal to trade off the systematic uncertainty against the random error, i.e., to construct a model that takes into account systematic deviations from the expected profile at the expense of the significance of the inferred values, is not achieved and a more sophisticated approach might be required. In addition, it is worth noting that also cases are observed in which 1) a single bright star does not lead to a drop in the dispersion profile (in many cases it actually leads to an increase) and 2) the position of dips in the dispersion profile does not correspond to positions with an enhanced contribution of bright stars. We will discuss this further below.

3) In many cases positions with strongly enhanced $L_\star/L_{tot}$ are accompanied by distinct peaks rather than dips in the velocity dispersion curve. This is apparent at $\sim -12.5''$,$\sim$

4″, and ~ 11″ for NGC1851, and ~ −36″ and ~ −32″ for NGC104. Again, under the assumption that the amplitude variations are correlating with the position of bright stars and thus are of stellar origin, rapid rotation of individual stars seems to be a natural candidate to explain the observed features.

In this context, analyses by de Medeiros & Mayor (1999) yielded a mean rotation velocity $v \sin i \approx 2\ \mathrm{km\,s^{-1}}$ for K giants (the typical classification for stars on the RGB), and Carlberg et al. (2011) found that only 2.2% of their sample of ~ 1300 K giants can be considered rapid rotators with $v \sin i \gtrsim 10\ \mathrm{km\,s^{-1}}$, proposing that the rotation is a result of interaction with a companion. In detail, the rapid rotation might be caused by tidally locked binaries, where the giant star is co-rotating with an unseen binary companion. This implies that more evolved stars have higher probability of being rapid rotators, since their radii are more extended (lower surface gravities), and thus a given distance to the companion (i.e., co-rotation period) results in higher rotational velocities for the giant. While this effect produces rapid rotators preferentially at the tip of the RGB (implying that it correlates positively with the total luminosity of star), stars at the base of the RGB (with relatively small radii) can be accelerated due to interaction with a planetary companion. Models indicate that the accretion of a few Jupiter masses can be sufficient to increase the rotation of a $1\,M_\odot$,$10\,R_\odot$ star to more than $8\,\mathrm{km\,s^{-1}}$ (Carlberg et al. 2009).

In our data, the peaks seen for NGC1851 show an excess of ~ $2\,\mathrm{km\,s^{-1}}$ with respect to the underlying profile at ~ $8\,\mathrm{km\,s^{-1}}$, while the profile of NGC104 shows positive variations with an amplitude of ~ $8\,\mathrm{km\,s^{-1}}$ relative to a baseline of ~ $11\,\mathrm{km\,s^{-1}}$. Assuming that the peaks in the dispersion profiles are the luminosity-weighted square root of the quadratic sum of the GC velocity dispersion $\sigma_\bigcirc$ (responsible for the underlying profile) and the rotation velocity of a single star $v_\star \sin i$ (responsible for the peak), i.e.,

$$\sigma = \sqrt{w_\bigcirc \sigma_\bigcirc^2 + w_\star (v_\star \sin i)^2}, \tag{57}$$

where $w_\bigcirc$ is luminosity weight of the diffuse cluster component and $w_\star$ the luminosity weight of the single star, then $v_\star \sin i \approx 10\,\mathrm{km\,s^{-1}}$ for NGC1851 and ~ $17\,\mathrm{km\,s^{-1}}$ for NGC104. These values are compatible with the distribution of rapid rotator velocities shown by Carlberg et al. (2011, their Figure 3), which peaks ~ $12-15\,\mathrm{km\,s^{-1}}$, and thus rapid rotation of single bright stars, which are superimposed onto the GC composite light, has to be considered a viable explanation for the observed peaks in the dispersion profile (It should be noted, however, that this simple estimates relies on equal weights between the two components, and does not incorporate any instrumental broadening nor the intrinsic line broadening of the stellar atmospheres. A more realistic estimate is presented in Figures 54 and 55, and will be discussed below). In this context it is worth mentioning that, according to Equation 57, it is expected that slow rotators with $v_\star \sin i \lesssim 2\,\mathrm{km\,s^{-1}}$ do not bias the inferred profile strongly, and therefore it is generally assumed that $\sigma \approx \sigma_\bigcirc$ (Even for intrinsic velocity dispersions as low as $\sigma_\bigcirc \approx 5\,\mathrm{km\,s^{-1}}$ and assuming $v_\star \sin i = 2\,\mathrm{km\,s^{-1}}$, the measured value would be $\sigma \approx 5.4\,\mathrm{km\,s^{-1}}$, and hence the expected systematic uncertainty is less than 10%).

In addition to rotating stars, unresolved and non-co-rotating binary systems are likewise expected to impact the measured dispersion profile. Depending on the mass ratio, they can affect the dispersion in two different ways. If both primary and secondary have approximately similar masses (and thus luminosities), the spectral lines of both stars could be blended to mimic a single set of broad lines. If the systemic velocity of the binary system inside the cluster potential is zero, i.e., the center of mass of the binary has the same radial velocity as the cluster on average, then the position of the binary-broadend lines would coincide with the lines of the diffuse cluster light. In this case, the motion inside the binary system would be the only effect being responsible for the observed broadening in the composite spectrum. If the binary shows an additional systemic velocity component relative to the cluster average, the set of broadend-lines will be offset with respect to the diffuse cluster light, and this offset—if sufficiently strong—might mimic another velocity broadening component in the composite spectrum. Conversely, if the companion is considerably fainter, the velocity component due to the motion in the binary system should only produce a line-shift in the spectrum of the primary and no significant broadening. In order to produce the observed variations, the resulting radial velocity displacement of the bright star spectrum would need to be sufficiently large so that the combined blend of diffuse cluster light and bright star mimics a spectrum with enhanced Doppler-broadening. In this scenario, the peak in the velocity dispersion profile should be accompanied by a corresponding offset in the radial velocity curve. This effect is also expected for single bright stars that gained recoil from previous interactions with binaries. This can happen during core collapse and may leave the single star with a significantly enhanced velocity, which can even lead to an escape of the star from the cluster potential (Gebhardt et al. 1995). In this context it is important to mention that the spectral contribution of individual bright stars will always be offset relative to the diffuse cluster average by an amount that corresponds to their motion in the cluster potential, i.e., we expect on average that $v_{r,\bigcirc} - \sigma_\bigcirc \lesssim v_{r,\star} \lesssim v_{r,\bigcirc} + \sigma_\bigcirc$ with $\sim 68\%$ probability.

In summary, a binary system with stars of similar mass can increase the line-width both with or without an accompanying shift of the inferred radial velocity, while a binary with a dominating primary requires an additional line shift. By contrast, single bright stars—rotating or not—will show an offset in radial velocity that reflects their motion in the cluster. While rotating stars can broaden the lines of the composite spectrum even for $v_{r,\star} = v_{r,\bigcirc}$, non-rotating stars need to be offset significantly to have an enhancing effect (Otherwise their impact is even expected to reduce the measured dispersion; see explanations above)[5].

Cross-comparing the velocity dispersion estimates with the radial velocity profile (fourth panel in Figure 43) indeed reveals that many observed σ-peaks are accompanied by significant variations in the measured radial velocity, e.g., at $\sim -13''$,$\sim 0''$, and $\sim 6''$ for NGC1851 and $\sim -36''$,$\sim -32''$, and $\sim -2''$ for NGC104. In order to qualitatively test if the observed

5 In this context it is interesting to note that two independent groups recently reported about similar systematic variations in their integral-field unit (IFU) spectroscopy data (Bianchini et al. 2015; Lützgendorf et al. 2015). They propose to assess the problem in a statistical way by simulating luminosity-weighted realizations of the stellar positions along the line-of-sight.

peaks in the velocity dispersion can be explained by a sole radial velocity offset of the respective brightest star, i.e., without any additional broadening by stellar rotation or a line blend due to an unresolved binary, we constructed a simple toy model that mimics the line blend between the composite GC light and the radial-velocity shifted contribution of the brightest star. Figure 54 illustrates the setup.

A Gaussian line profile $\mathrm{LSF}_{\bigcirc}$, which indicates a spectral feature in the diffuse cluster light is centered at $v_r = 0$ (solid red curve). The velocity broadening of the profile is assumed to be $11\,\mathrm{km\,s^{-1}}$, which is approximately the velocity dispersion of NGC104 at positions where it is free of contaminations. The total width of the profile is the quadratic sum of the instrumental LSF, the intrinsic width of the line due to the broadening mechanisms in the stellar atmosphere, and the velocity dispersion. The combined sum of the first two effects has been estimated with an RGB template (degraded to X-SHOOTER's resolution) and is $\sim 8.5\,\mathrm{km\,s^{-1}}$ on average. The LSF of a single star $\mathrm{LSF}_{\star}$ (overplotted in dot-dashed red) is offset in radial velocity exactly by the width of the dispersion, i.e., $\Delta v_r = \sigma_{\bigcirc} = 11\,\mathrm{km\,s^{-1}}$, which should be an upper limit for $\sim 68\%$ of the cases. The flux contribution of the star to the total light was assumed to be 0.4, which is a realistic scenario according to the values presented in panel two of Figure 43. The width of $\mathrm{LSF}_{\star}$ is the quadratic sum of instrument, intrinsic line width, and $v_{\mathrm{rot}} = 2\,\mathrm{km\,s^{-1}}$, where the last term reflects an upper limit for slowly rotating RGB stars (de Medeiros & Mayor 1999; Carlberg et al. 2011). The fact that, despite $L_{\star}/L_{\bigcirc} = 0.67$, the amplitude of $\mathrm{LSF}_{\star}$ is still higher than that of $\mathrm{LSF}_{\bigcirc}$ relates to the velocity dispersion broadening, which affects the diffuse light, but not the bright star. Overplotted in black is the cumulative line profile, which is slightly assymetric in shape and peaks close to $\Delta v_r = \sigma_{\bigcirc}$. The dashed blue curve depicts an upscaled version of $\mathrm{LSF}_{\bigcirc}$ (shifted so that it aligns with the peak of the cumulative LSF). This profile is presented for comparison, since it represents the line shape that would be measured in the absence of single star contamination. Notably, the sum of the two displaced individual profiles ($L_{\star}$ and $L_{\bigcirc}$) produces a combined width that is smaller than the width of the diffuse component only. This comes as no surprise, and was already discussed at length above.

In order to estimate whether the non-rotating and non-binary stars can be responsible for the observed peaks in the composite velocity dispersion, we varied the radial velocity displacement of the star $\Delta v_{r,\star}$ from 0 to $3\,\sigma_{\bigcirc}$ for the above explained setup and fitted the resulting cumulative profile with a simple Gaussian to measure the composite width. This width is then transformed back to a velocity dispersion by subtracting the instrumental + intrinsic broadening accordingly. The results are presented in Figure 55 (solid black curve). As can be seen, small displacements lead to an under- rather than an overestimate of the measured line-width, since for $\Delta v_{r,\star} \lesssim 10\,\mathrm{km\,s^{-1}}$ the inferred dispersion is *smaller* than the true cluster dispersion $\sigma_{\bigcirc}$. In order to obtain a measured dispersion $\sigma_{\mathrm{out}} \approx 20\,\mathrm{km\,s^{-1}}$, which corresponds to the peak at $\sim -32''$ for NGC104 (see Figure 44, panel three), our simple model suggests that a displacement of $\sim 27\,\mathrm{km\,s^{-1}}$ for the dominating star is required, which corresponds to $2.5\sigma_{\bigcirc}$. While it cannot be excluded, it is somewhat unlikely that the brightest star exhibits such a high radial velocity if homogenous motions in the cluster potential are assumed. If, however, the displacement is only partly caused by

the motion in the cluster potential, and the dominating star is additionally part of a binary system and / or has gained recoil from interactions with binaries (as expected e.g., during core collapse, see Gebhardt et al. 1995), then a value of $\Delta v_{r,\star} \approx 27\,\mathrm{km\,s^{-1}}$ seems much more realistic. It should be noted that the radial velocity displacement of the cumulative LSF (i.e., the one that is measured) is always a luminosity- and profile-shape-weighted average of the two individual LSF components. In the case of equal widths and equal luminosities, the displacement of the cumulative profile should exactly be $0.5\Delta v_{r,\star}$. This consideration has to be kept in mind in the interpretation of the radial velocity profile: If outliers in the dispersion curve are caused by a displacement of the brightest star, then the resulting σ-peak should be accompanied by an according variation in v_r. More importantly, the radial velocity displacement of the responsible bright star will always be higher than the amplitude of the v_r-variation (i.e., the peak of $\mathrm{LSF}_\star$ will always be shifted more than that of the cumulative LSF).

To estimate the influence that rapid rotation of the brightest star potentially has on the composite spectrum, we re-performed the analysis with our toy model, but set the rotation velocity to $v_{rot} = 20\,\mathrm{km\,s^{-1}}$. Moreover, we significantly increased the star's contribution to the total flux and set $L_\star/L_\odot = 2.33$, which corresponds to a flux fraction of 0.7. The obtained result is plotted with a dashed red curve in Figure 55. As expected, even for very small displacements, the inferred dispersion is now dramatically increased. Nevertheless, a displacement by $\sim 20\,\mathrm{km\,s^{-1}} \approx 1.9\sigma_\odot$ is still required to obtain a composite velocity dispersion of $20\,\mathrm{km\,s^{-1}}$, which suggests that stellar rotation is unlikely to be the sole cause for the observed peaks.

In summary, our presented toy model suggests that simple displacements of the brightest stars due to their motions in the cluster potential represent an unlikely cause for the observed peaks in the measured dispersion profile. Additional motion in a binary system or previous interaction with binaries in combination with the resulting recoil seem to be a natural way to increase the required radial velocity displacement. If stellar rotation is added, the necessary shift in radial velocity is accordingly lower, but still seems too high to be explicable by the velocity dispersion alone.

With respect to the considerations presented here, it should be noted that our toy model is based on the simplistic assumption that the composite light can be split up into two components, one reflecting the brightest star and one reflecting the diffuse rest. It is clear that this is an oversimplified treatment, as there might be more stars whose impact onto the composite LSF (both in shape and displacement) needs to be individually modeled. A detailed treatment of this kind, however, is beyond the scope of this work and might be addressed with future N-body simulations. In addition, the presented model relies on well sampled line profiles and does not account for any form of measurement uncertainties. It goes without saying that neither of these assumptions is fulfilled by our observational data and so it remains somewhat inconclusive which effects are exactly responsible for the observed amplitude variations in the dispersion profiles. We speculate that most likely it is a combination of all scenarios presented here.

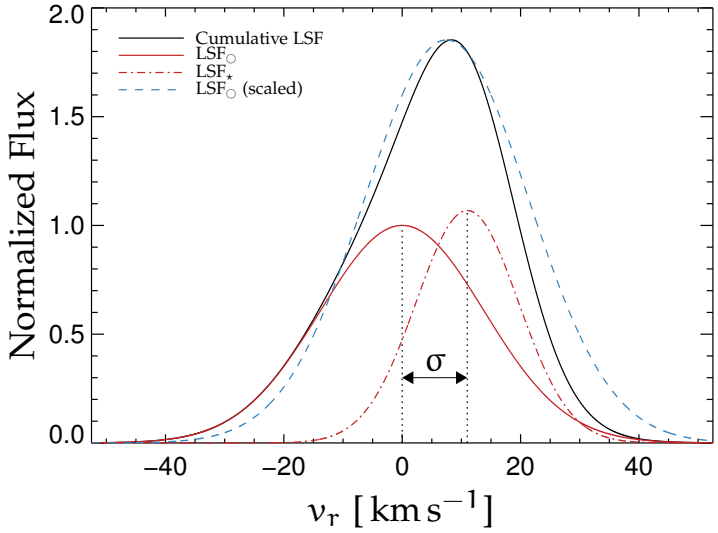

Figure 54: Toy model illustrating a spectral line blend between the diffuse cluster light (solid red line) and a bright star (dot-dashed red line). The spectral axis is converted to velocity-space. The width of the diffuse-light LSF$_\odot$ is the quadratic sum of the stellar atmospheric broadening, the instrumental broadening, and the velocity dispersion $\sigma_\odot$. The combined effect of the first two components is modeled with $\sim 8.5\,\mathrm{km\,s^{-1}}$, and $\sigma_\odot = 11\,\mathrm{km\,s^{-1}}$. The width of the bright star LSF$_\star$ contains the same atmospheric and instrumental contributions, and is assumed to be rotationally broadened with $v_{\mathrm{rot}} = 2\,\mathrm{km\,s^{-1}}$. The displacement between both LSFs corresponds to $\sigma_\odot$. Both LSFs have been normalized such that $\int \mathrm{LSF}_\star\,\mathrm{d}v_r = 0.67 \int \mathrm{LSF}_\odot\,\mathrm{d}v_r$. The cumulative LSF is indicated with a solid black curve. The dashed blue curve depicts a rescaled version of LSF$_\odot$, which approximately matches the peak and displacement of the cumulative LSF.

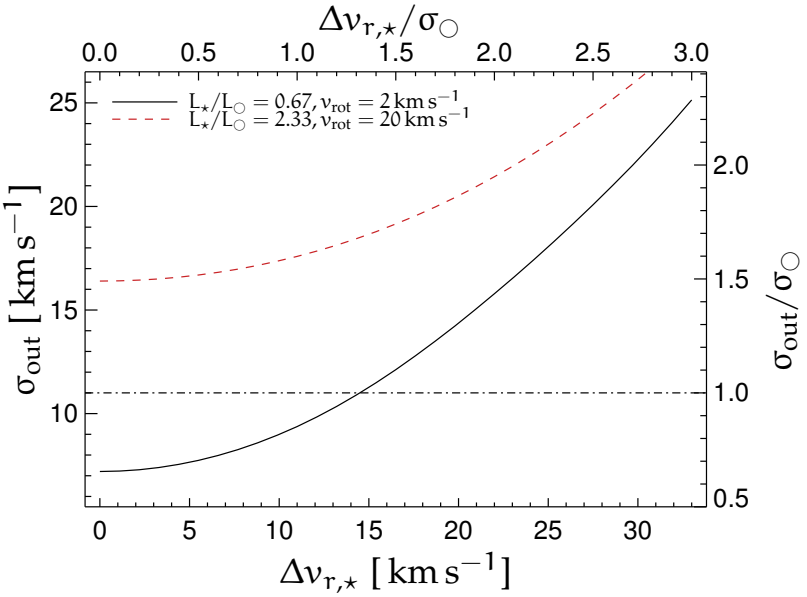

Figure 55: Toy model predictions for the measured cumulative velocity dispersion σ_{out} as a function of the radial velocity displacement of the bright star $\Delta v_{r,\star}$ relative to the diffuse light component (see Figure 54 for a sketch of the setup). The solid black curve indicates the recovered velocity dispersion if the bright star is only insignificantly rotating ($v_{\mathrm{rot}} = 2\,\mathrm{km\,s^{-1}}$) and produces 40% of the total flux. The dashed red curve is predicted in the extreme scenario, where the bright star is rapidly rotating ($v_{\mathrm{rot}} = 20\,\mathrm{km\,s^{-1}}$) and contributes 70% of the integrated light. The top (right) axis indicates the displacement (recovered velocity dispersion) in units of the true cluster velocity dispersion $\sigma_\odot$. The case where the cluster velocity dispersion is exactly recovered is indicated by the dot-dashed black line.

4) Bright foreground stars located along the line-of-sight between the observer and the GC can potentially have similar effects on the velocity dispersion profile as bright cluster member stars. If their radial velocity is close to the systemic velocity of the cluster then all considerations presented above apply in the same way. Fortunately, a comparison between the cross-dispersed profiles of the observed spectra and the templates yields information about possible candidates: because the distribution of cluster stars in the CMD is relatively confined, the *HST/ACS* photometry is mostly free from foreground stars and so we expect that the template only reflects true cluster members. By contrast, our drift-scans contain integrated information about all stars along the line-of sight and so we expect foreground stars to show up as *positive outliers* in the observation flux profile. Such differences are indeed seen, e.g., at $\sim -9''$ for NGC1904 or at $-20''$ (and to a smaller degree at $5''$) for NGC2808. In both clusters, the velocity dispersion (see panel three in Figures 47 and 49, respectively) is dramatically increased at these positions, which is expected according to our toy model from above. Interestingly, Lützgendorf et al. (2012a) performed a search for high-velocity stars in the inner region of NGC2808 and found five stars with $\Delta v_r \gtrsim 40\,\mathrm{km\,s^{-1}}$. The two brightest of these stars are listed with coordinates such that they would be contained in our drift-scan spectrum at slit position $s \approx 5''$, and thus it is highly likely that the respective peak in the dispersion profile is a result of these stars and not caused by foreground stars. Adjusting our toy model to a cluster velocity dispersion of $\sigma_\circ \sim 15\,\mathrm{km\,s^{-1}}$ (approximately the value for NGC2808 at unaffected slit positions) yields $\sigma_{out} \approx 30\,\mathrm{km\,s^{-1}}$ for $\Delta v_{r,\star} = 40\,\mathrm{km\,s^{-1}}$ and $L_\star = 0.4\,L_{tot}$, which is in good agreement with the observed dispersion feature at $\sim 5''$. In this context we note, however, that our toy model is not expected to produce accurate estimates, but was rather designed to qualitatively illustrate the effect that rotating bright stars with displaced radial velocity can have on the inferred composite velocity dispersion. Considering the case of NGC1904, deviations between the observed and synthetic cross-dispersed profiles might also originate from an incomplete *HST/WFPC2* sampling of the area covered by our drift-scans (compare Figure 6). Since this cluster was not observed with *HST/ACS*, it has a considerably sparser photometric sampling, and thus a greater probability that bright cluster stars have been missed and their contribution accounted for in the synthetic template spectrum.

With the above said, it becomes apparent that any derivation of a *smooth* velocity dispersion profile from our observational drift-scan data is not straight-forward and requires a careful slit bin-by-bin analysis of all available information. Providing a smooth profile is desired, since then it can be directly compared with correspondingly adjusted simulations. A procedure of this kind can in principle be used to infer the (one-dimensional) GC mass profile and will be pursued in a subsequent project. Here, we want to present our approach to fit the measured velocity dispersion profile in a way that down-weights any positions that might be contaminated by the influence of single stars.

The starting point for the fit to the dispersion profile is given by the uncertainties of the *pPXF* fit. These, however, only depict the random uncertainty due to observational errors and do not account for any perturbations of the profile produced by single stars. In due consideration of all the effects presented above it becomes apparent that the weight of each slit bin should reflect the information that the slit contains about the velocity dispersion

of the diffuse cluster component $\sigma_{\bigcirc}$. Bins whose spectra are dominated by the impact of individual stars will need to be weighted down accordingly, whereas slit positions whose spectrum is a homogenous average over all stars along that line-of-sight should have a respectively higher weight. Nevertheless, the *pPXF* errors must not be ignored, as they contain valuable information about the quality of the fit, and thus the S/N.

We therefore propose an implementation, in which the measurement errors are re-weighted by an amount that reflects the potential contamination due to single stars. The exact estimate is based on the shape of the cross-dispersed flux profile and on the flux fraction of the brightest star. While the flux fraction seems a natural choice to account for any perturbations caused by bright stars, we suggest to include the global flux profile for two reasons. First, foreground contamination can only be conclusively estimated by means of the flux profile, as foreground stars (which can have a major influence on the respective slit bin) will not be contained in the template, and thus also not in the flux contribution profile. Second, even if the contribution of the brightest star is only moderate (e.g., $\sim 20\%$), any pronounced peak in the global cross-dispersed profile is most likely the result of only a small number of $\sim 5-10$ of stars; compare Figure 35 for an example of how the distribution of stars in the cluster forms the composite profile of our observational data. As this number is very low, we expect the cumulative LSF to show significant deviations from the ideal dispersion-broadened average value in these cases. Consequently, the fitting weights should be constructed such that they are inversely proportional to the strength of the peaks in the flux profile. For this, we fit a smooth low-order polynomial to all local minima in the observed flux profile (blue line in panel one of Figure 43) and for each slit bin compute the ratio between data F and fit B (F denotes measured flux and B denotes baseline fit). The rescaling is then achieved by multiplying the measurement errors with this ratio. The contribution of the brightest star $L_\star/L_{tot}$ is propagated into the final error by subtracting it from unity and dividing the measurement error by this quantity. This way, the rescaled error becomes

$$\delta'_{pPXF} = \frac{\delta_{pPXF}}{1 - \frac{L_\star}{L_{tot}}} \cdot \frac{F}{B}, \tag{58}$$

where δ_{pPXF} are the *pPXF* measurement uncertainties on the inferred line-of-sight velocity dispersion σ_{LOS}. The final fitting weights, which we present in panel two (top part), correspond to $(\delta'_{pPXF})^{-2}$ (as they should for a variance-weighted fit) and illustrate the desired scaling: For most clusters, they show a negative radial gradient, which is produced by the *pPXF* measurement uncertainties, and is a result of the S/N (arising from the light profile of the cluster). Superimposed is a combined "negative image" of the cross-dispersed profile and the single star contributions. The fact that the fitting weights for single-component measurements are on average higher than for multi-component data relates to smaller *pPXF* uncertainties if only one kinematic component is fitted (compare the red and blue error bands in panel three).

Nevertheless, our δ'_{pPXF} values still suffer from a general underestimation of the measurement errors, i.e., the inferred δ_{pPXF} values do not reflect the above discussed system-

atic deviations of the measured velocity dispersion about the smooth model. In consequence, any fit to the presented dispersion profiles that is based solely on the (rescaled) *pPXF* errors will, on the one hand, show a dramatically enhanced χ^2 because the deviations of the data from the model function are not reflected in the fitting weights. On the other hand, the obtained model uncertainties will be fundamentally underestimated, which is problematic if the inferred model curve is compared to simulations. To account for this issue, we try to estimate the average scatter that the measurement has about a given smooth model. The model is parametrized with a parabola, i.e.,

$$\sigma^{\text{fit}} = \gamma\,(s - s_0)^2 + \sigma_0, \tag{59}$$

where s denotes the distance to the cluster center s_0 (in arcseconds), σ_0 is the central velocity dispersion, and γ is a numerical scale parameter (This particular parametrization has been chosen since it reflects the observed shapes of the dispersion profiles reasonably well. We note that there is physical motivation for this parametrization). In a first iteration, this model is fitted to the measured velocity dispersion profile utilizing the errors δ'_{pPXF}. The average scatter is then evaluated by computing the 68% confidence interval around the median residual between data and fit. This is in principle comparable to an RMS, but is more robust against single outliers. The value for the average scatter obtained in this way is $\langle\delta\rangle \approx 1-2\,\mathrm{km\,s^{-1}}$ for all clusters, which is plausible judging from a comparison between data and fit as illustrated in panel three of Figure 43. Eventually, the parabolic fit is re-performed, however this time we add $\langle\delta\rangle$ in quadrature to the re-weighted measurement errors, i.e.,

$$\delta_{\text{tot}} = \sqrt{(\delta'_{pPXF})^2 + \langle\delta\rangle^2}. \tag{60}$$

In this fit setup, typically $\chi^2 \approx 0.7-1.3$, whereas without accounting for $\langle\delta\rangle$ we obtain $\chi^2 \approx 5-10$. Consequently, the uncertainties on the fitted parameters should represent more realistic estimates for the true measurement uncertainty, given that the measured data show considerable deviations from the expected smooth model due to systematic issues arising from the observational strategy. At this point it should be noted that δ_{tot} still does not account for any form of template mismatch and / or uncertainties in the measurement of the instrumental LSF, i.e., the errors cannot tell if the inferred dispersion estimates are systematically under- or overestimated due to wrong predictions of the stellar atmosphere line-widths and wrong estimates of the instrumental broadening. These two effects, however, will not be considered further in this work since they would require comprehensive Monte-Carlo simulations to appropriately explore the involved parameter spaces.

When analyzing the model function (see Equation 59), it is evident that the three parameters will be strongly correlated, as most clusters do not show a pronounced maximum in their dispersion profile, which implies that the central position s_0 will only be marginally constrained in these cases. Nevertheless, we left the central position as a free fit parameter because the utilized cluster coordinates are somewhat uncertain and do not necessarily reflect the true cluster center. In order to obtain error bands on the fitted model we first

generated correlated random numbers, based on the covariance matrix of the model fit, and then performed 10^3 Monte-Carlo realizations of the parabolic model. The fit shown in panel three of Figure 43 (purple: single-component mode; orange: multi-component mode) depicts the median value of the realizations at each slit position, and the associated error bands reflect the 68%-confidence interval. The obtained best-fit parameter γ is listed in Table 9 and can be used in numerical simulations to compare simulated dispersion profiles with results based on our observational data.

For most clusters, the parabolic fits of both kinematic modes are consistent within the errors and also agree with the literature values (as indicated by the arrow on the left hand side on the plot). Major deviations from the literature values are found for NGC288, NGC362, and NGC7089, however it should be noted that for NGC288 the profile is very uncertain in general, and it seems that for this cluster at least the actual *pPXF* measurement values at the very cluster center are marginally compatible with the reference value. This is different for the other two clusters, which both show significantly less scatter in their profile and the suggested deviation from the literature value thus seems to be real.

In this context it is interesting to note that both NGC1851 and NGC7078 show a significant rise of the velocity dispersion at their respective centers. Although we cannot exclude the possibility of stellar contamination with the data hand (as explained above, although it should be noted that the stellar density is much higher in the central cores of GCs, which makes a contamination of individual stars less likely in this region), we speculate that the observed peaks might be caused by an intermediate mass black-hole (IMBH). Lützgendorf et al. (2012b, 2013) explored this possibility based on IFU spectroscopy and found an upper limit of $\sim 2 \times 10^3\,M_\odot$ for the IMBH in NGC1851. Their innermost velocity dispersion estimate (being located at a distance $s \approx 0.2''$ from the center), however, is $\sim 10.5 \pm 2\,\mathrm{km\,s^{-1}}$, which is significantly more uncertain than our single-component measurement (we find $\sim 11.0 \pm 0.5\,\mathrm{km\,s^{-1}}$). Unfortunately, NGC7078 is not contained in their sample so we cannot perform a direct comparison. Nevertheless, McNamara et al. (2003) analyzed stellar proper motions in this cluster (based on *HST/WFPC2* data) and estimated a central velocity dispersion of $14.5 \pm 2.5\,\mathrm{km\,s^{-1}}$, concluding that this imposes only minor constraints on a potential IMBH. By contrast, van den Bosch et al. (2006) suggest a $500^{+2500}_{-500}\,M_\odot$ dark central mass based on ground-based and HST line-of-sight velocities and proper motions (They find a velocity dispersion of $\sim 11.5 \pm 2\,\mathrm{km\,s^{-1}}$ at $r \approx 1''$ from the cluster center). Furthermore, their results indicate strong ordered rotation in the very center of NGC7078, which is suprising, given the fact that two-body relaxation is expected to remove any form of rotation within 10^7 yr in this dense region (Akiyama & Sugimoto 1989; Gebhardt et al. 2000). The rotation axis is misaligned with the observed position angle at outer radii, which might be interpreted as a signature of a fast-spinning decoupled core. In this context it is important to note that the invocation of an IMBH would indeed significantly increase the relaxation time (by lowering the stellar density), and would thus allow for both an enhancement in velocity dispersion and the occurrence of ordered rotation. Additionally, Lardo et al. (2015) have recently studied radial velocities of individual stars and give an estimate of $13.2\,\mathrm{km\,s^{-1}}$ for the central dispersion in NGC7078, but care should be exercised because this value is extrapolated from outer

radii. In our measurements, we find a central dispersion as high as $\sim 18 \pm 1\,\mathrm{km\,s^{-1}}$ (at the very center), which is significantly larger than all previous measurements, but could contain also the contribution of ordered rotation that was reported by van den Bosch et al. (2006). Thus, it remains to be clarified to which degree our drift-scan based data are comparable to other observational techniques. The detailed implications of our velocity dispersion profiles on the internal GC kinematics will be explored with specially adjusted simulations and only then reliable conclusions can be drawn. We note in passing that Lützgendorf et al. (2013) also analyzed NGC1904 and found evidence for an IMBH with a mass $1.5 \times 10^3\,\mathrm{M_\odot} \lesssim \mathcal{M}_{\mathrm{IMBH}} \lesssim 4 \times 10^3\,\mathrm{M_\odot}$, based on a central dispersion of $\sim 9 \pm 1.5\,\mathrm{km\,s^{-1}}$. Judging from Figure 47, it seems that we can reproduce a similar, but more significant value ($\sim 9.5 \pm 0.5\,\mathrm{km\,s^{-1}}$), however only if the utilized coordinate system is slightly shifted (our profile peaks at $s \approx 3''$). An offset of amplitude between the two data sets seems possible, however requires a more detailed investigation that also addresses potential stellar contaminations (i.e., binaries and / rapidly rotating stars) as possible causes for the peak.

In regard to the findings presented in this section it becomes evident that an interpretation of the velocity dispersion profiles with respect to the underlying cluster kinematics is far from simple. Detailed analyses that explicitly account for the special drift-scan nature of our observations are of fundamental importance to accurately interpret the measured shapes. This modeling process should ideally be supported by accordingly adjusted numerical simulations in order to explore a wider range of parameter spaces (i.e., velocity anisotropy, ordered rotation, IMBH, decoupled cores, etc.). These analyses are planned to be carried out in future projects. Here, we proceed with an interpretation of the measured radial velocity curves.

GC	σ_0^{ref}	σ_{obs} ($\lvert r\rvert \leqslant 0.5 r_c$)	σ_{obs} ($\lvert r\rvert \leqslant 0.5''$)	σ_{fit} ($r = 0$)	$\gamma^{\mathrm{fit}} \times 10^4$	$v_{r,0}^{\mathrm{ref}}$	$v_{r,0}^{\mathrm{fit}}$	$\max(\lvert\Delta v_r\rvert)$
NGC104	11.0±0.3	$12.2 \pm 0.1 \pm 0.3$	11.1 ± 0.2	12.6 ± 0.1	-8.9 ± 1.0	-18.0 ± 0.1	-17.0 ± 0.1	5.2 ± 0.2
NGC288	2.9±0.3	$4.6\,(4.4) \pm 0.5 \pm 0.3$	5.4 ± 2.3	8.1 ± 1.0	2.1 ± 6.4	-45.4 ± 0.2	-45.2 ± 0.3	1.4 ± 0.7
NGC362	6.4±0.3	$8.4 \pm 0.1 \pm 0.3$	7.9 ± 0.2	8.4 ± 0.7	2.2 ± 5.2	223.5 ± 0.5	224.5 ± 0.1	1.3 ± 0.3
NGC1851	10.4±0.5	$10.2 \pm 0.1 \pm 0.3$	10.8 ± 0.1	9.5 ± 0.1	-106.3 ± 9.3	320.5 ± 0.6	320.1 ± 0.1	2.7 ± 0.4
NGC1904	5.3±0.4	$6.5 \pm 0.1 \pm 0.3$	8.9 ± 0.3	6.2 ± 1.2	-15.5 ± 22.7	205.8 ± 0.4	206.0 ± 0.2	0.9 ± 0.5
NGC2298	—	$4.6 \pm 0.4 \pm 0.3$	4.0 ± 1.6	7.4 ± 0.6	11.1 ± 20.1	148.9 ± 1.2	147.0 ± 0.2	0.5 ± 0.6
NGC2808	13.4±1.2	$15.8 \pm 0.1 \pm 0.3$	15.3 ± 0.1	15.2 ± 0.2	-41.4 ± 5.6	101.6 ± 0.7	104.5 ± 0.1	8.2 ± 0.4
NGC6656	7.8±0.3	$10.6 \pm 0.1 \pm 0.3$	6.5 ± 1.1	9.7 ± 4.2	-0.7 ± 2.1	-146.3 ± 0.2	-146.9 ± 0.2	3.9 ± 0.5
NGC7078	13.5±0.9	$13.6 \pm 0.1 \pm 0.3$	15.9 ± 0.3	12.6 ± 0.2	-34.0 ± 7.1	-107.0 ± 0.2	-105.5 ± 0.2	3.3 ± 0.7
NGC7089	8.2±0.6	$10.4 \pm 0.1 \pm 0.3$	9.6 ± 0.2	10.2 ± 0.1	17.1 ± 7.8	-5.3 ± 2.0	-2.7 ± 0.1	6.0 ± 0.3
NGC7099	5.5±0.4	$4.9 \pm 0.3 \pm 0.3$	6.3 ± 0.9	5.9 ± 0.3	16.3 ± 11.2	-184.2 ± 0.2	-184.4 ± 0.2	0.9 ± 0.5

Table 9: Kinematics parameters for our sample of GCs. First column: cluster number. Second column: central velocity dispersions taken from Harris (2010). Third column: luminosity-weighted average velocity dispersions within $\lvert r\rvert \leqslant 0.5 r_c$ ($r_c \equiv$ core radius). Fourth column: luminosity-weighted average velocity dispersions within the innermost arcsecond. Fifth column: central velocity dispersions of the fitted profile. Sixth column: scale parameters of parabolic fit (see Equation 59). The values are derived from a fit in which the distances from the cluster center have been measured in arcseconds. Seventh column: heliocentric radial velocities taken from Harris (2010). Eighth column: heliocentric radial velocities at the central position of the fitted profile. Ninth column: radial velocity difference between the two opposite ends of the fit. All values except the scale parameter are given in $\mathrm{km\,s^{-1}}$. The scale parameter is given in $\mathrm{km\,s^{-1}\,arcsec^2}$.

5.7 ORDERED ROTATION

The radial velocity profile has already been explored in Section 5.6, with a particular emphasis on the apparent scatter, which we argued is most likely an imprint of single bright stars along the line-of-sight. In this section we want to briefly discuss the global gradient that is observed for some clusters in our sample. In order to quantify the exact scaling we fitted a linear function and rescaled the *pPXF* errors in a similar way as explained for the velocity dispersions and indicated by Equation 60. The obtained fits (with error bands estimated from Monte Carlo realizations) are overplotted in purple (single-component mode) and orange (multi-component mode). The central fit value represents a good approximation to the systemic radial velocity and we list the respective values for our sample in column eight of Table 9 (we also list the literature values from Harris (2010) in column seven; a comparison will be made in Section 5.9) A linear trend in the obtained fits is particularly significant for NGC104, NGC2808, and NGC7089, which show a radial velocity difference of $\gtrsim 5\,\mathrm{km\,s^{-1}}$ if the fit values at the opposite limits of the probed spatial range s_{min}, s_{max} are intercompared, i.e., $\max(|\Delta v_r|) \equiv |v_r^{fit}(s_{max}) - v_r^{fit}(s_{min})|$ (the obtained values are listed in column nine of Table 9). A slope of this kind could be a signature of ordered rotation inside the GC, however, the rotation axis has to have a significant projected component onto the R.A.-axis for the signal to be contained in our data set.

In this context we note, however, that a particular difficulty in the interpretation of the radial velocity profiles, inherent to our data set, is imposed by the instability of the wavelength calibration, which potentially originates from residual instrumental flexure. This effect was discussed at length in Section 3.4.11 and is able to mimic a drift in radial velocity from scan to scan—exactly in the same way as rotation would be expected to work. The amplitude of the wavelength-solution drift is on the order of ~ 0.05 Å between the first and the last scan of one cluster (see Figure 24, which translates into a typical radial velocity shift of $\sim 2-5\,\mathrm{km\,s^{-1}}$, depending on the particular wavelength region. Although the residual flexure corrections presented in Section 3.4.11 have been applied to all GC spectra prior to the kinematic analysis, there still remains a slight uncertainty in the measured radial velocities, because the corrections for UVB arm data are based on a single sky line. We therefore expect that the true uncertainty of the measured radial velocity difference $\max(|\Delta v_r|)$ is on the order of $\sim 1\,\mathrm{km\,s^{-1}}$.

From an observational point-of-view, there is now growing evidence for internal rotation in a number of Galactic GCs (e.g., Meylan & Heggie 1997; Bianchini et al. 2013; Kacharov et al. 2014). Cross-checking the literature with our sample of three candidate detections, we find that rotation in NGC104 has been previously measured with $\sim 6\,\mathrm{km\,s^{-1}}$ (Meylan & Mayor 1986; Anderson & King 2003), although a direct comparison with our results ($\max(|\Delta v_r|) \approx 5\,\mathrm{km\,s^{-1}}$) seems not straight-forward in regard to the special setup of our drift-scan observations. For NGC7089 Pryor et al. (1986) report a maximum velocity difference of $4.9 \pm 2\,\mathrm{km\,s^{-1}}$ between two samples of stars located at opposite sides of the cluster center along a line that is orientated 15° with respect to the north celestial pole, i.e., DEC-axis (note that the rotation axisis rotated by $\pi/2$ relative to this line). Our values ($\sim 6\,\mathrm{km\,s^{-1}}$)are compatible with this finding, as—by definition of our observation

setup—we measure radial velocity differences along the DEC-direction, and thus only the projected rotation velocity onto this axis (in this particular case one needs to multiply the value of Pryor et al. (1986) by $\cos 15^\circ \approx 0.97$ to compare it to ours). Lardo et al. (2015) find a maximum rotation amplitude of $4.7\,\mathrm{km\,s^{-1}}$ for NGC2808 from *Gaia*-ESO survey data, which covers stars with distances $0.5' \leqslant |r| \leqslant 8'$ from the center. This makes NGC2808 one of the fastest rotators in their data set, which is in general agreement with the our finding. The exact amplitudes, however, are hardly comparable because the data are sampling different parts of the cluster. As an additional validation check, we propose to cross-match our obtained profiles with existing morphological parameters from the literature, i.e., apparent ellipticity and position angle of the GCs, in order to deproject the radial velocity onto the sky-plane. Chen & Chen (2010) recently compiled a catalogue with morphological data for 116 Galactic GCs (all clusters in our sample are covered by their catalogue), which might be suitable for this task.

5.8 CORE VELOCITY DISPERSION

For the GCs studied in this work the drift scans are performed along the R.A.-axis and thus the resulting spectra at a given declination contain the contribution of all stars comprised in a stripe of length $t_{exp} \times \Delta\,\mathrm{R.A.}$ ($\Delta\,\mathrm{R.A.}$ is the drift-speed of the telecope) at this declination (see Section 4.9). Along R.A.-dimension the drift-scans have been set up symmetrically about the cluster center with a distance r_h, i.e, they start $\mathrm{R.A.}_{cen} - r_h$ and stop at $\mathrm{R.A.}_{cen} + r_h$, and thus for each cluster the relative spatial coverage along the R.A.-dimension is approximately equal (in terms of r_h), which is achieved by adjusting the drift-speed accordingly. By contrast, the sampling of the perpendicular direction, i.e., along DEC, is determined by the length of the slit, which is $11''$ and the same for all observations, and the number of executed scans (which varies from cluster to cluster). The half-light radii in our sample range from $\sim 30''$ (NGC1851) to $\sim 200''$ (NGC6656), and so it is evident that the relative spatial coverage along the DEC-dimension varies from cluster to cluster, given the finite total observing time of our data set. In addition, the luminosity profiles in our sample are vastly different, with core radii ranging from $3''$ (NGC7099; core-collapsed) to $\sim 80''$ (NGC288), and so our spectra probe different regions within the GCs. With this said, it becomes apparent that differences in the shape of the measured dispersion profiles are expected. A detailed modeling, however, requires the incorporation of additional information like, e.g., luminosity profiles, and is beyond of the scope this work.

Nevertheless, Equation 22 still offers a robust means to compute the dynamical mass based on the central velocity dispersion σ_0, assuming spherical symmetry and isotropic orbits. In order to estimate the required central dispersion value our data set offers several approaches. The first possibility is to use the *measured* velocity dispersion at the central position, which, however, will be strongly affected by noise for a number of clusters in our sample (e.g., NGC288, NGC2298, or NGC6656). This problem can be partly alleviated by averaging over the innermost bins, however then the exact number of bins needs to be consistently estimated across the sample.

Instead, the central value of the fitted profile presents a second alternative, which is devoid of any bin-to-bin fluctuations, and has a well-defined noise level that can be used to infer proper uncertainties on the derived dynamical mass. On the other hand, this quantity does not account for any small scale variations across the innermost core regions, which might originate from core-collapse or the presence of an IMBH. In addition, a robust fit is extremely difficult to achieve and might be easily biased by strong features due to bright stars along the line of sight (see Section 5.6).

In order to put the presented velocity dispersion measurements onto a common scale so that consistent mass estimates can be obtained, we therefore propose the implementation of a third approach. We first integrate the drift-scan spectra of each cluster over a common distance from the center, and then measure the central velocity dispersion on the integrated spectrum with a single *pPXF* fit. A natural length scale for this approach is the core radius r_c, but for some clusters this distance is not entirely sampled by our data. The limits are imposed by NGC288, which has an exceptionally large core radius, and we find that our data approximately sample its central region within $|r| \leqslant 0.5 r_c$. Although the exact range for NGC288 is difficult to determine because it is asymmetrically sampled and one scan is entirely missing due to a problem with the drift mode, we adopt this distance as common length scale for all clusters. In the particular case of NGC288, we integrate over all available bins and note that the obtained spectrum will marginally differ from the luminosity-weighted average integrated over $|r| \leqslant 0.5 r_c$.

The integration offers multiple advantages with respect to a bin-by-bin measurement. Above all, summing over a number of slit bins significantly increases the S/N of the resulting spectrum and the subsequent measurement will yield results with a greater significance. This will be especially helpful for NGC288, whose dispersion profile shows a considerable bin-to-bin scatter. In addition, the integration naturally weights down any contamination of single bright stars along the line-of-sight. With the proposed integration limits, a minor contamination risk still persists for NGC7078 and NGC7099, as for these core-collapsed clusters the integration area corresponds to $\sim 3''$, and thus is still on the order of a single PSF (both clusters were observed at a $\sim 1.2''$ FWHM seeing).

Before the integration can be performed, however, any slope in the radial velocity has to be removed first, as otherwise systematic radial velocity gradient will mimic an increase in the velocity dispersion. This is achieved by shifting each spectrum along the spectral direction by an amount that corresponds to the radial velocity difference from the central cluster position. This difference is estimated based on the smooth fit the radial velocity profile. The necessary resampling has to be applied with care because a preservation of the noise characteristics is crucial for a subsequent line-width measurement. The resampling is performed with a kernel convolution interpolation and for the filter function we utilize a Lanczos kernel ($a = 3$, i.e. five lobes), which is a practical approximation of the theoretically optimal *sinc* filter (e.g., Duchon 1979) and is known for its good noise characteristics. We evaluated the amount of additional correlation due to this convolution by re-measuring the complete velocity dispersion profile with the resampled data. A direct comparison to the profile obtained with the non-resampled data yielded systematic differ-

ences $\lesssim 0.3\,\mathrm{km\,s^{-1}}$ for all clusters. We thus consider this error as a source for systematic uncertainties and add it in quadrature to the error budget.

The "core" spectrum $|r| \leqslant 0.5 r_c$ is obtained by integrating the velocity-corrected and resampled spectra over the respective slit bins $|r| \leqslant 0.5 r_c$. The same step is applied to the template spectra and the subsequent *pPXF* measurement is conducted in the same way as explained in Section 5.5, although this time only the single-component analysis is performed. The resulting values are listed in the second column of Table 9, where the first error corresponds to the (random) *pPXF* measurement error, and the second reflects the (systematic) uncertainty due to the required resampling. For comparison, we also list the central dispersion integrated over the innermost arcsecond, i.e., $|r| \leqslant 0.5''$ (third column of Table 9), and the the central value of the smooth fit (fourth column). For most clusters, the core-averaged dispersion is located between the other two estimates, which reflects the basic fact that the core values are averaged over a larger area than just the innermost arcsecond, whereas the correlation length of the parabolic fit is even larger. For some clusters, e.g., NGC288 and NGC7099, the core value is the lowest of all three presented estimates. This might hint at a systematic overestimation of the velocity dispersion at low S/N (i.e., if each slit bin is fitted individually), because these two clusters (together with NGC2298) are the faintest in our sample. To further address this issue, we performed additional *pPXF* runs on the core-average spectra and used the *oversample* keyword, with which the accuracy of the computed line-profile parameters can be further increased for low-S/N data. According to Cappellari & Emsellem (2004), an oversampling of the template spectra is recommended if the velocity dispersion drops below 0.7 times the velocity scale (i.e., the pixel scale of the logarithmically rebinned data). We thus expect potential problems for NGC288, whose central dispersion is listed with $2.9 \pm 0.3\,\mathrm{km\,s^{-1}}$ (Harris 2010), and for which we obtain an average core dispersion of $4.6 \pm 0.5\,\mathrm{km\,s^{-1}}$. Nevertheless, using an oversampled template does not alter the inferred value significantly and we obtain a best-fit dispersion of $4.4 \pm 0.5\,\mathrm{km\,s^{-1}}$ (listed in parentheses in Table 9). As our estimates for NGC2298, for which no literature is listed, are very similar overall to the values inferred for NGC288, we suspect that the measurements for this cluster might be affected by the same systematics. Interestingly, re-estimating the core-averaged dispersion with an oversampled template does not change the results within the given accuracy, and so we abstain from listing the obtained value in Table 9. An interpretation of this consistency check should be made with care, since the apparent robustness of the measurement does not necessarily imply that the derived results are free from systematic biases. Follow-up high-S/N data with a resolution $R \approx 100,000$ would be needed to obtain a better sampling of the LSF in these cases, but even then the inferred value might be contaminated by bright stars along the line-of-sight. For the work presented here, it remains inconclusive whether our measurement suffers from systematic biases for very small dispersion values, and thus the dynamical masses that will be discussed in Section 6.2 have to be viewed in this context.

5.9 SUMMARY

In this section we present for each cluster a brief summary of the various effects that can be found in the corresponding flux-, velocity dispersion-, and radial velocity profiles, respectively. This is of particular importance with regard to the accuracy of the kinematic parameters presented in Table 9 and should be considered if the dynamical masses (see Section 6.2) are interpreted. For the remainder of this work we will solely focus on the kinematic parameters measured with the single-component *pPXF* implementation, but it should be noted that most, if not all conclusions also apply to the multi-component approach, given the similarity of the results of the two approaches. The following descriptions are based on Figures 44 to 53, and the values presented in Table 9.

NGC**104**: The apparent mismatch in the cross-dispersed flux profile is likely caused by systematic uncertainties in the drift-scan motion. We suspect that the scan-velocity and / or scan-direction were not appropriately chosen. The measured dispersion profile shows several distinct outliers, which are potentially caused by bright binaries along the line-of-sight. The parabolic fit shows a significant decrease with increasing distance from the center. Such a trend is generally expected for simple Plummer profiles, where the velocity dispersion drops as $\sigma \propto (1 + r^2/r_s^2)^{-\frac{1}{2}}$ (the scale radius r_s is connected to the core radius via $r_s \approx 1.56 r_c$), but the exact amount depends on the true shape of the potential. The apparent discrepancy between fit and the measurement at the cluster center (the fitted values are on average larger by $\sim 1\,\mathrm{km\,s^{-1}}$) could be due to the contamination of bright stars at larger radii, which have not been weighted-out sufficiently accurately in the fit. Support for this hypothesis is given by the measured plateau of $\sim 11\,\mathrm{km\,s^{-1}}$ at $s \approx -10''$, where the composite spectrum is expected to be devoid of any strong contamination, and so this value might come closest to the true central velocity dispersion. The peak at $s \approx -3''$ has a different characteristic shape than the central peaks observed for NGC1851, NGC1904, and NGC7078, and we thus believe that this is no sign for an IMBH, but rather an artifact from bright stars. This view is supported by the shape of the radial velocity profile at this slit position, which shows a distinct short-scale deviation from the cluster average. This is a typical feature that is expected if very few bright stars with the respective radial velocities dominate the spectrum. The global shape of the radial velocity profile shows a significant slope across the entire spatial range. Ordered rotation has been observed before for this cluster (Meylan & Mayor 1986; Anderson & King 2003), and thus it seems realistic that the expected v_r-gradient is contained in our data. A detailed investigation that incorporates known morphological parameters is required to check if our measurements are consistent with previous results. The cluster's systemic radial velocity, as estimated by the fitted value at the central position, deviates by $1\,\mathrm{km\,s^{-1}}$ from the one given listed in Harris (2010) (column seven inTable 9). We cannot conclusively answer whether this a true difference or an artifact resulting from a slight displacement of the assumed cluster center in the utilized coordinates.

NGC288: The flux profile is reproduced astonishingly well by the synthetic templates. Nonetheless, the measured velocity dispersion profile is highly uncertain, which is a combined effect of the low-S/N of the data and the low instrinsic velocity dispersion of the cluster. Due to the low surface brightness of the cluster ($\mu_V \approx\sim 20$ mag per square arcsecond; compare NGC104: $\mu_V \approx 14.5$ mag per square arcsecond; values taken from (Harris 2010)), almost all slit positions are strongly affected by single bright stars along the line-of-sight. All three velocity dispersion estimates presented in this work are systematically higher than the reference value (which is originally taken from Pryor & Meylan (1993) and based on the radial velocities of ~ 30 stars; however the actual position of stars within the cluster is not given). Checking the literature for additional estimates, we find that Lane et al. (2010) give a value of $2.7 \pm 0.8\,\mathrm{km\,s^{-1}}$ for the central velocity dispersion, based on individual radial velocities of ~ 100 stars. This value, however, is an extrapolation from their innermost data point at $r \approx 2\,\mathrm{pc}$ to the cluster center (based on a Plummer profile), whereas our data set truely samples the innermost regions $r \lesssim 1\,\mathrm{pc}$. It therefore becomes clear that for this cluster all available central dispersion estimates might suffer from their own systematic uncertainties, which makes an accurate cross-comparison hardly feasible. In this context it should be noted that around slit position $s \approx -15''$ we do see a plateau of low dispersion that is in good agreement with the lower literature values, indicating that the *pPXF* fit is in principle able to recover velocity dispersions as low as $\sim 3\,\mathrm{km\,s^{-1}}$ from our data set. It is thus likely that the higher average value originates from stellar contamination and a more sophistcated masking would be desirable to deal with this issue. A possible implementation could be to exclusively include slit positions that coincide with local minimia in the cross-dispersed flux profile. Moreover, any ordered rotation around the DEC-axis will additionally increase the line-width in our drift-scan spectra and thus mimics an enhanced velocity dispersion. Although we have no means to correct for this effect ad-hoc, it needs to be considered if our values are compared with other measurements. The fit to the dispersion profile is consistent with being flat ($\gamma = 0$) for the probed spatial range, which is consistent with the large core radius of this cluster. Detailed numerical simulations are required to see if our data can further constrain the cluster potential within r_c. The systemic radial velocity agrees well with previous estimates within the error bars. The slope of the v_r-profile shows minor indications of slow rotation, which has indeed been reported by Lane et al. (2010).

With this said, we also put forward another, more speculative attempt to explain the unexpectedly high velocity dispersion of $\geqslant 4\,\mathrm{km\,s^{-1}}$. It was noted in Section 4.7 that NGC288 shows an unusually high relative flux contribution of blue-straggler stars. This has been reported before (Bellazzini & Messineo 2000) and Figure 31 suggests that a 3% excess of BSS light is expected with respect to the other GCs in our sample. Interestingly, recent observation indicate that a significant fraction of BSSs ($\sim 40\%$ in the GCs M4 and ω Centauri) are fast rotators with rotational velocities $v \sin i \geqslant 40\ \mathrm{km\,s^{-1}}$ (Lovisi et al. 2010; Mucciarelli et al. 2014). As outlined in Section 5.6, rapidly rotating stars along the line-of-sight can potentially broaden the composite LSF, if their contribution to the cumulative flux is sufficiently high. In combination with the recent finding of Simunovic & Puzia (2014) that rapidly rotating BSSs are preferentially concentrated inside the cores of

GCs, we speculate that NGC288 might be especially susceptible to this effect, given its intrinsically very low velocity dispersion, its overabundance of BSSs, and the central spatial sampling of our spectra ($|r| \lesssim 0.5 r_c$). On the other hand, if rotation velocities are *very high* with respect to the intrinsic GC velocity dispersion, they are not expected to influence the cumulative LSF dramatically. In this case, the stellar spectrum is almost entirely washed out and its contribution to the composite spectrum is not significantly different from an additional continuum flux. The cumulative LSF will still be dominated by the diffuse composite light in this scenario and we therefore conclude that dedicated simulations will be needed to quantify this effect better. Until then, the idea of attributing parts of the elevated composite velocity dispersion to the influence of BSSs remains merely speculative. In summary, NGC288 is certainly the most difficult cluster in our sample in terms of an accurate interpretation of the inferred kinematic quantities.

NGC**362**: The match quality between observed cross-dispered profile and the synthetic counterpart is moderate. Especially for $|r| \leqslant 15''$ there are many slit bins that are only marginally affected by bright star contamination. The presented central velocity dispersions should therefore represent meaningful and robust estimates. Nevertheless, they are significantly larger than the one listed in Harris (2010). In this context it should be noted, however, that Carretta et al. (2013) report a similar systematic difference for their kinematic data. They have measured radial velocities of individual stars at various radii (the innermost bin is located at $r \approx 15''$) and require $\sigma_0 = 7.5\,\mathrm{km\,s^{-1}}$ for an acceptable fit (although their data would still be consistent with even higher values). We therefore believe that the difference of our values with respect to the literature originates—at least partly—from the fact that our values are true measurements at the innermost regions of NGC362, whereas previous studies focused on measurements at outer radii and relied on subsequent extrapolations. The fit to the dispersion profile is consistent with zero curvature, which is somewhat surprising, given that we are sampling distances more than two core radii away from center. A detailed conclusion, however, can only be drawn if our measurements are supplemented by specifically tailored numerical simulations. The radial velocity profile indicates minor rotation, although the listed significance has to be treated with care in regard to the wavelength calibration instability of our data. We note that Carretta et al. (2013) found a rotation amplitude of $2.1\,\mathrm{km\,s^{-1}}$.

NGC**1851**: The template represents a very good match to the observed profile. Due to the high surface brightness ($\mu_V = 14.25$) individual stars have less impact on the integrated light, and consequently many slit bins are available for which the brightest star contributes $\lesssim 10\%$. The fit to the dispersion profile shows significant negative curvature, suggesting follow-up simulations for an appropriate interpretation. The observed central peak might be an indication for an IMBH (Lützgendorf et al. 2013), but we refrain from premature conclusions, since bright stars along the line-of-sight could dominate the integrated LOSVDat this position. The radial velocity profile is consistent with minor rotation, as reported by Scarpa et al. (2011), who found a mean rotation velocity of $0.8\,\mathrm{km\,s^{-1}}$ for stars within $r \leqslant 11\mathrm{pc}$ (note that we probe only the innermost regions $r \lesssim 1\mathrm{pc}$). The systemic radial

velocity is in good agreement with the one listed in Harris (2010).

NGC**1904**: The observed flux profile is well matched by the synthetic templates. One strong outlier at $s \approx 12''$ can be seen, which might be caused by the incomplete spatial coverage of the *HST/WFPC2* data or by a foreground star located along the line-of sight. Similar to NGC1851, we find many bins with $L_\star/L_{tot} \lesssim 0.15$, which facilitates a robust estimate of the central velocity dispersion. The obtained smooth fit is in agreement with the utilized literature value, whereas the central *pPXF* measurements indicate a significantly higher velocity dispersion. This is in agreement with the results of Lützgendorf et al. (2013) under the assumption that the peak in our data is not caused by stellar contamination. In this case, our values can even be used to further constrain the mass of the black-hole, given the lower random uncertainties of our data. The shape of the fit is consistent with flat, which needs to be verified in numerical simulations. The indications for ordered rotation, as given by the systematic difference of the radial velocities at opposite sides of the cluster center, are barely significant. Scarpa et al. (2011) measured a rotation velocity of $1.1\,\mathrm{km\,s^{-1}}$ within the central $3'$, which is hardly comparable to our results because we only sample the innermost regions $|r| \lesssim 15''$. Our estimate on the systemic cluster motion is fully consistent with the value taken from Harris (2010). We note that the central dispersion values for NGC1904 presented in Table 9 were obtained by shifting the spatial axis by $2.7''$, so that the cluster center coincides with the apparent peak in the velocity dispersion profile.

NGC**2298**: Although this cluster has a similarly low surface brightness as NGC288, and thus may be strongly affected by single bright stars, the reproduction of the observed cross-dispersed profile is exceptionally good—even the relative strengths of the individual peaks are mostly matched. We note in passing that this could imply that *all* member stars are consistently described by the (single) utilized isochrone, which in turn has implications for cluster formation models. The measured velocity dispersion profile shows considerable scatter and one very pronounced outlier at $s \approx -7''$. A cross-check with the radial velocity data reveals that it is likely caused by a bright (foreground) star, which shows a huge radial velocity displacement with respect to the systemic motion of the cluster. Both the $\sigma(|r| \leqslant 0.5 r_c)$ and $\sigma(|r| \leqslant 0.5'')$ are significantly lower than the central value of the fit, indicating that the fit is likely biased due to stellar contamination. There is no reference value listed by Harris (2010), however a search in the literature revealed an estimate of $3.6\,\mathrm{km\,s^{-1}}$ for the central velocity dispersion (Webbink 1985). This value has to be treated with care, since it is merely the result of a model. By contrast, Geisler et al. (1995) measured radial velocities of nine RGB stars with a distances of $\sim 1 - 1.5'$ from the center. The standard deviation of the velocities in their sample is $3.7\,\mathrm{km\,s^{-1}}$, although the accuracy of the measurement is only $\sim 2\,\mathrm{km\,s^{-1}}$. Finally, de Marchi & Pulone (2007) modeled the evolution of NGC2298 based on the central velocity dispersion given by Webbink (1985) and find $\sigma(r \approx 1 - 1.5') \approx 3\,\mathrm{km\,s^{-1}}$, which is in agreement with the value from Geisler et al. (1995). Our estimate for the innermost $0.5''$ is consistent with both values, whereas the core average is already significantly larger. As in the case of NGC288, this

indicates that the *pPXF* measurement is in principle able to recover the true LOSVD if it is not dominated by single stars. Since we did not correct for any outliers in the integration over the core region, the strong outlier at $\sim -7''$ is included in the integrated spectrum and potentially impacts the composite LOSVD. An improved analysis with a careful masking of this star is therefore desirable. The radial velocity curve is slightly offset relative to the literature value and consistent with no rotation. The offset might originate from the above discussed outlier and the fit should be repeated with the respective slit bins excluded. As a concluding remark it should be mentioned that, like NGC288, NGC2298 shows a slight overabundance of BSS light in its CMD with respect to the bulk of GCs in our sample (see Figure 31). Thus, the same (theoretical) arguments as put forward for NGC288 also apply to this cluster (see above), however, in a decreased manner since the potential BSS excess is significantly less pronounced.

NGC**2808**: The constructed template provides only a moderate match to the observed flux profile. We speculate that this might be caused by uncertainties in the drift-scan observations, which were conducted in service mode for this cluster. The velocity dispersion profile shows a significant negative curvature, which needs to be addressed with follow-up simulations. In addition, it shows two strong positive outliers. The peak at $\sim -20''$ seems to be caused by a foreground star (compare the flux profiles of the observation and template, respectively), while the sharp feature at $\sim 5''$ coincides with the position of two known high-velocity stars (Lützgendorf et al. 2012a), which have relative velocities as high as $\sim 40\,\mathrm{km\,s^{-1}}$. Our obtained estimates for the central dispersion are slightly higher than the literature value and also disagree on the 1σ-level with the values of Lützgendorf et al. (2012b), who find $\sigma_0 \approx 12 \pm 2\,\mathrm{km\,s^{-1}}$ at $r = 1.2''$. Judging from the shape of the profile and considering the potential contamination by bright stars, we cannot see an obvious reason for this deviation rooting in our data and so we are left somewhat inconclusive on this issue. The radial velocity profile shows strong indication for rotation, in agreement with the findings of Lardo et al. (2015). Our estimate on the systemic velocity of the cluster is offset by $\sim 3\,\mathrm{km\,s^{-1}}$ with respect to the value listed by Harris (2010) and is of considerably higher significance. It is worth mentioning that Carretta et al. (2006) find a value of $102.4 \pm 0.9\,\mathrm{km\,s^{-1}}$ for the systemic radial velocity of NGC2808, which is already in better agreement with our result. The residual difference might originate from a slight displacement of the assumed cluster center in our work, which would directly influence the inferred central value, given the relatively strong slope in the profile.

NGC**6656**: The match quality between template and observation is good for this cluster. The dispersion profile shows significant scatter, comparable with the level observed for NGC2298. The velocity dispersion within the central arcsecond is consistent with the reference value. The fit predicts a central value that is considerably higher, but the fit is constrained only weakly in general. The large core average value might originate from the strong outlier at $s \approx -18''$, and should ideally be excluded from the integration. Since this outlier is also in the radial-velocity profile, we suspect that it is a binary along the line-of-sight, which contaminates the composite LOSVD due to its v_r-displacement with

respect to the systemic cluster motion. Our radial velocity results indicate ordered rotation, which is in agreement with the findings of Peterson & Cudworth (1994), who find a rotation velocity $\sim 6\,\mathrm{km\,s^{-1}}$ for $1' \leqslant r \leqslant 3'$. In this context, however, we emphasize again that our observational setup is only sensitive to the projected rotation onto the R.A.-axis. The systemic motion of the cluster is marginally consistent with the literature value and the observed deviation can easily be explained if the cluster center is slightly shifted.

NGC**7078**: The template profile is in excellent agreement with the observed data. The strong variations in the dispersion curve for $|r| \gtrsim 10''$ are consistent with both increased flux contributions of the brightest stars and significant deviations from the systemic radial velocity, and we thus conclude that the composite light of our drift scan is contaminated by few single bright stars along the line-of-sight for these positions. The strongly enhanced velocity dispersion in the cluster center does neither show a corresponding increase in $L_\star/L_{tot}$, nor any significant deviations from the average cluster radial velocity, and we therefore conclude that the peak is real. Detailed numerical simulations will be needed to investigate whether this feature can solely be explained by core-collapse or if an additional IMBH is required. The gradient in the radial velocity profile indicates minor rotation, in agreement with the results of Lardo et al. (2015), who find a rotation velocity of $3.6\,\mathrm{km\,s^{-1}}$. Our estimate on the systemic radial motion of the cluster is significantly lower than the value listed by Harris (2010), but in reasonable agreement with the one of Lardo et al. (2015), who find $-106.4 \pm 0.7\,\mathrm{km\,s^{-1}}$.

NGC**7089**: The synthetic and observed flux profiles match very well. The bright star contributions indicate that there should be a sufficiently high number of slit bins available, for which the expected stellar contamination is only marginal. We therefore believe that the central dispersion as indicated by the fit represents a good approximation to the true value. Interestingly, the low dispersions at $\sim -14''$, $\sim 2''$, $\sim 5''$, $\sim 9''$, and $\sim 15''$ are in better agreement with the literature results, but the LOSVD at these positions is expected to be dominated by single stars, which renders the measured values unreliable. The positive curvature of the fit, however, is probably an artifact caused by the strong positive outliers at the outer regions of the probed spatial range. Our radial velocity profile shows a strong indication for rotation, which is in agreement with the previously reported rotation velocity of $4.9 \pm 2\,\mathrm{km\,s^{-1}}$ (Pryor et al. 1986). It should be noted that most of the strong peaks in the velocity dispersion profile are accompanied by significant deviations in the radial velocity curve from the average cluster velocity. This clearly indicates a contamination of the LOSVD at these positions and is caused by a considerable displacement of individual bright stars in radial-velocity space. The derived systemic radial velocity is significantly different from the value listed in Harris (2010), but, given the large error bars of the reference value, such a difference is not unexpected. We note that (Pryor et al. 1986) find a median value of $-4.3\,\mathrm{km\,s^{-1}}$ for their sample of 69 stars, which is already in better agreement with our results.

NGC**7099**: The templates for this cluster achieve the best match to the observed cross-dispersed profile in our sample. The $L_\star/L_{tot}$-profile indicates a great contamination risk of the composite light by individual stars especially for outer radii. This effect could also be responsible for the positive curvature of the fit, but it should be noted that the significance is only very low and the result is almost consistent with a flat fit. All three presented central dispersion estimates are consistent with the literature value within the measurement uncertainties. The radial velocity profile shows a weak sign of rotation, compatible with a previous result of $1.1 \pm 0.8\,\mathrm{km\,s^{-1}}$ (Gebhardt et al. 1995), which is based on spectroscopy of individual stars. The estimate of the systemic radial velocity is in excellent agreement with the literature value.

In summary it can be stated that the findings presented in this section are not only helpful for the determination of the cluster kinematics, but will be of tremendous value for all subsequent analyses of our spectral data. The combined utilization of all available information in the form of the cross-dispersed flux profile, the flux contributions of individual bright stars, and the variations in the kinematic profiles will be a fundamental tool to help decoding the integrated light contained in our drift scan spectra. This will become particularly important for chemical abundance measurements, where we can apply the presented approach to attenuate the influence of single stars onto the respective cluster average values, and thus better recover any hidden gradients in the spatial distribution.

Part VI

DYNAMICAL MASSES

For the dynamical mass measurements we use the Scalar Virial Theorem, which is directly applicable to all isotropic and spherically symmetric systems in virial equilibrium, and does not require any assumption on the mass-to-light ratio of their stellar content. The masses derived with this approach span a range from $\log \mathcal{M}^{\rm dyn}/\,{\rm M}_\odot = 5.04$ to $\log \mathcal{M}^{\rm dyn}/\,{\rm M}_\odot = 6.14$, and give a median mass-to-light ratio $\left\langle \Upsilon_{\rm V}^{\rm dyn} \right\rangle = 1.7\ {\rm M}_\odot\ {\rm L}_\odot^{-1}$. These values are in agreement with previous observational and theoretical findings, however the associated random measurement uncertainty is significantly reduced. In particular, the median mass-to-light ratio is fully compatible with GCs that entirely consist of stars and their remnants, and does not require any additional dark gravitating component.

6 DYNAMICAL MASS MEASUREMENTS AND MASS-TO-LIGHT RATIOS

In this chapter we want to utilize the central velocity dispersions derived in Section 5.9 to compute the dynamical masses $\mathcal{M}^{dyn}$ and the V-band mass-to-light ratios Υ_V^{dyn} for our sample of GCs. There is a multiplicity of ways to estimate the mass of a stellar system, and most implementations are based on velocity dispersion measurements at various radii in combination with constraints inferred from the surface brightness profile (e.g., King 1966; Cappellari 2002, 2008; Wolf et al. 2010; Lützgendorf et al. 2013).

There has been a number of systematic mass measurements of Galactic GCs in the past (Illingworth & Illingworth 1976; Illingworth 1976; Mandushev et al. 1991; McLaughlin & van der Marel 2005), but they are mostly based on similar data and similar approaches. We therefore utilize a slightly complementary method and compare the obtained values with previous results.

In Section 6.1 we briefly sketch how mass measurements (including the above mentioned ones of Galactic GCs) are typically carried out. In Section 6.2 we present our own mass estimates based on the Scalar Virial Theorem.

6.1 THEORETICAL CONSIDERATIONS

In most measurements, the surface profiles of GCs are fitted with a *King*-profile (King 1966), which is a single-mass, isotropic, modified isothermal sphere. With respect to the classical isothermal sphere, the King model is less dense at larger radii and well behaved at the origin. Following the derivations given of Binney & Tremaine (1987), in this model the distribution function of stellar energies E is given by

$$f(E) \propto \begin{cases} \exp\{-E/\sigma_m^2\} - 1, & E < 0; \\ 0, & E \geqslant 0 \end{cases} \tag{61}$$

where σ_m is a velocity scale parameter and must not be confused with the actual velocity dispersion. This parameter is related to a radial scale length

$$r_0^2 \equiv \frac{9\sigma_m^2}{4\pi G \rho_0}, \tag{62}$$

where ρ_0 is central mass density of the model (G is the gravitational constant). The parameter r_0 is the radius at which the projected density of the isothermal sphere falls to approximately half (0.5013) of its central value, and thus is often assumed to be equivalent

to the "core" radius r_c in analogy with the common observational definition. In addition, r_t is the "tidal" radius, beyond which the density of the cluster vanishes, i.e. $\rho(r \geqslant r_t) = 0$. The concentration parameter c is defined by

$$c \equiv \log_{10}(\frac{r_t}{r_c}), \tag{63}$$

and it can be shown that there exists a one-to-one relationship between the (observable) concentration and the dimensionless central potential $-\Phi(0)/\sigma_m > 0$. King models are used in a dimensionless form, i.e., $\tilde{\rho} = \rho/\rho_0$, $\tilde{r} = r/r_0$, and $\tilde{\sigma} = \sigma_{obs}/\sigma_m$, and are fully specified by the value of the concentration parameter. Fixing c (or equivalently the central potential) essentially defines the shapes of both the velocity-dispersion profile and the internal density profile. Since r_0, ρ_0, and σ_m are connected through Equation 62, the specification of two is sufficient to determine the third parameter. In application, the (theoretical) velocity profile is obtained by solving the spherical Jeans equation (Jeans 1915) based on the best-fit density profile, where the latter itself is constrained by the surface brightness profile (assuming a constant mass-to-light ratio Υ). If the radial scale r_0 is known, the theoretical dispersion profile is scaled to match the observational data (which for most clusters is only available for outer radii, i.e., $r \gtrsim r_c$), and thus the dimensionless potential at the center receives physical values. Since the shape of the potential is known from the Jeans integration, the total mass can be inferred by evaluating the potential at the cluster's limiting radius, i.e., $r = r_t$.

In practice, the model fit in the inner parts is mostly determined by the observed surface brightness profile, and depends implicitly on the assumed value for the mass-to-light ratio. It remains unclear a priori whether the predicted value for the central velocity dispersion is a good approximation to the cluster's true kinematics, as most measurements suffer from a lack of data for the inner regions. Although King models have proven fairly successful in a number of applied cases (e.g., McLaughlin & van der Marel 2005, hereafter MM05), it is sometimes observed that the predicted dispersion deviates significantly from the innermost available kinematical data (as can be seen e.g., in Lardo et al. 2015), indicating that the model description may not be appropriate for the inner parts of the respective cluster[1]. This mismatch effect was systematically analyzed by Zocchi et al. (2012), who find that King models indeed offer a good representation of the observed brightness profiles, but often lead to less satisfactory fits to the available kinematical data. Moreover, their results indicate that the derived GC mass is significantly model dependent and can be constrained better only with an improved spatial sampling of the available kinematical data.

A somewhat complementary approach for the measurement of dynamical masses is based on the Scalar Virial Theorem. This theorem does not require any assumption on

1 It should be noted that although King models are generally assumed to represent the Galactic GCs reasonably well, they are known to be inadequate for many old GCs (see MM05 for a comprehensive discussion on the utilization of King models). This is usually explained by mass segregation that results from energy equipartition and / or velocity anisotropy in well-relaxed stellar systems with a range of stellar masses (i.e, with a spatially non-constant Υ). To account for this issue, extensions to the King model have been developed (Da Costa & Freeman 1976; Gunn & Griffin 1979)

Υ_V^{dyn}, and is directly applicable to all isotropic and spherically symmetric systems in virial equilibrium. For a stellar system in isolation, i.e., with no external field, the Virial Theorem reads

$$2T = -W \approx 0.4\, GM^2/r_h, \tag{64}$$

where T and W are the kinetic and potential energy, respectively, and the numerical constant is a useful approximation to the expected density distributions in all kinds of stellar systems[2]. Rewriting Equation 64 finally yields the commonly used estimator for the dynamical mass $\mathcal{M}^{dyn}$,

$$\mathcal{M}^{dyn} \simeq 2.5\frac{3\,\sigma_0^2\,r_h}{G} \approx 1743\left(\frac{\sigma_0^2}{km^2\,s^{-2}}\right)\left(\frac{r_h}{pc}\right)M_\odot, \tag{65}$$

where $T = 3/2\,\mathcal{M}^{dyn}\,\sigma_0$ was used. It relates the central line-of-sight velocity dispersion and the size of the cluster (as traced by the half-light radius) to the total mass of the cluster. In this context it should be noted that the Virial Theorem makes predictions only for time averages, i.e., it relates the quadratic deviations of the velocities from their mean value to the spatial extent of the cluster, once it is in virial equilibrium. It is generally assumed that this velocity scatter is best measured along a line-of-sight that crosses the cluster center, as only then the projections onto the observed direction are truly radial. While the absolute value of the inferred dynamical mass might be only approximate with this approach, Equation 65 should still yield self-consistent results for our sample of GCs, as all clusters are reduced and analyzed in the same way. The Virial Theorem is sensitive to *all* mass components along the line of sight, and thus potential variations in the mass-to-light ratios within our sample of GCs, arising from different stellar populations and / or dark gravitating mass components, should be naturally accounted for.

For the sake of completeness we note that Wolf et al. (2010) recently compared different mass estimator both theoretically and observationally, and find that the most robust "half-mass" estimate $\mathcal{M}_{1/2}$ is given by

$$\mathcal{M}_{1/2} = 4\frac{\langle\sigma_{los}^2\rangle\,r_h}{G} \simeq 930\left(\frac{\langle\sigma_{los}^2\rangle}{km^2\,s^{-2}}\right)\left(\frac{r_h}{pc}\right)M_\odot. \tag{66}$$

Here, however, $\langle\sigma_{los}^2\rangle$ is the luminosity-weighted average line-of-sight velocity dispersion measured over an area that encompasses the full half-light radius. This implies, however, that Equation 66 cannot be applied to our data in a straight forward manner, because for some GCs our drift scans do not sample a sufficiently large area (these clusters will therefore be biased to higher dispersion values since the cluster center has a higher relative contribution in these cases). We therefore did not include Equation 66 in our dynamical

2 The exact value ranges between 0.44 and 0.38 for polytropic spheres of index n between 2 and 5, respectively, and the value of 0.4 has been adopted from Spitzer (1969, 1987). For King models this parameter is confined to $(0.4, 0.51)$ (Binney & Tremaine 1987).It generally reflects the relation between the half-mass (half-light) radius and the overall extent of the gravitational potential.

mass estimates, but it might be worth considering to use it as an additional consistency check in follow-up measurements.

6.2 DYNAMICAL MASS AND MASS-TO-LIGHT RATIO ESTIMATES

Before we apply Equation 65 to our sample of clusters we want to emphasize that the underlying theoretical model explicitly assumes velocity isotropy, i.e., $\sigma_{tot}^2 = 3\sigma_r^2$, where σ_r is the radial component of the three-dimensional velocity dispersion. This is not necessarily the case for GCs in case of ordered rotation (see Section 5.7) or if the gravitational potential deviates from spherical symmetry. By definition, our data contains all velocity components that contribute to the line-of-sight broadening of a given spectral line, and it is therefore only an assumption that the measured line-width is caused exclusively by random motions. Any rotation with an axis that has a non-zero projection onto the DEC-dimension will be implicitly contained in the Doppler-broadening in our scans, and thus the utilization of Equation 65 will only yield an approximation for the true mass. If we use $\max(|\Delta v_r|)$ of Table 9 as a measure for ordered rotation and assume that the observed linear gradients in the radial velocity profiles represent the scaling of the rotation amplitudes in the cluster centers, then the rotation velocity v_{rot} within $|r| \leqslant 0.5 r_c$ is very small compared to the measured velocity dispersion, in particular $v_{rot}/\sigma \lesssim 0.3$ for all our clusters. It should be noted, however, that this estimate is based on the assumptions that the measured gradient in the v_r-profile is representative for true amplitude of ordered rotation (which is only partly fulfilled because we measure the rotation in projection), and the measured velocity dispersion is a good approximation to the true velocity dispersion.

Moreover, it is worth mentioning that even the most central scan positions do not contain "purely" radial information. Because of the special drift-scan technique the recorded light is a luminosity-weighted composite of all stellar spectra confined in a band of length $2r_h$, which is positioned symmetrically about the cluster center. For some clusters, the dispersion of velocities at outer radii is significantly lower than the line-of-sight dispersion measured along the central axis (see Section 5.9 for a discussion of our measured profiles and Binney & Tremaine 1987 for detailed theoretical considerations), which in turn implies that our estimate is only a lower limit for the true central velocity dispersion. In this context, however, the luminosity weighting comes as an advantage, as a GC is typically much brighter in the center than at r_h, and so we expect the respective spectral signal to be still dominated by the cluster's central part. An accurate treatment, however, needs dedicated N-body simulations, whose analysis should ideally be similar to the setup of our observations, i.e., they should be "scanned" in similar way, and only then a one-to-one comparison between the observed dispersion profile and model predictions can be made. These considerations have to be kept in mind for any interpretation of the results presented below.

We computed the dynamical masses for our sample of eleven GCs with Equation 65 and the central velocity dispersion estimates presented in Table 9. The required half-light radii (in arcseconds) were taken from the catalog of Harris (2010) and converted to the

GC	$\log_{10} \mathcal{M}^{\mathrm{dyn}} / \mathrm{M}_\odot$	$\Upsilon_V^{\mathrm{dyn}}$ $[\mathrm{M}_\odot\ \mathrm{L}_\odot^{-1}]$	$\Upsilon_{V,\mathrm{pred}}$ $[\mathrm{M}_\odot\ \mathrm{L}_\odot^{-1}]$	$\Upsilon_{V,\mathrm{lit}}^{\mathrm{dyn}}$ $[\mathrm{M}_\odot\ \mathrm{L}_\odot^{-1}]$
NGC104	$6.06^{+0.02}_{-0.02}$	$1.95^{+0.12}_{-0.11}$	$2.68^{+0.25}_{-0.25}$	$1.33^{+0.59}_{-0.48}$
NGC288	$5.35^{+0.11}_{-0.12}$	$4.55^{+1.33}_{-1.13}$	$1.42^{+0.37}_{-0.29}$	$2.15^{+0.98}_{-0.80}$
NGC362	$5.44^{+0.04}_{-0.04}$	$1.13^{+0.12}_{-0.11}$	—	—
NGC1851	$5.53^{+0.05}_{-0.05}$	$1.67^{+0.20}_{-0.19}$	$2.21^{+0.09}_{-0.09}$	$1.61^{+0.71}_{-0.58}$
NGC1904	$5.26^{+0.05}_{-0.05}$	$1.43^{+0.19}_{-0.18}$	$2.02^{+0.07}_{-0.13}$	$1.16^{+0.52}_{-0.42}$
NGC2298	$5.14^{+0.09}_{-0.10}$	$3.11^{+0.70}_{-0.61}$	—	—
NGC2808	$6.14^{+0.03}_{-0.03}$	$1.43^{+0.12}_{-0.11}$	—	$1.46^{+0.72}_{-0.56}$
NGC6656	$6.01^{+0.03}_{-0.03}$	$1.73^{+0.12}_{-0.11}$	$2.05^{+0.03}_{-0.09}$	$2.07^{+1.15}_{-0.85}$
NGC7078	$6.06^{+0.03}_{-0.03}$	$2.02^{+0.16}_{-0.14}$	—	—
NGC7089	$5.87^{+0.03}_{-0.03}$	$1.72^{+0.14}_{-0.13}$	$2.06^{+0.03}_{-0.03}$	$0.98^{+0.44}_{-0.36}$
NGC7099	$5.04^{+0.08}_{-0.08}$	$1.17^{+0.23}_{-0.21}$	—	—

Table 10: Dynamical masses and mass-to-light ratios for our sample of eleven GCs. Consecutive columns list the cluster number, the logarithm of the dynamical mass (this work), the dynamical mass-to-light ratio (this work), the predicted mass-to-light ratio of KM09 based on population synthesis models and dynamical evolution, and the inferred dynamical mass-to-light ratio of MM05. The superscript index denotes the uncertainty to larger values, the subscript index to lower values.

correct scale by means of the distance modulus μ_V (taken from the same catalogue)[3]. The decadal logarithms of the obtained dynamical masses for the core velocity dispersion $\sigma(|r| \leqslant 0.5 r_c)$ are listed in column two of Table 10 (We only list the values based on the core velocity dispersion because they are considered to be the most consistent estimate across our sample; in what follows we generally refer to these values unless otherwise noted). The uncertainties were estimated with 10^4 Monte-Carlo realizations based on the standard errors of the velocity dispersions, and assuming a $3''$ uncertainty on r_h and 0.05 on μ_V, respectively. The latter two values were assumed ad hoc, as no consistent error estimates could be found in the literature. The uncertainties listed in Table 10 denote the 68% confidence interval for our measurement. The masses in our sample span a typical GC mass range from $\log \mathcal{M}^{\mathrm{dyn}}/\mathrm{M}_\odot = 5.04 \pm 0.08$ for NGC7099 to $\log \mathcal{M}^{\mathrm{dyn}}/\mathrm{M}_\odot = 6.14 \pm 0.03$ for NGC2808, with a homogenous sampling across the covered range.

We also computed the mass-to-light ratios $\Upsilon_V^{\mathrm{dyn}}$ based on the integrated V-band magnitudes listed by Harris (2010). Following Mandushev et al. (1991), we plot the distribution of GCs in the $\left\{\mathcal{M}^{\mathrm{dyn}}, \Upsilon_V^{\mathrm{dyn}}\right\}$-plane in Figure 56. The obtained mass-to-light ratios are listed in column three of Table 10. It is evident that, by construction, the errors of $\Upsilon_V^{\mathrm{dyn}}$

3 Note that we did not use the distances of D10 (which were used for the template construction), because we suspect that their values might be contaminated by Galactic extinction. This issue was already discussed in Chapter 4.

and $\mathcal{M}^{\rm dyn}$ are strongly correlated, since for most clusters the uncertainty on the velocity dispersion dominates the total error budget (which enters both quantities). We therefore performed the same Monte-Carlo simulation for the mass-to-light ratios and computed the covariance between the obtained realizations for $\mathcal{M}^{\rm dyn}$ and $\Upsilon_V^{\rm dyn}$. For the V-magnitude we assumed an error of 0.03, Furthermore, following standard conventions we assumed $M_{V,\odot} = 4.83$, $R_V = 3.1$, and used the reddening estimates from Harris (2010) to account for Galactic extinction. The correlated 1σ errors are plotted as ellipses in Figure 56. The color-shading of the error ellipses marks the size of r_h and can be read off from the color bar at the right hand side of the plot. Finally, the size of the utilized plotting symbol indicates the size of the core radius (taken from Harris 2010), with bigger symbol meaning larger cores. The exact translation, however, is somewhat arbitrary and thus the scaling is merely qualitative.

Figure 56 reveals that the distribution of GCs in the $\left\{\mathcal{M}^{\rm dyn}, \Upsilon_V^{\rm dyn}\right\}$-plane is approximately consistent with the assumption that mass follows light, i.e., $\Upsilon_V^{\rm dyn} \approx$ const. Furthermore, no clear correlation of the distribution with the respective core or the half-light radii can be seen, which indicates that the dynamical parameters are mostly independent of the structural parameters. The median mass-to-light ratio based on the core velocity dispersion is $\left\langle \Upsilon_V^{\rm dyn} \right\rangle = 1.72^{+0.74}_{-0.40}$ (denoted by the triple-dot-dashed line), which is in agreement with previous results by McLaughlin (2000) and MM05, who found a median of $\Upsilon_V^{\rm dyn} \simeq 1.5$ over a sample of ~ 40 Galactic GCs by fitting King-models to the available observational data. The relative difference of $\sim 15\%$ can be easily accounted for by the usage of a different mass estimator. It is apparent that both NGC288 and NGC2298 show exceptionally high mass-to-light ratios with correspondingly large error bars. Nevertheless, for both clusters at least the mass-to-light ratio for which the mass is based on the central velocity dispersion within $|r| \leqslant 0.5''$ is consistent with the sample median (black diamonds and large ellipses). For NGC1904, and NGC7078 the same estimator produces significantly higher values than obtained with the other two dispersions, which is expected from the steep increase of the dispersion profile at the innermost arcseconds. We already argued in Sections 5.6 and 5.9 that this could be an indication for an IMBH, and it remains to be clarified if the Virial Theorem is a good approximation for these cases. We also overplot with a dot-dashed curve (and denoted MA91) the sequence found by Mandushev et al. (1991), who derived mass-to-light ratios for 32 GCs based on King (1966)-model masses (The exact parametrization of the curve is given in Equation 67 and will be used later to assess the quality of our results). Their trend, that $\Upsilon_V^{\rm dyn}$ scales weakly with $\mathcal{M}^{\rm dyn}$, i.e., that the most massive clusters have the largest mass-to-light ratios, is weakly supported by our data (especially if the two problematic cases of NGC288 and NGC2298 are excluded), although we did not attempt to fit our own relation, given the rather small sample size. Kruijssen & Mieske (2009, hereafter KM09) investigated this trend in a more theoretical manner and analyzed the dissolution time scales of GCs, based on their orbits in the Galaxy. Their models account for dissolution due to two-body relaxation and Galactic disc shocking (Kruijssen 2008), and they argue that the preferential loss of low-mass, high-M/L stars is a plausible explanation for, first, a general depletion of $\Upsilon_V^{\rm dyn}$ in most, if not all Galactic

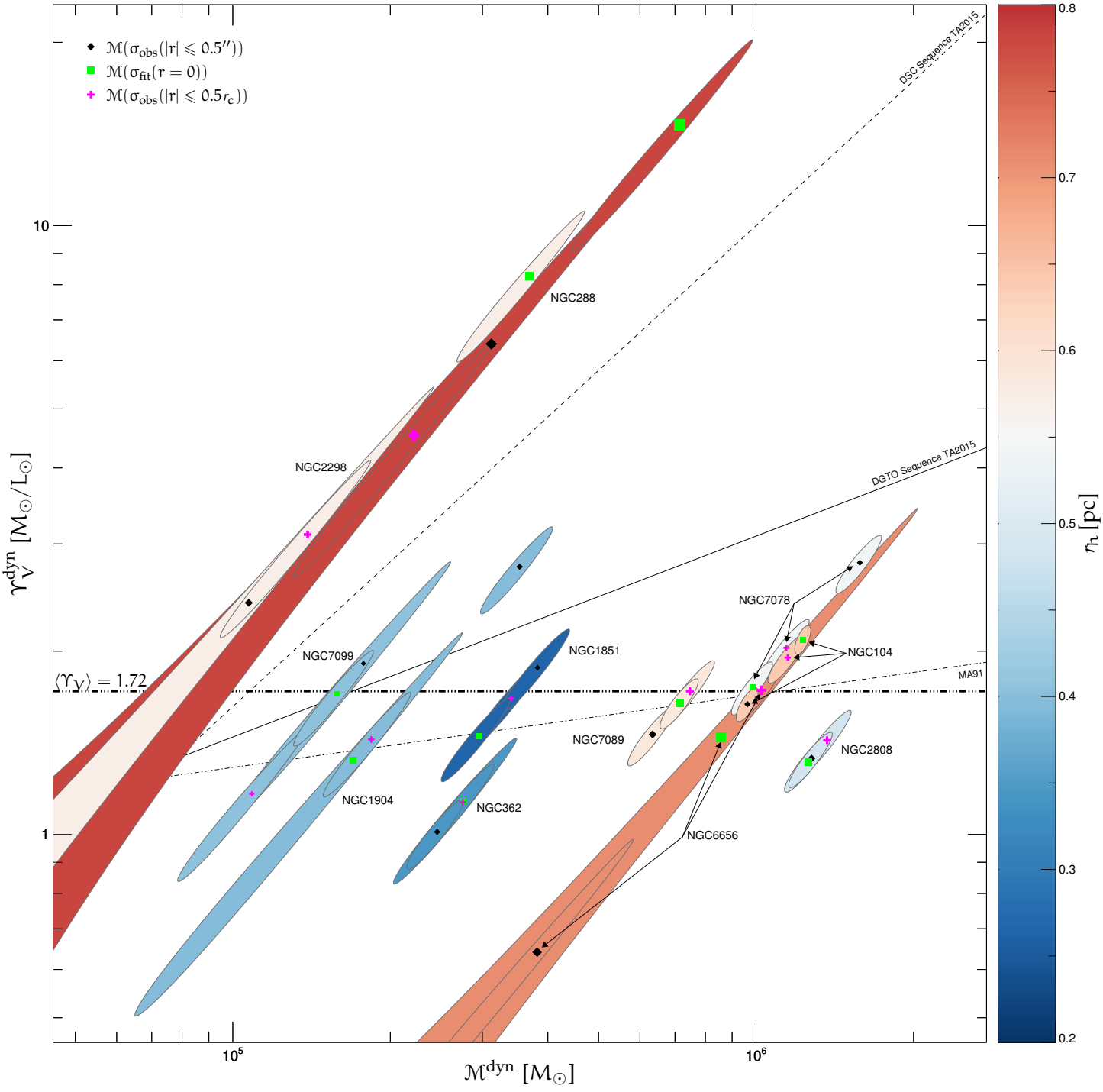

Figure 56: GC distribution in the $\left\{\mathcal{M}^{dyn}, \Upsilon_V^{dyn}\right\}$-plane. Each cluster is represented by three values, corresponding to the three velocity dispersion estimates in the single-component *pPXF*-mode (see Table 9; black diamonds: $\sigma_{obs}(|r| \leqslant 0.5'')$; green squares: $\sigma_{fit}(r = 0)$; magenta crosses: $\sigma_{obs}(|r| \leqslant 0.5r_c)$). The ellipses represent the 68%-confidence regions and their color-coding denotes the size of the respective half-light radius (see color bar on the right hand side). The size of the plot symbols scales with the size of the core radius, with larger symbols indicating larger radii. Overplotted are the sequences for Galactic GCs of Mandushev et al. (1991, dot-dashed black line), and the "dwarf-globular transition object" (DGTO; solid black) and "dark star cluster" (DSC; dashed black) sequences of Taylor et al. (2015). The median mass-to-light ratio $\langle \Upsilon_V \rangle = 1.72$ is denoted by the triple-dot-dashed black line. The *V*-band luminosities for the derivation of Υ_V^{dyn} have been taken from Harris (2010).

GCs, and, second, a mass-dependence of this depletion such that low-mass clusters are more strongly affected by this scaling. As energy equipartition causes high-mass stars to sink into the cluster center, low-mass stars are simultaneously carried to the outer parts, and thus internal evaporation and / or tidal shocking due to passages through the Galactic disc preferentially remove low mass-stars from the GC potential. As low-mass clusters have an overall weaker potential, they should be affected more strongly, and thus their mass-to-light ratios are expected to suffer from depletion most. This effect has been observed in other studies as well, both theoretically (e.g., Baumgardt & Makino 2003) and observationally (e.g., de Marchi & Pulone 2007), and, as pointed out above, implies that *all* clusters should be affected to a degree that depends on internal dynamics, as well as their location in the Galactic potential. In this context it should be noted that theoretical investigations of Banerjee & Kroupa (2011) even suggest that rapid removal of stars from the outer parts of a cluster by the strong tidal field in the inner region of our Galaxy can potentially unveil strongly concentrated sub-clusters of stellar remnant black holes, which would subsequently appear as star clusters that are gravitationally bound by an invisible mass.

KM09 computed *canonical* mass-to-light ratios based entirely on simple stellar populations and evolved them in time, based on the orbital parameters of Dinescu et al. (1999) and accounting for effects of stellar evolution, stellar remnant production, energy equipartition and cluster dissolution. Their predicted ratios for the intersection with our sample (comprising six GCs) are listed in column four of Table 10, and are denoted $\Upsilon_{V,\mathrm{pred}}$. For reference, we also list the corresponding values from MM05, based on King models, which were used as the comparison sample in the KM09 analysis. Interestingly, when compared to the MM05 values, the difference to the theoretical predictions of KM09 is considerably lower for our $\Upsilon_V^{\mathrm{dyn}}$ estimates in four out of six cases. We obtain worse agreement only for NGC288 and NGC6656, but NGC288 probably suffers from systematic problems in our dispersion measurement, and thus no statement with relevant significance can be made for this cluster anyway. On the other hand, NGC6656 is consistent with $\Upsilon_{V,\mathrm{pred}}$ at the 1.5σ-level, which can be considered still acceptable, given the fact that the theoretical predictions suffer from significant uncertainties themselves (see KM09 for a detailed discussion). In this context it should be mentioned, however, that these two clusters also have the largest uncertainties in the MM05 sample, and thus it seems that a proper mass-to-light estimate is difficult to obtain for these clusters in general. Nevertheless, we refrain from any claims related to the achieved absolute accuracy of our measurements, as the utilized mass estimator is expected to be only an approximation to the true mass (see discussion above). Furthermore, MM05 used an entirely different estimator and a systematic deviation between the two estimates would not be surprising. On the other hand, however, despite the fact the median mass-to-light ratio is larger by $\sim 0.15\%$, our data does not seem to show a significant systematical bias with respect to the MM05 values: while NGC7089's mass-to-light ratio is almost twice as high with our estimated mass, NGC1851 and NGC2808 are on par, and $\Upsilon_V^{\mathrm{dyn}}$ for NGC6656 is lower by $\sim 15\%$. Unfortunately, the two clusters with the lowest $\Upsilon_V^{\mathrm{dyn}}$ in our sample, NGC362 ($\Upsilon_V^{\mathrm{dyn}} = 1.13$) and

NGC7099 ($\Upsilon_V^{dyn} = 1.17$), are not covered by MM05, but a comparison with the Mandushev et al. (1991) results reveals that they are listed with $\Upsilon_V^{dyn} = 0.9 \pm 0.32$ and 2.37 ± 1.09, respectively, which puts them on roughly the opposite ends of the Υ_V^{dyn}-range spanned by their sample. Although the utilization of yet another reference sample may introduce additional inconsistencies, the values of Mandushev et al. (1991), at least, indicate that systematic deviations of our measurements are, if existent, not very pronounced.

Another way to assess the quality of our measurements is to consider the internal scatter of our sample in the $\left\{\mathcal{M}^{dyn}, \Upsilon_V^{dyn}\right\}$-plane. Under the assumption that there is a true, physically motivated trend underlying the observed distribution, the scatter of the data about this trend should directly represent the uncertainties of the individual measurements, and thus be a robust estimator for the achieved accuracy. As mentioned above, an increased depletion in Υ_V^{dyn} is expected with decreasing cluster mass, which, according to Mandushev et al. (1991), can be parametrized[4] as

$$\log\left(\Upsilon\,(\,M_\odot/L_\odot)^{-1}\right) = 0.12\log\left(\mathcal{M}/M_\odot\right) - 0.49. \tag{67}$$

The general shape of this function is supported by the theoretical predictions of KM09, who find a marginally different slope in the $\left\{\mathcal{M}^{dyn}, \Upsilon_V^{dyn}\right\}$-distribution of their simulated GCs. As the difference is only minor, we shall adopt Equation 67 to represent the "ideal" scaling of the mass-to-light ratio and compute the scatter of our individual $\mathcal{M}^{dyn}$-Υ_V^{dyn}-measurements about this relation. For comparison, we also compute the scatter of the data presented by MM05, assuming the Harris (2010) V-band magnitudes to infer masses from their listed Υ_V^{dyn} values. For the set of seven clusters common to both data sets we find a median residual $\Delta\Upsilon_V^{dyn} = 0.08^{+0.27}_{-0.07}$ for our mass estimates, and $\Delta\Upsilon_V^{dyn} = -0.19^{+0.54}_{-0.14}$ for the reference values, where the sub- and superscript values represent the 1σ scatter of the residuals in either direction of the assumed scaling relation. Although the smaller median residual of our data relative to the Mandushev et al. (1991)-parametrization has to be interpreted with care because our data might suffer from systematic biases, the scatter about the scaling relation is significantly lower than for the MM05 values. While this finding is certainly reassuring, it needs definite confirmation by extending the presented mass measurements to our full observational sample, which contains additional ~ 20 GCs. We note in passing that the result of the quality comparison still holds if the scatter is directly computed for Υ_V^{dyn}, i.e., without subtracting Equation 67 first. In this case the actual values for $\Delta\Upsilon_V^{dyn}$ change, but still the scatter in our measurements is significantly lower.

The fact that our sample of GCs is consistent with a constant mass-to-light ratio $\Upsilon_V^{dyn} \approx 1.7$ is intriguing for another reason. Population synthesis models that account for the evolution of a stellar population for a given age and chemistry predict typical GC mass-to-light ratios ~ 2 (e.g. McLaughlin & van der Marel 2005; McLaughlin & Fall 2008; Kruijssen

4 Note that we adopted a V-band magnitude $M_{V,\odot} = 4.83$ for the Sun to obtain Equation 67 (Mandushev et al. (1991) only give a relation between mass and $V-$band magnitude, which, however can be easily transformed into Equation 67).

& Mieske 2009). This value represents the combined Υ_V^{dyn} of all stars and their remnants in a cluster, where, according to the utilized isochrones in Chapter 4, stars close to the tip of the RGB with a mass $\sim 0.8\,M_\odot$ can be approximated by $\Upsilon_V^{dyn} \approx 10^{-2}$, low-mass stars with $\sim 0.3\,M_\odot$ have $\Upsilon_V^{dyn} \approx 30$, and faint stellar remnants even higher values. Our median value $\left\langle \Upsilon_V^{dyn} \right\rangle = 1.72^{+0.74}_{-0.40}$ is thus in perfect agreement with a population that *entirely* consists of stars (and their remnants). This is particularly interesting when compared to the recent findings of Taylor et al. (2015), who systematically analyzed the GC system of the giant elliptical galaxy NGC5128 (Centaurus A) and derived consistent dynamical masses and *V*-band magnitudes for 112 compact star clusters. Surprisingly, the distribution of these objects in the $\left\{ \mathcal{M}^{dyn}, \Upsilon_V^{dyn} \right\}$-plane forms two distinct linear sequences, which are well separated within the obtained measurement accuracy. Both sequences have a steeper slope than Equation 67, and Taylor et al. (2015) conclude that members of the shallower sequence (black solid line in Figure 56, exact parametrization provided by M. Taylor; private communication) are "dwarf-globular transistion objects" (DGTO; see also Haşegan et al. 2005), while objects on the steeper sequence (black dashed line) are termed "dark star clusters" (DSC), because they require significant dark gravitating components such as central massive black holes and / or exotically concentrated dark matter distributions to achieve $\Upsilon_V^{dyn} \geqslant 10$ (their sample extends up to $\mathcal{M}^{dyn} \approx 10^7\,M_\odot$ and $\Upsilon_V^{dyn} \approx 60\,M_\odot/L_\odot$). In our sample, only NGC288 and NGC2298 show an elevated mass-to-light ratio $\Upsilon_V^{dyn} \approx 4$, but given the large uncertainties in the respective measurements, the values cannot be considered significant enough to provide a strong statement. The fact that they approximately align with the DSC-sequence is probably a spurious artifact related to the covariance in the measurement errors. It thus remains to be seen whether the addition of the rest of our observational sample to the analysis presented here will support the relation found by Mandushev et al. (1991, and theoretically verified by KM09), or if previously undetected trends, similar to the ones reported by Taylor et al. (2015), emerge from this data set. Irrespective of the outcome, our measurements carry the potential to provide both accurate and, with respect to previous measurements, somewhat complementary mass estimates for Galactic GCs, which in turn can be used to improve our understanding of the kinematics that drive the evolution of these fascinating objects.

Part VII

SUMMARY

7

SUMMARY AND OUTLOOK

In this work we have presented consistent velocity dispersion measurements for a sample of eleven Galactic GCs. We have covered all involved steps, from the observations and the accompanying reductions, to the spectral template construction process and the subsequent kinematics measurements. We have also used the inferred velocity dispersions to compute the dynamical masses and the mass-to-light ratios. In the paragraphs below we provide a brief summary of each of these steps and conclude with a future outlook.

OBSERVATIONS

Our data set consists of VLT/X-SHOOTER spectroscopic observations of 29 GCs in the Milky Way and the Magellanic Clouds. X-SHOOTER is a single target, slit échelle spectrograph that covers a very wide spectral range ($3,000\,\text{Å} - 25,000\,\text{Å}$) at moderate resolving power $R =\approx 10,000$. By splitting the incoming beam into three independent arms (ultraviolet-blue, UVB: $3,000\,\text{Å} - 5,900\,\text{Å}$; visible, VIS: $5,300\,\text{Å} - 10,200\,\text{Å}$; near-infrared, NIR: $9,800\,\text{Å} - 25,000\,\text{Å}$), each one equipped with optimized optics, coatings, dispersive elements, and detectors, X-SHOOTER allows for an extremely high sensitivity throughout the entire spectral range (Vernet et al. 2011). Our observations utilized a slit width of $0.5''$ for the UVB arm ($R \approx 9,100$) and $0.4''$ for the VIS ($R \approx 17,400$) and NIR arms ($R \approx 11,300$), respectively. The observations were conducted in two distinct visitor-mode observing runs of four nights each and an additional service-mode run. The median seeing was $\sim 1''$ and the median airmass was ~ 1.5. The observations have been performed in drift-scan mode, where the telescope is slewed across the cluster during integration. This technique allows us to collect in one scan the average spectrum of all GC stars located in a stripe defined by the GC half-light diameter and the slit length ($11''$). In order to statistically sample the stellar content of each GC we have mapped the area within its half-light radius with repeated scans at various positions. For the sky frames the telescope has been typically offset by $\sim 1^\circ$ relative to the cluster center, and then slewed in the same way as for the object frames. Most clusters are covered with $4 - 5$ science frames and $1 - 2$ sky frames.

REDUCTIONS

Due to the échelle layout of the individual spectrographs, the target spectral energy distribution (SED) is split into 12−16 curved and highly distorted spectral orders per arm, which necessitates a sophisticated reduction process for the best possible results. We evaluated the quality of the X-SHOOTER reduction pipeline provided by ESO (Modigliani et al. 2010, v.1.5.0) by reducing a significant number of flux standard star observations from the X-SHOOTER web archive, and concentrated on X-SHOOTER's UVB and VIS arms.

For UVB arm data, we discovered a time-variable pick-up noise component, which manifests itself as an additional periodic pattern with an amplitude of ~ 2 counts. For bias frames, this feature is removed with a one-dimensional Fourier filtering technique, while for science frames we model it as part of the inter-order illumination background with one-dimensional polynomials, which are constrained at pixel positions between the curved echelle orders.

X-SHOOTER's wavelength calibration is based on ThAr lamp frames and is adjusted automatically during science mode to account for instrumental flexure occurring at off-zenith telescope positions. The required flexure compensation frames, however, have been only taken once at the start of the observation sequence of each cluster, which causes a significant shift of $\Delta\lambda \approx 0.05$ Å in the wavelength solutions between the first and the last frame of some GCs. We correct for this effect in VIS arm data by fitting the centroids of a number of sky emission lines in our cluster spectra and adjusting the wavelength solution such that the obtained spectral positions align with the expected wavelengths from the literature. This adjustment is of critical importance for subsequent radial velocity measurements of our GC sample, since a residual wavelength drift of $\Delta\lambda \approx 0.05$ Å corresponds to a radial velocity difference of $\sim 2-5\,\mathrm{km\,s^{-1}}$ and thus may mimic signatures of cluster rotation. Our correction facilitates a global wavelength accuracy of 0.02 Å, which corresponds to the instrumental limit. For UVB arm data only one sky line can be reliably fitted and the applied residual flexure correction remains with a higher uncertainty.

The implementation of the rectification process in the ESO pipeline does not account for the wavelength-dependent dispersion relation of X-SHOOTER , which leads to inaccurate uncertainty estimates of the rectified spectra. We correct for this issue by tracing the spectral pixel sizes through the rectification, and rescale the rectified error map based on the size ratio between input and output pixels.

To correct the rectified spectra for pixel-to-pixel variations we rectify a median stack of quartz lamp exposures and correct for the global structure of the measured count distribution. The utilized D2 lamp for the UVB orders $1-4$ shows a significant number of emission lines, which are removed by normalizing each wavelength bin by its median, as otherwise they would be imprinted as "pseudo absorption lines" in the GC spectra.

For extended objects like our GCs, we also recommend to account for systematic illumination inhomogeneities along the cross-dispersed direction. These are distinct on a $\pm 2\%$ level for the narrowest slit widths and we calibrate them out with dedicated sky flat field frames.

The sky subtraction for point-like objects is implemented with a spline-fit to two sky windows at either slit end of the rectified data and a subsequent interpolation to all slit positions. The break point stepping is automatically adjusted to the smoothness of the sky signal and allows for a robust removal of both weak and strong sky lines. The sky subtraction of our GC spectra is performed by averaging over all obtained sky frames in the observation sequence of each cluster and subtracting the average likewise from all cluster frames. In this context it should be noted that we did not correct for telluric absorptions and exclude the affected wavelength regions from further analyses.

The PSF in our spectrophotometric standard star observations is analytically modeled with an asymmetric Moffat profile, which accounts for the observed instrumental distortions. The subsequent extraction of the point-like object from the two-dimensional spectrum is performed by selecting an optimal extraction aperture that maximizes the S/N of each wavelength bin. We use our analytical PSF model to compensate for the associated flux losses as well as for additional flux losses at slit transit. In this way we can reconstruct the target flux to an absolute uncertainty $\lesssim 10\%$ even for narrow slit observations, while simultaneously increasing the S/N typically by a factor of ~ 1.5.

The sensitivity functions required for an absolute flux calibration are derived from spectrophotometric standard star observations and their comparison to model SEDs. For continuum regions, the systematic errors in this procedure are typically dominated by model uncertainties ($2-4\%$) and the stability of the atmosphere, but increase locally to $5-10\%$ in regions of spectral features or atmospheric absorption windows, where the smooth fit to the data is less constrained. The spectral overlap region between UVB and VIS arm ($\sim 5,300\,\text{Å} - 5,900\,\text{Å}$) is affected by the temporal variability of the dichroic transmission function and is therefore excluded from any further analysis. We have only one reliable flux standard star observation available in our data set, and so all GC frames are flux-calibrated with the same sensitivity functions. Thus, any differencesof in the photometric conditions of the observing nights are not taken into account.

Our presented reduction cascade facilitates a calibration to an uncertainty level of $\sim 0.02\,\text{Å}$ in the wavelength accuracy and $\lesssim 10\%$ in the absolute flux accuracy, which is expected to be sufficient for the kinematics measurements presented in this work.

TEMPLATE CONSTRUCTION

Our utilized approach to measure the velocity dispersion from the Doppler-broadening of the spectral features relies on fitting Doppler-broadend template spectra to the observed GC spectra. Since our drift-scan spectra typically contain contributions of $10^3 - 10^4$ stars, a detailled modeling of the template spectra becomes necessary.
For this, we use resolved *HST/ACS* photometry from Sarajedini et al. (2007) and *HST/WFPC2* photometry from Piotto et al. (2002) in combination with stellar evolutionary models from Dotter et al. (2007) to convert for each cluster star the photometric data to the fundamental stellar parameters: the effective temperature T_{eff} and the surface gravity $\log g$. All GC stars from the lower main sequence to the tip of the red giant branch are projected onto the best-fitting cluster isochrone, whose parameters (age, metallicity [Fe/H], α−element abundance [α/Fe], reddening, and distance modulus) are taken from Dotter et al. (2010) for most clusters. For GCs not covered by their analysis we obtained the necessary parameters from the literature. Blue straggler stars are modeled with isochrones of accordingly younger ages and the horizontal branch population is synthesized with a specific model that statistically accounts for mass loss in the red giant phase. The classification of a star's evolutionary phase is based on its locus in the CMD and a first approximate allocation is performed with manual color cuts. For stars that potentially belong to the main sequence, sub-giant phase, or red giant branch, this mapping is further improved by evaluating

the width of the stellar distribution about the utilized cluster isochrone, and applying a consistent clipping to remove photometric outliers.

For each considered star we compute the Euclidean distances to all model bins in the color-magnitude-space and infer the stellar parameters from the model bin for which this distance is minimal. This procedure transforms the photometric data to the $\{T_{\rm eff}, \log g\}$-plane and yields as a third parameter the bolometric luminosity of each star. We apply this technique to all stars contained within the respective GC half-light radius and rebin the obtained $\{T_{\rm eff}, \log g\}$-distribution to match the sampling of the PHOENIX stellar spectral library (Husser et al. 2013). The bolometric luminosity of each star is propagated accordingly to get the correct luminosity weights for the rebinned distribution.

The PHOENIX library offers a comprehensive set of consistently computed synthetic stellar spectra up to $T_{\rm eff} = 12,000$ K at various metallicities and α-element abundances, although it should be noted that spectra with $[\alpha/Fe] \neq 0.0$ are only available for $3,500\,{\rm K} \leqslant T_{\rm eff} \leqslant 8,000\,{\rm K}$. As a consequence, we model stars with effective temperatures $T_{\rm eff} > 12,000$ K with a temperature $T_{\rm eff} = 12,000$ K and stars with $T_{\rm eff} > 8,000$, but non-solar α-abundance, are synthesized with $[\alpha/Fe] = 0.0$. For each bin in the $\{T_{\rm eff}, \log g\}$-plane we select the appropriate spectrum from the PHOENIX library and scale the total flux with the respective luminosity weight. Integrating over all spectra finally yields the GC composite spectrum for the area covered by the GC half-light radius. We also apply this procedure to the sub-distributions of stars belonging to the individual evolutionary phases and this way obtain an average spectrum and an associated luminosity weight for each phase.

We convolve the obtained spectra with the U, B, V, R, I transmission functions of the Johnson-Cousins filter system (Johnson & Morgan 1953; Cousins 1974) and present the relative flux contributions of the various phases for each filter (see Table 6). This information can be used to improve the accuracy of spectral templates for kinematics studies of extragalactic GCs, where no resolved photometry is available, although we note that the presented values represent only approximations since we have not corrected the photometric data for observational incompleteness.

Interestingly, the obtained relative flux contributions suggest an anti-correlation between the blue straggler contribution and the main sequence contribution, with the two clusters NGC288 and NGC2298 showing an excess of blue straggler light (Figure 31). Furthermore, the main sequence contribution to the total light of a GC increases with increasing half-light radius, whereas the horizontal branch contribution decreases at the same time (Figure 32). It should be strongly emphasized, however, that it is likely that these scalings are merely a result from the photometric incompleteness of the *HST/ACS* observations, and follow-up investigations are needed to conclusively answer this question.

For our velocity dispersion measurements, we construct the approriate synthetic composite spectrum for each spatial slit bin of our drift-scan spectra individually. For this, we use the distribution of all stars in the $\{T_{\rm eff}, \log g\}$-plane, and integrate for each slit position only over the corresponding stars contributing to this position in the drift-scan. The resulting two-dimensional composite spectra show an overall satisfactory match to the observed drift-scan spectra, but are differentially shifted along the cross-dispersed direction

for some GCs. We address this issue by differentially displacing the cross-dispersed pixel grid of the synthetic spectra until a good alignment with the observed spectra is obtained. The cause for this offset remains unknown, but we suspect that it might be related to uncertainties in the VLT pointing and / or drift scan direction.

In a last step we degrade the spectral resolution of the synthetic composite spectra to match X-SHOOTER's line spread function. We measure the instrumental LSF with ThAr frames that are regularly taken as part of the standard calibrations. We fit a set of non-blended ThAr emission lines with an expanded Moffat profile to account for the negative kurtosis that is observed in the shape of the spectral lines. With the obtained parameters we construct a wavelength-dependent LSF model and convolve the synthetic composite spectra with it. This is performed for the two spectral ranges corresponding to the two considered instrumental arms (UVB,VIS) independently. The convolved spectra are subsequently usable as spectral templates in the velocity dispersion measurements.

VELOCITY DISPERSION MEASUREMENTES

We measure the kinematic properties of the eleven Galactic GCs NGC104, NGC288, NGC362, NGC1851, NGC1904, NGC2298, NGC2808, NGC6656, NGC7078, NGC7089, and NGC7099 at different distances from their centers. For each slit position, we convolve the constructed template spectrum with a velocity-broadening kernel and fit the resulting model spectrum to our observed drift-scan spectrum. We use *pPXF*, a publicly available spectrum-fitting code that reliably extracts kinematic information even at very low S/N (CE04).

In a first step, our spectra are rebinned to a logarithmic grid. This implies that the intrinsic pattern of an object's spectrum is preserved under the Doppler-shift, and facilitates a convolution with a velocity-broadening kernel in Fourier space. We use a Gauss-Hermite parametrization for the broadening kernel, which is a higher-order expansion of a Gaussian profile with which it is possible to model complex kinematic profiles arising from multiple dynamical components. The higher orders, however, are excluded in our fit, since fitting a regular Gaussian yielded the most reliable results. As a result from the fit, we obtain for each slit position the radial velocity and the velocity dispersion.

Prior to the kinematic measurements, we first evaluate the match quality between synthetic templates and observed spectra. We use the reddening law of Cardelli et al. (1989) to redden the templates, which facilitates a subsequent comparison with the observations. The match quality is best for NGC104, where almost the entire spectrum is well reproduced by the template (see Figure 38). One feature at $\sim 6,800$ Å sticks out with an elevated flux in the observed spectrum, and, interestingly, this feature is seen in the spectra of all clusters with varying strengths, however, it is not reproduced in any of the constructed templates. A residual artifact from the flux calibration seems unlikely because then the strength and shape of the feature are expected to be approximately similar for all clusters. A comparison with spectra from the literature suggests that this feature may be due to a CN absorption band, as is observed, e.g., in the spectra of carbon stars. These stars are not very common, however, and so it remains unclear whether their imprint is strong enough to show up in the GC composite spectrum. An alternative explanation could be a general

overabundance of carbon in the atmospheres of a high number of stars in the GC population. CN abundance variations have indeed been measured for this cluster (Harbeck et al. 2003), but previous studies concentrated on the absorption bands in the blue part of the spectrum and so no definite conclusions can be drawn for the true cause of the feature at $\sim 6,800$ Å.

Although the general template match quality for the other GC spectra in our sample is satisfactory as well, it is still worse than for NGC104, in particular for absorption bands associated with α-elements. A possible cause could be related to the limited parameter space of the PHOENIX spectral library, which offers $[\alpha/Fe] \neq 0.0$ only for $3,500\,K \leqslant T_{eff} \leqslant 8,000\,K$, however all GCs in our sample have $[\alpha/Fe] \gtrsim 0.2$. Since all clusters except NGC104 have a horizontal branch population that extends past the upper limit of this temperature range and, in consequence, have to be modeled with $[\alpha/Fe] = 0.0$, the contributions of the horizontal branches to the GC composite spectra in the corresponding wavelength ranges might be systematically misestimated. This discrepancy could be further enhanced due to the effect of radiative levitation, in which selected elements couple to the radiation momentum, and are brought up from the stellar interior to the outer atmospheric layers. This effect occurs for horizontal branch stars with $T_{eff} \gtrsim 11,500\,K$ and is able to increase the observed abundances for some (α-)elements by a factor of ~ 100. With this said, detailed chemical abundance measurement are required before quantitative conclusions can be drawn on this issue.

The *pPXF* fit to infer the cluster kinematics is performed in two slightly different ways. In the single-component mode we use the cumulative composite template spectrum that comprises the stars of all evolutionary phases and convolve it with a single velocity kernel. In the multi-component mode we utilize the individual composite spectra of each considered evolutionary phase and allow their relative luminosity weights to be re-estimated in the *pPXF* fit. In addition, we use an individual template for the brightest star in the drift scan at the respective slit position, which can contribute up to $\sim 50\%$ of the total flux, and assign it a separate velocity kernel with fixed zero velocity dispersion. In this way the fit is able to shift the spectrum of the brightest star relative to the other templates (which resemble the diffuse cluster light) to account for the radial velocity displacement of the star with respect to the GC systemic motion. On the other hand, any required velocity broadening can only be applied by adjusting the velocity kernel with which the diffuse cluster light templates are convolved. The idea behind this approach is to attenuate the influence of very bright stars onto the measured composite spectrum, since slit positions that are dominated by single stars are expected to show a decreased line-width in their spectra if the bright star is not rotating.

In both kinematic modes, the obtained velocity dispersion profiles show distinct variations that are not expected from theoretical models and are, therefore, explored in detail. The variations (both minima and maxima) mostly occur at slit positions where the spectrum is dominated by the flux of a single star. While deviations to lower velocity dispersions are expected if composite GC spectrum is dominated by an individual star, the reasons for positive outliers in the velocity dispersion profiles are not clear at first glance.

We explore possible causes with a toy model that blends the velocity-disperion broadened line spread function of the diffuse cluster spectrum with a second line spread function that resembles a single star. Free parameters in this model are the relative flux ratio, the radial velocity displacements between the line spread functions and the rotational broadening of the stellar line spread function. Our model suggests that the brightest star often needs to be displaced in radial velocity by $\gtrsim 2\times$ the velocity dispersion to cause the observed positive deviations in the measured velocity dispersion profiles. If random motions of the stars in the cluster potential are the only contribution to the measured velocity dispersion, then a deviation of this amplitude is rather unlikely. If the bright star, however, is part of a binary systems, or has gained recoil in previous interactions with binaries (as expected during core collpse of the cluster), then a radial velocity deviation of $\gtrsim 2\sigma$ seems much more likely and we suspect that this is the dominant cause for the observed variations in the velocity dispersion profile.

We attenuate the influence of bright stars by fitting the obtained velocity dispersion profiles with a smooth function and adjust the fitting weight such that the slit positions that show strong variations are accordingly down-weighted. Follow-up numerical simulations may be used in conjunction with the derived smooth velocity dispersion curves to constrain the radial mass profile of the globular clusters.

NGC1851, NGC1904, and NGC7078 show a distinct cusp in their velocity dispersion profiles at the respective cluster center. In the literature, this feature has been widely interpreted as a signature of an intermediate mass black hole. Although our random measurement errors are significantly smaller than most uncertainties in the literature (and thus our obtained profiles might be preferred to further constrain the black hole masses), we cannot exclude the possibility that the central cusp is also due to the contamination by bright stars, and so no quantitative conclusions can be drawn on this subject.

In order to obtain a consistent velocity dispersion estimate across our entire GC sample, we integrate for each cluster the drift scan spectra over the central core radius, i.e., over all radii $|r| \leqslant 0.5\, r_c$, and perform one *pPXF* fit on the resulting spectrum. These core-averaged velocity dispersions are in reasonable agreement with central velocity dispersions from the literature, although it should be noted that the latter are typically extrapolations from measured values at outer radii and so no direct comparison is possible.

The radial velocity profiles of NGC104, NGC2808, and NGC7089 show a significant slope. This may be interpreted as a signature of ordered rotation, which, in fact, has been reported before for these clusters. Nevertheless, our results remain somehwat uncertain because the responsible shift in wavelength might be partly caused by a residual flexure drift of the wavelength solution in the UVB arm data (our applied corrections in the UVB arm are based on the position of a single sky line and thus are only approximate).

DYNAMICAL MASSES AND MASS-TO-LIGHT RATIOS

For the dynamical mass measurements we use the Scalar Virial Theorem, which is directly applicable to all isotropic and spherically symmetric systems in virial equilibrium, and which does not require any assumption on the mass-to-light ratio of their stellar content.

We use the core-averaged velocity dispersions and take the required structural parameters (the half light radius in units of arcseconds and the distance modulus) from Harris (2010).

The dynamical masses $\mathcal{M}^{\rm dyn}$ in our sample span a typical GC mass range from $\log \mathcal{M}^{\rm dyn}/\,{\rm M}_\odot = 5.04 \pm 0.08$ for NGC7099 to $\log \mathcal{M}^{\rm dyn}/\,{\rm M}_\odot = 6.14 \pm 0.03$ for NGC2808, with a homogenous sampling across the covered range. We also compute the mass-to-light ratios $\Upsilon_V^{\rm dyn}$ based on the integrated V-band magnitudes from Harris (2010) and analyze the distribution of GCS in the $\left\{\mathcal{M}^{\rm dyn}, \Upsilon_V^{\rm dyn}\right\}$-plane. The distribution is approximately consistent with the assumption that mass follows light, i.e., $\Upsilon_V^{\rm dyn} \approx$ const. Our obtained median value is $\left\langle \Upsilon_V^{\rm dyn} \right\rangle = 1.72^{+0.74}_{-0.40}$, and thus fully compatible with GCs that entirely consist of stars and their remnants, as predicted by stellar evolutionary models (McLaughlin & van der Marel 2005; Kruijssen & Mieske 2009). NGC288 and NGC2298 have an exceptionally high mass-to-light ratio $\Upsilon_V^{\rm dyn} \gtrsim 3$, however this is likely a result from an overestimated velocity dispersion, as these two objects are among the clusters with the lowest intrinsic dispersions on the one hand, and have the lowest S/N in our data set on the other hand. If we exclude these clusters from our sample, our data support the sequence of Mandushev et al. (1991), which states a weak positive correlation between $\Upsilon_V^{\rm dyn}$ and $\mathcal{M}^{\rm dyn}$. This sequence is also expected from theoretical considerations (e.g. Kruijssen & Mieske 2009) and reflects the fact that GCs preferentially lose low-mass (i.e., high mass-to-light ratio) stars, which occupy the outer parts of a GC and are stripped in tidal interactions or lost due to internal evaporation.

To assess the quality of our mass and mass-to-light ratio measurements we compare our values to previous measurements of McLaughlin & van der Marel (2005) and the theoretical predictions of Kruijssen & Mieske (2009), who computed GC mass-to-light ratios based on internal and external dynamical evolution. Surprisingly, our estimates are closer to the theoretical predictions than the measured values by McLaughlin & van der Marel (2005), however it should be mentioned that they determine the masses based on King profiles, and thus systematic differences between the measured values may be expected. On the other hand, however, our data show a significantly reduced scatter about the sequence of Mandushev et al. (1991), which may be a result of the high consistency with which our measurements have been performed.

The recently reported sequence of "dark star clusters" in the giant elliptical galaxy NGC5128 with values as high as $\mathcal{M}^{\rm dyn} \approx 10^7\,{\rm M}_\odot$ and $\Upsilon_V^{\rm dyn} \approx 60\,{\rm M}_\odot/\,{\rm L}_\odot$ (Taylor et al. 2015) can not be confirmed for the Galactic GC system with our measurements, and, consequently, no additional dark gravitating matter component is required to explain the mass-to-light ratios resulting from our measurements.

OUTLOOK

Although the work presented here offers a self-consistent description of dynamical mass measurements for eleven Galactic GCs—including observations, data reductions, and the subsequent measurements—there is still a great number of ways to further improve the

obtained results on the one hand, and to extend the analysis to a larger sample and more comprehensive methods on the other hand.

It is certainly desirable to extend the presented data reduction cascade to the near-infrared (NIR) arm data. First steps have already been taken and the obtained results indicate that the reductions of the packaged pipeline are comparably incomplete as they are for the other two arms. In detail, the inter-order background sutbraction seems to produce similarly unsatisfactory results as in the VIS arm, especially for bright objects. The NIR arm detector (or better its electronics) seem to suffer from the "Hammer effect" (Sako et al. 2003), where the bias voltage is pertubed by the signal of a bright object. This effect manifests itself as rows that show an enhanced bias level if some pixels of this row receive a high amount of light, but since it is a very localized effect, fitting a smooth polynomial surface is insufficient. On the other hand, however, our presented algorithm for the inter-order background subtraction in UVB / VIS arm frames (see Section 3.2.2) is well suited fur this purpose, since it is based on a row-by-row treatment of the data. We have already adjusted our code to the NIR spectral format (i.e., the positions of the échelle orders on the detector) and hope to complete the implementation of the full reduction cascade soon.

In particular with regard to potential availability of NIR data in the near future, telluric corrections are a second calibration step that we hope to implement soon. The publicly available code *Molecfit* (Smette et al. 2015; Kausch et al. 2015) seems to be a promising candidate for this task, and a successful application to our data set opens up the possibility to include the telluric absorption windows in subsequent analyses (see Table 8 for currently excluded ranges).

The third major issue that still remains uncorrected in our current reduction procedures is the variable throughput of the dichroic. Theoretical considerations as well as first practical implementations, however, suggest that the signal in the affected wavelength range $5,300\,\text{Å} - 5,900\,\text{Å}$ may be fully reconstructable. Under the assumption of photon number conservation, i.e., all photons that are not transmitted into the VIS spectrograph are reflected into the UVB arm, it should in principle be possible to infer the correct object signal. In this scenario, the signals of the UVB and VIS arm need to be combined before the flux calibration, i.e., the sensitivity function needs to be computed on the merged spectrum. Adding up the count contributions of the two arms to a particular wavelength bin, however, is insufficient, since both arms have greatly different responses in the overlapping range. This difference in response implies that, although the total number of photons might be conserved, the total number of counts / electrons is not. This can be illustrated with some simple numbers: let the VIS arm typically receive 1000 photons at wavelength bin λ and let the UVB arm typically receive 100 photons at the same wavelength bin. If, due to the dichroic throughput variability, at a particular point in time only 990 photons are imaged into the VIS arm, then this change corresponds to a 1% relative decrease, while at the same time the ten additional photons correspond to a relative increase of 10% in the UVB arm. In our data, we do not not measure the absolute number of photons in a GC spectrum, but rather the relative count number with respect to the flux standard star

observation. As a consequence, the above example would lead to a 10% flux increase in the UVB GC spectrum, while the VIS arm spectrum is lower by 1%. The merged spectrum would have a ~ 9% larger flux at the respective (assuming equal weights in the merging process), although the total number of photons is conserved. Thus, to address the dichroic variability issue, one would need to know the exact response of the two spectrographs without the additional contribution of the dichroic. First tests, however, indicate that with at least three standard star observations under photometric conditions (i.e., all other parameters affecting the global throughput of the observation remain constant) the true instrumental response (without the impact of the dichroic) can be reconstructed, and thus the dichroic issue can be calibrated out. We plan to include this technique as part of our presented reduction cascade and hope to publicly release our code soon.

In the template construction process we can think of various improvements. First, a better treatment of binaries in the projection of the stars in the CMD onto the model isochrone would be preferable. Ji & Bregman (2013) show an approach which is based on evaluating the main sequence shape in the CMD. They fit multiple physically-motivated models with which they do not only to try to disentangle between single stars and binaries, but also to get an approximate estimate on the occurring mass fractions. A second improvement could be achieved by distinguishing between multiple stellar populations in the mapping process. This could be implemented by using various isochrones with different ages and chemistries. Regrettably, these parameters are only poorly known for many clusters and exhibit a certain degree of degeneracy (e.g., age-metallicity degeneracy, Worthey 1999), however recent observational studies provide promising results at least for some clusters, e.g., NGC1851 (e.g. Milone et al. 2008; Han et al. 2009), and so it is worth considering to implement this information if available.

Nevertheless, it should not be forgotten that on optimized mapping procedure is of no use if the inferred stellar parameters [Fe/H], [α/Fe], $T_{\rm eff}$, and log g are not covered by the utilized spectral library. Probably the strongest limitation of the PHOENIX library is its limited range to high effective temperatures and the non-availability of α-enhanced spectra for $T_{\rm eff} \geqslant 8,000\,\mathrm{K}$. This imposes particular restrictions on the correct modeling of the horizontal branch population, and thus prevents a direct exploration of the impact of effects like radiative levitation (Landsman 1999; Grundahl et al. 1999) onto the composite GC spectra. According to Husser et al. (2013), however, the current PHOENIX library is work in progress and future extensions to higher temperatures are planned.

A different solution to the stellar parameter coverage problem could be obtained by using an entirely different spectral library. This seems particularly desirable in the context of the "bump" feature at 6,800 Å, which may be caused by an unusually strong CN absorption. Spectral templates with a range of C/O and C/N ratios would be preferred to explore this effect further and may help to constrain the potential carbon enhancement in the atmospheres of the GC stellar populations. The *MARCS* model atmospheres (Gustafsson et al. 2008) might be a suitable tool for this task and a further investigation of the bump feature seems worthwhile to be considered—in particular in the context of detailed chemical abundance measurements, which are planned for a future project.

Furthermore, switching to an empirical, rather than a synthetic, stellar spectral library might offer the possibility to validate the obtained velocity dispersion results with respect to systematic uncertainties. In particular, the X-SHOOTER Spectral Library (Chen et al. 2014) offers ~ 200 stellar spectra, which were observed with virtually the same observational setup as our data, implying that the instrumental broadening is naturally accounted for if these spectra are used as spectral templates in the *pPXF* fit. On the other hand, the sampling in T_{eff} and log g is relatively sparse for this library (especially for the horizontal branch), and so a detailed investigation would be required first, to assess whether these spectra can be used in the template construction process.

In a future project we also plan to extend the presented mass measurements to all GCs in our observational sample. The sub-sample of eleven GCs presented in this work have been selected because they have high-accuracy *HST/ACS* or *HST/WFPC2* photometry available (Piotto et al. 2002; Sarajedini et al. 2007), which formed the basis of the presented template construction process. This, however, will not be possible for the other clusters in our sample and so we have to think of different ways to construct the required templates. A potential solution could be obtained by using the relative flux contributions and the average stellar parameters presented in Tables 6 and 7, respectively. These values depict, for a given age an metallicity, the average flux contribution of each evolutionary phase to the total composite spectrum, as well as the luminosity-weighted average stellar parameters of the phase constituent population. With these parameters it is in principle possible to construct the composite GC spectrum. Since most, if not all, of our clusters have ages and metallicities available (Harris 2010), this possibility seems worth to be pursued in a future project.

To further explore the intriguing anti-correlation between the cumulative blue straggler flux and the cumulative main sequence flux as depicted in Figure 31, detailed corrections for the photometric incompleteness are inevitable. The same holds for the correlations illustrated in Figure 32, which suggest that the relative main sequence flux increases with half light radius of the GC, while the horizontal branch contribution decreases. As a consequnce, no conclusions are drawn in this work and we plan to address this question in a future project.

The course of this work showed that it can be extremely difficult to extract proper kinematic information from our drift-scan spectra, in particular for clusters like NGC288 that have both a very low velocity dispersion and low-S/N spectral data. On the other hand, however, this does not imply that clusters that have high-S/N spectra available and exhibit alarge velocity dispersion, are easily handled in such an analysis. The reason for this difficulty roots in the drift-scan nature of our observations, which makes the integrated-light spectra susceptible to the influence of individual very bright stars contained in the scan. As a consequence, at affected slit positions the spectrum will always be biased against the kinematics of the dominating stars, and it seems that there is no easy way to resolve this issue. Our attempt to address this problem by fitting multiple-kinematic components did not yield satisfactory results, and thus it remains unclear whether we will find a future way to cope with this problem.

Nevertheless, we can think of a possible and straight-forward way to improve the accuracy of the presented core-averaged velocity dispersions. Instead of simply integrating over all slit bins with a distance $|r| \leqslant 0.5\, r_c$ from the center, one could compute a weighted average spectrum. A natural choice of the fitting weights could be given the weights that we use in the smooth fit to the velocity dispersion profile (see Equation 58), as they have been specifically constructed to down-weight slit bins whose kinematics information is potentially contaminated by single stars. It remains to be seen if this really increases the robustness of the inferred values, but it is worth to be considered in a future test.

The presented dynamical mass measurements are based on the robust, but rather simplistic Scalar Virial Theorem, which implicitly assumes isotropy, spherical symmetry, and virial equilibrium. While the dynamical structure of GCs is typically well approximated by these assumptions, recent observations suggest that a significant number of Galactic GCs can show deviations in the form of ordered rotation (e.g., Meylan & Heggie 1997; Bianchini et al. 2013; Kacharov et al. 2014) and / or strongly elongated shapes (Chen & Chen 2010). For this reason, a more sophisticated modeling process would be desirable that takes into *all* available information (e.g., apparent ellipticity, surface brightness, etc.). A possible implementation could be based on (modified) King profiles, but in this case the drift-scan mode of our observations, which implies that the contained spectral information is a luminosity weighted average across the GC half-light radius, would not be naturally included in the treatment.

In our opinion, the cleanest way to improve the accuracy on the inferred dynamical masses is to perform numerical simulations that are adjusted to resemble the observations as close as possible. In particular, they should be "scanned" in the same way, as only then a one-to-one comparison is possible. By varying the initial conditions of the simulated cluster, i.e., total mass, amount of velocity anisotropy, ordered rotation, stellar mass-to-light ratios, etc., it should be possible to use our observationally inferred velocity dispersion profile to constrain the one-dimensional mass profiles of our sample of GCs. A similar argument applies to the investigation of the presence of an intermediate-mass black hole, although it should be noted that simulations suggest that these objects are hardly detectable with velocity dispersion measurements alone (Baumgardt et al. 2005; Vesperini & Trenti 2010). It thus remains inconclusive whether our data will help to constrain the masses of these objects.

Although the approaches and techniques presented in this work were mainly developed to infer the internal kinematics of our sample of GCs, we expect them to be of tremendous value also for all future analyses of our drift-scan spectra. They will become particularly important in detailed chemical abundance measurements, which were the primary goal when proposing the project and setting up the observation campaign. The combined utilization of all available information in the form of the cross-dispersed flux profile, the flux contributions of individual bright stars, and the variations in the kinematic profiles (both velocity dispersion and radial velocity) will be a fundamental tool to help decoding the integrated light contained in the our GC spectra. When analyzing the GCs for radial

chemical gradients, the presented techniques will be certainly used to attenuate the influence of single giant stars, an thus to improve the extraction quality of the underlying cluster chemistry. In turn, the extracted information may help to better understand the dynamical evolution of the GCs on the one hand, and the assembly history of our Milky Way in the early phases of the Universe on the other hand.

BIBLIOGRAPHY

Abadi, M. G., Navarro, J. F., & Steinmetz, M. 2006, MNRAS, 365, 747

Akiyama, K. & Sugimoto, D. 1989, PASJ, 41, 991

Allard, F. 1990, PhD thesis, Centre de Recherche Astrophysique de Lyon

Altamirano, D., Belloni, T., Linares, M., et al. 2011, ApJ, 742, L17

Anderson, J. & King, I. R. 2003, AJ, 126, 772

Antonov, V. A. 1962, Solution of the problem of stability of stellar system Emden's density law and the spherical distribution of velocities

Antonucci, R. 1993, ARA&A, 31, 473

Banerjee, S. & Kroupa, P. 2011, ApJ, 741, L12

Barnbaum, C., Stone, R. P. S., & Keenan, P. C. 1996, ApJS, 105, 419

Bastian, N., Covey, K. R., & Meyer, M. R. 2010, ARA&A, 48, 339

Baumgardt, H., De Marchi, G., & Kroupa, P. 2008, ApJ, 685, 247

Baumgardt, H. & Makino, J. 2003, MNRAS, 340, 227

Baumgardt, H., Makino, J., & Hut, P. 2005, ApJ, 620, 238

Beasley, M. A., Brodie, J. P., Strader, J., et al. 2004, AJ, 128, 1623

Beasley, M. A., Brodie, J. P., Strader, J., et al. 2005, AJ, 129, 1412

Bedin, L. R., Piotto, G., Anderson, J., et al. 2004, ApJ, 605, L125

Behr, B. B. 2003, ApJS, 149, 67

Behr, B. B., Cohen, J. G., & McCarthy, J. K. 2000, ApJ, 531, L37

Behr, B. B., Cohen, J. G., McCarthy, J. K., & Djorgovski, S. G. 1999, ApJ, 517, L135

Bellazzini, M. & Messineo, M. 2000, in The Evolution of the Milky Way: Stars versus Clusters, ed. F. Matteucci & F. Giovannelli, 213

Belokurov, V., Zucker, D. B., Evans, N. W., et al. 2006, ApJ, 642, L137

Benacquista, M. J. & Downing, J. M. B. 2013, Living Reviews in Relativity, 16, 4

Bettwieser, E. & Sugimoto, D. 1984, MNRAS, 208, 493

Bianchini, P., Norris, M., van de Ven, G., & Schinnerer, E. 2015, ArXiv e-prints

Bianchini, P., Varri, A. L., Bertin, G., & Zocchi, A. 2013, ApJ, 772, 67

Binney, J. & Tremaine, S. 1987, Galactic dynamics

Bohlin, R. C. 2000, AJ, 120, 437

Bohlin, R. C. 2007, Photometric Calibration of the ACS CCD Cameras, Tech. rep.

Bohlin, R. C. & Landolt, A. U. 2015, AJ, 149, 122

Bonatto, C. & Bica, E. 2012, MNRAS, 423, 1390

Borncamp, D., Kozhurina-Platais, V., Anderson, J., & Avila, R. J. 2015, in American Astronomical Society Meeting Abstracts, Vol. 225, American Astronomical Society Meeting Abstracts, 338.04

Boyer, R., Sotirovski, P., & Harvey, J. W. 1975, A&AS, 19, 359

Braes, L. L. E. & Miley, G. K. 1971, Nature, 232, 246

Bristow, P., Vernet, J., Kerber, F., Moehler, S., & Modigliani, A. 2010, in Society of Photo-Optical Instrumentation Engineers (SPIE) Conference Series, Vol. 7735, Ground-based and Airborne Instrumentation for Astronomy III, ed. I. S. McLean, S. K. Ramsay, & H. Takami

Brodie, J. P. & Strader, J. 2006, ARA&A, 44, 193

Bullock, J. S. & Johnston, K. V. 2005, ApJ, 635, 931

Burstein, D., Faber, S. M., Gaskell, C. M., & Krumm, N. 1984, ApJ, 287, 586

Cannon, R. D., Croke, B. F. W., Bell, R. A., Hesser, J. E., & Stathakis, R. A. 1998, MNRAS, 298, 601

Cappellari, M. 2002, MNRAS, 333, 400

Cappellari, M. 2008, MNRAS, 390, 71

Cappellari, M. & Emsellem, E. 2004, PASP, 116, 138

Cardelli, J. A., Clayton, G. C., & Mathis, J. S. 1989, ApJ, 345, 245

Carlberg, J. K., Majewski, S. R., & Arras, P. 2009, ApJ, 700, 832

Carlberg, J. K., Majewski, S. R., Patterson, R. J., et al. 2011, ApJ, 732, 39

Carney, B. W. 1996, PASP, 108, 900

Carney, B. W. 2001, in Saas-Fee Advanced Course 28: Star Clusters, ed. L. Labhardt & B. Binggeli, 1

Carollo, D., Beers, T. C., Lee, Y. S., et al. 2007, Nature, 450, 1020

Carretta, E., Bragaglia, A., Gratton, R., D'Orazi, V., & Lucatello, S. 2009a, A&A, 508, 695

Carretta, E., Bragaglia, A., Gratton, R. G., et al. 2006, A&A, 450, 523

Carretta, E., Bragaglia, A., Gratton, R. G., et al. 2009b, A&A, 505, 117

Carretta, E., Bragaglia, A., Gratton, R. G., et al. 2013, A&A, 557, A138

Carretta, E., Bragaglia, A., Gratton, R. G., et al. 2010, A&A, 516, A55

Carretta, E., Gratton, R. G., Clementini, G., & Fusi Pecci, F. 2000, ApJ, 533, 215

Carretta, E., Lucatello, S., Gratton, R. G., Bragaglia, A., & D'Orazi, V. 2011, A&A, 533, A69

Carroll, B. W. & Ostlie, D. A. 1996, An Introduction to Modern Astrophysics

Casares, J. 2007, in IAU Symposium, Vol. 238, IAU Symposium, ed. V. Karas & G. Matt, 3–12

Cassisi, S. & Salaris, M. 2013, Old Stellar Populations: How to Study the Fossil Record of Galaxy Formation

Catelan, M. 2000, ApJ, 531, 826

Catelan, M. & de Freitas Pacheco, J. A. 1993, AJ, 106, 1858

Cenarro, A. J., Cardiel, N., Gorgas, J., et al. 2001a, MNRAS, 326, 959

Cenarro, A. J., Gorgas, J., Cardiel, N., et al. 2001b, MNRAS, 326, 981

Chandrasekhar, S. 1943a, ApJ, 97, 255

Chandrasekhar, S. 1943b, ApJ, 97, 263

Chen, C. W. & Chen, W. P. 2010, ApJ, 721, 1790

Chen, Y.-P., Trager, S. C., Peletier, R. F., et al. 2014, A&A, 565, A117

Conroy, C. & Spergel, D. N. 2011, ApJ, 726, 36

Côté, P., Hanes, D. A., McLaughlin, D. E., et al. 1997, ApJ, 476, L15

Cousins, A. W. J. 1974, Monthly Notes of the Astronomical Society of South Africa, 33, 149

Cushing, M. C., Vacca, W. D., & Rayner, J. T. 2004, PASP, 116, 362

Da Costa, G. S. & Freeman, K. C. 1976, ApJ, 206, 128

Dabringhausen, J., Hilker, M., & Kroupa, P. 2008, MNRAS, 386, 864

D'Antona, F., Caloi, V., Montalbán, J., Ventura, P., & Gratton, R. 2002, A&A, 395, 69

Davidge, T. J. & Harris, W. E. 1996, ApJ, 462, 255

de Marchi, G. & Pulone, L. 2007, A&A, 467, 107

de Medeiros, J. R. & Mayor, M. 1999, A&AS, 139, 433

Demarque, P., Woo, J.-H., Kim, Y.-C., & Yi, S. K. 2004, ApJS, 155, 667

Demarque, P. R. & Percy, J. R. 1964, ApJ, 140, 541

Dinescu, D. I., Girard, T. M., & van Altena, W. F. 1999, AJ, 117, 1792

D'Odorico, S., Dekker, H., Mazzoleni, R., et al. 2006, in Society of Photo-Optical Instrumentation Engineers (SPIE) Conference Series, Vol. 6269, Ground-based and Airborne Instrumentation for Astronomy, ed. I. S. McLean & M. Iye

Dotter, A., Chaboyer, B., Jevremović, D., et al. 2007, AJ, 134, 376

Dotter, A., Sarajedini, A., Anderson, J., et al. 2010, ApJ, 708, 698

Drinkwater, M. J., Gregg, M. D., Hilker, M., et al. 2003, Nature, 423, 519

Duchon, C. E. 1979, Journal of Applied Meteorology, 18, 1016

Duffau, S., Zinn, R., Vivas, A. K., et al. 2006, ApJ, 636, L97

Elmegreen, B. G. 1999, Ap&SS, 269, 469

Ernst, A., Just, A., & Spurzem, R. 2009, MNRAS, 399, 141

Falcón-Barroso, J., Sánchez-Blázquez, P., Vazdekis, A., et al. 2011, A&A, 532, A95

Ferrarese, L. & Merritt, D. 2000, ApJ, 539, L9

Fitzpatrick, E. L. 1999, PASP, 111, 63

Forbes, D. A. & Bridges, T. 2010, MNRAS, 404, 1203

Forbes, D. A. & Kroupa, P. 2011, PASA, 28, 77

Frank, M. J., Grebel, E. K., & Küpper, A. H. W. 2013, Mem. Soc. Astron. Italiana, 84, 212

Frank, M. J., Hilker, M., Mieske, S., et al. 2011, MNRAS, 414, L70

Freeman, K. & Bland-Hawthorn, J. 2002, ARA&A, 40, 487

Fregeau, J. M., Ivanova, N., & Rasio, F. A. 2009, ApJ, 707, 1533

Fusi Pecci, F., Ferraro, F. R., Bellazzini, M., et al. 1993, AJ, 105, 1145

Gebhardt, K., Pryor, C., O'Connell, R. D., Williams, T. B., & Hesser, J. E. 2000, AJ, 119, 1268

Gebhardt, K., Pryor, C., Williams, T. B., & Hesser, J. E. 1995, AJ, 110, 1699

Geisler, D., Piatti, A. E., Claria, J. J., & Minniti, D. 1995, AJ, 109, 605

Gerhard, O. E. 1993, MNRAS, 265, 213

Gieles, M. & Baumgardt, H. 2008, MNRAS, 389, L28

Girardi, L., Bressan, A., Bertelli, G., & Chiosi, C. 2000, A&AS, 141, 371

Gnedin, O. Y. & Ostriker, J. P. 1997, ApJ, 474, 223

Goodwin, S. P. 1997, MNRAS, 284, 785

Goodwin, S. P. & Bastian, N. 2006, MNRAS, 373, 752

Gratton, R., Sneden, C., & Carretta, E. 2004, ARA&A, 42, 385

Gratton, R. G., Carretta, E., & Bragaglia, A. 2012, A&A Rev., 20, 50

Gray, R. O. & Corbally, J., C. 2009, Stellar Spectral Classification

Grebel, E. K. 2000, in Astronomical Society of the Pacific Conference Series, Vol. 211, Massive Stellar Clusters, ed. A. Lançon & C. M. Boily, 262

Greggio, L., Falomo, R., Zaggia, S., Fantinel, D., & Uslenghi, M. 2012, PASP, 124, 653

Grillmair, C. J. 2009, ApJ, 693, 1118

Grillmair, C. J. 2014, ApJ, 790, L10

Grundahl, F., Catelan, M., Landsman, W. B., Stetson, P. B., & Andersen, M. I. 1999, ApJ, 524, 242

Gunn, J. E. & Griffin, R. F. 1979, AJ, 84, 752

Gustafsson, B., Edvardsson, B., Eriksson, K., et al. 2008, A&A, 486, 951

Haşegan, M., Jordán, A., Côté, P., et al. 2005, ApJ, 627, 203

Hamuy, M., Suntzeff, N. B., Heathcote, S. R., et al. 1994, PASP, 106, 566

Han, S.-I., Lee, Y.-W., Joo, S.-J., et al. 2009, ApJ, 707, L190

Harbeck, D., Smith, G. H., & Grebel, E. K. 2003, AJ, 125, 197

Harris, W. E. 1996, AJ, 112, 1487

Harris, W. E. 2001, in Saas-Fee Advanced Course 28: Star Clusters, ed. L. Labhardt & B. Binggeli, 223

Harris, W. E. 2009, ApJ, 703, 939

Harris, W. E. 2010, ArXiv e-prints

Harris, W. E. & van den Bergh, S. 1981, AJ, 86, 1627

Hauschildt, P. 1991, Non-LTE Modellatmosphären für Novae und Supernovae.

Hauschildt, P. H., Allard, F., & Baron, E. 1999a, ApJ, 512, 377

Hauschildt, P. H., Allard, F., Ferguson, J., Baron, E., & Alexander, D. R. 1999b, ApJ, 525, 871

Heggie, D. C. & Ramamani, N. 1989, MNRAS, 237, 757

Helmi, A., White, S. D. M., de Zeeuw, P. T., & Zhao, H. 1999, Nature, 402, 53

Hénault-Brunet, V., Gieles, M., Agertz, O., & Read, J. I. 2015, MNRAS, 450, 1164

Hertzsprung, E. 1911, Publikationen des Astrophysikalischen Observatoriums zu Potsdam, 63

Herwig, F. 2005, ARA&A, 43, 435

Hilker, M., Infante, L., Vieira, G., Kissler-Patig, M., & Richtler, T. 1999, A&AS, 134, 75

Horne, K. 1986, PASP, 98, 609

Horrobin, M., Goldoni, P., Royer, F., et al. 2008, in 2007 ESO Instrument Calibration Workshop, ed. A. Kaufer & F. Kerber, 221

Hubeny, I. 1997, in Lecture Notes in Physics, Berlin Springer Verlag, Vol. 497, Stellar Atmospheres: Theory and Observations, ed. J. P. De Greve, R. Blomme, & H. Hensberge, 1

Husser, T.-O., Wende-von Berg, S., Dreizler, S., et al. 2013, A&A, 553, A6

Hut, P., McMillan, S., Goodman, J., et al. 1992, PASP, 104, 981

Ibata, R. A., Gilmore, G., & Irwin, M. J. 1994, Nature, 370, 194

Illingworth, G. 1976, ApJ, 204, 73

Illingworth, G. & Illingworth, W. 1976, ApJS, 30, 227

Indahl, B. & Pessev, P. 2014, in American Astronomical Society Meeting Abstracts, Vol. 223, American Astronomical Society Meeting Abstracts #223, 152.12

Jeans, J. H. 1915, MNRAS, 76, 70

Ji, J. & Bregman, J. N. 2013, ApJ, 768, 158

Johnson, H. L. & Morgan, W. W. 1953, ApJ, 117, 313

Kacharov, N., Bianchini, P., Koch, A., et al. 2014, A&A, 567, A69

Kains, N., Bramich, D. M., Figuera Jaimes, R., et al. 2012, A&A, 548, A92

Kausch, W., Noll, S., Smette, A., et al. 2015, A&A, 576, A78

Kay, A. 1984, The AI Business: Commercial Uses of Artificial Intelligence, ed. P. H. Winston & K. A. Prendergast (Cambridge, MA, USA: Massachusetts Institute of Technology)

King, I. R. 1966, AJ, 71, 64

Koekemoer, A. M., McLean, B., McMaster, M., & Jenkner, H. 2006, in The 2005 HST Calibration Workshop: Hubble After the Transition to Two-Gyro Mode, ed. A. M. Koekemoer, P. Goudfrooij, & L. L. Dressel, 417

Koleva, M., Prugniel, P., Ocvirk, P., Le Borgne, D., & Soubiran, C. 2008, MNRAS, 385, 1998

Kristian, J., Brucato, R., Visvanathan, N., Lanning, H., & Sandage, A. 1971, ApJ, 168, L91

Kroupa, P. 2001, MNRAS, 322, 231

Kroupa, P. 2002, Science, 295, 82

Kroupa, P. 2008, in IAU Symposium, Vol. 246, IAU Symposium, ed. E. Vesperini, M. Giersz, & A. Sills, 13–22

Kruijssen, J. M. D. 2008, A&A, 486, L21

Kruijssen, J. M. D. & Mieske, S. 2009, A&A, 500, 785

Kulkarni, S. R., Hut, P., & McMillan, S. 1993, Nature, 364, 421

Kurucz, R. 1969, in Theory and Observation of Normal Stellar Atmospheres, ed. O. Gingerich, 375

Kurucz, R. L. 1970, SAO Special Report, 309

Kurucz, R. L. 1979, ApJS, 40, 1

Landsman, W. 1999, in Astronomical Society of the Pacific Conference Series, Vol. 192, Spectrophotometric Dating of Stars and Galaxies, ed. I. Hubeny, S. Heap, & R. Cornett, 235

Lane, R. R., Kiss, L. L., Lewis, G. F., et al. 2010, MNRAS, 406, 2732

Lardo, C., Pancino, E., Bellazzini, M., et al. 2015, A&A, 573, A115

Le Borgne, J.-F., Bruzual, G., Pelló, R., et al. 2003, A&A, 402, 433

Lee, H. M. 1987, ApJ, 319, 801

Lee, M. H. 1993, ApJ, 418, 147

Lee, Y.-W., Joo, J.-M., Sohn, Y.-J., et al. 1999, Nature, 402, 55

Leigh, N., Sills, A., & Knigge, C. 2011, MNRAS, 416, 1410

Leitherer, C., Alloin, D., Fritze-v. Alvensleben, U., et al. 1996, PASP, 108, 996

Lovisi, L., Mucciarelli, A., Ferraro, F. R., et al. 2010, ApJ, 719, L121

Lowrance, P. J., Kirkpatrick, J. D., & Beichman, C. A. 2002, ApJ, 572, L79

Lützgendorf, N., Gualandris, A., Kissler-Patig, M., et al. 2012a, A&A, 543, A82

Lützgendorf, N., Kissler-Patig, M., Gebhardt, K., et al. 2015, ArXiv e-prints

Lützgendorf, N., Kissler-Patig, M., Gebhardt, K., et al. 2013, A&A, 552, A49

Lützgendorf, N., Kissler-Patig, M., Gebhardt, K., et al. 2012b, A&A, 542, A129

Lützgendorf, N., Kissler-Patig, M., Noyola, E., et al. 2011, A&A, 533, A36

Lynden-Bell, D. 1967, MNRAS, 136, 101

Lynden-Bell, D. 1982, The Observatory, 102, 202

Makino, J., Tanekusa, J., & Sugimoto, D. 1986, PASJ, 38, 865

Mandushev, G., Staneva, A., & Spasova, N. 1991, A&A, 252, 94

Marigo, P., Girardi, L., Bressan, A., et al. 2008, A&A, 482, 883

Marino, A. F., Sneden, C., Kraft, R. P., et al. 2011, A&A, 532, A8

Markwardt, C. B. 2009, in Astronomical Society of the Pacific Conference Series, Vol. 411, Astronomical Data Analysis Software and Systems XVIII, ed. D. A. Bohlender, D. Durand, & P. Dowler, 251

Martin, N. F., Ibata, R. A., Chapman, S. C., Irwin, M., & Lewis, G. F. 2007, MNRAS, 380, 281

McClure, R. D. 1985, JRASC, 79, 277

McLaughlin, D. E. 2000, ApJ, 539, 618

McLaughlin, D. E. & Fall, S. M. 2008, ApJ, 679, 1272

McLaughlin, D. E., Harris, W. E., & Hanes, D. A. 1994, ApJ, 422, 486

McLaughlin, D. E. & van der Marel, R. P. 2005, ApJS, 161, 304

McLennan, J. C. 1925a, Nature, 115, 382

McLennan, J. C. 1925b, Nature, 115, 607

McNamara, B. J., Harrison, T. E., & Anderson, J. 2003, ApJ, 595, 187

Mengel, J. G. & Gross, P. G. 1976, Ap&SS, 41, 407

Merritt, D. 1997, AJ, 114, 228

Meylan, G. 2000, in Astronomical Society of the Pacific Conference Series, Vol. 211, Massive Stellar Clusters, ed. A. Lançon & C. M. Boily, 215

Meylan, G. & Heggie, D. C. 1997, A&A Rev., 8, 1

Meylan, G. & Mayor, M. 1986, A&A, 166, 122

Mieske, S., Hilker, M., Jordán, A., et al. 2008, A&A, 487, 921

Milone, A. P., Bedin, L. R., Piotto, G., & Anderson, J. 2009, A&A, 497, 755

Milone, A. P., Bedin, L. R., Piotto, G., et al. 2008, ApJ, 673, 241

Milone, A. P., Marino, A. F., Dotter, A., et al. 2014, ApJ, 785, 21

Milone, A. P., Piotto, G., Bedin, L. R., et al. 2012, Memorie della Societa Astronomica Italiana Supplementi, 19, 173

Modigliani, A., Goldoni, P., Royer, F., et al. 2010, in Society of Photo-Optical Instrumentation Engineers (SPIE) Conference Series, Vol. 7737, Observatory Operations: Strategies, Processes, and Systems III, ed. D. R. Silva, A. B. Peck, & T. Soifer

Moehler, S., Bristow, P., Kerber, F., Modigliani, A., & Vernet, J. 2010, in Society of Photo-Optical Instrumentation Engineers (SPIE) Conference Series, Vol. 7737, Observatory Operations: Strategies, Processes, and Systems III, ed. D. R. Silva, A. B. Peck, & T. Soifer

Moffat, A. F. J. 1969, A&A, 3, 455

Morton, D. C. 1991, ApJS, 77, 119

Mucciarelli, A., Lovisi, L., Ferraro, F. R., et al. 2014, ApJ, 797, 43

Murphy, M. T., Tzanavaris, P., Webb, J. K., & Lovis, C. 2007, MNRAS, 378, 221

Murphy, T. & Meiksin, A. 2004, MNRAS, 351, 1430

Newberg, H. J., Yanny, B., Rockosi, C., et al. 2002, ApJ, 569, 245

Noll, S., Kausch, W., Kimeswenger, S., et al. 2014, A&A, 567, A25

Norris, J. 1983, ApJ, 272, 245

Norris, J., Cottrell, P. L., Freeman, K. C., & Da Costa, G. S. 1981, ApJ, 244, 205

Norris, J. & Freeman, K. C. 1979, ApJ, 230, L179

Oda, M., Gorenstein, P., Gursky, H., et al. 1971, ApJ, 166, L1

Pace, G., Recio-Blanco, A., Piotto, G., & Momany, Y. 2006, A&A, 452, 493

Pancino, E., Rejkuba, M., Zoccali, M., & Carrera, R. 2010, A&A, 524, A44

Pasham, D. R., Strohmayer, T. E., & Mushotzky, R. F. 2014, Nature, 513, 74

Pasquali, A., De Marchi, G., Pulone, L., & Brigas, M. S. 2004, A&A, 428, 469

Patat, F. 2003, A&A, 400, 1183

Peñarrubia, J., Walker, M. G., & Gilmore, G. 2009, MNRAS, 399, 1275

Peterson, R. C. 1982, ApJ, 258, 499

Peterson, R. C. & Cudworth, K. M. 1994, ApJ, 420, 612

Pietrinferni, A., Cassisi, S., Salaris, M., & Castelli, F. 2004, ApJ, 612, 168

Pietrinferni, A., Cassisi, S., Salaris, M., & Castelli, F. 2006, ApJ, 642, 797

Piotto, G., Bedin, L. R., Anderson, J., et al. 2007, ApJ, 661, L53

Piotto, G., King, I. R., Djorgovski, S. G., et al. 2002, A&A, 391, 945

Portegies Zwart, S. F. & McMillan, S. L. W. 2000, ApJ, 528, L17

Portegies Zwart, S. F. & McMillan, S. L. W. 2002, ApJ, 576, 899

Prestwich, A. H., Kilgard, R., Crowther, P. A., et al. 2007, ApJ, 669, L21

Pritzl, B. J., Venn, K. A., & Irwin, M. 2005, AJ, 130, 2140

Prugniel, P. & Soubiran, C. 2001, A&A, 369, 1048

Prugniel, P. & Soubiran, C. 2004, ArXiv Astrophysics e-prints

Pryor, C., Hartwick, F. D. A., McClure, R. D., Fletcher, J. M., & Kormendy, J. 1986, AJ, 91, 546

Pryor, C. & Meylan, G. 1993, in Astronomical Society of the Pacific Conference Series, Vol. 50, Structure and Dynamics of Globular Clusters, ed. S. G. Djorgovski & G. Meylan, 357

Puzia, T. H., Kissler-Patig, M., & Goudfrooij, P. 2006, ApJ, 648, 383

Puzia, T. H., Kissler-Patig, M., Thomas, D., et al. 2005a, A&A, 439, 997

Puzia, T. H., Perrett, K. M., & Bridges, T. J. 2005b, A&A, 434, 909

Puzia, T. H., Saglia, R. P., Kissler-Patig, M., et al. 2002, A&A, 395, 45

Puzia, T. H. & Sharina, M. E. 2008, ApJ, 674, 909

Quinlan, G. D. & Shapiro, S. L. 1989, ApJ, 343, 725

Renzini, A. 2008, MNRAS, 391, 354

Richer, H. B., Heyl, J., Anderson, J., et al. 2013, ApJ, 771, L15

Rodríguez-Merino, L. H., Chavez, M., Bertone, E., & Buzzoni, A. 2005, ApJ, 626, 411

Russell, H. N. 1913, The Observatory, 36, 324

Sako, S., Okamoto, Y. K., Kataza, H., et al. 2003, PASP, 115, 1407

Salaris, M. & Cassisi, S. 2005, Evolution of Stars and Stellar Populations

Sánchez-Blázquez, P., Peletier, R. F., Jiménez-Vicente, J., et al. 2006, MNRAS, 371, 703

Sandage, A. & Wildey, R. 1967, ApJ, 150, 469

Sarajedini, A., Bedin, L. R., Chaboyer, B., et al. 2007, AJ, 133, 1658

Savage, B. D. & Mathis, J. S. 1979, ARA&A, 17, 73

Scarpa, R., Marconi, G., Carraro, G., Falomo, R., & Villanova, S. 2011, A&A, 525, A148

Scheiner, J. 1899, Astronomische Nachrichten, 148, 325

Schiavon, R. P., Caldwell, N., Morrison, H., et al. 2012, AJ, 143, 14

Schiavon, R. P., Rose, J. A., Courteau, S., & MacArthur, L. A. 2005, ApJS, 160, 163

Schödel, R., Ott, T., Genzel, R., et al. 2002, Nature, 419, 694

Schönebeck, F., Puzia, T. H., Pasquali, A., et al. 2014, A&A, 572, 22

Schönrich, R., Asplund, M., & Casagrande, L. 2014, ApJ, 786, 7

Schultz, G. V. & Wiemer, W. 1975, A&A, 43, 133

Schwarzschild, K. 1916, Sitzungsberichte der Königlich Preußischen Akademie der Wissenschaften (Berlin), 1916, Seite 189-196, 189

Searle, L. & Zinn, R. 1978, ApJ, 225, 357

Sharina, M., Aringer, B., Davoust, E., Kniazev, A. Y., & Donzelli, C. J. 2012, MNRAS, 426, L31

Sigurdsson, S. & Hernquist, L. 1993, Nature, 364, 423

Sills, A. 2010, in American Institute of Physics Conference Series, Vol. 1314, American Institute of Physics Conference Series, ed. V. Kalogera & M. van der Sluys, 105–112

Silverman, B. W. 1985, Journal of the Royal Statistical Society. Series B (Methodological), 47, pp. 1

Simunovic, M. & Puzia, T. H. 2014, ApJ, 782, 49

Simunovic, M., Puzia, T. H., & Sills, A. 2014, ApJ, 795, L10

Smette, A., Sana, H., Noll, S., et al. 2015, A&A, 576, A77

Smith, G. H. & Langland-Shula, L. E. 2009, PASP, 121, 1054

Sneden, C., Gehrz, R. D., Hackwell, J. A., York, D. G., & Snow, T. P. 1978, ApJ, 223, 168

Sparke, L. S. & Gallagher, III, J. S. 2007, Galaxies in the Universe: An Introduction (Cambridge University Press)

Spitzer, L. 1987, Dynamical evolution of globular clusters

Spitzer, Jr., L. 1969, ApJ, 158, L139

Strader, J., Chomiuk, L., Maccarone, T. J., Miller-Jones, J. C. A., & Seth, A. C. 2012, Nature, 490, 71

Tamura, N., Sharples, R. M., Arimoto, N., et al. 2006, MNRAS, 373, 588

Taylor, M., Puzia, T., Gomez, M., & Woodley, K. 2015, ArXiv e-prints

Taylor, M. A., Puzia, T. H., Harris, G. L., et al. 2010, ApJ, 712, 1191

Thomas, D. & Davies, R. L. 2006, MNRAS, 366, 510

Thomas, D., Johansson, J., & Maraston, C. 2011, MNRAS, 412, 2199

Trager, S. C., Faber, S. M., & Dressler, A. 2008, MNRAS, 386, 715

Trager, S. C., Faber, S. M., Worthey, G., & González, J. J. 2000a, AJ, 120, 165

Trager, S. C., Faber, S. M., Worthey, G., & González, J. J. 2000b, AJ, 119, 1645

Urry, C. M. & Padovani, P. 1995, PASP, 107, 803

van den Bergh, S. 2008a, MNRAS, 385, L20

van den Bergh, S. 2008b, MNRAS, 390, L51

van den Bosch, R., de Zeeuw, T., Gebhardt, K., Noyola, E., & van de Ven, G. 2006, ApJ, 641, 852

van der Marel, R. P. 2004, Coevolution of Black Holes and Galaxies, 37

van der Marel, R. P. & Franx, M. 1993, ApJ, 407, 525

van Dokkum, P. G. 2001, PASP, 113, 1420

VandenBerg, D. A., Bergbusch, P. A., & Dowler, P. D. 2006, ApJS, 162, 375

Vernet, J., Dekker, H., D'Odorico, S., et al. 2011, A&A, 536, A105

Vernet, J., Kerber, F., Mainieri, V., et al. 2010, Highlights of Astronomy, 15, 535

Vesperini, E. & Heggie, D. C. 1997, MNRAS, 289, 898

Vesperini, E., McMillan, S. L. W., D'Antona, F., & D'Ercole, A. 2013, MNRAS, 429, 1913

Vesperini, E. & Trenti, M. 2010, ApJ, 720, L179

Wallerstein, G. & Knapp, G. R. 1998, ARA&A, 36, 369

Webbink, R. F. 1985, in IAU Symposium, Vol. 113, Dynamics of Star Clusters, ed. J. Goodman & P. Hut, 541–577

West, M. J., Côté, P., Marzke, R. O., & Jordán, A. 2004, Nature, 427, 31

White, S. D. M. & Rees, M. J. 1978, MNRAS, 183, 341

Willman, B. & Strader, J. 2012, AJ, 144, 76

Wolf, J., Martinez, G. D., Bullock, J. S., et al. 2010, MNRAS, 406, 1220

Worthey, G. 1999, in Astronomical Society of the Pacific Conference Series, Vol. 192, Spectrophotometric Dating of Stars and Galaxies, ed. I. Hubeny, S. Heap, & R. Cornett, 283

Yi, S. K., Demarque, P., & Kim, Y.-C. 2004, Ap&SS, 291, 261

Yoon, S.-J., Yi, S. K., & Lee, Y.-W. 2006, Science, 311, 1129

Zocchi, A., Bertin, G., & Varri, A. L. 2012, A&A, 539, A65

Zolotov, A., Willman, B., Brooks, A. M., et al. 2009, ApJ, 702, 1058

The future is not laid out on a track.
It is something that we can decide, and to the extent that we do not violate any known laws of the universe, we can probably make it work the way that we want to.

— Alan Kay (1984)

ACKNOWLEDGMENTS

First and foremost, I would like to thank Prof. Eva Grebel for offering the project, for her guidance, her confidence in my work, and also the generous financial support throughout my PhD time. This is very much appreciated!

I also want to express my deep gratitude to my co-advisors Prof. Thomas Puzia and Dr. Anna Pasquali, in whom I found sincere mentors.

In particular, I thank Thomas for offering to work on this challenging data set, for providing multiple opportunities to come to Chile, and for his optimistic attitude, which helped pushing the limits.

Anna deserves my deepest gratitude for spending numerous hours at my desk and helping with the data reduction, for patiently listening to my endless questions, and for creating a good mood at ARI.

Although not involved in my project, Dr. Robert Schmidt was always available for inspiring and productive discussions, both work and non-work related, and therefore deserves my deep gratitude as well.

I am profoundly grateful to PD Sabine Reffert, who immediately agreed to referee this thesis despite the short-term nature of the request. Furthermore I would like to thank Prof. Cornelis Dullemond and Prof. Michael Hausmann for joining my examination comittee.

Helga Ballmann has had substantial impact on this work, by providing uncountable cups of coffee throughout my PhD time. Peter Schwekendiek was always available when I needed a faster computer, more storage, or simply somebody to talk to about nerdy tech stuff. Special thanks also to Guido Thimm for numerous conversations about cars, life, and everything. This is very much appreciated!

Without listing individual names (because I would certainly forget somebody) I thank all previous and current members of the "Galaxy-group" for making life at ARI so much fun.

A very big thanks goes to my friends Anne, Elias, Linda, Fabi, and Stefan, who made life in Heidelberg (and Chile) so much enjoyable. I will never forget this special time.

A special acknowledgement goes to my brothers, sisters, and parents for providing a world of possibilities, love, and understanding without which this work would not have been possible.

Last but certainly not least, I would like to express the deepest of all gratitudes to Yvonne, my love, my soulmate, my wingman. Thank you for your tireless support even in the most difficult situations, for your cheerful attitude, for numerous cakes, and for

teaching our wonderful son Levin to say “Papa” while I was writing this thesis. You have become such an important part of my life!